Toward the ultimate Wave-Front-Sensor for High Contrast Imaging : Application to Large Binocular and European Extremely Large Telescopes

Nicolas Levraud

To cite this version:

Nicolas Levraud. Toward the ultimate Wave-Front-Sensor for High Contrast Imaging : Application to Large Binocular and European Extremely Large Telescopes. Engineering Sciences [physics]. Université Aix-Marseille, 2023. English. NNT : 2023AIXM0001 . tel-04745974

HAL Id: tel-04745974
https://hal.science/tel-04745974v1

Submitted on 21 Oct 2024

NNT : 2023AIXM0001

THÈSE DE DOCTORAT

Soutenue à Aix-Marseille Université
le 11 Décembre 2023 par

Nicolas Levraud

Toward the ultimate Wave-Front-Sensor for High Contrast Imaging : Application to Large Binocular and European Extremely Large Telescopes

Discipline
Physique et Sciences de la Matière

Spécialité
Instrumentation

École Doctorale
ED 352 PHYSIQUE ET SCIENCES DE LA MATIERE

Laboratoire/Partenaires de recherche
Office National d'Etudes et Recherches Aérospatiales (ONERA)

Laboratoire d'Astrophysique de Marseille (LAM)

Osservatorio Astrofisico di Arcetri (INAF)

Composition du jury

Yann CLENET Directeur de recherche, LESIA	Rapporteur
Olivier LAI Chargé de recherche, OCA	Rapporteur
Maud LANGLOIS Directrice de recherche, CRAL	Présidente du jury
Samuel LEVEQUE Ingénieur, ESO	Examinateur
Thierry FUSCO Directeur de recherche, ONERA/LAM	Directeur de thèse
Simone ESPOSITO Directeur de recherche, INAF	co-Directeur de thèse
Vincent CHAMBOULEYRON Chercheur, UCSC	Invité
Jean-François SAUVAGE Ingénieur de recherche, ONERA/LAM	Invité

Affidavit

Je soussigné, Nicolas Levraud, déclare par la présente que le travail présenté dans ce manuscrit est mon propre travail, réalisé sous la direction scientifique de Thierry Fusco et Simone Esposito, dans le respect des principes d'honnêteté, d'intégrité et de responsabilité inhérents à la mission de recherche. Les travaux de recherche et la rédaction de ce manuscrit ont été réalisés dans le respect à la fois de la charte nationale de déontologie des métiers de la recherche et de la charte d'Aix-Marseille Université relative à la lutte contre le plagiat.

Ce travail n'a pas été précédemment soumis en France ou à l'étranger dans une version identique ou similaire à un organisme examinateur.

Fait à Marseille le 22/09/2023

Liste de publications et participation aux conférences

Liste des publications et/ou brevets réalisées dans le cadre du projet de thèse :

1. "Strategy for sensing petal mode in presence of AO residual turbulence with pyramid wavefront sensor", *Nicolas Levraud, Vincent Chambouleyron, Jean François Sauvage, Benoit Neichel, Mahawa Cisse, Olivier Fauvarque, Guido Agapito, Cédric Plantet, Anne Laure Cheffot, Enrico Pinna, Simone Esposito, and Thierry Fusco*, submitted in A&A

Participation aux conférences et écoles d'été au cours de la période de thèse :

1. Wavefront Sensing in the VLT/ELT era V, 2020, attended
2. SPIE : Optical Instrument Science, Technology, and Applications II (September 2021), presented "Current status of PAPYRUS : the pyramid based adaptive optics system at LAM/OHP "
3. Wavefront Sensing in the VLT/ELT era VI 2021, presented : "Differential piston tracking : variations around the Pyramid Wavefront Sensor"
4. SPIE : Astronomical Telescopes + Instrumentation (July 2022), presented "Adapting the pyramid wavefront sensor for pupil fragmentation of the ELT class telescopes"
5. Wavefront Sensing in the VLT/ELT era VII 2022, presented "Petal mode measurement and reconstruction with pyramid assisted by spatial filtering"

Résumé

Mot clé : Optique Adaptative, Extremely Large Telescope (ELT), Senseur Pyramide, Mode pétale

L'une des questions les plus importantes de l'astronomie moderne est l'existence d'une forme de vie extraterrestre. Et malgré les efforts et théories remontant jusqu'au 16e siècle, pour la science l'univers reste terriblement silencieux et vide. La recherche moderne de la vie extra-terrestre a recommencé en 1995 avec la découverte de la première exoplanète 51Peg b. Il a fallu une décennie de plus pour enfin détecter la lumière directe d'exoplanètes et pouvoir commencer à y étudier la présence de bio-marqueurs. Cette avancée a été permise par la génération des 'très grands télescopes' (miroirs de 6 à 10m) et leurs instruments, en particulier les avancées de l'optique adaptative. L'optique adaptative est une méthode qui mesure la turbulence atmosphérique grâce à un senseur de front d'onde. Puis grâce à un miroir déformable on compense cette turbulence atmosphérique. Cette étape concentre la lumière de l'étoile, facilitant sa suppression par un coronographe et rendant visible les objets proches de l'étoile comme les exoplanètes. La nouvelle génération de télescopes extrêmement grands en cours de construction (ELT, TMT et GMT, miroir de 39 à 29m) devrait augmenter le nombre d'exoplanètes directement observables. Ceci est permis par leur grande taille si l'optique adaptative permet de corriger l'‘atmosphère. Les instruments de ces télescopes sont en phase de conception et les simulations ont révélé un nouveau type de défaut, le mode pétale. Ce mode apparaît à cause de la complexité des télescopes géants, la pupille du télescope se trouvant séparée en plusieurs fragments. L'optique adaptative traite ces fragments comme des zones indépendantes, qui se trouvent déphasées les unes des autres. Cela réduit la taille effective de la pupille pour ce qui est de la résolution à la taille d'un de ces fragments de pupille. Pour l'ELT cela signifie que la résolution finale serait celle d'un télescope de 15m et pas de 39m. L'objectif de cette thèse est d'étudier le mode pétale et sa correction par l'optique adaptative. Une première étude approfondie du senseur d'optique adaptative des télescopes géants, le senseur pyramide, a été conduite pour montrer dans quelles conditions ce senseur devenait insensible au mode pétale. Ce senseur a besoin d'une étape de modulation pour étendre la dynamique de mesure et la rendre compatible avec la mesure de la turbulence atmosphérique. On a montré que cette étape de modulation empêche la mesure du mode pétale. Pour quand même être capable de mesurer le mode pétale, il est proposé de se servir de deux senseurs, l'un dédié à l'atmosphère et l'autre à la mesure du pétale. Fort de l'étude de la pyramide nous avons étudié dans quelles conditions la pyramide pourrait être utilisée comme senseur de pétale. Cela a donné naissance à des pyramides modifiées pour faciliter la mesure du mode pétale : l'ajout d'une étape de filtrage spatial pour réduire les effets de la turbulence résiduelle, et une asymétrisation de la pyramide pour augmenter la réponse à ce signal.

Les différents senseurs proposés ont été testés en simulation, et se sont montrés satisfaisants pour les conditions médianes de turbulence de l'ELT. Les solutions proposées devraient donc corriger le mode pétale et restaurer la résolution d'un miroir de 39m de l'ELT.

Abstract

Keywords : adaptive optics, Extremely Large Telescope (ELT), Pyramid Wavefront Sensor, petal mode

One of Astronomy's most important subjects is the existence of extraterrestrial life. Science started working and theorizing seriously on the subject as far as the 16th century. But so far, the universe remains empty and silent. The discovery of the first exoplanet in 1995, 51Peg b, started the modern search for extraterrestrial life. A decade later the first direct imaging of exoplanet allowed the study of the presence of biomarkers. This achievement was allowed by the 'Very Large' telescope generation (mirror from 6 to 10m) and their instruments. Adaptive optics (AO) in particular was the game-changer. A wavefront sensor allows the measurement of atmospheric turbulence, and a deformable mirror allows the correction of this turbulence. This leads to the concentration of the starlight making its suppression to study its close environment possible (this is called coronography).

The new 'extremely large' telescope generation is under construction (ELT, GMT, and TMT, with mirrors from 29 to 39m). Their size should make more exoplanets directly observable if AO functions correctly. But during the current design phase of the instrument, a new kind of defect has appeared called the petal mode. This mode appears due to the complexity of the new telescope's pupil. These pupils appear to the AO separated into multiple fragments. The AO then treats each fragment as independent areas, which ends up with dephasing between each other. The consequence is that their resolutions are limited by the size of a fragment. This makes the ELT as efficient as a 15m telescope instead of a 39m. The aim of this thesis is to study the petal mode. In particular, we studied the origin of this mode and proposed solutions. At first, we studied in detail the designated wavefront sensor of the new giant telescopes : the pyramid sensor. We showed the conditions making this sensor unable to measure the petal mode.We showed that with the modulation the PyWFS can't measure the petal mode. We propose to use 2 sensors to allow the AO to control the petal mode. One will be dedicated to the atmospheric turbulence and one to the petal mode. From our study of the pyramid we studied in which conditions (in particular the absence of modulation) the pyramid could be used as the petal mode sensor. This led to different modifications of the pyramid to ease the measurement of petal : the addition of a spatial filter to reduce the effect of residual turbulence (extendable to other wavefront sensor), and an asymetrisation of the pyramid to increase its response to petal mode. The different proposed sensors have been tested in simulation and show satisfying result for median conditions of the ELT. The proposed solutions should then correct the petal mode for the ELT and restore the expected resolution of a 39m telescope.

Résumé étendu

Mot clé : Optique adaptative, Senseur Pyramide, Extremely Large Telescope (ELT)

L'un des objectifs de l'Astronomie est de répondre à la question : Existe t-il des formes de vies extra terrestres ? La question a pendant longtemps été hors de portée de la recherche scientifique et confinée à la philosophie et la fiction. Le système solaire est le premier espace qui a pu être étudié scientifiquement et on l'a confirmé exempt de vie extra-terrestre. Mais depuis 1995 et la découverte de la première exoplanète, un nouveau champ d'analyse astronomique s'est ouvert. La question de l'existence de la vie en dehors de la Terre se résout maintenant par l'étude spectrale de la lumière d'une exoplanète. Grâce à une étude spectromètrique on peut déduire la composition de la planète a la recherche de biomarqueurs, molécules liées à la présence de la vie.

Mais l'obtention de ce fameux spectre est extrêmement difficile. Pour y arriver, la première étape est la capacité d'imager directement une exoplanète. En effet les exoplanètes sont bien moins lumineuse que leur étoile et de plus situées très proches de leur étoile. L'intense lumière de cette dernière éblouit l'instrument et rend difficile la séparation des deux sources lumineuses. Ainsi il a fallu attendre 2004 pour enregistrer la première image d'une exoplanète 2M1207b (Chauvin et al. (2004)). Mais cette exoplanète est une géante gazeuse (5 fois la masse de Jupiter) et est situé très loin de son étoile (46 ua) et n'est donc pas un candidat à la présence de vie. Pour détecter des planètes plus petites et plus proches de leur étoile il faut des instruments capable de mieux concentrer la lumière de l'étoile ce qui veut dire améliorer leur résolution angulaire. La résolution est définie par la taille angulaire de la tache image créée par une étoile au plan focal du télescope. On appelle cette image la fonction d'étalement de point (Point Spread Fonction, PSF en anglais) et sa taille minimale théorique est de $1.06\lambda/D$ avec D la taille de la pupille du télescope et λ la longeur d'onde d'observation. Améliorer la résolution angulaire d'un instrument passe donc nécessairement par l'augmentation du diamètre du télescope.

A cause de la difficulté d'envoyer de grands objets dans l'espace, les plus grands télescopes sont situés au sol. Ces télescopes terrestres sont limités par un phénomène supplémentaire : la turbulence atmosphérique qui floute les images au delà de quelques dizaines de centimètres de diamètre. L'atmopshère est mise en mouvement par les différences de températures de l'air. Ces mouvements perturbent la porpagation de la lumère. Un observateuyr constate des modification désordonnées rapides de la tache image, qui devient une image flouté quand un instrument acquiert une image longue pause. Pour quantifier l'amplitude de la turbulence atmosphérique on utilise le paramètre de Fried noté r_0. Ce paramètre quantifie la taille équivalent de télescope qui verrait sa résolution réduite par la turbulence atmosphérique. Cette grandeur est

typiquement de 10 à 20cm dans les bons sites astronomiques. En présence de turbulence atmosphérique la taille moyenne de la PSF devient λ / r_0. Dans des bons sites, ceci correspond à une résolution angulaire de l'ordre de l'arcseconde. Par exemple on a besoin d'une résoltuion de 0.1 arcseconde pour résoudere un couple Terre Soleil situé a 10 parsecs. Un télescope de 8m a une résolution limité par la diffraction en bande spectrale H de 0.04 arcseconde. Mais la turbulence atmosphérique limite sa résolution a 1 arcseconde sur les bon sites, ce qui rend l'observation impossible si on est limité par la turbulence atmosphérique.

Une technique permettant de corriger le flou atmosphérique est apparue dans les années 90 : l'optique Adaptative (OA). Cette technique mesure les aberrations optiques créées par l'atmosphère en mouvement, et applique une correction (les aberrations opposées) grâce à un miroir déformable ce qui restaure la résolution maximum du télescope. L'effet de l'OA sur la PSF est montré en Figure 1 L 'OA concentre la lumière étalée par la turbulence dans la PSF théorique du télescope. La qualité de cette concentration dépend de la qualité de l'OA et entre autre du nombre d'actuateurs du télescope qui va déterminer la taille de la zone où la lumière est concentrée. Au delà de cette taille, la PSF redevient celle limitée par la turbulence atmosphérique.

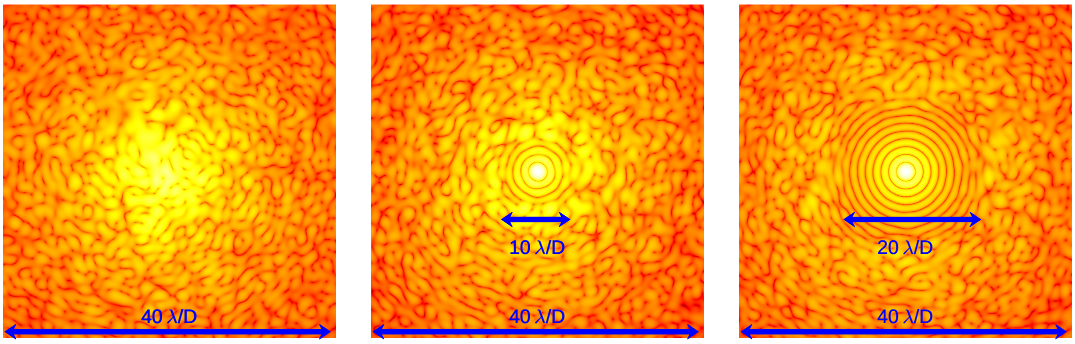

(a) PSF turbulente au plan focal d'un télescope avec $D = 10 \times r_0$, échelle logarithmique

(b) PSF au plan focal d'un télescope avec $D = 10 \times r_0$, corrigée par un miroir déformable 10x10 actuateurs, échelle logarithmique. La PSF est restaurée sur une surface de $10\lambda / D$ de large

(c) PSF au plan focal d'un télescope avec $D = 10 \times r_0$, corrigée par un miroir déformable 20x20 actuateurs, échelle logarithmique. La PSF est restaurée sur une surface de $20\lambda / D$ de large

FIGURE 1 – Effet de la correction d'OA sur une PSF. Dans le rayon de correction fixé par le nombre d'actuateurs, l'OA restaure la PSF du télescope. Au-delà, la PSF est non corrigée.

Tous les télescopes modernes de la classe des 10m sont équipés d'optique adaptative ce qui a permis la première imagerie directe entre autre et bien d'autres résultats avec le perfectionnement de l'OA depuis. On peut citer les études du trou noir Sagitarius A* et de ses étoiles proches (Gillessen et al. (2013)). On a aujourd'hui imagé directement 200 exoplanètes sur les 5000 découvertes. 'imagerie directe d'exoplanète est biaisée par les moyens instrumentaux : on n'image que les planètes suffisamment éloignées de leur étoile hôté, et suffisamment larges. Mais aujourd'hui la génération des télescopes de 30m esten cours de construction. Ces télescopes de 30m, alliés à une OA performante, pourront délivrer une image de planète plus favorable à la vie

Cette génération des télescope de 30m (Extremely Large Telescope de 39m, Giant Magellan Telescope de 25m et Thirty Meter Telescope de 30m) sont collectivement appelés les Télescopes Segmentés Géants (GST pour Giant Segmented Telescope). Ce nom vient de leur miroir primaire (celui de l'ELT est visible sur la Figure 2a) qui ne peuvent être fait d'une seule pièce optique a cause des déformations mécaniques que subirait un miroir aussi grand fait d'une seule pièce. Avec la taille de ces télescopes, toute la structure a grandit, en particulier les structures mécaniques soutenant le miroir secondaire, appelées araignées, ont vu leur taille multipliée par 10 entre la génération des 10m et la génération des 30m (en Figure 2b on voit les araignées sur l'ELT). Cela cause l'apparition d'une nouvelle forme de défaut de phase après une OA appelée le mode pétale. Le mode pétale apparait comme des discontinuités de phase d'un fragment de pupille à son voisin, tandis qu'à l'intérieur d'un fragment le défaut de phase est bien corrigé par l'OA. L'effet de ce mode de phase sur la résolution est que ce n'est plus la taille du télescope qui définit la résolution, mais la taille du fragment (pour l'ELT on passe de 39 a 16m) ce qui réduit considérablement le gain de la génération des 30m en résolution. Le but de cette thèse est d'étudier ce mode de phase et sa mesure par l'optique adaptative dans le cadre des télescopes géants segmentés.

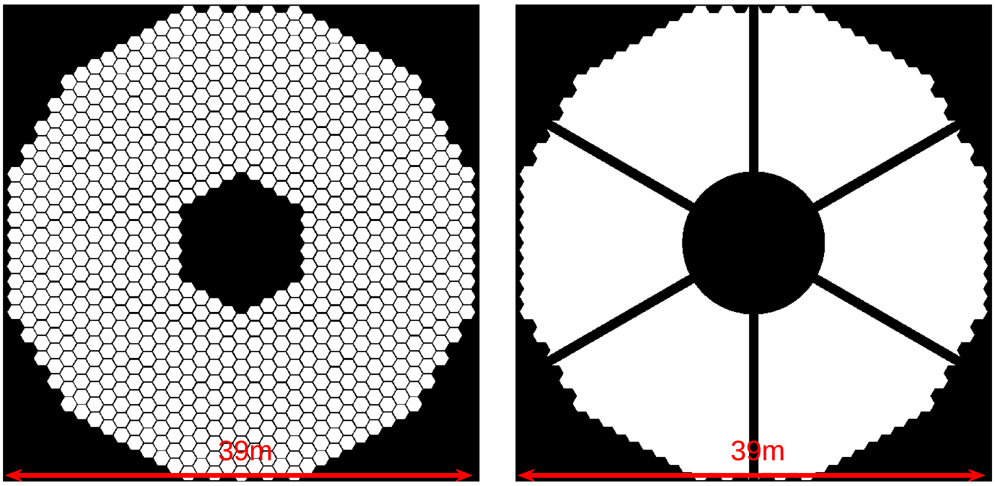

(a) Pupille de l'ELT avec ses 798 segments hexagonaux (espace intersegments éxagéré pour bien voir les segments)

(b) Pupille de l'ELT avec araignée et obstruction centrale. Notez la taille des araignées (50cm)

FIGURE 2 – Pupille de l'ELT, plus grand des GST, première lumière prévue pour 2028

On montre dans le chapitre 2 que le mode pétale a deux origines. Tout d'abord ces différences de phase entre les fragments sont présentes dans la turbulence atmosphérique. Le mode pétale apparaît dans les résidus après correction par l'OA comme cité pour l'instruments HARMONI de l'ELT ou pour le GMT, alors que les deux télescopes ont les moyens de corriger correctement ce mode (les miroirs déformables permettent de contrôler ce mode). Cela signifie que l'optique adaptative ne mesure pas ce mode correctement et aplatie la phase de chaque fragment de façon indépendante.CLa présence du mode pétale dans les résidus d'OA peut être amoindrie par la techniques dite du minioning (sbirisation en français ?) qui consiste à forcer une continuité de la phase de part et d'autre de l'araignée. Cela réduit le mode pétale a des valeurs acceptables pour les instruments de première génération. On montre en Figure 3 l'effet de cet asservissement sur une coupe des phases résiduelles. La coupe de gauche (figure 3a) montre une coupe des phases turbulente et de correction, dans le cas d'un DM segmenté et d'une spider. Les phases de correction ne suivent pas la phase atmosphérique et le résidu présentera un saut de phase.

Dans le cas d'un contrôle asservi (les positions des actionneurs à droite du spider sont copiées (ou asservies) sur les tensions à gauche du spider, la phase de correction suit bien la phase atmosphérique. Un léger résidu est néanmoins visible, mais le saut de phase ne sera quasiment plus visible dans les résidus. Bien sûr le contrôle par asservissement a ses limites : si un saut de phase est réellement présent en entrée (par exemple causé par un déphasage réel des fragments de la pupille, ou une contribution de Low Wind Effect), alors le boucle d'OA sera incapable d'agir sur ce mode.

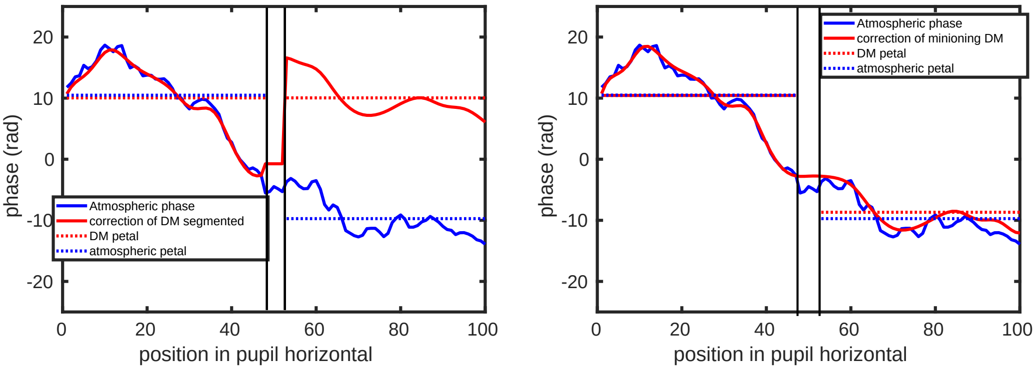

(a) Correction d'une phase turbulent par un miroir segmenté. La phase de chaque miroir reste au même piston moyen, celle ci peut s'éloigner grandement de la turbulence atmosphérique causant une grande différence de la phase moyenne dans les résidus

(b) Correction de la turbulence atmosphérique par un DM avec minioning. La phase de chaque miroir commence a la même valeur de part et d'autre de l'araignée. Seul la variation de phase sous l'araignée se traduit par une différence dans les résidus.

FIGURE 3 – Comparaison de la coupe de la correction de la turbulence atmosphérique par un miroir segmenté et par un miroir avec minioning

La seconde source est l'effet de vent faible (low wind effect LWE en anglais). Les araignées sont des structures métalliques, dont la température dépend du transfert radiatif et de la température du fond de ciel. Dans un cas astronomique de ciel dégagé, ce fond de ciel a tendance à refroidir les araignées en dessous de la température de l'air ambiant, parfois de plusieurs degrés. Au passage du vent autour d'une des araignées, l'air va se refroidir substantiellement, d'autant plus que la vitesse du vent est faible (d'où le nom) et le changement de température se traduit en première approximation par des sauts de phase entre l'amont et l'aval de l'araignée. Cela se traduit en modes pétales qui s'ajoutent à ceux de l'atmosphère. A cause du LWE le minioning ne sera pas suffisant sur ciel pour empêcher le mode pétale et la compensation du mode pétale va devoir passer par l'ajout un moyen de mesurer ce mode. Cette mesure du mode pétale, et donc d'une discontinuité de phase, est complexe. Ce mode pétale n'est pas orthogonal au modes de Zernike de bas ordre par exemple, en particulier le Tip-Tilt. C'est souvent la contribution du TT qui est mesurée à la place du mode pétale. De plus le mode pétale a une ambiguité de λ sur sa mesure. Pour simplifier notre problème on va utiliser une pupille plus simple que l'ELT et ses 6 fragments, et réduire à seulement 2 fragments dans une pupille circulaire montrée en Figure 4 que l'on appelle le toy model.

(a) pupille modèle

(b) pétale mode du modèle

FIGURE 4 – Pupille modèle ou toymodel. L'unique araignée de cette pupille est prise de largeur égale à celle de l'ELT. Cette valeur pourra éventuellement être amenée à changer, et sera clairement indiquée.

Le chapitre 3 étudie le senseur de front d'onde utilisé sur les GST, le senseur Pyramide et explique pourquoi il est insensible au mode pétale. Ce senseur a besoin d'une opération appelée modulation qui augmente sa dynamique pour pouvoir mesurer la turbulence atmosphérique. Sans la modulation ce senseur ne peut pas mesurer les variations de phase de l'atmosphère précisément et l'OA ne fonctionne pas. Mais cette modulation affecte grandement la mesure du mode pétale en concentrant le signal du mode pétale sous l'araignée, là justement ou il n'y a pas de lumière pour porter ce signal jusqu'au senseur Pyramide comme montré sur la Figure 5. Cela se traduit par une très basse sensibilité à ce mode ce qui rend sa mesure complexe voire impossible, et son contrôle très sujet au bruit.

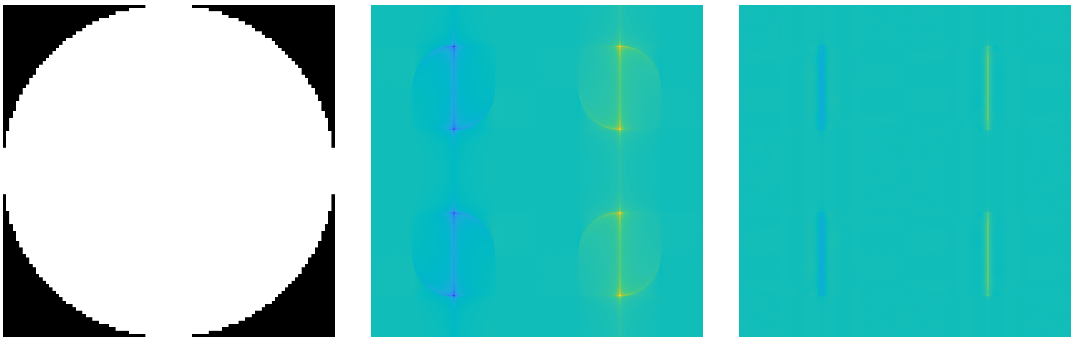

(a) Pupille modèle sans spider

(b) signal de la pyramide non modulée sans araignée. On voit du signal dans chacune des 4 sous pupilles du senseur pyramide

(c) signal de la pyramide modulée sans araignée. Le signal est concentré au niveau du saut de phase du mode pétale, plus de signal visible dans toute la pupille

(d) Pupille modèle avec spider (50cm)

(e) signal de la pyramide non modulée sans araignée. On voit toujours du signal dans chacune des 4 sous pupilles du senseur pyramide

(f) signal de la pyramide modulée sans araignée. Le signal a disparu, caché par les araignées

FIGURE 5 – Changement du signal pyramide pour le mode pétale pour le cas avec/sans spider, et avec/sans modulation

On a ensuite cherché à améliorer la sensibilité au mode pétale en créant une interaction optique entre les fragments du télescope. Pour cela on a utilisé l'exemple du Large binoculary Telescope (LBT) qui peut être considéré comme un télescope avec 2 fragments et une très large araignée (6m). La pyramide est très peu sensible au mode pétale de ce télescope, même non modulée. Mais en asymétrisant la pyramide on peut forcer les fragments gauche et droite à se superposer pour faire apparaitre un nouveau signal. On appelle ce senseur la pyramide asymétrique et elle montre un gain en sensibilité intéressant. De plus la même technique peut être utilisé avec la pupille ELT pour des gains comparables comme résumé dans la Figure6

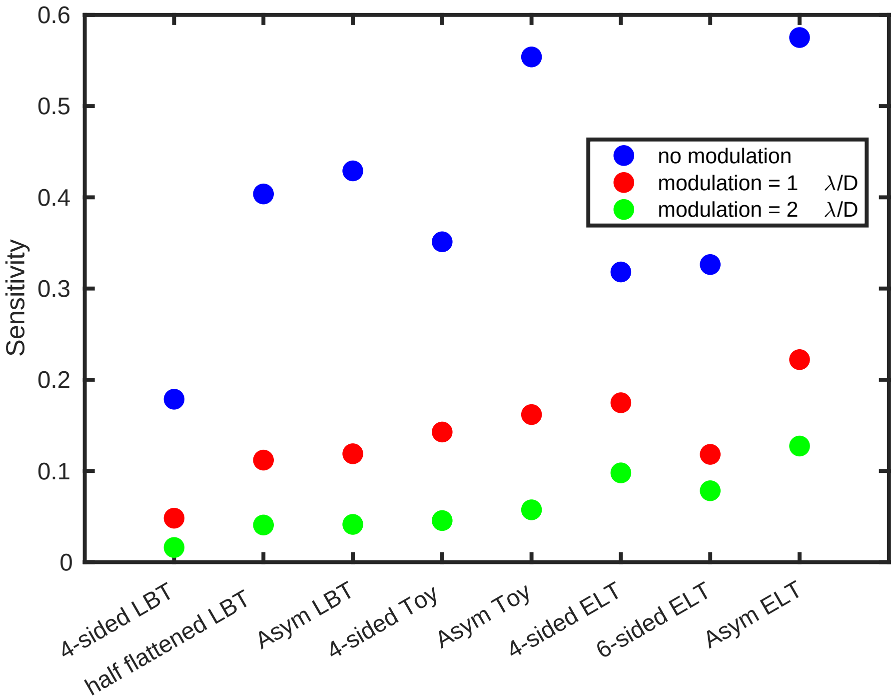

FIGURE 6 – Sensibilité au mode pétale en fonction du type de pyramide utilisé pour le mesurer pour différentes pupilles.

Ces gains sont cependant insuffisant pour compenser la perte due à la modulation. En particulier ces senseurs, même plus sensible au pétale, n'arrivent pas à mesurer le pétale mélangé à l'atmosphère. On préconise donc un système à deux senseurs représenté en Figure 7. On y trouve un premier senseur pyramide modulée controllant un miroir déformable dans une configuration de type minioning qui réduit déjà considérablement le petalling et surtout la turbulence atmosphèrique. On ajoute un deuxième senseur qui ne mesure et ne contrôle que le mode pétale dans la boucle : un pétalomètre. On espère ainsi pouvoir mesurer le pétale parmi les résidus de la première voie sans avoir à moduler. Le chapitre 4 test le concept du pétalomètre en utilisant une pyramide non modulée.

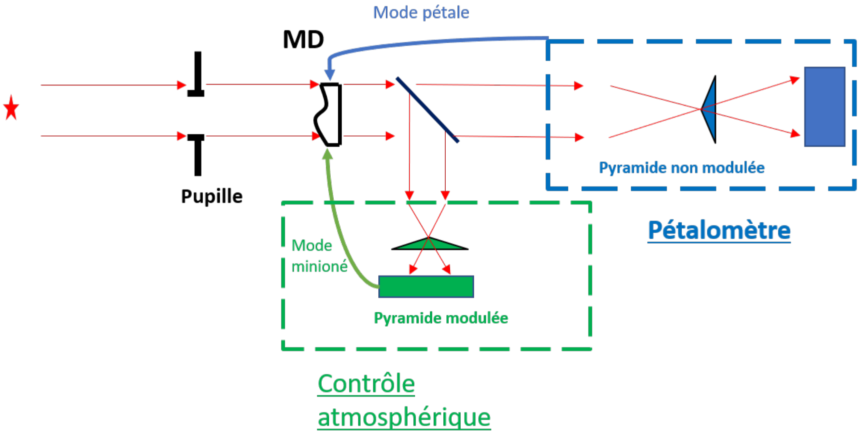

FIGURE 7 – Schéma du système a 2 senseurs. Chacun contrôle des modes différents sur le Miroir Déformable 5(MD)

Dans le chapitre 4 on teste la reconstruction du mode pétale par la pyramide non modulée non pas en pleine atmosphère, mais après un premier étage. Pour se faire on étudie la linéarité de la mesure du pétale en présence de ces résidus. On s'attend a une courbe sinusoïdale (pointillés noirs) a cause de l'ambiguïté de λ. On constate sur la Figure 9 que pour une pyramide non modulée (uPyWFS, pointillés bleus) on a bien une réponse sinusoidale. Celle-ci subit néanmoins deux défauts : son amplitude est réduite d'un facteur (noté g), et sa valeur en zéro n'est pas nulle mais subit un biais (noté c). g est un effet bien connu pour le senseur pyramide, il s'agit des gains optiques. c par contre semble un effet peu connu qui dégrade la mesure du mode pétale par les senseurs pyramide et semble spécifique au mode pétale. Plus intéressant, là où les gains optiques sont relativement stables pour une amplitude d'atmosphère donnée même avec des tirages d'atmosphères différents, la confusion de pétale est bien plus aléatoire. On a finalement identifié un mode spécifique responsable de cette confusion. C'est la discontinuité de phase proche de l'araignée qui créé cet effet et est mesurée par la Pyramide comme un mode pétale.

Pour pouvoir améliorer la mesure du mode pétale par le pétalomètre il faut réduire cette discontinuité de phase. Ce mode discontinuité vient des résidus de phase laissés par la première voie et a donc une signature dans le plan focal au delà du rayon de correction dans la PSF limité par l'erreur de fitting du DM. Le mode pétale lui est surtout présent dans le centre de la PSF. On, propose d'ajouter un étage de filtrage spatial, en pratique un trou de taille très réduite au niveau d'un plan focal, pour supprimer la lumière portant le mode de pétale confusion mais laissant passer la lumière portant le mode pétale. Si on se place seulement dans l'espace des phases on peut déjà constater une réduction des résidus par rapport au mode pétale après ce filtre spatial comme montré en figure 8

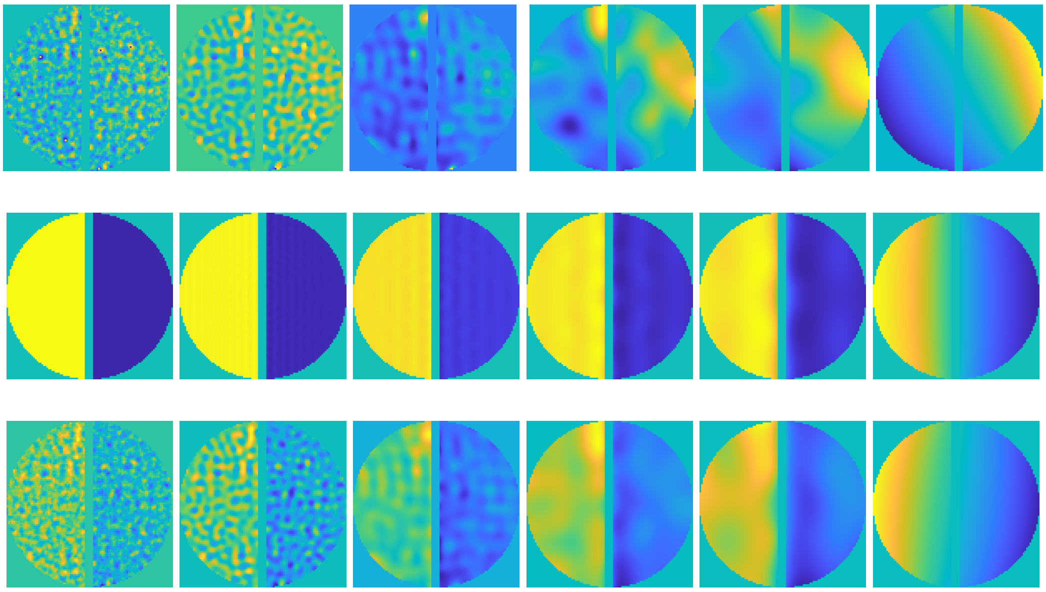

(a) Sans filtrage (b) r = 20 λ/D (c) r = 10 λ/D (d) r = 5λ/D (e) r = 3 λ/D (f) r = 1 λ/D

FIGURE 8 – Effet du filtrage spatial dans l'espace des phases. 1ère ligne : résidus après premier étage d'OA avec DM 20x20. 2e lgne mode pétale pure. 3e ligne : somme des deux

Ce filtrage spatial est facile à implémenter avec une Pyramide car le sommet de la pyramide est déjà situé dans un plan focal. On propose donc un nouveau senseur : la pyramide filtrée spatialement. On voit dans des premiers résultats, en Figure 9 sur la courbe rouge, que l'utilisation de cette pyramide avec filtrage spatial réduit considérablement la confusion du mode pétale (en moyenne divisé par 6). Quand on essaye de fermer une boucle d'OA, on voit que la pyramide avec filtrage spatiale est effectivement un meilleur pétalomètre que la pyramide non modulée et permet à l'OA de minimiser le mode pétale jusqu'à des r_0 de 15cm (valeur médiane attendue pour l'ELT) comparé à 30cm (pas réaliste) pour la pyramide sans filtrage spatial.

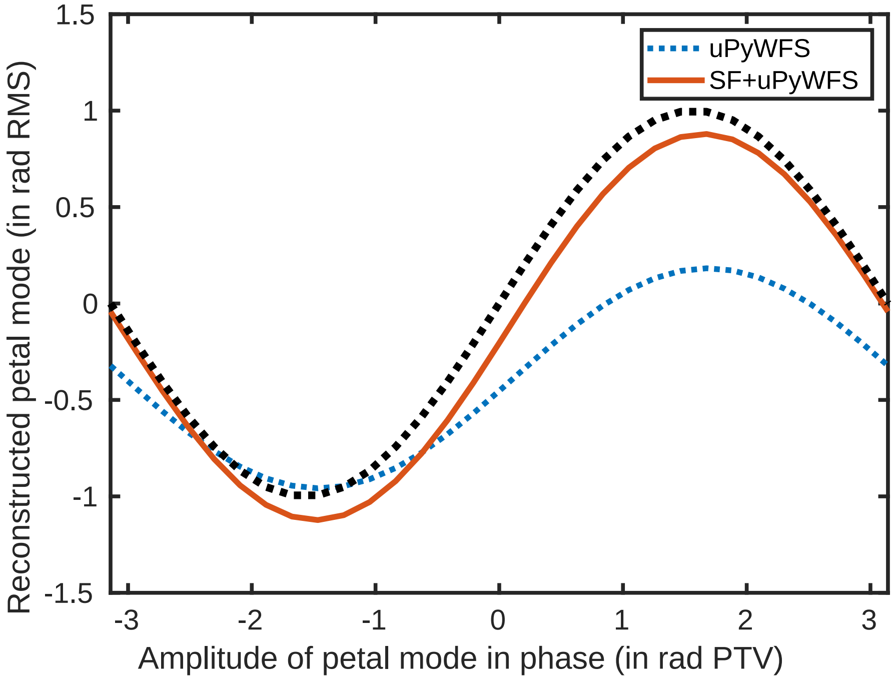

FIGURE 9 – Courbe de linéarité de la reconstruction du mode pétale pour une pyramide non modulée (pointillés bleus) et une pyramide non modulée avec filtrage spatial (rouge). La meilleure réponse possible étant la courbe en pointillés noirs

On a dans cette thèse étudiée en profondeur le problème du pétale. On a en particulier identifié un mode capable de créer du mode pétale en sortie d'OA alors qu'il n'est pas présent en entrée d'OA : le mode discontinuité et sa version plus complète le mode de confusion de pétale. On a proposé deux types de solutions. Premièrement on a trouvé un senseur de front d'onde de type pyramide particulièrement sensible à ce mode. Deuxièmement on a proposé d'ajouter un étage de filtrage spatial pour permettre à la pyramide non modulée de mesurer le mode pétale en présence de résidus d'OA typiques. Ces deux solutions peuvent être combinées, le filtrage spatial pouvant être appliqué a tout pétalomètre à filtrage de Fourier. Cette première pierre devrait permettre à terme de maîtriser le mode pétale sur l'ELT.

Acknowledgement

In this document you will find the result of my blood, toil, tears and sweat (and most importantly, coffee). This documents represents the sum of all the work of my life thus far. But I am not the only one who participated directly or indirectly to this document. This space is dedicated to all the other people who helped me to live through these 3.25 years and carry the thesis through.

As Newton said, *I was able to see a little farther because I stood on the shoulders of giants*. The first section is directed toward the people who helped me scientifically, the aforementioned Giants. This quote can be interpreted as science (or any knowledge) being essentially a giant human pyramid of people supporting the people over them and providing the basis for their new ideas.

The two first person I wanna thank are essentially bearing most of my weight on their shoulder : Jean-François Sauvage and Vincent Chambouleyron. Three quarters of what is original in my thesis comes from a conversation with either of you, you wonderful people. In particular, Vincent thank for your understanding of the Pyramid and the multiple times you explained it to me. As we were in the same office for the first 1.5 year of my thesis I relied on you when I had a problem and you helped me solve most of them. Jeff, Thank you for your understanding of AO system and the pragmatic approach I was able to keep. I have a lot of memory of very interesting discussion either around the coffee machine or after some weekly meetings with you.

The second group is the restrained AO team of LAM : Thierry Fusco, Benoit Neichel and Olivier Fauvarque. You helped me through the day to day questions and interrogations. Thierry, thank for beeing a harsh but fair type of director. Even though It made me dread a lot of my meeting with you, when I was able to carry my meaning or you were agreeing with me it made these moments much more worth it (I suspect you have a good cop/bad cop arrangement with Jef). Benoit thank you for being generally knowledgeable in anything AO related. And also as the manager of the GRD group you helped me avoid a lot of headache when dealing with administrative stuff. Olivier thank you for your thesis which was basically the main source of my work for the first year. I know you work at Ifremer but spiritually you were part of the team all these years.

The next group is what I would call the HARMONI SCAO discussion club. During my first year and a half, there was a meeting every Thursday morning where I would meet Charlotte Bond, Carlos Correia and Noah Schwartz. It was on of the first place where I could show my result to 'exterior' people. It helped me develop a sens of how to format and display results. During these meetings we talked a lot about the different forms that petalling could take as well.

Finally the last group are the people with whom I worked in Italy, at the Osservatorio

Astrofisico di Arcetri. I worked there under the superivison of Enrico Pinna and Simone Esposito and with Anne-Laure Cheffot, and Cedric Plantet. I got more insight from the GMT side of petalling.

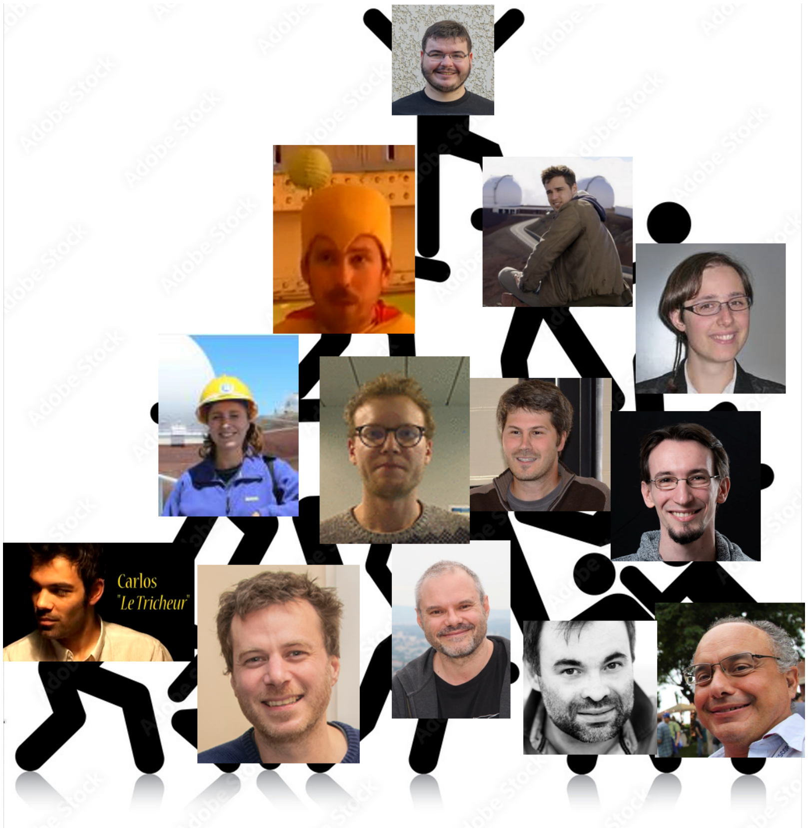

FIGURE 10 – My final personnal science pyramid

The second section is dedicated to the people who pushed me toward science and AO in particular.

Truth is, the game was rigged from the start as my parents are good friends with some known figures in AO, specifically Laurent Mugnier and Jean Pierre Véran. In a sense I was already wedged toward astronomy and AO in particular before even reaching high school. It was very rewarding during my thesis to finally be able to talk of science with these old acquaintances.

Then I would like to thank the teachers who pushed me toward science as well. Even though most teachers are unsung heroes (in middle school in particular), I would like to thank in particular Mme Cécile Delanée and the science workshop she organised during 4e. It was a formative experience where I learned the basic of scientific presentation and vulgarisation.

Another important step was once I reached IOGS Saint Étienne. the trio of teachers directing the Saint-Étienne site made it my best student years. So thanks to Mathieu Hébert, Raphael Clerc, and Thierry Lépine. And in particular they helped greatly for the internships. I would also like to apologize to Pierre Chavel, who desperately tried to teach us "optique physique", where I utterly failed and which turned out to be the main subject of this PhD.

The internship were also a very important moments. My first internship was in Corsica, in the proud city of Erbajolo. An hotel opened an astronomical observatory to take advantage of the Corsican mountains. I would like to thank Mr Stéphane Natalini, who trusted me around his brand new telescopes.

Laurent Mugnier helped and pushed me to to apply an internship at Caltech, in Dimitri Mawet's lab (exoplanet technology lab). There I got my first experience about high contrast imaging. In particular I worked with Garrteh Ruane, Nemanja Jovanovic and Daniel Echeverri.

My third internship was at ONERA with Laurent Mugnier. But thanks to the Covid I spent only 2 weeks at ONERA. I got a lot of insight on PSF formation and AO performances, but did not work with Laurent as much as I hoped. But i managed to meet Thierry and get my PhD there.

But the event which prepared this thesis the most was my gap year at ESO. There I got my very own ELT prototype segment to torture to test the warping harness of the ELT segments. So I would like tho thank Thierry Lépine from IOGS who came to me at the end of my 2nd year asking if I had any idea for someone who would be interested by a gap year at ESO and Samuel Lévéque, Stéphane Guisard, Thibaut Guerlet and Anne Laure Cheffot who were overseeing me at ESO.

Finally the last category of people I would like to thank are the ones who allowed me to survive the 3 years of PhD without going mad (in particular the last year).

The first persons who supported me during these 3 years are my family. Thanks to first my parents who inspired me to pursuit science, helped me through my studies and formed the basis for who I am. Thank to Cecile, my little sister and Marc my little brother. As a trio of siblings we are a very good demonstration that genetics and education play strangely little part in the tasted and life trajectory of each one, but we cans till fit together despite having radically different aims.

The next group I want to thank is the core group of friend I formed between high and middle school. Thanks to my dad initiating us to TTRPGs and the advancement of the internet, we stayed close and participate in weekly RPG sessions. In particular I started the thesis stopping my role as dungeon master because I wouldn't have the time to do that. On of my former players became the new official group DM. 3 months after the start I played a small session oneshot because I was missing the feeling. And it spiraled into a whole second campaign we played together with me as the DM. Thanks to this player for taking my role, and thanks to the others for humoring me.

The next group is the group of friends I formed into the prépa at Lakanal. Since our friendship formed more about movie it was harder to keep in touch regularly once everyone spread around France in engineering school. But we always meet in september at the soirée Nanarland. So thanks to Martin, Alex, JB, Paul and Adrien.

The next group are the different group of friends I made in IOGS. Because I moved site and then changed promotion with my gap year, it's probably the fuzziest group. But I want to highlight in particular the 1st year group : Olivier, Timothé, Antoine and Elliot. And also the supop sainté 2nd year group and the RPG group which is still ongoing : EY, Vincent, Alice, Alexis, Paul and Adèle.

I would also like to rapidly thank my pet snake : Aghankhatosh. I adopted him at the end of my PhD's first year and watched him grow to adulthood over the course of the PhD. As most people know snakes are not a social animal and the highest honour they can give to a human is consider them a comfortable tree branch. But his presence alone was soothing to me and helped me through the harder days of the manuscriptwriting.

Finally the last group and probably the most directly involved, is the group of friends I made during my PhD. It was mostly comprised of PhD students themselves and I would add Romain Fétick and Maxime Lopez as well. Thank first to the students of GRD LAM, with whom I spent a lot of coffee break ~~procrastinating~~ talking about serious topics. The main culprits here are Mahawa and Alexis with whom we took advantage regularly of Marseille's sun (keep taking advantage, Paris is depressing in comparison). But Vincent, Romain, Arnaud, Jordi, Mona, Francisco and Maxime(x2) surely deserve a mention. Then there were the people of Onera Chatillon, technically my closest coworkers. So thanks to Pablo, Alix, Yann, Inès,Léa, Emile, Perrine, Laurie and Eve. Those f****** Phd days at ONERA would have been even longer without you all. Finally I would like to thank the larger LAM environment. I am really reluctant to going out but you managed to take me out a few times to bars and made the whole experience of PhD a lot more fun in general. This group includes but is not limited to : Diana, Lisa, Ilias, Paulo, Martin, Mathilde, Sia, Rayssa and Merriam. Special thanks to the members of the 'walks with me in hell' mattermost channel.

So now at the end of this thanks section what to say ? First sorry to the people I forgot and who could be angry that a snake got more mentions than them (to be fair you did not force me to move every piece of furniture in my apartment three times already). The poor memories for people is one of the curse I'm afflicted with.

If you are still reading at this point I would like to thank you as well unnamed reader, even more if you intend to carry on to the dry prose constitutive of serious scientific discussion. I would like to share 2 citations from Sir Terry Pratchett which I believe are topical on this thesis. The first is mostly due to the context of the Covid pandemics in which this thesis took place : **"Every scientific statement is provisional. Politicians hate this. How can anyone trust scientists ? If new evidence comes along, they change their minds."**, *The science of discworld.* It is important to remember that in science the evidence is right. Not the professor, not the paper published a year ago in Nature, certainly not the ”"'Doctor R.”"' in a TV studio. Following science gives the best results because it naturally adapts to the circumstances. **"Sometimes, if you pay real close attention to the pebbles you find out about the ocean."**, *Lord and ladies.* I hope this thesis is one of the pebbles which will pave the route to the study of more exoplanets and eventually answer on of the biggest questions : is there life elsewhere in the universe. You can loose yourself to the study of the pebble (I certainly did) but it always help to remember the larger goals you are chasing.

Table des matières

Table des figures

Liste des tableaux

List of Acronyms

AO
Adaptive Optics.

COG
Center of Gravity.

DM
Deformable Mirror.

ELT
Extremely Large Telescope.

EM
Electro Magnetic.

FFWFS
Fourier Filtering Wavefront Sensor.

FOV
Field Of view.

FT
Fourier Transform.

FWHM
Full Width Half Max.

GMT
Giant Magellan Telescope.

IF
Influence Function.

LBT
Large Binocular Telescope.

MTF
Modulation Transfer Function.

NCPA

Non Common Path Aberration.

OG

Optical Gains.

OPD

Optical Path Difference.

OTF

Optcal Transfer Function.

PSD

Power Spectral Density.

PSF

Point Spread Function.

PV

Peak to Valley.

PyWFS

Pyramid Wavefront Sensor.

RMS

Root Mean Square.

RTC

Real Time Computer.

SCAO

Single Conjugated Adaptive Optics.

SF

Spatial Filter.

SF+uPyWFS

Spatially filtered Pyramid Wavefront sensor.

SH

Shack-Hartmann.

SLM

Spatial Light Modulator.

SNR

Signal to Noise Ratio.

SR

Strehl Ratio.

SVD
Single Value Decomposition.

TMT
Thirty Meter Telescope.

uPyWFS
unmodulated Pyramid Wavefront Sensor.

WFE
Wavefront Error.

WFS
Wavefront Sensor.

Introduction

The search for Extra-Terrestrial life has been for the longest part of history a mostly theoretical and philosophical field. One of the most documented examples was the theory of Giordano Bruno, in 1584, proposing that the universe was infinite with an infinity of worlds equivalent to ours. But the test of this theory needed more efficient astronomical instruments, able to resolve the sky objects. The first practical step was an exploration of the solar system. This investigation was mostly focused on Mars where "canals" were observed after the 1877 opposition. This discovery was then expanded on by Percival Lowell who built his own observatory in Flagstaff Arizona and observed more canals and green bands around them as he presented in its "Mars and Its Canals" book in 1906. It appeared later that by a defect of the telescopes design, he was probably seeing his own retina and the blood vessels reflected in his telescope's eyepiece. Despite numerous observation by other astronomer that Lowell's canals did not exist, the theory stayed in the common consciousness until the on-site observations by Mariner 4. This episode shows how critical it is to understand the observation tools we are using, especially in a subject as emotionally loaded as extra-terrestrial life.

But after confirmation during the 20th century that Mars was a lifeless planet the search turned to the stars and the second step for the search of extraterrestrial life became the search for exoplanets, planets orbiting other 'Suns'.

The concept of exoplanets remained theoretical until 1992 when it turned into reality for the first time when exoplanets were discovered around pulsar PSR B1257+12 (see Wolszczan & Frail (1992)). The first discovery ever was met with skepticism as a pulsar is a dead star and has very little chance to shelter any life, and a similar discovery was announced and then retracted the previous year. The first announcement of exoplanet detection around a Sun-type star was in 1995 by Michel Mayer and Didier Queloz (see Mayor & Queloz (1995)) and was awarded a Nobel prize in 2019.

This planet, 51Peg b, was an unexpected object as astrophysicians did not know how it could exist. 51 Peg b is the first 'hot Jupiter' discovered, with a mass of 0.45 M_J and orbiting at a distance of 0.05 ua, closer than Mercury is from the Sun. A planet the size of Jupiter so close to its star was totally unforeseen by the planet formation models so far. The technique of radial velocity (or Doppler method) used by the discovery provided the first characteristic of exoplanets : their mass (or rather a minimal mass depending on the orbital parameters Brown (2015)). A second technique was successfully demonstrated in 1999 with the discovery of HD 209458 b using the transit method. This method gave us a second physical characteristic of exoplanets : their size. When the two methods were available for the same object its density became therefore available. This density gives a first estimation of the planet's composition. It allowed in particular to separate the exoplanets between gaseous and telluric ones. But both these techniques rely on the study of the light of the star, not directly the exoplanet. To get more characteristics of exoplanets a breakthrough was needed : the direct imaging of exoplanets, which means analyzing the starlight reflected by the planet, or the light emitted by the planet itself. This new method requires to be able to separate the light of the exoplanet from the light of its host star. The physical measurement that xenobiologists are looking for is a light spectrum of the exoplanet's atmosphere. This spectrum would allow the identification of the chemical species in the atmosphere and in particular biomarkers, chemical species which are associated with biological activities. The spectrum needs also a high number of points to be able to separate the multiple species making up the atmosphere.

This is a tremendous challenge. The light coming from the star is 10^6 to 10^9 times brighter than the planet's depending on the wavelength, the planet's characteristics, and the star type. It would also mean reaching an angular resolution never achieved before as interstellar distances are much larger than interplanetary distances. For an exo-earth orbiting at 1ua around a star at 10 parsecs, an angular resolution of less than 100 milliarcseconds is necessary. That requires an optical system with a pupil of at least 1.20 m for visible light (500nm). But the resolution of a ground telescope is limited by the atmospheric turbulence to the resolution of a 20cm telescope at best, meaning only space-based telescopes could hope to separate exoplanets from their star.

But in the 1990s a new technology able to offset the effects of atmospheric turbulence was developed : Adaptive Optics (AO). It could restore the resolution of the telescope and allowed in 2004 the first direct imaging of an exoplanet by the VLT (Very Large Telescope, see Chauvin et al. (2004)). The first few points of a spectrum made the estimation of a new characteristic available : the surface temperature.

AO works by measuring the atmospheric turbulence and adding an opposite effect with a deformable mirror. This allows one to not be limited by the atmosphere in terms of resolution but by the size of the telescope. AO is the core of this thesis and is described in more detail in Chapter 1. Another technique has been developed in parallel for the study of circumstellar disks : coronagraphy which allowed the discovery of the first disk around β Pic B in 1984 (see Smith & Terrile (1984)). Coronagraphy works by subtracting (or filtering) the light of the star after concentrating it as much as possible to avoid subtracting the light of any close object of interest as well. It allows us to see faint objects without being blinded by the star. Naturally, coronagraphy and AO were quickly assembled to allow the detection of fainter exoplanets such as in Figure 11 with HR8799 (imaged here by the VLT and first imaged by Keck Gemini in 2008, see Marois et al. (2008))

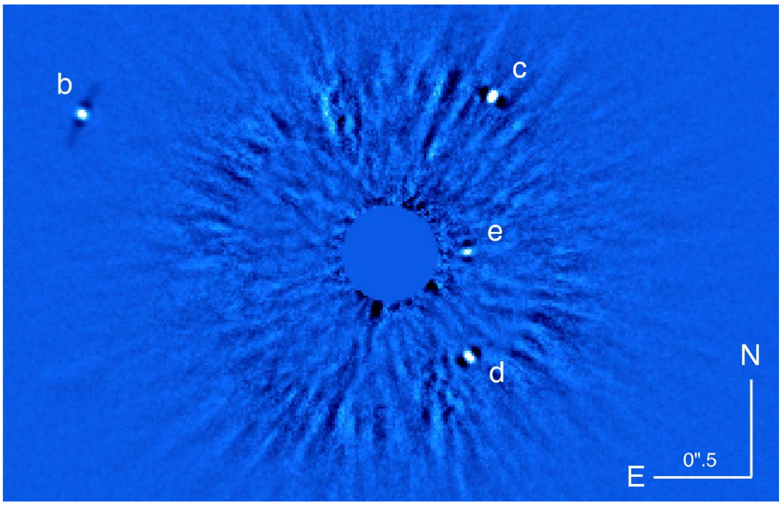

FIGURE 11 – Image of HR8799 planetary system taken by VLT/SHERE, the center star has been occulted. Defects of the AO correction are visible with the speckles of light. *Credit : Olivier Wertz*

Today with more than 5000 exoplanets discovered, of which 69 (according to exoplanetarchive.ipac.caltech.edu) have been discovered by direct imaging, one could expect that we have a better idea whether any of them harbors life. But most characteristics of exoplanets such as their composition or atmosphere remain unknown. The main problem is that our current detection methods are highly biased toward large exoplanets (due to their size allowing them to emit or reflect more light) and planets which are very far for direct imaging or very close for transit and radial velocity method. This result is displayed in Figure 12 where we see which exoplanets have been discovered depending on their mass and distance from their star. we see that there are no exoplanets directly comparable to an Earth, and the exoplanets directly imaged are all further away from their star than Earth. Furthermore, exoplanets are already very dim with a broadband imager. Obtaining a light spectrum means dividing their light between multiple wavelengths. This reduces drastically the number of exoplanets for which a detailed light spectrum is available (less than 20 exoplanets have more than 100 spectroscopy data points on the NASA Exoplanet Archive).

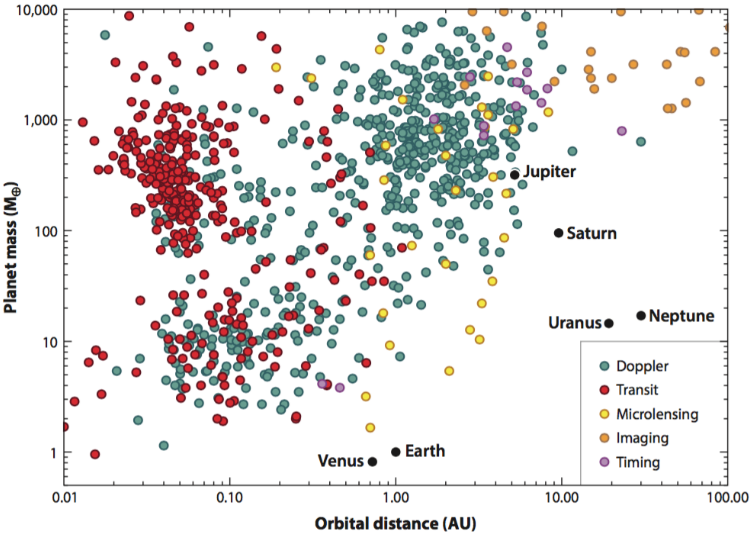

FIGURE 12 – Diagram of exoplanet discovered (in 2018) as a function of their mass and distance from their host star. The directly imaged exoplanets are all of large mass and too far from their star to be hosting life (1 au, = distance between the sun and the Earth).*Credit : Karna Desai, ScIU Indiana University Bloomington*

To answer the question of extraterrestrial life we need instruments able to collect more light to detect fainter exoplanets and resolve smaller objects to separate exoplanets closer from their star. This will allow direct imaging of an exo-earth. Building larger telescopes solves both problems at first glance. However, the atmosphere limits the resolution of giant ground telescopes, while space telescopes are limited in size due to the constraints of satellite building.

The space telescope problem has been solved partially by segmentation of the primary mirror, allowing the launch of JWST in 2021 and its first scientific result with one of the first detailed exoplanet spectrum (see Miles et al. (2023)). For ground telescopes as mentioned, AO in theory restores the resolution of the telescope so as not to be limited by atmospheric turbulence. This method has shown incredible results on the 10-meter generation of telescopes with numerous discoveries. But the next generation of telescopes, the 30-m generation is under construction and should see its first light in the 2020s. These telescopes, unprecedented in size for optical astronomy will need the most efficient AO. On Figure 13 we see a comparison between the different pupils of the previous 10m telescopes (like VLT, Keck) and the 30m telescopes (ELT, GMT, and TMT).

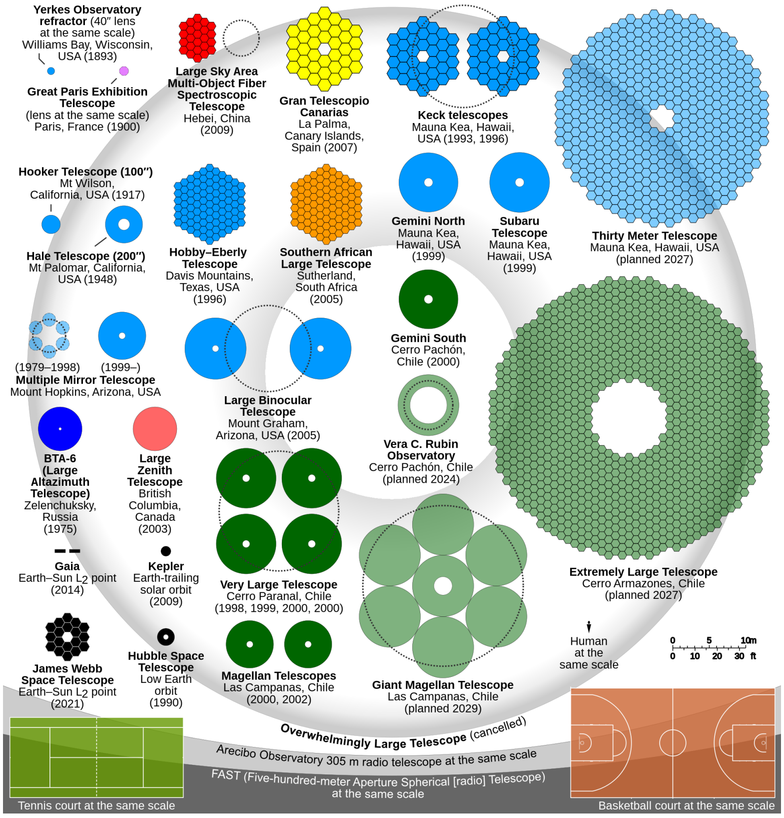

FIGURE 13 – Plot comparing the pupil and in particular the size of current telescopes and future 30m-class telescopes. *Credit : user Cmglee, wikipedia*

An important characteristic of the 30-m telescope generation is their segmentation. Due to their sheer size, there was no way to design a monolithic telescope. Mechanical constraints such as gravity would bend a monolithic primary mirror. But every element of the telescope got up-scaled as well. The most relevant change of size for this thesis is the growth of the spiders. The spider is a structure of metal bars that hold the secondary structures above the primary mirror, generally the secondary mirror. With the growth in scale in the ELT, these structures went from 2.5cm wide in the VLT to 50cm wide for the ELT. Originally they had limited effect on the telescope images and the AO (most notably creating the diffraction spikes around stars). But as they are above the telescope they block light from being collected and create dark areas where the AO can't measure the atmospheric turbulence. Furthermore, it appeared on the SPHERE instrument on the VLT that they could even create their own turbulence effects with the Low Wind Effect (LWE) (see Sauvage et al. (2015)). This resulted in having a good correction of the turbulence in each area separated by the spiders, which we call fragments, but, no continuity between fragments. The effect on the final image after Adaptive Optics (AO) correction is akin to the fringes of Young's double slit experiment where the size of the whole telescope determines the distance between fringes, but the size of each fragment determines the envelope inside of which the fringes move. If this discontinuity effect is not stable, the fringe will move randomly and the final resolution will be determined by the size of each fragment, which for the ELT is the resolution of a 17m telescope, not a 39m one. This reduces the resolution and the performance in terms of starlight reduction of the Coronagraphs. The exoplanets that such an ELT would be able to directly image wouldn't be as close to their host star, nor as faint, as for a properly cophased one.

This thesis aims to study where this continuity problem comes from in the AO system and find innovative solutions to restore this continuity and allow the ELT to use its size to its full potential.

1 General principles

The aim of this first chapter is to present the general principle and the type of optical instrument studied in this thesis. We present the process by which an image forms in a telescope, how the atmospheric turbulence ruins it and the process put in place to reduce the effect of the atmospheric turbulence : the Adaptive Optics. In particular we focus on the component of AO central to this thesis : the Pyramid Wavefront sensor.

1.1 Image Formation

The primary goal of a Telescope is to collect a fraction of the light coming from a distant object and to concentrate it in an image. As such there are two planes whose relation is critical to the telescope : the pupil plane where light is collected, and the focal plane where the image is created.

1.1.1 From pupil to focal plane

The light is first collected in the pupil plane. For a telescope the pupil plane is generally defined by the primary mirror of the telescope. We represent the light collected as the Electro Magnetic (EM) field in the pupil plane $\psi_{p|(x,y)}$ which contains the information of both amplitude $a_{p|(x,y)}$) and phase $\phi_{p|(x,y)}$ (in rad) of the pupil plane :

$$\psi_{p|(x,y)} = a_{p|(x,y)} \times exp(-i\phi_{p|(x,y)}) \tag{1.1}$$

The case of astronomical observation, where the line of sight is globally vertical, helps to simplify this model. In this case, the EM model can be simplified to a pure phase contribution. The amplitude in the pupil plane should be homogeneous so the amplitude of the EM field is approximated to a binary map $\mathbb{I}_{p|x,y}$ with 1 where the primary mirror reflects light and 0 where the light is not reflected due to the limited size of the telescope or components in the optical beam such as the central obstruction due the secondary mirror and spiders. From the pupil plane the light get diffracted. Then the light passes through a focusing element (such as a lens or a mirror), the diffracted EM field is focused on the detector at a distance equal to the focal length. Following the Fraunhofer approximation, we have the relation for the EM in the focal plane :

$$\psi_{f|x,y} = \frac{1}{(f\lambda)^2} \times \mathscr{F}[\psi_{p|\frac{x}{f\lambda},\frac{y}{f\lambda}}] \tag{1.2}$$

with $\mathscr{F}[f]$ representing the Fourier transform for function f, ψ_f is the EM field in a focal plane. It is generally simplified to the relation $\psi_f = \mathscr{F}[\psi_p]$ and the resizing factor of focal length and wavelength is integrated in the Fourier transform. This relation is central to the comprehension of image formation and is shortened as saying that the focal plane is a Fourier transform of the pupil plane (which is true for EM, but not for intensities). In practice the EM is not measurable directly for optical wavelengths, what is measured is the intensity :

$$I = |\psi|^2 \tag{1.3}$$

As in our case we consider the amplitude of the pupil fixed, the intensity in focal plane is considered depending only on the phase in pupil plane ϕ_p. The main exception are the scintillation effects for AO which are not taken into account in this thesis. it is not obvious how scintillation would impact the findings of this thesis and would require a dedicated study. There is a specific intensity pattern important for our analysis which is the intensity created by a point source at infinity. In that case the phase $\phi_{p|x,y}$ is null. The intensity pattern in the focal plane of an imager therefore depends only on the pupil of the optical system is the reference Point Spread Function (PSF).

$$PSF = I_f(\phi = 0) = |\mathscr{F}[I_{p|x,y}]|^2 \tag{1.4}$$

The PSF is the distribution of intensity created by a point source for a given optical system. In astronomy stars as unresolved objects appear as PSF on imagers. The reference PSF for a circular pupil is the well known Airy pattern shown on Figure 1.1b. The image formation when observing an extended object $\mathscr{O}$ can be modeled with a convolution operation. The extended object is assimilated as a collection of point-like sources of different position in sky, and the extended image is an incoherent summation of shifted point-like image.

$$\mathrm{Im} = \mathscr{O} \star PSF \tag{1.5}$$

Each point of the object creates a corresponding PSF in the focal plane. Each point of the object therefore becomes a blurred image of the object. The larger the PSF is the blurrier the image gets compared to the object. In spatial frequency space this is written as :

$$\mathscr{F}[Im] = \mathscr{F}[\mathscr{O}] \times \mathscr{F}[PSF] \tag{1.6}$$

This expression shows the spectral content of the PSF in term of spatial frequencies. $\mathscr{F}[PSF]$ is known as the Optcal Transfer Function (OTF). This OTF is a complex quantity, what is generally presented is its modulus, the Modulation Transfer Function (MTF).

$$MTF = |OTF| = |\mathscr{F}[PSF]| \tag{1.7}$$

The MTF represents the attenuation of each spatial frequency as the telescope pupil acts as a low-pass filter. In most cases the MTF and OTF gives similar result. The name OTF is sometimes used even though what is computed is the MTF. For a reference PSF, the OTF reaches 0 at D/λ with D the diameter of the pupil in the direction considered, meaning that this is the maximum observable spatial frequency transferred by the optical system for a given pupil size and observing wavelength. The OTF associated with the airy disk is seen on Figure 1.1c

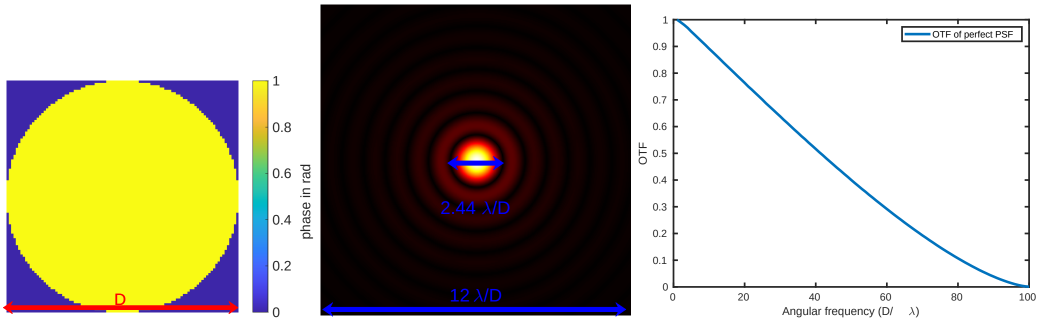

(a) Phase screen for perfect PSF (b) Airy pattern = perfect PSF (c) OTF of perfect PSF

FIGURE 1.1 – Perfect PSF only limited by the diffraction of the system

1.1.2 Introduction of optical aberrations

Following the idea that the EM in focal plane is the Fourier Transform (FT) of the EM in pupil plane, any added phase is interpreted as a Fourier series of sine and cosine phase functions. The effect of such a sinusoidal phase on the PSF is showed in Figure 1.2. A cosine phase creates 2 secondary spots in the direction of the cosine and reduces the light in the central coherent peak. In term of OTF, that aberration lowers the OTF, which means that the final image gets blured more and more. Furthermore changing the frequency of the sine used changes the distance from these lobes to the center and consequently the number of dips in the OTF. Changing the amplitude of the sinus phase changes the intensity of the secondary lobes and consequently the depth of the OTF dip. These defects make the OTF worse as the amplitude of the cosine increases and effectively the system will not be able to resolve spatial frequencies for which the OTF dips at 0. For instance on Figure 1.3 we put the amplitude of the cosine so that the secondary lobes of the OTF are as intense as the central PSF. It becomes impossible to separate the 3 PSF lobes, meaning the resolution has been divided by 3 in the direction of the cosine. This appears in the OTF as the OTF reaching 0 at a third of the previous angular resolution.

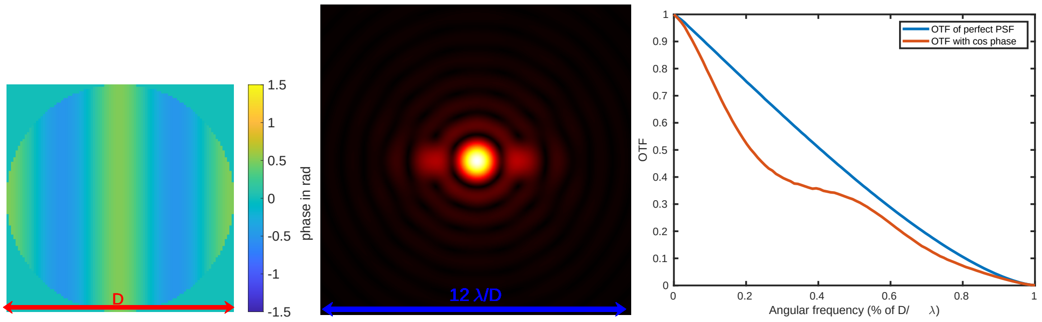

(a) Phase screen for cosine signal, with $\pi/4$ rad amplitude
(b) PSF associated with a cos phase signal
(c) MTF with cos phase in entrance pupil

FIGURE 1.2 – PSF and OTF with small sinusoidal phase in the pupil

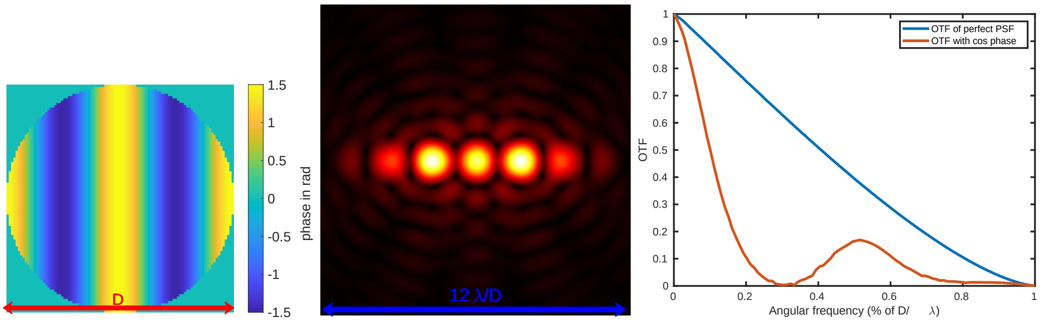

(a) Phase screen for cosine signal, with $\pi/2$ rad amplitude
(b) PSF associated with a cosine phase signal
(c) MTF with cos phase in entrance pupil

FIGURE 1.3 – PSF and OTF with large sinusoidal phase in the pupil

Any difference from the flat wavefront is called an optical aberration. Some common phase shape like the defocus, tip or tilt are well known by opticians and their effect are well documented (see Zernike (1934)). They are organised in orthonormal basis following the scalar product :

$$< f|g >= \frac{1}{\pi}\int_0^{2\pi} d\theta \int_0^1 \quad d\rho f(\rho,\theta) g(\rho,\theta) \tag{1.8}$$

with ρ and θ the spherical coordinates. With this scalar product the Root Mean Square (RMS) norm is defined as $|| \times || = \sqrt{< \times | \times >}$. An orthonormal basis ϕ_i is composed of unit vector for this norm. Using such a base any base can be decomposed as :

$$\phi(r) = \sum_{i=0}^{i=\inf} a_i \phi_i(r) \tag{1.9}$$

The Fourier basis is such an orthogonal basis. However, it is not efficient for optical aberrations. For the purpose of this thesis, we present another more commonly used phase mode basis :

The Zernike basis The Zernike basis proposed by Zernike (1934) was proposed to be adapted to optical aberrations. Its base is ordained by a radial degree n and azimuthal degree m following the equation :

$$R_n^m(\rho) = \sum_{k=0}^{\frac{n-m}{2}} \frac{(-1)^k (n-k)!}{k!(\frac{n+m}{2}-k)!(!(\frac{n+m}{2}-k)!} \rho^{n-2k} \tag{1.10}$$

for the radial coordinate $\rho \in [0,1]$

$$Z_n^m(\rho,\theta) = R_n^m(\rho) cos(m\theta) Z_n^{-m}(\rho,\theta) = R_n^m(\rho) sin(m\theta) \tag{1.11}$$

for the azimutal coordinates

This Zernike basis definition is explicit, and orthonormal if the system uses a full circular pupil. Central obstruction and spiders break this orthonormality. The first 11 modes of the basis are well known of opticians as they are the most common optical aberrations on optical systems. The modes on Figure 1.4 alongside their effect on the PSF for some amplitudes. For simplicity, the modes that differ from one another (like tip and tilt) by a rotation are not plotted.

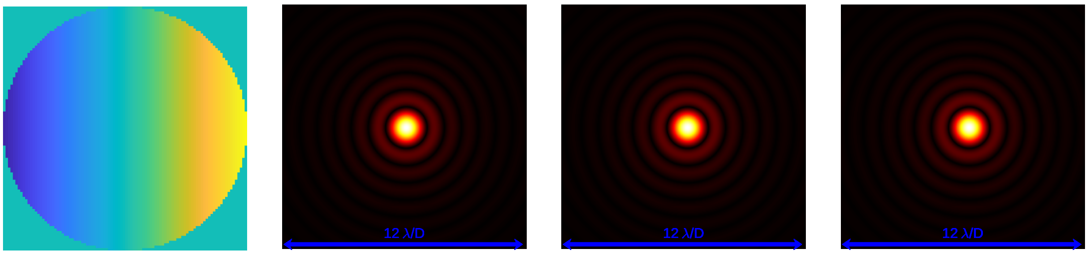

(a) Zernike mode 2 : Tip ,phase and effect on a PSF for 0.1 0.3 and 0.5 rad rms

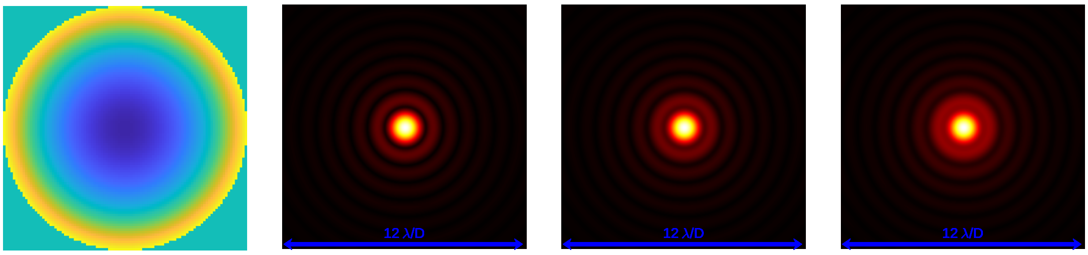

(b) Zernike mode 4 : defocus,phase and effect on a PSF for 0.1 0.3 and 0.5 rad rms

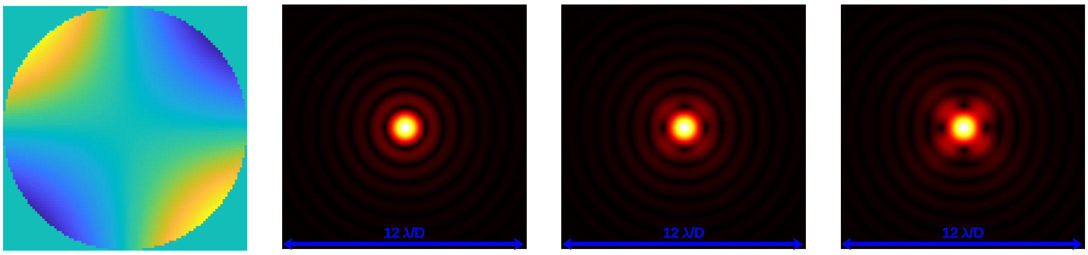

(c) Zernike mode 5 : astigmatism, phase and effect on a PSF for 0.1 0.3 and 0.5 rad rms

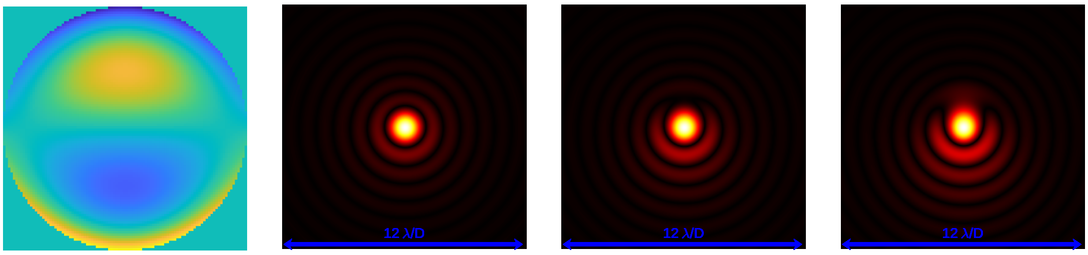

(d) Zernike mode 7 : coma, phase and effect on a PSF for 0.1 0.3 and 0.5 rad rms

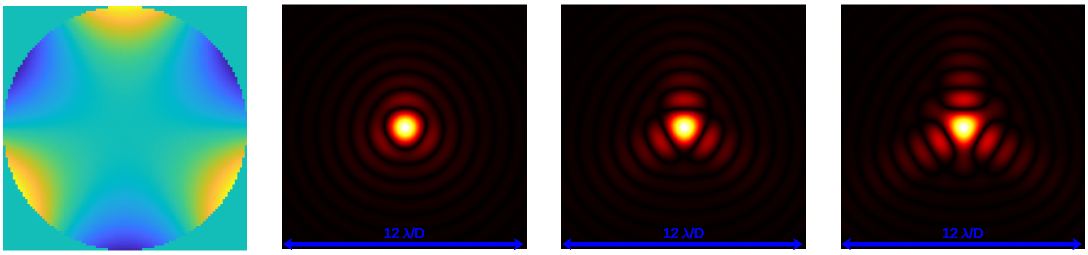

(e) Zernike mode 9 : Trefoil phase and effect on a PSF for 0.1 0.3 and 0.5 rad rms

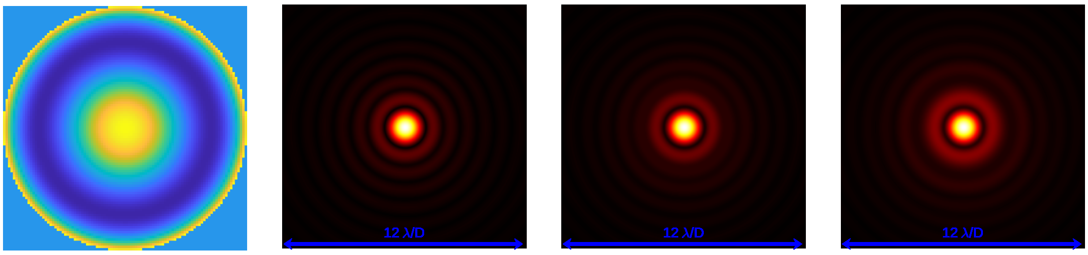

(f) Zernike mode 11 : Spherical phase and effect on a PSF for 0.1 0.3 and 0.5 rad rms

FIGURE 1.4 – effect of the first Zernike modes mode on the PSF

There are various ways to order the Zernike basis. In the rest of this thesis we use the Noll ordering (see Noll (1976)).

There is another popular basis for AO : the Karhunen-Loève basis. We study a specific mode (the petal mode described in chapter 2) and the Zernike and Fourier basis are enough for this thesis.

1.2 Atmospheric turbulence

The highest resolution is achieved for a constant phase. Any added phase in the pupil spreads the PSF, enlarging it and lowering the OTF. The goal of optical designers throughout history has been to keep the aberrations of optical systems as small as possible to keep OTF as high as possible and resolution as small as possible. In the absence of phase aberrations, the resolution of the PSF is limited by the size of the telescope and the wavelength of measurement. While generally optical aberrations come from the optical system itself, for ground based astronomical system there is an added source of aberrations. While light travels in space without being impacted by any aberrations for light-years of distance, the last kilometers through the atmosphere impact heavily the optical wavefront and reduce the quality of ground astronomical images.

1.2.1 Physical and statistical description

The effect of temperature gradient on the light propagation in the atmosphere is a well known phenomenon. The most commonly known consequences are mirages but sky observers know the enlargement of a star PSF as another effect of atmosphere turbulence. It was already described by Newton in its *Opticks, 1704, page 98 : One broad lucid Point, composed of those many trembling Points confusedly and insensibly mixed with one another by very short and swift Tremors, and thereby cause the Star to appear broader than it is, and without any Trembling of the whole.*

The physical description of the turbulent movement was proposed by Kolmogorov Kolmogorov (1941). This effect comes from movement of air masses in the atmosphere. A large convective cell of size $L0$ (outer scale, around 30m) dissipates energy by splitting into smaller cells, which transfer energy to smaller cells until the energy dissipated by viscosity outgrows the energy of a convective cell of size $l0$ (inner scale, around the mm). The distribution of energy follows a $-5/3$ power law between the inner and outer scales, called the inertial range, due to equipartition of energy.

These convective cells create local changes of temperature which translate in changes of refractive index of the air as in first approximation : $n_{air} = 1 + K\mu(T)$ with μ the density of air which depends on T the temperature, and K a constant. This fragmentation is generally supposed to be stationary for a given altitude(see Oboukhov (1962)) by making the assumption that the atmospheric turbulence is stratified (eg the strength of turbulence only depends on the altitude and not the x,y coordinates, and the distance between two points considered) following the equation :

$$D_n(r,h) = C_n^2(h)r^{2/3} \tag{1.12}$$

With C_n^2 the structure constant of the refractive index, characterising the strength of turbulence at altitude h, and r the distance between two points of the atmosphere.

As we neglect the scintillation effects, the EM field collected in the pupil suffers dephasing effect due to the variations of refractive index while it crosses atmospheric layers. The phase shift is equal to :

$$\phi(r,h) = \frac{2\pi}{\lambda}\int_h^{h+\delta h}(n(r,h')-1)dh' \tag{1.13}$$

The phase structure function can then be expressed as shown by Tatarski et al. (1961) as :

$$D_\phi(r) =< |\phi(x)-\phi(x+r)|^2 >= 2.91(\frac{2\pi}{\lambda})^2|r|^{\frac{5}{3}}cos^{-1}(\gamma)\int C_n^2(z)dh \tag{1.14}$$

With γ the angle between the pointing and the zenith. Fried (1965) introduced a useful parameter for comprehension here, the Fried parameter r_0 :

$$r_0 = [0.423(\frac{2\pi}{\lambda})^2\frac{1}{cos(\gamma)}\int_0^{\inf} C_n^2(h)dh]^{\frac{3}{5}}] \propto \lambda^{6/5}cos^{3/5}(\gamma)[\int C_n^2(z)dz] \tag{1.15}$$

The phase structure function in the pupil plane has a much simpler expression using this parameter :

$$D_\phi(r) = 6.88\left(\frac{|r|}{r_0}\right)^{5/3} \tag{1.16}$$

The phase statistics also known as the Kolmogorov spectrum follows :

$$W_\phi(f) = 0.00229 r_0^{-5/3} f^{-11/3} \tag{1.17}$$

An important characteristic of the atmospheric turbulence appears in the Kolmogorov spectrum's equation 1.17 : most of the atmospheric turbulence is concentrated in the low spatial frequencies. It is a very good news as it means with only a few 'correction pixels' we can correct the bulk of the atmospheric turbulence.

1.2.2 Influence of L_0

Equation 1.16 is true using a Kolmogorov approximation, so as long as the distance considered are negligible compared to L_0. For Large base interferometry or telescope as large as L_0 the outer scale introduced by Von-Karman must be taken into account. The equations were developed by Conan et al. (2000) and Tokovinin (2002).

$$D_\phi^{vK}(r) = 0.1717\left(\frac{L_0}{r_0}\right)^{5/3}\left[1.0056 - \left(\frac{2\pi r}{L_0}\right)^{5/6} K_{5/6}\left(\frac{2\pi r}{L_0}\right)\right] \tag{1.18}$$

using the numerical values and development proposed by Conan (1994)

$$\frac{\Gamma\left(\frac{1}{6}\right)}{2^{11/6}\pi 8/3}\left[\frac{24}{5}\Gamma\left(\frac{5}{6}\right)\right]^{5/6} = 0.17172^{-1/6}\Gamma\left(\frac{5}{6}\right) = 1.0056; \tag{1.19}$$

with Γ the Gamma function and $K_{5/6}$ the McDonald function (also 2nd type Bessel function). The main effect of the outer scale is to attenuate the low spatial frequencies when the scale gets close to L_0. The final phase statistics for a von Kármán spectrum :

$$W_{\phi}^{vK}(f) = 0.0229 r_0^{-5/3}\left(f^2 + \frac{1}{L_0^2}\right)^{-11/6} \tag{1.20}$$

This function tends toward the Kolmogorov spectrum when L_0 tends toward infinity.

This has been used by Conan et al. (2000) for the purpose of computing the variance of the dephasing or differential piston between 2 telescopes $\sigma_{\delta_p}^2$ for large base interferometery :

$$\sigma_{\delta_p}^2 = (\frac{\lambda}{2\pi})^2 \mathscr{D}_{\phi}(B) = (\frac{\lambda}{2\pi})^2 \int_0^{\infty} f W_{\phi}(f)\left(1 - J_0(2\pi B f)\right)\left[\frac{2J_1(\pi D_p f)}{\pi D_p f}\right]^2 df \tag{1.21}$$

with B the 'baseline' meaning the distance between the center of the two telescopes, D_p the size of each telescopes, J_n the Bessel function.

1.2.3 Temporal variation of phase

From a temporal point of view, of the turbulence are found to be small compared to the mean movement of the mass of air. This is called the frozen flow hypothesis (or Taylor hypothesis). The result is that the temporal variation comes only from the speed of the wind of the atmosphere. Fried (1965) showed there is an equivalent to r_0 for the temporal variation of atmospheric turbulence, τ_0 which is related to r_0 as follows :

$$\tau_0 = 0.314\frac{r_0}{\bar{v}} \tag{1.22}$$

With $\bar{v}$ the mean wind speed of the atmosphere seen by the telescope.

These parameters depend on the region of the world. Astronomers of course favor sites with large r_0 and small wind speed. Cerro Armazones, the building site of the Extremely Large Telescope (ELT) is used as the specification for this thesis and the properties of the corresponding turbulence parameters are summarised in Vernin et al. (2008) with a median wind speed of $5 m/s$ and a median seeing of 0.7arcsec = 15cm@500nm. Seeing is usually preferred to r_0 to describe the turbulence as seeing is much less chromatic ($\propto \lambda^{\frac{-1}{5}}$) than r_0 ($\propto \lambda^{\frac{6}{5}}$). Moreover seeing is directly observable by pointing the telescope to a star.

1.2.4 Effect of Turbulence on the PSF

François Roddier was among the first to explain the link between the atmospheric turbulence and astrophysical imaging in Roddier (1981) For a circular pupil of diameter $D = r_0$, the phase variance created by the turbulence equals 1 as shown by Fried (1965). This is a limit of the size of the pupil over which the effect of atmospheric turbulence is significant. The OTF of the atmospheric turbulence can be computed and follows the equation :

$$\mathrm{OTF}_{\mathrm{atmos}}(f) = e^{-\frac{1}{2}\mathscr{D}_\phi(\lambda f)} = e^{-3.44(\frac{\lambda f}{r_0})^{5/3}} \tag{1.23}$$

With this equation we see that the cutoff frequency of the atmospheric OTF is $f_c = \frac{r_0}{\lambda}$. Contrary to a telescope OTF, the atmospheric OTF is an efficient filter for spatial frequencies under r_0 as seen in Figure 1.5c. When going through a telescope, the final OTF is :

$$\mathrm{OTF}_{\mathrm{tot}}(f) = \mathrm{OTF}_{\mathrm{tel}}(f) \times e^{-\frac{1}{2}\mathscr{D}_\phi(\lambda f)} \tag{1.24}$$

On Figure 1.5 we show the change of PSF and OTF when the size of the pupil diameter gets larger than 1, 2 and 5 r_0.

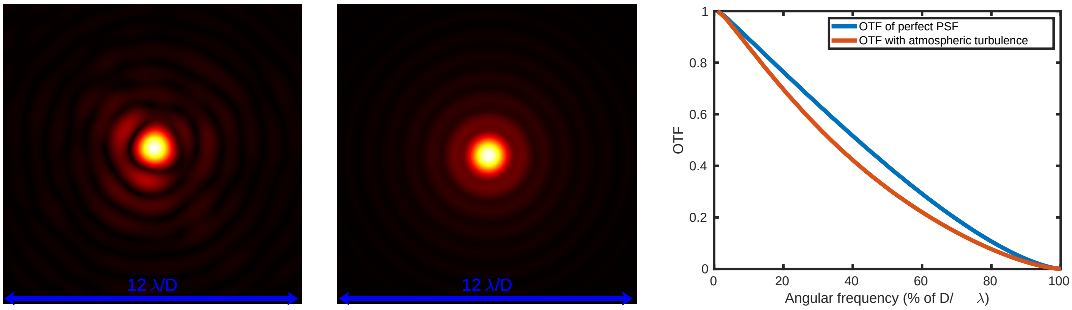

(a) Effect of atmospheric turbulence for a telescope where r_0=D on short exposure PSF, long exposure PSF and OTF

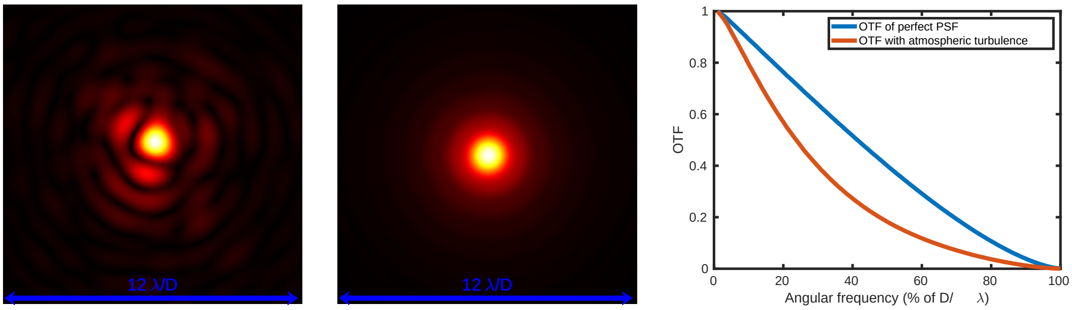

(b) Effect of atmospheric turbulence for a telescope where $r_0 = D/2$ on short exposure PSF, long exposure PSF and OTF

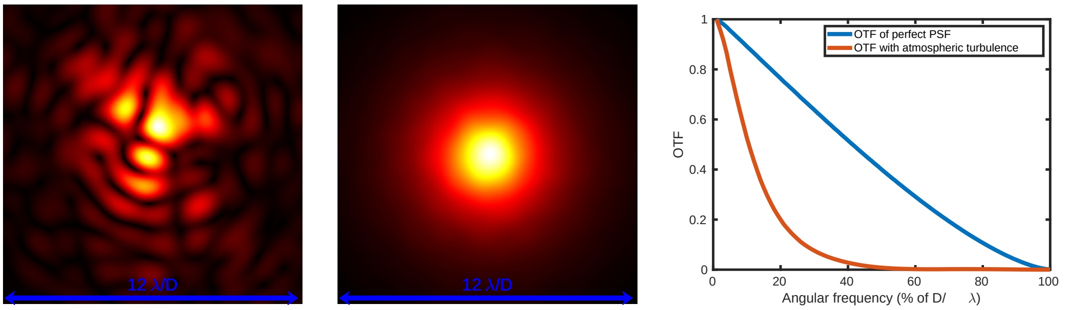

(c) Effect of atmospheric turbulence for a telescope where $r_0 = D/5$ on short exposure PSF, long exposure PSF and OTF

FIGURE 1.5 – effect of r_0 smaller than D on the PSF and OTF of a telescope respectively the same size, 2 times larger and 5 times larger than r_0

We see in particular that for diameters larger than r_0, a telescope's resolution is limited not by the size of its pupil anymore, but by the size of the Fried parameter. In the short exposure image the telescope diameter is responsible for the size of the speckles inside of the larger PSF which is defined by the r_0. In practice the r_0 can represent a much smaller fraction of the telescope diameter : for instance, modern telescopes can reach diameters of about 10 meters while median r_0 is around 15 cm in visible for the best astronomical sites. The Fried parameter is generally given in cm for a given r_0 but can also be given in angular resolution measured by the size of the

Full Width Half Max (FWHM) disk of the PSF called seeing s using the formula :

$$s = \mathrm{FWHM}_{\text{Long exposure PSF}} = 0.98\frac{\lambda}{r_0} \tag{1.25}$$

For a r_0 of 10cm taken at 0.5 μm λ, that gives a seeing if $1''$

As shown by equation 1.15 the Fried parameter is chromatic (almost linearly) meaning that using a longer wavelength will increase the r_0 and allow a larger telescope pupil before being seeing limited. It also means that for a given pupil, the PSF is closer to a diffraction limited PSF when observing at longer wavelengths. For this reason, a lot of instruments aim to collect IR photons instead of visible ones.

A very common metric for the quality of the final PSF is the Strehl Ratio (SR). The historical definition is the fraction between the Intensity of the current PSF, and the intensity of the diffraction limited PSF both taken on the optical axis :

$$SR = \frac{I(x=0, y=0)}{I_{diff}(x=0, y=0)} \tag{1.26}$$

The historical definition is difficult to apply to real images, where the on-axis position is poorly defined, and the PSF position usually not aligned perfectly with the detector pixels. To reduce the sensitivity of a single point measurement, the Strehl ratio can be defined using the ratio between the integral of the OTF with phase aberration and the diffraction limited OTF (which is mathematically equivalent to the historical definition) :

$$SR = \frac{\int_{\mathscr{R}^2} \left|\mathrm{OTF}_{\phi}(f)\right| df}{\int_{\mathscr{R}^2} \left|\mathrm{OTF}_{diff}(f)\right| df} \tag{1.27}$$

In the low aberrations case, the Mahajan approximation can be used to link aberration amplitude and SR from Mahajan (1982) :

$$SR = e^{-\sigma_{\phi}^2} \tag{1.28}$$

This approximation always underestimates SR compared to the real one. The difference reaches 10% error for SR under 0.6. As the phase residuals depend on the wavelength the SR will also depend on the wavelength.

1.3 Adaptive Optics

To compensate for the atmospheric turbulence and its effect on astronomical imaging a solution emerged in the 80s-90s called Adaptive Optics (AO) though it was proposed for the first time in 1953 (Babcock (1953)). It consists in 3 main components : a Deformable Mirror (DM), a Real Time Computer (RTC) and a Wavefront Sensor (WFS). In this thesis we describe the simplest implementation of an AO system : the Single Conjugated Adaptive Optics (SCAO). The light coming from the telescope reaches first the DM, is then separated between two paths. The first is the ’science path’ where the astrophysical instrument takes place, gathers photons in the corresponding bandwidth and provides the astronomical result. The other is the AO path where the light coming from an object is analysed by the WFS to measure thephase of the EM field in the pupil plane. This phase in pupil plane is then turned into commands sent to the DM. The schematics of a SCAO loop is shown on Figure 1.6.

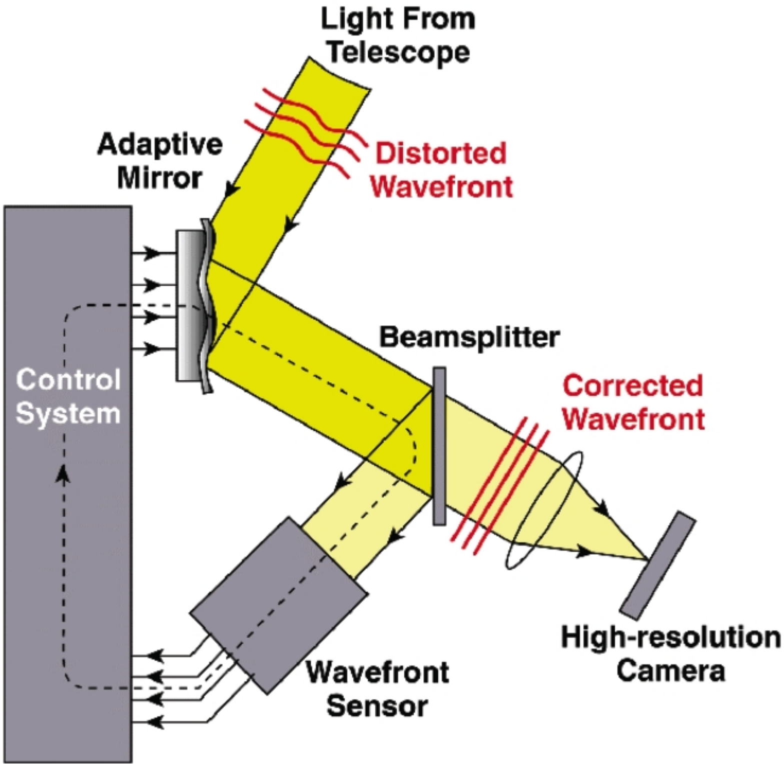

FIGURE 1.6 – General AO schematics *Credit : Claire Max, Center for Adaptive Optics, UC Santa Cruz*

Wavefront Sensor the WFS is a sensor which measures the aberrated phase coming from a source (a natural star in SCAO mode). There are 4 important constraints that drive the development of wavefront sensors used in astronomy : they should be self-referenced (i.e. not require a reference wavefront such as a Michelson interferometer), they need to be photon-efficient, giving the most precise measurement of a wavefront on stars as faint as possible, for which they need to be able to work with broadband light, and they require a fast (e.g. linear on some function of the phase) signal reconstruction.

Real Time Computer It is the computer which processes the data collected by the WFS and sends the commands to the DM. The RTC includes the algorithms used to perform the wavefront reconstruction. Two important parameters of the RTC are the frequency and the latency at which it operates. The RTC used in AO operate between a few hundred Hz and 3kHz, and aim at a latency between the WFS exposure time and the command of the DM of a few frames, typically two frames.

Deformable Mirror The optical deformable component which corrects the phase aberrations. Many technological solution exist for the DM. In the vast majority it is a mirror in AO (hence the name) but our eye's lens is an example of a refractive deformable optical component. Important parameters of the DM are the number of actuators in the diameter of the DM, the speed of the DM, and the stroke they can reach (the largest amplitude of deformation). Typically the DM requires several micrometers of mechanical stroke to be able to address the atmospheric turbulence seen in astronomy.

1.3.1 The closed loop of AO

The first principle of AO visible in Figure 1.6 is that it is a closed loop. The difference between the targeted wavefront and the phase remaining after the DM correction is called the **Residual Phase**. The system measures the deformation after this correction and aims at reducing the difference between this corrected wavefront and the target wavefront (generally a flat wavefront). There are a few vocabulary terms related to this. As an iterative process, the wavefront sensor usually measures the phase after the correction of the DM, which means that it measures only a residual wavefront. This notion in automatic is referred to "closed loop" process. We name an **open loop** measurement the measurement when the AO loop isn't closed, so the system measures uncorrected atmospheric turbulence. **Closing the loop** or **bootstrapping** means starting the AO loop. As the system measures its highest phase amplitude it's generally where the system has the most non linear behavior and it can be a delicate step where the loop can break.

The speed of this loop is a crucial element of the AO system. As the phase of the wavefront moves with the wind, the DM needs to follow this movement. Time can be lost at any of the three step (measurement by WFS, computation by RTC, correction by DM) but the most irreducible one is the time of integration of the WFS. To reduce that time of integration the WFS needs as much light as possible to be able to measure the aberrant phase on dim stars. For that reason generally the light is separated between science path and AO path by a Dichroic filter to transmit all the light of a given bandwidth to the AO. Though it is not required, AO generally uses lower wavelength than science path. This strategy only works because of the approximation the aberrations created by the turbulence have the same Optical Path Difference (OPD) for all wavelengths.

1.3.2 Effect of AO on PSF and OTF

The effect of AO correction on the PSF varies in the field of view. Inside the correction area, and outside. A DM has a limited number of points where the OPD created by its deformation can be controlled. Akin to the number of pixels in an image, that means that the spatial frequencies which a DM can act on is limited by the number of actuators in the diameter. The EM field in focal plane is the FT of the electric field in the pupil plane. So the quantity observed in the focal plane is somehow similar to a spatial frequencies domain for the electric field. Due to the limited number of actuators, the DM can only act on a limited range of spatial frequencies, and therefore in a limited area around the center of the PSF. If the DM actuators are on a square grid with N_{act} in a side this creates a square correction area around the PSF of size $N_{act} \times \frac{\lambda}{D}$ as seen on Figure 1.7

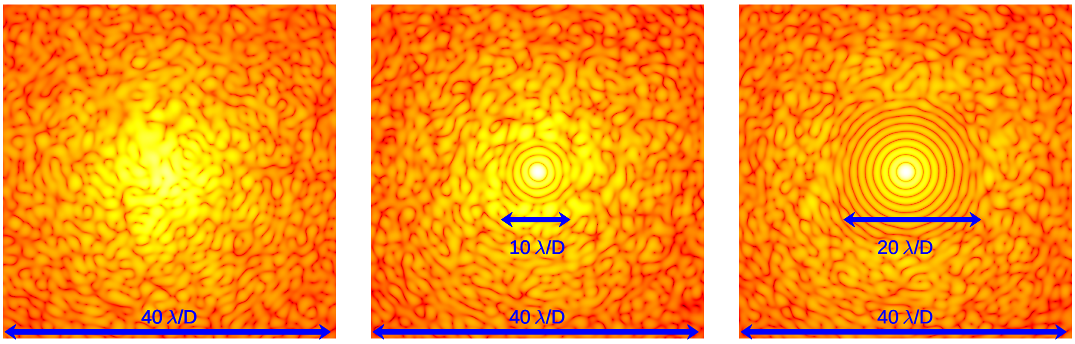

(a) PSF created by a telescope with $D = 10 \times r_0$, log scaling

(b) PSF created by a telescope with $D = 10 \times r_0$ corrected by a 10x10 DM, log scale

(c) PSF created by a telescope with $D = 10 \times r_0$ corrected by a 20x20 DM, log scale

FIGURE 1.7 – Effect of AO correction on a PSF

The important parameter is the size of the **pitch** which is $d_{act} = D/N_{act}$, the size between 2 actuators of the DM on the telescope pupil. The aim of AO correction is for the system to be diffraction limited which is defined by the Maréchal Criterion as $\sigma < \lambda/14$ in waves. If we are fitting limited, the fitting error reaches $\lambda/13$ in waves so it's generally considered that the system reaches diffraction limit for $d_{act} = r_0$. The effect of AO on the PSF is to concentrate the energy scattered by the atmospheric turbulence in the central PSF to restore the unaberated PSF. This effect can be seen on Figure 1.8b where we plot the radial average of the previous PSF fitting limited. We see that the fitting limited PSF follows the unaberated PSF for spatial frequencies lower than the correction area of the DM (half the number of actuator). Outside of this correction radius, the fitting limited PSF tends toward the uncorrected PSF.

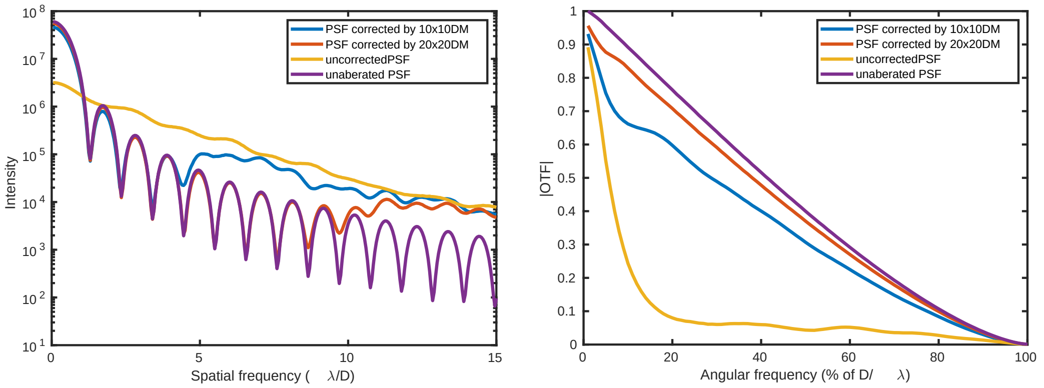

(a) Effect of a fitting limited AO correction on the PSF for variable number of actuator

(b) Effect of AO correction on the OTF for variable number of actuator

FIGURE 1.8 – Effect of AO correction of PSF and OTF

It is to be noted that while the pitch of an actuator (d_{act}) is the distance between two actuators, it is not necessarily representative of the influence area of the Influence Function (IF) of an actuator (In practice as the mechanical coupling is generally fixed both values are proportional). The shape on an influence function is approximately a Gaussian function with a FWHM different than the pitch. The factor used to determine the width of the IF is the mechanical coupling, and is defined as the height of the $n-th$ actuator's IF at the location of the neighbour $n+1th$ actuator. Though it is a parameter of the DM design, we use the the value of 0.3 mechanical coupling following the ELT M_4 (see Crépy et al. (2010)). For that mechanical coupling the FWHM of the actuator is $1.5 \times d_{act}$. That means the IF is over half its max value for $0.75 \times d_{act}$ on one side.

If the system is perfect the PSF in this corrected area would be very close to the Airy pattern intensity map and an uncorrected PSF outside of the correction area as was shown on figure 1.8b. In practice, other sources of errors raise the intensity level inside the correction area. The first of such source of error to be considered is the temporal error. A very important parameter to control this temporal error is the loop gain. The closed loop of AO is generally controlled by an integrator control law. The command sent to the DM at the $m-th$ iteration is determined using the following formula :

$$C_n = C_{n-1} - g \times c_{n-1} \tag{1.29}$$

with n the index of the n-th iteration, c_{n-1} the command corresponding to the residual phase measured by the WFS at the previous integration, g the gain chosen for the loop. This loop gain is generally between 0.2 and 0.5 for optimal performances. Sometimes a leaky integrator is used following the equation $C_n = l \times (C_{n-1} - g \times c_{n-1})$ with l equal 0.99 to avoid loop divergence on the limits of the pupil. In this thesis we limit ourselves to an integrator control law though alternatives exist such as those presented by Kulcsár et al. (2006) or Petit et al. (2004).

1.3.3 Error budget of an AO loop

After the AO correction, some phase residuals still subsist which impacts the quality of the science-path PSF. The quantity allowing an estimation of this error budget is the RMS amplitude of the phase aberrations remaining in the pupil plane σ^2_ϕ. This quantity can be separated in an error budget of its different sources as shown by Véran et al. (1997) :

$$\sigma^2_\phi = \sigma^2_{\text{fitting}} + \sigma^2_{\text{temporal}} + \sigma^2_{\text{aliasing}} + \sigma^2_{\text{noise}} + \sigma^2_{\text{NL}} + \sigma^2_{\text{aniso}} + \sigma^2_{\text{NCPA}} + \sigma^2_{\text{calib}} \tag{1.30}$$

with σ in rad. We detail the content of each term below :

fitting error $\sigma_{fitting}$ This error comes from the limits of the phase aberrations which the DM can correct. As we saw the PSF area which the DM can correct is limited by the number of actuators due to all the high spatial frequency phase aberrations. For a mirror with a square grid the expected variance in residual phase was computed by Hudgin (1977) :

$$\sigma^2_{fitting} = 0.23 \times \left(\frac{d_{act}}{r_0}\right)^{5/3} \tag{1.31}$$

With d_{act} the pitch, the distance between 2 actuators on the DM.

temporal $\sigma_{temporal}$ The temporal error has two main contributors : the speed of the loop and the latency. The latency is the number of loop iterations between the phase measurement of WFS and the DM applying the correction.

Aliasing $\sigma_{aliasing}$ For spatial frequencies higher than the sampling frequency of the WFS, an aliasing effect occurs. These high orders can be measured as low orders and therefore corrected by the loop, while they should not be. This effect and its corresponding wavefront error is called aliasing. Classical aliasing is only a question of spatial frequency inside or outside of the measurement space and would be reduced by increasing the number of measurement points, but in AO the term aliasing is used more generally for any effect of high order aberrations on low order signal. (chapter 4 identifies an example of non classical aliasing with the petal confusion effect 4.10).

Noise σ_{noise} This error in phase residual is a propagation of the error in the signal measured in the WFS. This error depends on the star magnitude as brighter stars create higher quality signals in the WFS. This term grows with a dimmer star and sets the limit of magnitude where the AO can be operated. The noise can be mitigated by increasing the exposure time of the AO loop, but this will increase the temporal error.

Non linearities σ_{NL} The WFS measurement can contain non-linearities which create errors in phase reconstruction. The non-linearities of the WFS are an important aspect of my PhD and are studied in chapter 4 for the petal mode on the Pyramid Wavefront Sensor (PyWFS) and briefly described later in this chapter for classical modes.

Anisoplanetism σ_{anis} The WFS measures the OPD created by the volume between the star and the telescopes pupil. If the scientific target is not the AO guide star, the light coming from an object at a different locations in the sky propagates through different part of the atmosphere and a different OPD is created than the one present on the guide star. Closer objects have more propagation environment in common. So this error grows as we see object further from the source used for AO. For SCAO this limits the corrected Field Of view (FOV) to a few arcseconds.

Non Common Path Aberration (NCPA) σ_{NCPA} The light going to the WFS and to science instrument goes through different optical paths. Different aberrations can appear between the WFS and science path causing an error in the science image unseen by the WFS, these aberrations are called NCPA. As we discuss in Chapter 2 the problem studied in this thesis originate mostly from the telescope pupil so we neglect this term in this thesis.

Calibration σ_{calib} This error contains any difference between the AO during calibration and on sky operation. Many different sources of error can contribute to this term, such as : Star light has a different spectrum than calibration source, the pupil shape has changed (rotation of the telescope field for instance), change in DM shape.

This error budget can also be separated in its different phase mode contribution. If using an orthogonal basis $[\phi_1, \phi_2, \phi_3 ... \phi_n]$, one can write

$$\sigma_{\phi}^2 = \sigma_{\phi_1}^2 + \sigma_{\phi_2}^2 + \sigma_{\phi_3}^2 + ... + \sigma_{\phi_n}^2 \tag{1.32}$$

with $\sigma_{\phi_n}^2$ the amplitude of the $n-th$ mode described earlier in this chapter.

Born & Wolf (2013) defines the limit of phase error for an optical system to be diffraction limited for a $\sigma^2 < \frac{\lambda}{14}$. For a $\lambda_{sensing} = 800$nm this means that the PSF is diffraction limited for a wavefront error RMS under 57nm.

1.3.4 Wavefront sensing in OA

The WFS's purpose is to turn the physical quantity we are interested in, ϕ into a measurable signal, the intensity. A WFS has 3 characteristics which determine whether they can be used in AO ;

Sensitivity Gives the efficiency of converting photons into an observable intensity related to the wavefront. As SCAO works with the limited light coming from a guide star, the sensitivity of the WFS determines the integration time of the WFS and is a major parameter setting the loop frequency or the limit magnitude of the guide star.

dynamic range The higher measurable phase by the WFS. In most cases is is antagonistic to sensitivity. It sets the amplitude of phase that the WFS can measure accurately. For this thesis it is in particular the phase regime for which the WFS remains linear that define the dynamic.

Inversion The method allowing one to go from the intensity measured to the phase map. In general in AO a linear inversion is preferred as it is fast to compute and allows a high loop frequency. The inversion is another major parameter setting the loop latency.

In this thesis we focus on the Pyramid Wavefront Sensor.

There is a parameter similar to the number of actuators of the DM in the WFS : the number of subapertures. It's the number of measurement points in the pupil plane. It limits the spatial frequency of the modes measurable by the WFS. The minimum number of subapertures to control a $n \times n$ actuator DM is $n \times n$ subapertures. This defines the number of points to compute for the wavefront measurement and can reduce the speed of the AO loop.

1.3.5 AO closed loop simulation

Studying Closed Loop simulation results is a big part of this thesis. All the AO simulations are done using the OOMAO package (Conan & Correia (2014)). Here we show a typical way to represent the result of an AO simulation. The metric we use in closed loop is the standard deviation of the residual phase : σ_{phi} in nm rms. The simulation is done with a point-like source monochromatic and the λ used for sensing is 850nm. As shown in Figure 3.20a we plot σ_{phi} for each iteration of the closed loop. As we consider different systems and telescopes we also plot the fitting error as the limit of what can be accomplished with the considered AO system. We generally present a side plot of the same closed loop but following a specific phase mode, here the astigmatism in Figure 3.20b. The residual phase has been projected at each iteration and the resulting amplitude in nm RMS is plotted on the accompanying figure for each iteration. Here as an example, we show the astigmatism of the residual and the atmosphere to compare.

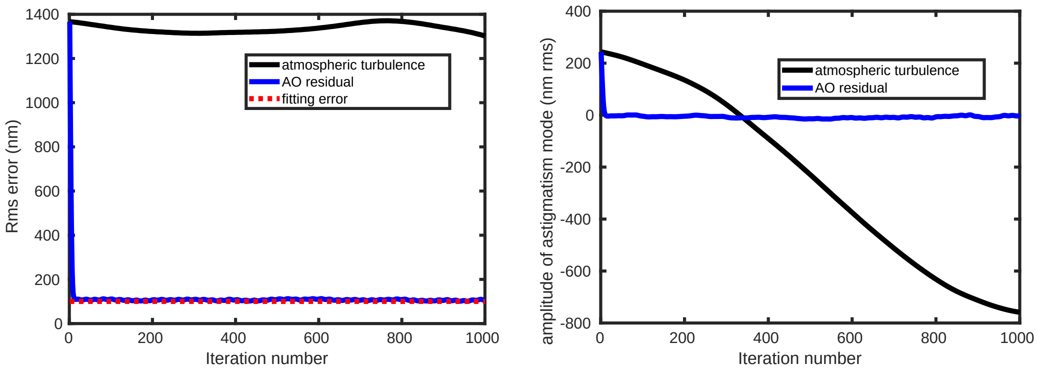

(a) Closed loop residuals at each iteration

(b) amplitude of astigmatism present in the residual at each iteration

FIGURE 1.9 – Exemple of a closed loop result

We can distinguish 2 parts in this plot. In the first few iterations after the loop closure, the AO residuals RMS starts from the atmospheric turbulence and decreases down to its stable residual value. This part is called the bootstrap and can be pretty difficult due to the non linearity that large phases can induce on the WFS. Once the bootstrap is achieved, the AO loop is in a stable state. The difference between the fitting error and the residual will depend on the other error terms of in the loop (1.30).

1.4 The ELT

Today all large ground telescopes use an AO system. The ELT will be the largest ground based telescope and will have AO capability built-in embedded in the telescope. It is currently under construction at the Cerro Armazones, close to the Very Large Telescope (VLT) site. With its 39m diameter, the expected resolution is six times better than the James Webb Space Telescope (JWST) for a larger collecting power (Tamai & Spyromilio (2014)). There are multiple astrophysical science cases covered by the ELT : Exoplanet studies, the early universe, our own galaxy, or even studying dark energy.

1.4.1 Optical layout of the ELT

To insure the quality of image, the ELT opted for a 5-mirrors configuration. They are called M_1 to M_5. (M_1 is the first mirror which collects light). The first 3 mirrors deliver a good quality in a large field with an anastigmat configuration and the M_4 and M_5 are meant to correct the aberration coming from the atmosphere and vibrations of the telescope.

Figure 1.10 summarizes the mirrors characteristics of the ELT and how the light propagates in the telescope. Of them $M1$ and $M4$ are of particular interest for this thesis and are further detailed in Chapter 2.

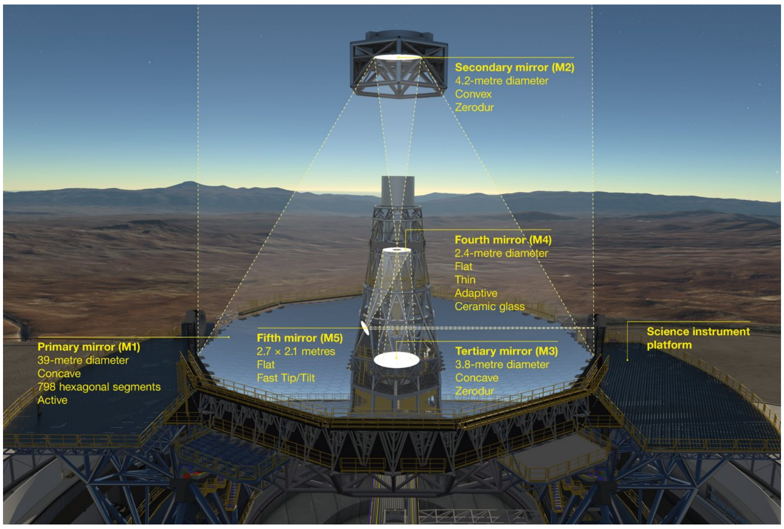

FIGURE 1.10 – Optical layout and characteristics of the ELT mirrors, *crédit : ESO*

Light from the telescope is then directed toward one of two Nasmyth platforms which can host 4 instruments each. There will be 4 instruments ready for first light at one of the Nasmyth focal platform :

1.4.2 ELT first light instruments

MICADO (*Multi-adaptive optics Imaging CamerA for Deep Observations* is a large field imager (up to 1 arcminute). The instrument can be used either with the integrated SCAO mode or using the MCAO capability of the MORFEO instrument for larger field of view. The SCAO system uses a PyWFS with ($\lambda_{sensing} = 750nm$). MICADO has 4 imaging modes : classical imaging with filter ranging from 800 to 2400nm, an astrometric mode, a coronographic mode and a slit spectrometer mode.

METIS (*Mid-infrared ELT Imager and Spectrograph*) is the long wavelength instrument of the ELT, with operating spectral band of $3-5\mu$m and $8-13\mu$m. It is mainly built for high contrast coronography and the direct imaging of exo-Earths. The WFS sensing can be conducted at much longer wavelength unused by the science path in this instrument : ($\lambda_{sensing} = 1650$ or $2200nm$). This makes the wavefront reconstruction easier for this instrument.

MORFEO (*Multi-conjugate Adaptive Optics RelaY*) is a multi-conjugate adaptive optics (MCAO) system designed to feed two instruments. The first is MICADO, the second instrument hasn't been decided yet. MORFEO will use 6 Laser Guide Stars (LGS) to measure the wavefront as well as two additional DM to supplement M_4 and $M5$ to correct multiple atmospheric layers. It will add a MCAO capacity to the MICADO instrument.

HARMONI (*High Angular Resolution Monolithic Optical and Near infrared Integral field Spectrograph*) is the main case study of this thesis. With its Integral field Spectrometer (IFS) it will provide the spectrometric capacity of the ELT. It is equipped with a large choice of available spectral bands and high resolutions. This allows the study of physical phenomenons in high red shift galaxies. The instrument comes with 4 AO modes : LTAO (Laser tomographic AO), SCAO, HCAO (High Contrast AO), and no AO. As HARMONI is the reference case we will try to emulate for the rest of this thesis we detail more its AO configuration. The AO system schematics is shown on figure 1.11

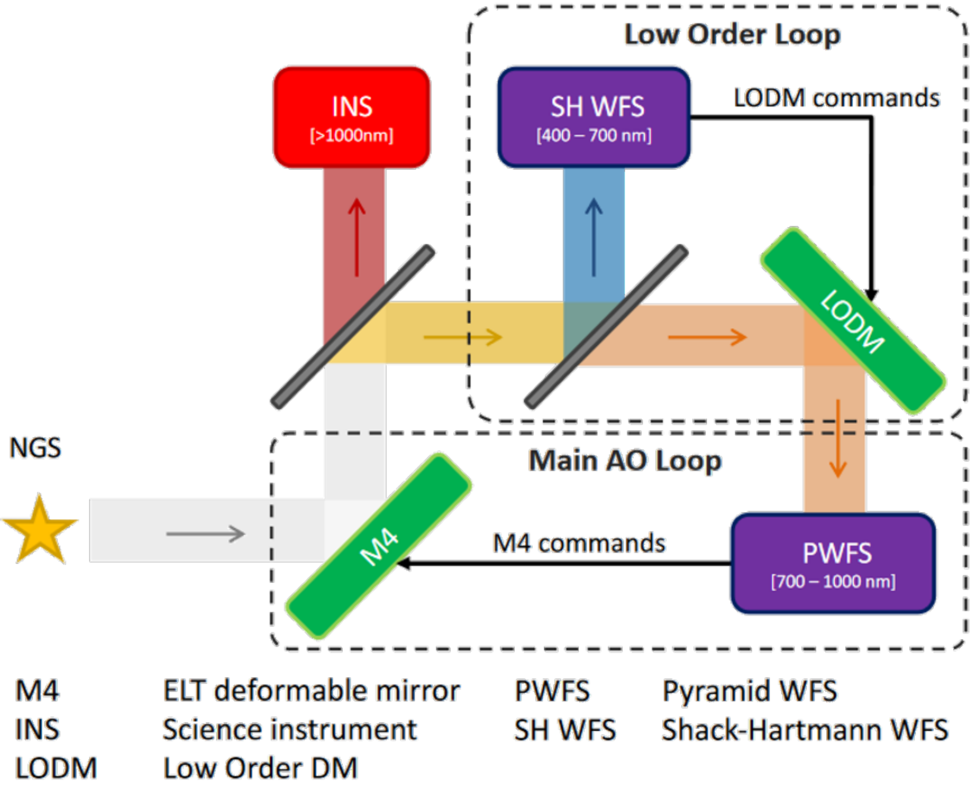

FIGURE 1.11 – AO schematic of the SCAO of the HARMONI instrument , *credit : Charlotte Bond*

It uses a modulated PyWFS in the visible ($\lambda_{sensing} = 800nm$). A second WFS with a Zernike Wavefront Sensor (ZWFS) (N'Diaye et al. (2016) in the IR ($\lambda_{sensing} = 1200nm$) measures the quasi-static residual to allow High Contrast AO. Finally the Low Order Loop using a Shack-Hartmann in blue $\lambda_{sensing} = 650nm$ dynamic compensation of NCPA.

1.5 Pyramid Wavefront Sensor for Adaptive Optics

1.5.1 From the Shack Hartmann to the PyWFS

For the last 30 years the Shack-Hartmann (SH) has been the most commonly used WFS. It's principle is illustrated on Figure 1.12. The quantity measured in a SH is the Center of Gravity (COG) of each subpupil. As such it is only the slope of the phase in each subpupil which is measured. It cuts the pupil in multiple subpupils analysed separately and as is shown by Plantet et al. (2015), the SHWFS is less sensitive than the PyWFS for a large number of points of phase measurement. As such it has been replaced for the future generation of AO systems.

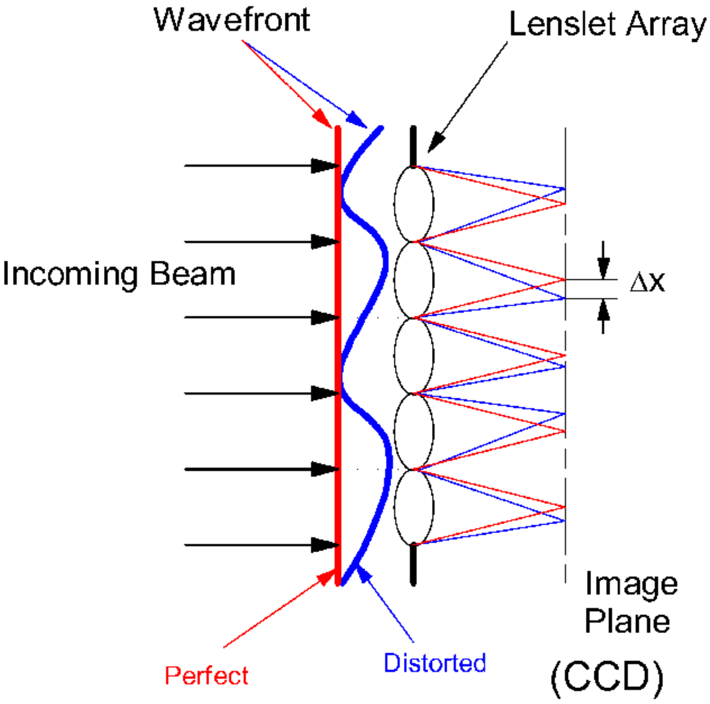

FIGURE 1.12 – Principle of a Shack-Hartmann WFS measurement, *credit : Michael A. Campbell*

The PyWFS was proposed by Ragazzoni (1996) as an alternative WFS. It is historically a generalisation of the Foucault Knife Edge test, used to measured the defects during the polishing of a mirror. The principle is to place a knife edge in the focal plane of the mirror, this edge suppressing half of the light, and to observe the diffracted light in a pupil plane. If there are phase defects (=defect in the shape of the mirror) they will translate into aberrations in the electromagnetic field and appears as a change in the PSF as shown on Figure1.13a. If the focal plane is hidden with a knife, the PSF light is blocked and the pupil will appear black, except the light moved by the shape defect which appears in the pupil plane as shown on Figure 1.13b. As the PyWFS and the

Foucault knife edge work by cutting the Fourier plane and separating its component to encode the phase into intensity signal, they are part of the family of sensor called the Fourier Filtering Wavefront Sensor (FFWFS). The Zernike Wavefront Sensor is another exemple of FFWFS.

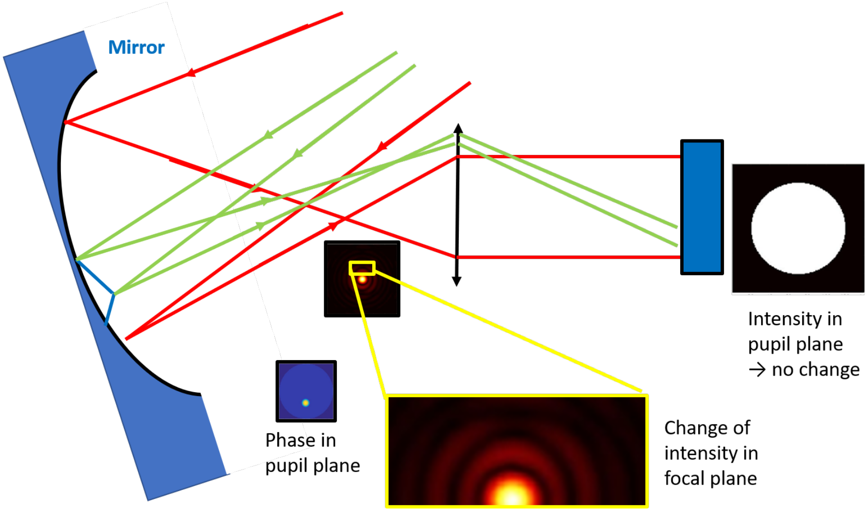

(a) Effect of a defect in the shape of a mirror = wavefront error. The PSF intensity distribution changes but not the intensity in the pupil plane intensity

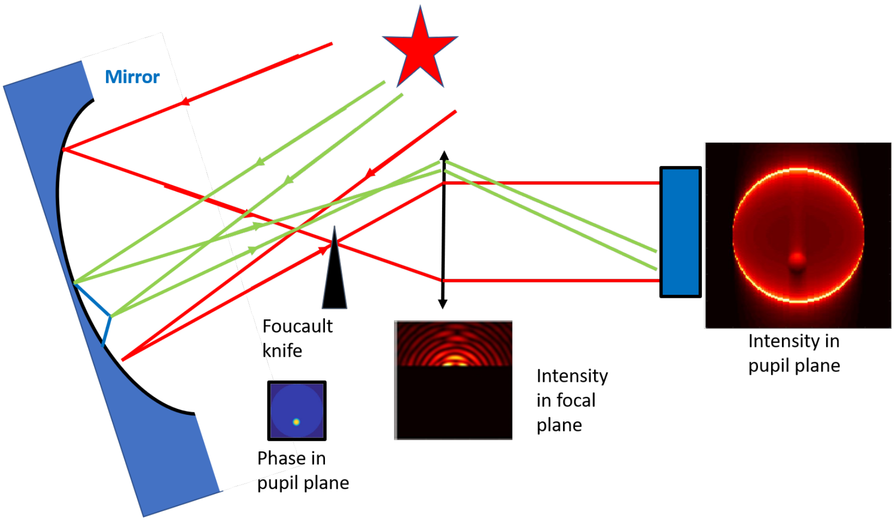

(b) Same phase defect but with Foucault knife in the focal plane. Intensity in pupil plane now shows the defect

FIGURE 1.13 – principle of the Foucault Knife Edge test

This historical tool, although allowing a WFS at a fraction of lambda, has nonetheless two disadvantages for being used as AO wavefront sensing : half the light is thrown out as it is absorbed by the knife, and it measures phase defects only in one direction. The proposition of Pyramid as a WFS in 1996 consists in turning the knife into a glass prism transmitting the light with the same filtering effect, and a second prism in the perpendicular direction is added, creating the classical 4-sided PyWFS. The optical layout of a 4-sided Pyramid is shown on Figure 1.14.

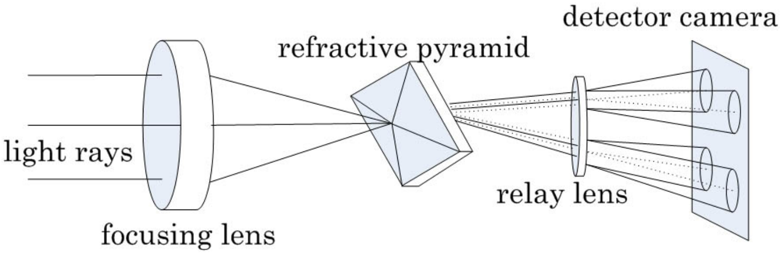

FIGURE 1.14 – Optical layout of a PyWFS

It consists in a focusing element, a four sides glass pyramid whose apex is in the focal plane, and a detector in pupil plane (generally after a second collimating element). As a habit of language, the term "subaperture" is still used to refer to the pixels of pupil imaging, as a reference to the SH WFS. This new sensor is promising as it separates the pupil in only 4 sides and doesn't lose sensitivity for large numbers of subapertures. This makes this sensor more efficient for large telescopes compared to SH, explaining its adoption in all 30-m telescopes under construction. The physical angle needed at the apex of the pyramid depends on the f-number after the focusing lens and how separated the 4 pupil images need to be. The separation on the detector was originally designed to be larger than 1 full pupil image as the cross-talk between the light of each pupil image was considered a pollution of the signal. It has been shown since by Fauvarque (2017) that it can on the contrary be interesting from a sensitivity point of view to reduce this separation, which we will exploit in Chapter 3. An example with the standard separation is shown on Figure 1.15. A first step to treat the pyramid signal is to identify and separate each pupil image $[I_1 I_2 I_3 I_4]$.

1.5.2 Slopes maps

There are two ways to use the pyramid in its linear range. The first historical method is the slopes map method presented by Ragazzoni (1996). The pupil images are numerically recombined using the linear combination in equation 1.33 to recreate the images of the Foucault knife edge test corresponding respectively to the first spatial derivative of the phase in the X and Y directions.

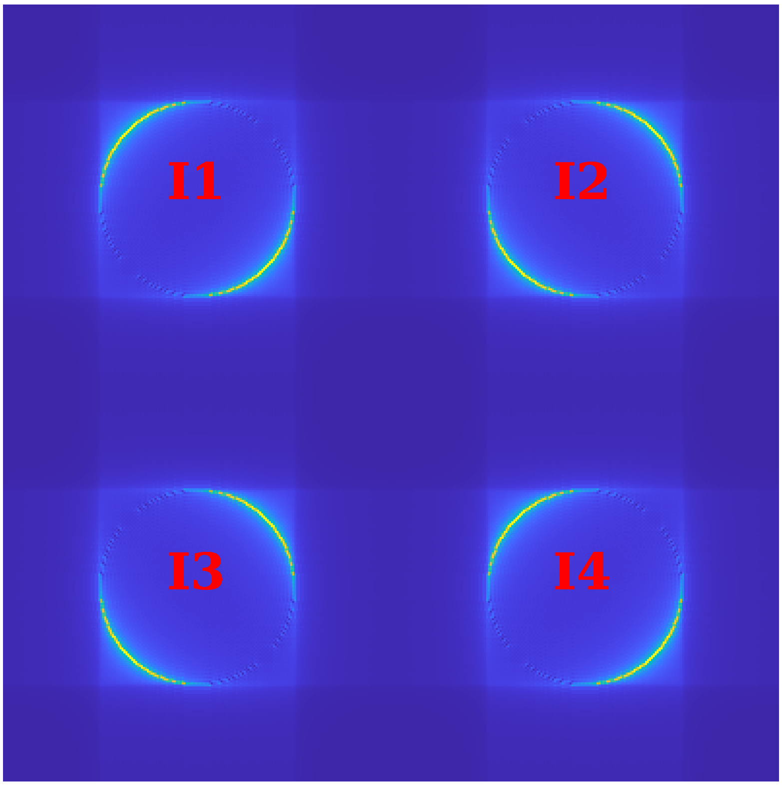

FIGURE 1.15 – Intensity measured on the PyWFS detector

$$S_X(\phi) = \frac{(I_1 - I_2) + (I_3 - I_4)}{I_1 + I_2 + I_3 + I_4} \quad ; S_Y(\phi) = \frac{(I_1 - I_3) + (I_2 - I_4)}{I_1 + I_2 + I_3 + I_4} \tag{1.33}$$

We define the push-pull δS for a given phase mode ϕ_i as

$$\delta S_X = \frac{S_X(\epsilon\phi_i) - S_X(-\epsilon\phi_i)}{2\epsilon} \quad \delta S_Y = \frac{S_Y(\epsilon\phi_i) - S_Y(-\epsilon\phi_i)}{2\epsilon} \tag{1.34}$$

Then the Interaction Matrix I_{MAT} for slopes map I_{SMAT} is, for a basis of modes $[\phi_1\phi_2\phi_3...\phi_n]$, as follows

$$I_{SMAT} = \begin{bmatrix} \delta S_X(\phi_1) & \delta S_Y(\phi_1) \\ \delta S_X(\phi_2) & \delta S_Y(\phi_2) \\ \delta S_X(\phi_3) & \delta S_Y(\phi_3) \\ ...... & \\ \delta S_X(\phi_n) & \delta S_Y(\epsilon\phi_n) \end{bmatrix} \tag{1.35}$$

ϵ is a small amplitude to make sure we are using the pyramid in its linearity regime. In simulation, this factor is very small and is $1e^{-10}$ for this thesis. This historical method is largely in use and has a few advantages. The first is its self-referenced. S_x and S_y tend toward 0 for a flat wavefront. For a system where NCPA are low and without a calibration source to calibrate the 0 wavefront point, this method gives good performances. Then from 4 subpupils we compute 2 images which contain all the phase informations. This means a reduction in the size of the matrix used for the reconstruction which allows the RTC to run quicker. On the disadvantages, the system becomes very sensitive to movements of the subpupil images which can modify the S_x and S_y combination and I_{MAT}. The constraints on the pyramid alignment are very high with this method. This method is adapted to the 4-sided PyWFS and the computation of S_X and S_Y cannot easily be extended to different FFWFS shapes.

1.5.3 Reduced Intensity

The Reduced intensity was shown first by Fauvarque et al. (2016). In this method all the pixels in the detector are used without making subpupil combinations. We define the reduced intensity ΔI as :

$$\Delta I(\phi) = \frac{I(\phi)}{N} - I_0 \tag{1.36}$$

With N : number of photons on the detector I_0 the intensity for a flat wavefront normalised by the number of photons N. This reduced intensity is the variation of intensity created by a phase in the pupil plane compared to the intensity obtained with a flat wavefront.

If the transparency function of the Fourrier filter is noted m, it was showed that the intensity pattern in pupil plane changes linearly with the incoming phase if TFm has both a real and imaginary component. As the PyWFS fits this definition, we know that the intensity of the pyramid can be described as a Taylor development : $\mathscr{I}(\phi) = I_0 + I_{\text{linear}}(\phi) + I_{\text{quadractic}}(\phi^2) + \ldots$

As a consequence for low phase amplitude $\Delta I(\phi) \approx I_{\text{linear}}(\phi)$

The interaction matrix is the computation of the variation of signal ΔI for a infinitesimal phase change $\epsilon\phi$ written as δI :

$$\delta I(\phi) = \frac{I(\epsilon\phi) - I(-\epsilon\phi)}{2 * \epsilon} \tag{1.37}$$

Then the I_{MAT} for the reduced intensity method $I_{\delta MAT}$ is computed as :

$$I_{\delta MAT} = \begin{bmatrix} \delta I(\phi_1) \\ \delta I(\phi_2) \\ \delta I(\phi_3) \\ \ldots \\ \delta I(\phi_n) \end{bmatrix} \tag{1.38}$$

The advantage of the full frame intensity is that it is extendable to a lot of FFWFS (by example pyramid and Zernike mask) and allows their comparison. It has an advantage for practical implementation : the exact location of the four pupil images with respect to the detector pixel grid can be relaxed a lot, there is no more need to have a 1 to 1 matching between the geometrical pupil images. As was shown by Deo et al. (2018) the pupil misalignment can be a major source of measurement error.

The main disadvantage is that a reference intensity is needed to compute the reduced intensity.For some systems measuring this reference intensity is not possible due to the absence of a calibration source. Slopes map and reduced intensity have close performances in term of phase reconstruction but the reduced intensity used twice as much pixels which can slow down the RTC.

1.5.4 Wavefront measurement

The linear intensities can be computed thanks to the following relation

$$\Delta I_{linear}(\phi) = I_{\delta MAT} \times \begin{pmatrix} a_1 \\ a_2 \\ \dots \\ a_n \end{pmatrix}, \quad or \quad [S_X(\phi) S_Y(\phi)] = I_{SMAT} \times \begin{pmatrix} a_1 \\ a_2 \\ \dots \\ a_n \end{pmatrix}, \tag{1.39}$$

with a_i the amplitude of the mode ϕ_i, $\Delta I_{linear}(\phi)$ the linear intensity appearing on the pyramid detector. What we want for the wavefront reconstruction is the inverse equation :

$$\begin{pmatrix} \hat{a}_1 \\ \hat{a}_2 \\ \dots \\ \hat{a}_n \end{pmatrix} = I^{-1}_{\delta MAT} \times \Delta I(\phi) \; or \; \begin{pmatrix} \hat{a}_1 \\ \hat{a}_2 \\ \dots \\ \hat{a}_n \end{pmatrix} = I^{\dagger}_{SMAT} \times [S_X(\phi) S_Y(\phi)] \tag{1.40}$$

$I^{\dagger}_{MAT}$ is computed using a Moore–Penrose inverse of I_{MAT}. The Moore-Penrose inverse relies on the computation of the eigenvalues and eigenmodes of the matrix. As such it also allows the filtering of the modes which are the most susceptible to amplify noise. This filtering is necessary in order to prevent reconstructing modes for which the WFS has poor sensitivity. Such a reconstruction would lead to noise amplification on these modes. In general the modes with the lowest sensitivity compared to the other modes of the basis are the filtered modes. This filtering can be automated by setting a Tolerance level, namely a minimal eigenvalue. In general in this thesis the tolerance level is set to 1% of the maximum eigenvalue. $I^{\dagger}_{MAT}$ is called the Control Matrix C_{MAT}.

Once we have the estimated amplitude through the equation 1.40, the estimated phasemap can be computed :

$$\widehat{\phi} = \sum_{i=0}^{n} \hat{a}_i \times \phi_i \tag{1.41}$$

1.5.5 PyWFS non-linearities

As was shown by Fauvarque et al. (2016) the PyWFS intensities do not contains only linear terms, but also higher order terms. This appears in practice as a saturation of the pyramid signal. On Figure 1.16 we plot the linearity curve of the pyramid with respect to the amplitude of a few classical Zernike modes.

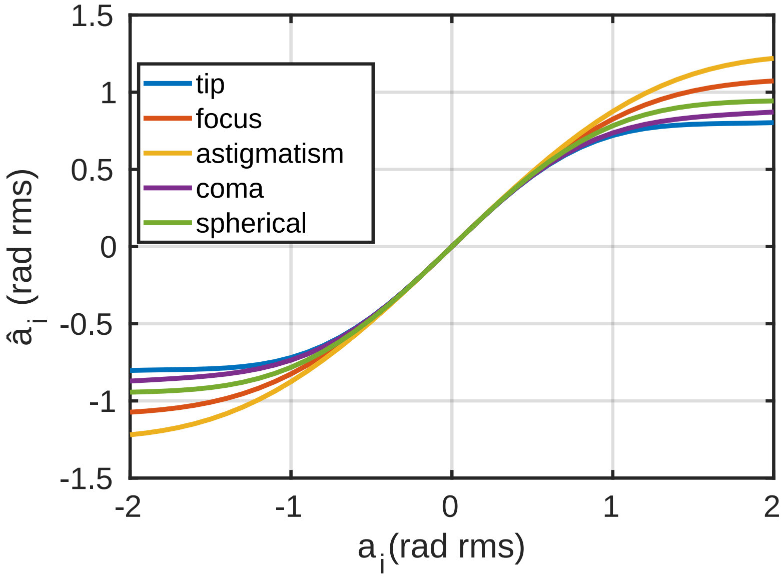

FIGURE 1.16 – Linearity plot of classical Zernike phase modes

This linearity curve is the comparison between the amplitude a_i of the mode and the reconstructed amplitude $\hat{a}_i$. The estimated amplitude deviates from a linear dependence when the amplitude becomes large. This corresponds to a saturation of the PyWFS signal. The mechanism is easy to understand for the tip tilt mode and is illustrated on Figure 1.17 as when all the light of the PSF is on only 1 pyramid face, we can move further from the apex and the light in the detector plane does not change as the PSF only goes through a tilted glass surface.

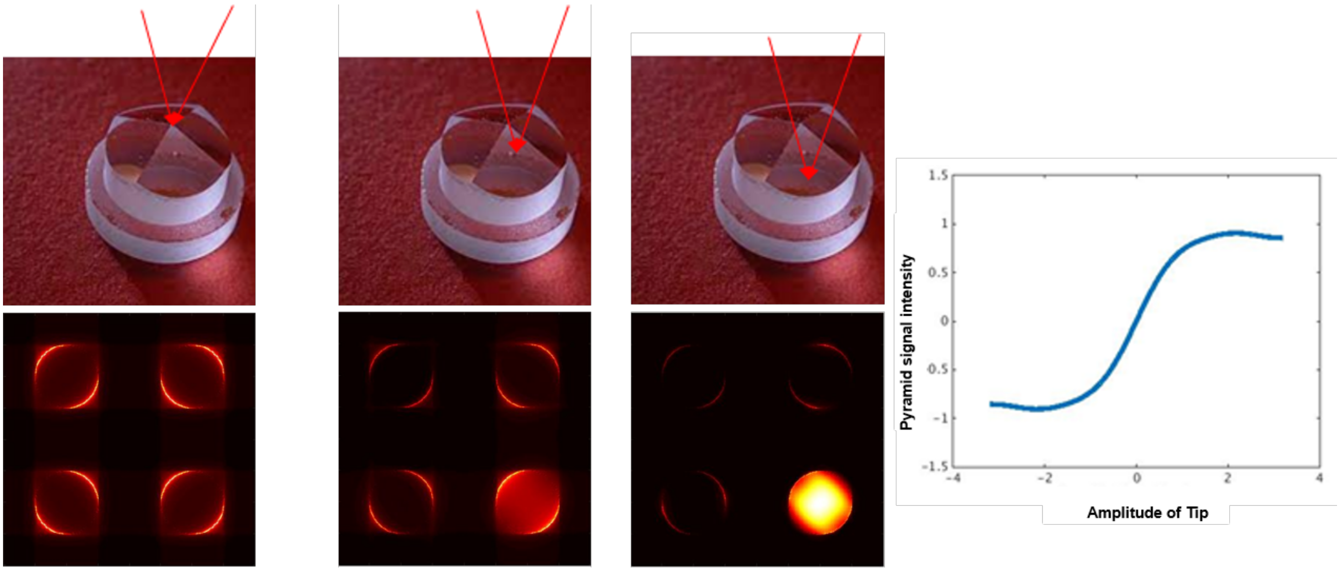

FIGURE 1.17 – Example of saturation for tip tilt mode on the PyWFS. The filtering effect for the pyramid stops when the PSF only reaches one face of the glass pyramid

To reduce this saturation and the associated non-linearities a solution was already proposed by Ragazzoni (1996) when the PyWFS was first proposed. Originally called 'vibration' of the glass pyramid in the PyWFS, it is today implemented as a fast circular modulation of the PSF around the glass pyramid. The PSF has to perform exactly 1 period during 1 exposure time of the WFS detector. This modulation is created by a fast tip-tilt mirror and its main parameter is the size of the modulation radius, expressed in λ/D. Other scheme than the circular modulation have been proposed such as the clover modulation proposed by Bertrou-Cantou (2021) but did not show a tremendous change in term of sensitivity. In this thesis we use only the circular modulation.

The effect of modulation can be seen on Figure 1.18 in term of linearity range and sensitivity for a few classical phase modes. While the linear range increases, the sensitivity decreases.

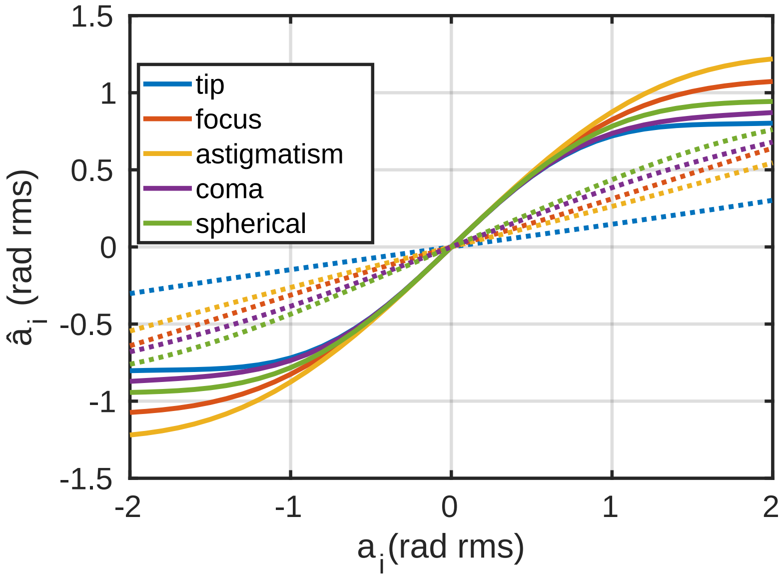

FIGURE 1.18 – Linearity plot made with a modulated pyramid in dotted line . we see the reduced sensitivity (= phase estimated is reduced compared to the entrance phase) but larger linearity range

The modulation affects more the phase modes whose spatial frequencies are smaller than the modulation radius. This is particularly visible when comparing the spherical mode, the higher frequency tested here, and the tip. While the spherical starts saturating, the tip remains linear for the amplitude tested here but has a smaller change of amplitude than the spherical mode. The impact of very low order modes (like Tip-tilt) is localized close to the optical axis. The modulation by enlarging the PSF and increases the dynamic range This is illustrated in Figure 1.19. The pyramid acts as a Fourier filtering device, as such it has any effect in the intensity measured on the detector only if the PSF intercepts the pyramid edges during the modulation. For a sinusoidal phase signal the secondary lobes do not intercept the pyramid edges if the modulation radius is smaller than the distance from the apex of the pyramid to the secondary lob, which is the spatial frequency of the sinus.

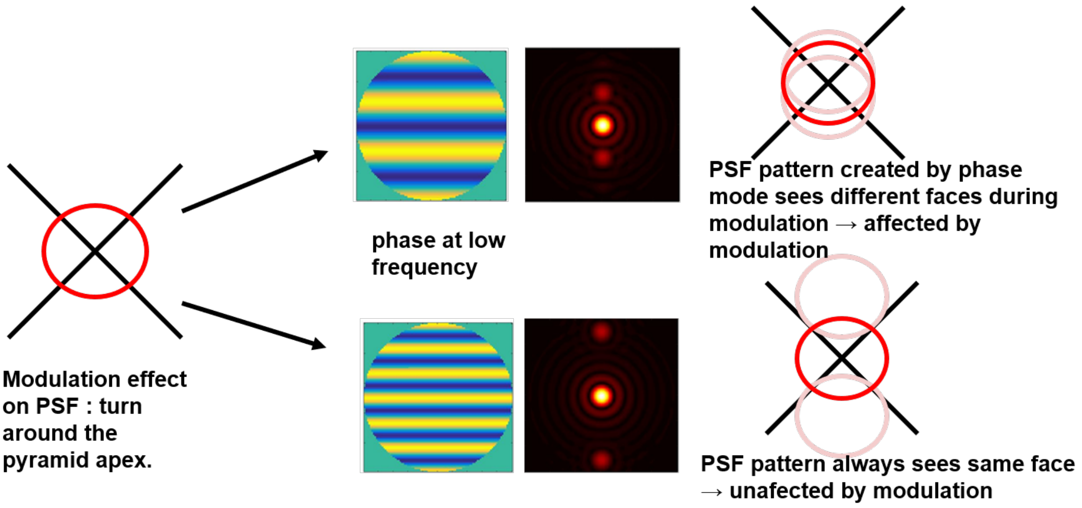

FIGURE 1.19 – Modulation affects only the mode whose effect on the PSF go through a different face of the PyWFS during modulation. Otherwise the mode see the same face and behave the same. If modulation radius is too small the mode will not be affected y the modulation of the PSF

Modulation is a accompanied as is visible on figure 1.19 by a loss of sensitivity for the mode affected (eg for a given amplitude of phase a smaller change of intensity is caused and consequently a smaller phase is measured). This loss of sensitivity will also be created by the presence of other mode in the phase. The enlargement of the PSF caused by the presence of another optical aberration will cause an effect very similar to modulation illustrated on figure 1.20 or the tip tilt mode in the presence of focus mode of different amplitude. This effect is called the Optical Gains (OG) as it behaves like a change of the AO loop gain due to optical aberrations.

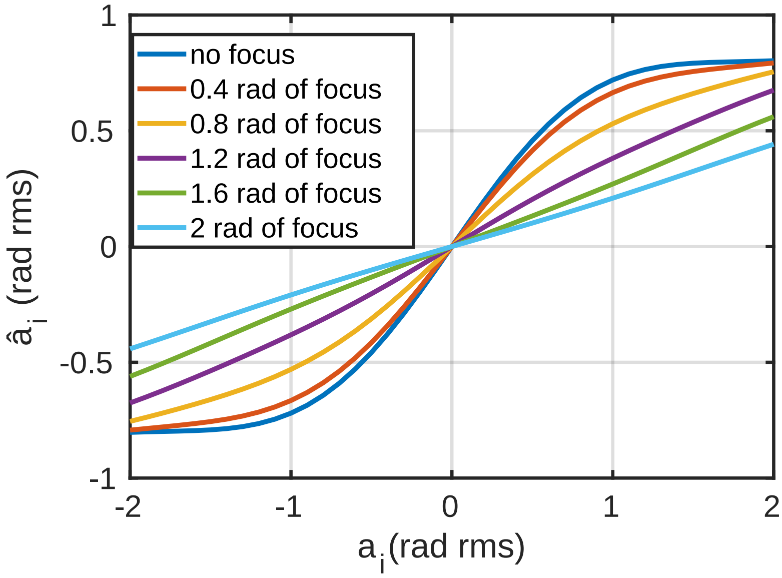

FIGURE 1.20 – Linearity plot for tip made with an unmodulated pyramid in presence of focus. We see that as more focus is introduced, the tip loses sensitivity and the linearity is extended.

As we see the effect of modulation and optical gains are very similar. To an extent, the modulation is a controlled optical gain from tip/tilt while the effect of other aberration in the atmosphere is unpredictable. This effect can reduce greatly the efficiency of the wavefront reconstruction. We don't focus on this effect in this thesis though it does appear clearly in chapter 4.

There are multiple models used for describing the pyramid signals and understanding its behaviour such as the convolutive model developed by Fauvarque et al. (2019) and expended by Chambouleyron et al. (2022). The convolutive model relies on the approximation of the floating pupil. In general it is more accurate with a large modulation radius and when the effect of the pupil edges are not important. As we describe in chapter 2 and 3, the problem tackled in this thesis is specifically the problem posed by complex pupil and is more favorable for low modulation radius. As such we are using the full propagation of the pyramid for our studies.

We have seen in this chapter the basis of image formation in astronomy and in particular the characteristics of AO. We also presented how the WFS of the 30m telescope era, the PyWFS, is used. In the next chapter we describe the main problem of this thesis, the petal mode and the problem it rises to the 30m telescopes AO.

2 A new problem for Adaptive optics : the Petal mode

Adaptive optics has progressed a lot since the first on-sky successful experimentation in the early 1990s. Today all telescopes of the 30m generation are designed to be equipped with an AO system from day one. But this generation of telescopes and their giant pupils are facing a new problem presented in this chapter : pupil fragmentation and its main consequence, the petal mode. In this chapter, we define the petal mode, its different sources, its impact on the image quality, and a Toymodel, a pupil made to create the simplest petal mode possible, allowing one to study this mode and its propagation in the AO system.

2.1 Fragmented pupil shape

The $8m$-class telescopes (VLT, Subaru, Gemini...) are the biggest monolithic telescopes. Due to the mechanical constraints imposed by their size, telescopes larger than 8m in diameter are not built with only one monolithic mirror but with multiple segments. The Keck twin telescopes, or the Gran Telescopio Canaria showed that segmented pupils were viable ways to create a large primary mirror for astronomy. The secondary mirrors of these giant telescopes are growing in size in proportion to the primary mirror. This adds unprecedented constraints on the mechanical structure of the telescopes, forcing the mechanical design to add larger spiders to support the secondary optics. This leads to the generation of telescopes larger than 10 meters to have fragmented pupils. There are 3 telescopes under construction in this new class of 30m-telescopes : the Extremely Large Telescope (ELT), the Thirty Meter Telescope (TMT), and Giant Magellan Telescope (GMT). They are designated by the term Giant Segmented Telescopes (GSTs).

2.1.1 ELT

The ELT pupil has 2 particularities in its primary pupil shape. First is the segmentation of the primary mirror (M1). It is comprised of 798 hexagonal segments of 1.45m tip-to-tip. These segments together create an overall 39m diameter primary mirror for the telescope. The strategy for phasing these segments was a major issue during the ELT design phase and gave rise to multiple experiments to ensure the phasing at a fraction of the wavelength of this telescope. This is not the issue we are discussing in this thesis so we consider the M1 of the ELT as a monolithic rigid pupil. The gap between these segments is 4mm (all parameters are described in Cayrel (2012)) and we consider that the segments of the ELT are phased (showed in HARMONI studies shown in Sauvage (2019) that the effect of phasing of the M1 segments should be negligible for SCAO). In Figure 2.1 we show the ELT pupil with its segmentation.

The second particularity is the size of the ELT spiders. The secondary mirror of the ELT (M2) of the ELT with its 4.25 meters of diameter and 3 tons of weight needs a larger structure than ever before to ensure the rigidity of the telescope optical combination. Furthermore, the size of the ELT structure makes it even more sensitive to wind shake and vibrations which this structure needs to absorb. These constraints led to a design with a spider's width of 51cm. It is also to be noted that the DM of ELT, M4 is a segmented mirror with 6 petals where the DM segmentation follows the fragmentation of the M1 pupil. M4 also uses an unusual triangular geometry for its actuators (though this does not affect the problem considered in this chapter). In Figure 2.2a we show the ELT pupil with its central obstruction and spiders.

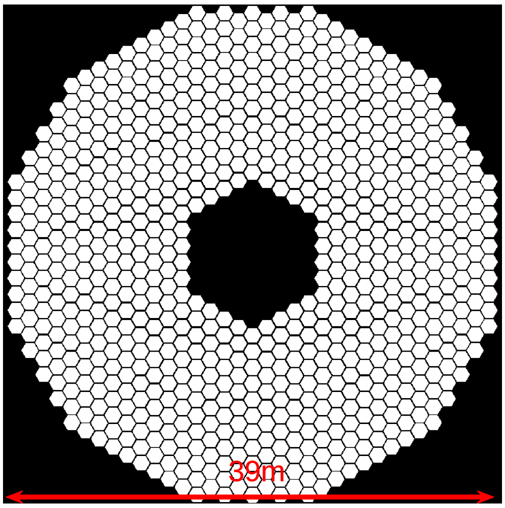

FIGURE 2.1 – ELT pupil with M1 segmentation, the gap between M1 segments has been exaggerated to be visible

We make a distinction between the **segmentation** of a pupil and the **fragmentation** of a pupil. A pupil is segmented when the gaps between each segment are very small in comparison to a measurement patch (sub-aperture size in the case of a SH-WFS). In particular, they are smaller than 1 subpupil considered for wavefront sensing. A telescope is fragmented when the gaps are larger than 1 WFS subpupill projected on sky.

The segmentation visible in Figure 2.1 is not considered in this thesis, but the fragmentation visible in Figure 2.2a is the source of the main problem studied in this thesis.

2.1.2 Thirty Meter Telescope (TMT)

The TMT has a very similar pupil to the ELT in terms of geometry. The M1 is comprised of 492 1.42 m hexagonal segments. The optical path is simpler than the ELT with only 3 mirrors before reaching the Nasmyth platform (compared to 5 for ELT). Furthermore, only the secondary mirror is over the primary mirror and it is not a deformable mirror, creating less mechanical constraints on the structure necessary to support it. As a consequence, the spiders are "only" 20cm wide after the 2013 change of design. It is the only northern hemisphere 30m class telescope. The pupil is shown in figure 2.2b.

2.1.3 Giant Magellan Telescope (GMT)

While ELT and TMT create their large pupils by combining small hexagonal mirrors, the GMT consortium decided to combine the largest monolithic mirror available into an even larger pupil. The design combines 7 8.4m mirror to create a 25m pupil. The smallest separation between mirrors is 40cm and it is aligned with the spiders. The spiders themselves are not visible on the pupil image except on the central 8.4m mirror. A particularity of the GMT is that each 8.4m fragment is conjugated to one 672 actuators DM. Following the fragmentation definition, GMT is only fragmented and not segmented. In Figure 2.2c we show the GMT pupil.

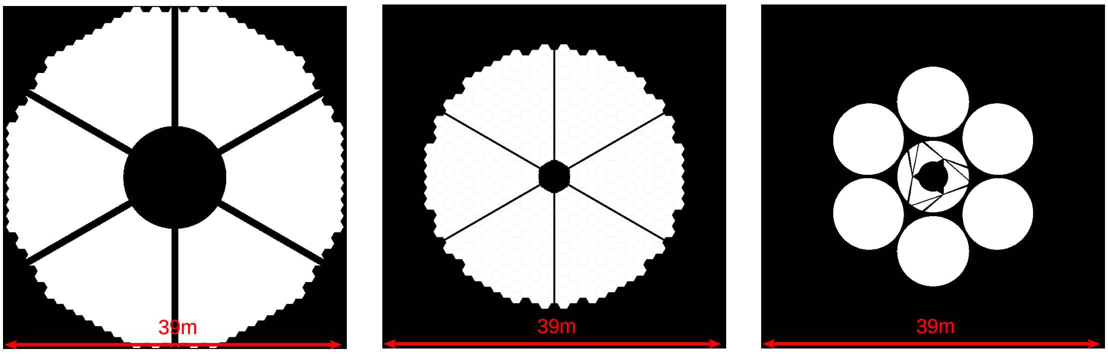

(a) ELT pupil with spider and central obstruction

(b) TMT pupil with spider and central obstruction (Courtesy of Jean-Pierre Véran)

(c) GMT pupil with spiders visible on central fragment. Spiders are in the gap between the pupil fragments. (Courtesy of Guido Agapito)

FIGURE 2.2 – Pupil of 3 GSTs under construction with same scaling

2.2 The consequence of Pupil fragmentation : The petal mode

Due to the width of the spider gaps, there are areas where no light reaches the detector. That creates blind areas in the wavefront measurement. The phase information in the blind gap cannot be measured due to the absence of signal. And we know from equation 1.16 that the phase is expected to change by $\sigma^2_{\text{spider}} = 1053 nm^2$ (for a sensing at @$850 nm$) over this gap. While the phase in a fragment is continuous, this continuity is not true over the spider gap. This will lead to the apparition of the so-called petal mode, as shown by Schwartz et al. (2017) where the phase is well controlled in a pupil fragment, but there are jumps of phase from one fragment to the next. Furthermore, the DM of GMT and ELT also are discontinuous following these large gaps. A continuous DM would reduce the phase which can be created under the spider. With the current configuration, each DM will maintain the mean piston of each fragment and the variation of phase in the gap is not taken into consideration. We show how the continuity of the DM reduces the effect of petal fragmentation in section 2.6.

2.2.1 Petal mode definition

From the fragmentation of the pupil we can define a mode basis composed of the piston of each fragment taken separately. For a pupil separated in N fragments, we can define a piston mode for each fragment : $[\phi_{p1}\phi_{p2}...\phi_{pN}]$ with a Peak to Valley (PV) = 1. In Figure 2.3 we show the ELT and GMT piston basis. It is to be noted that this basis is orthogonal but not normalized for the scalar product defined in Chapter 1.

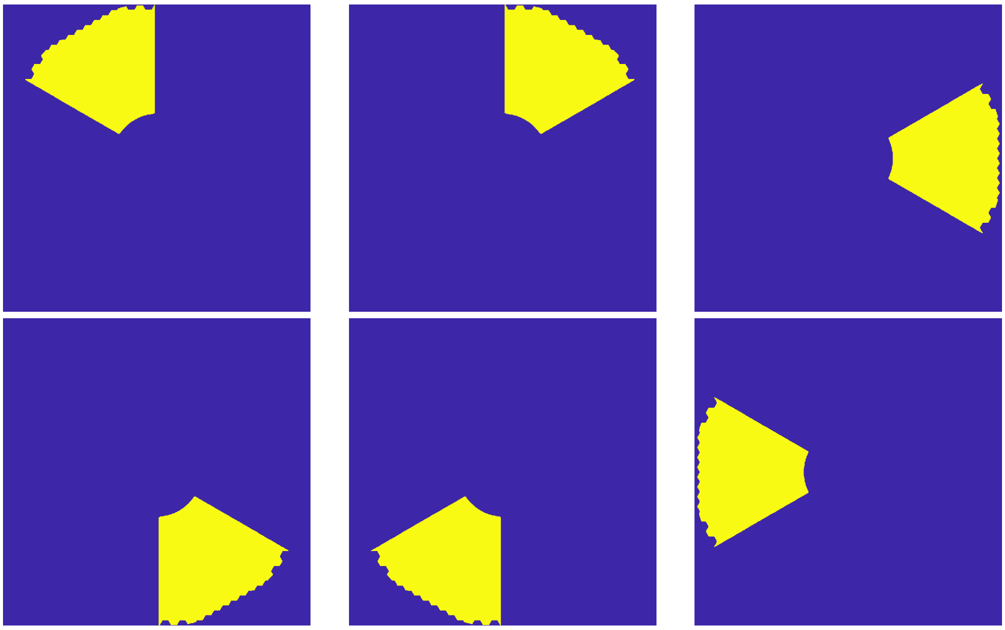

(a) ELT ϕ_{pN} piston basis

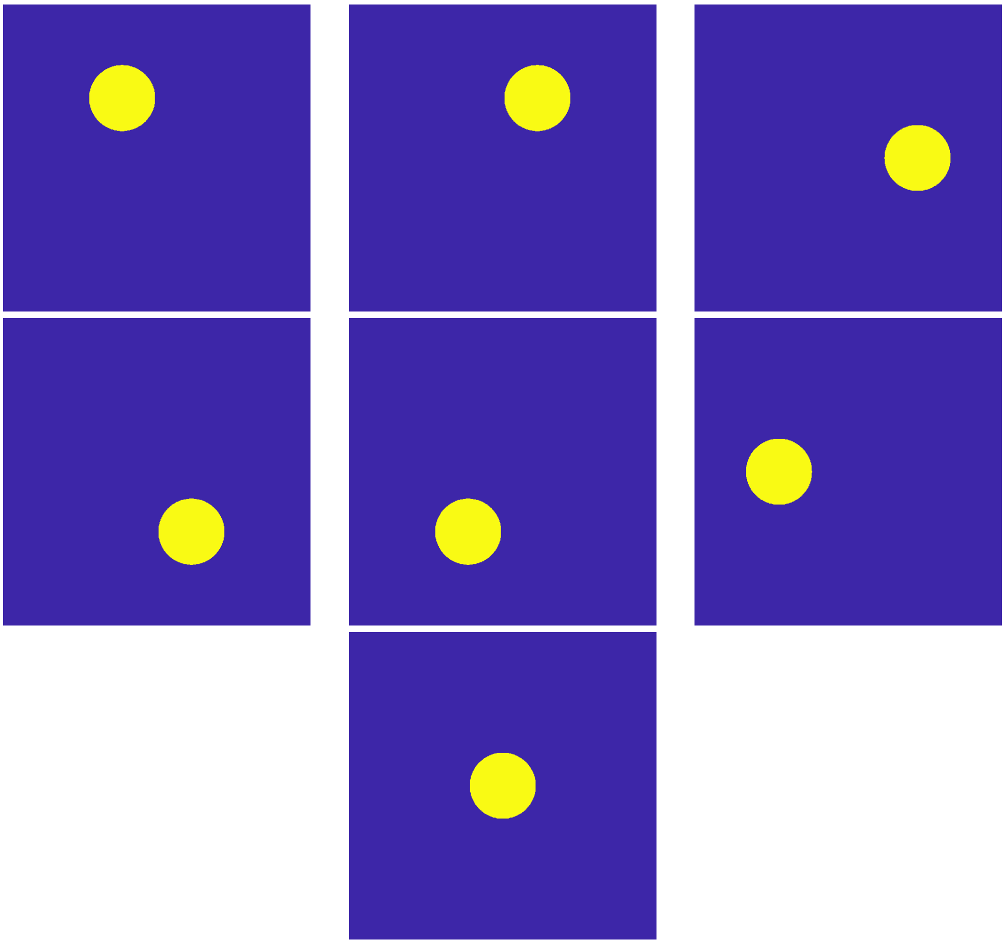

(b) GMT ϕ_{pN} piston basis

FIGURE 2.3 – piston p_n basis for GMT and ELT

This basis is not orthogonal to classical basis used in optics such as Zernike or KL, in particular, it is not orthogonal to the piston mode. This makes the value of the aberration p_n of little use to evaluate the optical quality of the wavefront. The important parameter is the difference of piston between each fragment. That way we can define a basis of differential piston between a reference fragment and another fragment.

$$\delta p_i = p_1 - p_i \quad \text{for} \quad i \quad \in [2,6] \tag{2.1}$$

This aberration is more useful from a physical point of view but we prefer to define a more global petal mode basis in the next section to be used for the remainder of this thesis.

It is also important to remind that, in a monochromatic case δp_i suffers a λ ambiguity as a difference between pure piston, That mean that for an OPD of λ, the final intensity is the same. It is then not possible to differentiate any phase map with an integer number of λ petal mode.

2.2.2 Petal mode phase definition

The basis of piston modes presented in Figure 2.3 can be seen as a complement to the IF matrix of a DM (especially in the case of the ELT where the M4 is segmented). For a phase aberration basis, we would prefer that the mode basis be orthogonal using the scalar product defined previously. From the eigenmodes showed by Schwartz et al. (2017) we fixed some of the modes which would appear in this basis and used a Gram-Schmidt algorithm to complete it. The resulting mode basis is shown in Figure 2.4a. The same reasoning was followed using the GMT pupil and gave the petal mode basis in Figure 2.4b. this mode basis is the petal mode basis considered in the rest of this thesis when it comes to the ELT and GMT.

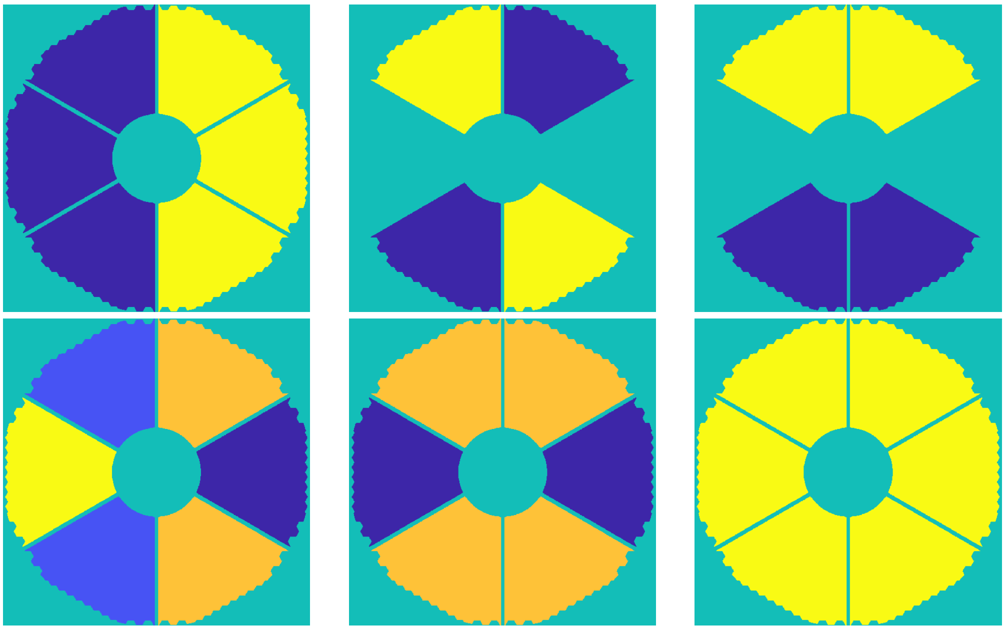

(a) ELT Petal mode basis

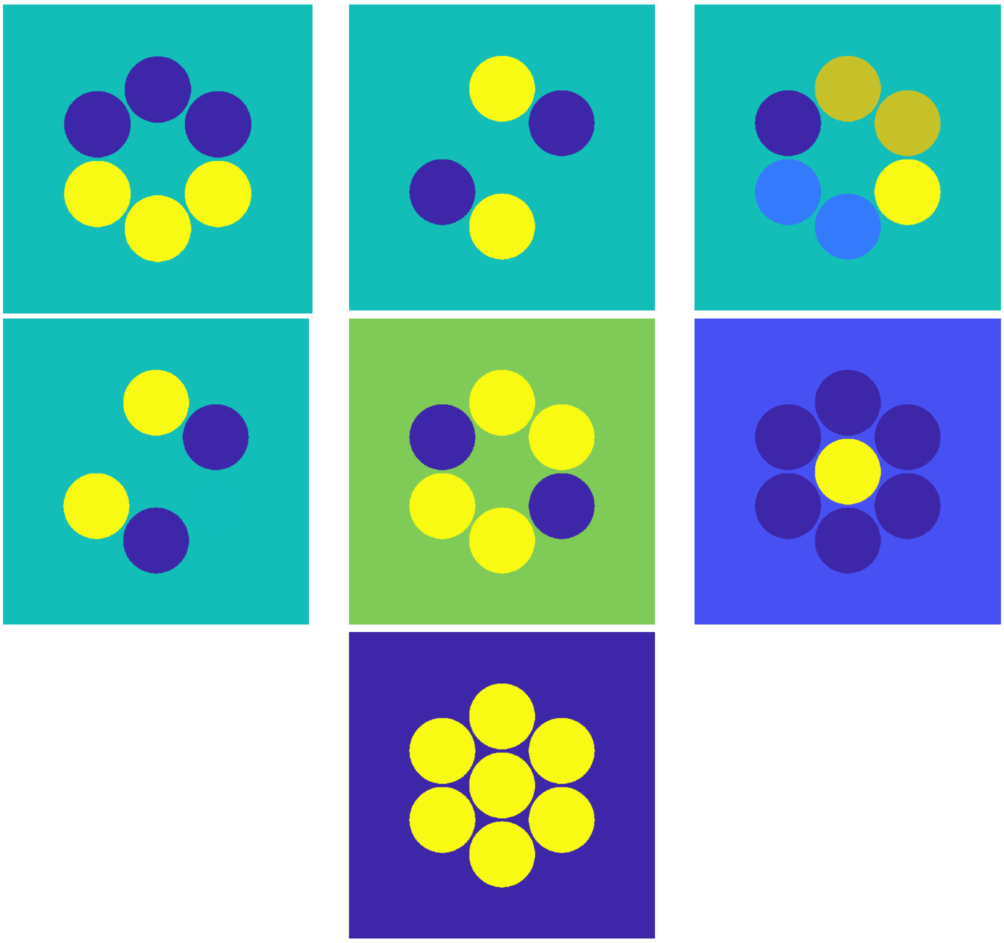

(b) GMT Petal mode basis

FIGURE 2.4 – Petal mode basis for GMT and ELT

This basis contains the global piston mode but is not orthogonal to classical basis like Zernike of KL. The petal modes can be projected sometimes for a very large amplitude on classical modes. For the ELT for instance 80% of the first petal mode is projectable on tip-tilt. This can lead to confusion when analyzing the petal mode. For instance, a lot of the atmospheric petal comes from a global tip-tilt. We talk about this problem in more detail later in this chapter, in section 2.4.

It has to be noted that in this thesis we only consider the piston of each fragment as the origin of the mode basis. For each fragment, tip-tilt can be defined (as well as higher frequency modes like focus or astigmatism ...). As these modes are measured by the WFS and corrected by the AO, we don't consider them. For instance GMT defines the mode basis on each fragment separately so these differential tilt or focus appear explicitly in the control matrices and they don't appear as an issue in the residuals.

2.2.3 Atmospheric turbulence contribution to petal mode

The atmospheric turbulence, projected on the piston or petal modes, not surprisingly shows a non-zero value and even micrometer-values of wave-front. The differential piston can be treated as a dephasing problem between two separated telescopes. When viewed as petal mode it is equivalent to petal mode between 2 fragments. This problem has already been treated for stellar interferometry. (from Conan et al. (2000)), the value of the atmospheric petal has 2 important parameters : the size of each fragment D_f, and the distance between the center of each fragment B (baseline in interferometry). The variance of δp_i can be computed from equation 1.21. This equation is adapted to a circular pupil and is much more adapted to the GMT pupil than the ELT. But as shown by Bertrou-Cantou (2021) it is still a good approximation for ELT. Between two adjacent ELT fragments, we get for a median seeing of 15cm (@550nm) and at 30° azimuth $\sigma p_n = 3.0\mu m$ (@850nm) This is comparable to first simulations for the HARMONI instrument which reported (see Schwartz et al. (2017)) $\delta p_i = 5.5\mu m@750nm$ piston RMS error for the 6 petals combined. Corrected for the correct wavelength and divided by $sqrt(3)$ to account for the 3 pairs of opposite petals, that would give for HARMONI 3.8μm

This first type of petal mode appears due to the atmospheric turbulence only. This term of error was totally unacceptable for the ELT and was reduced by a technique called minioning detailled in section 2.5, later in this chapter.

2.2.4 Low Wind Effect (LWE)

Due to their width, there is a large surface of contact between the spiders and the air around them. During the testing of SPHERE on the VLT it appeared that the spiders are at a colder temperature than the surrounding air. They therefore cool down the air during its passage around it (see Sauvage et al. (2015)). This change of temperature creates a change of refractive index and consequently an optical path difference (OPD) between upstream and downstream volume of air. The LWE degrades performances. It creates local variation of the OPD difficult to measure and correct with AO (even a very efficient one like SPHERE) as was shown by Pourré et al. (2022). The LWE evolution follows the change in wind speed and direction and is expected to change over the course of a few seconds. When it was visible on SPHERE it was shown to be static for integration time under 0.1s and variable for integration times of 10s according to Sauvage et al. (2015). One particularity of the LWE is that the slower the wind is the longer the air stays at the contact of the spider, the larger temperature changes this create between upstream and downstream air and consequently the larger OPD changes this create. This goes against the general tendency of AO performances to improve at lower wind speeds. On the VLT, LWE was reduced by coating the spiders to reduce the temperature difference between the air and the spiders. With the larger spiders of the 30m class telescopes this effect is amplified and first modelling was presented by Martins et al. (2022).The simulation results suggest m range OPD change ; an example of the result of such a simulation is shown in Figure 2.5.

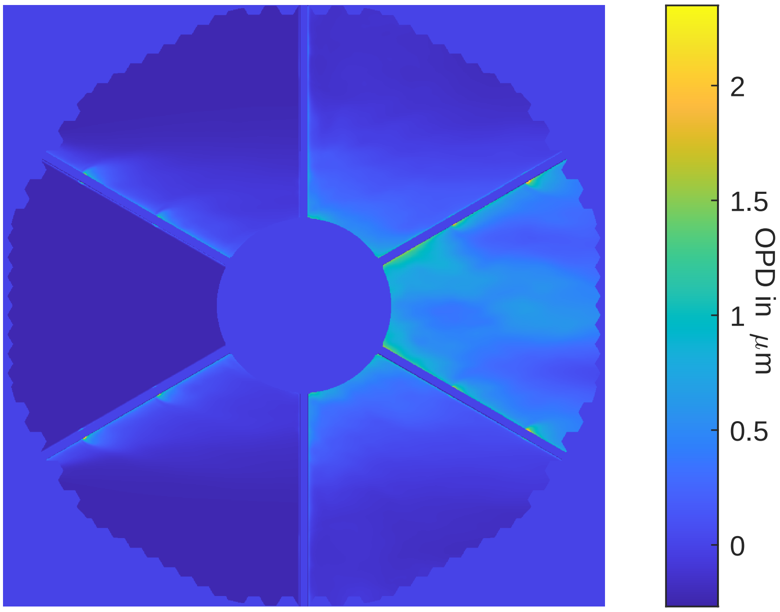

FIGURE 2.5 – Instantaneous OPD maps for the1 m/s, simulations computed for the ELT M2 structure and support . Crédit : Martins et al. (2022)

This LWE adds a very slow varying phase screen on top of the atmospheric turbulence which contains large phase discontinuities around the spider.

2.2.5 Deformable mirror phasing - contribution to petal

The ELT and GMT deformable mirrors geometry follows the primary mirror geometry. This means that the surface of the DM itself is fragmented and could add differential piston if not controlled properly. This behaviour has been seen in the GMT AO simulation where the segmented DM looses phasing and move by λ, as appears in Quirós-Pacheco et al. (2022). In order to avoid this phase wrapping ambiguity, the

GMT telescope has implemented a specific sensor able to sense large differential piston values between each monolithic fragment. For the ELT the minioning described in Section 2.5 should guarantee this effect doesn't appear. As the mirror is segmented, the metrology of each segment is used for minioning and to ensure that no differential piston appears between segments.

2.3 Effect of petal mode on PSF

2.3.1 Effect of petal modes on PSF of GSTs

With the segmentation of the pupil, the PSF of GSTs can be compared to Young interference. The petal modes blur these interference fringes. If the petal modes are left totally uncontrolled, and evolves randomly between all fragments, the resolution is not limited by the diameter of the whole pupil but by the diameter of 1 fragment.

For GMT the diameter of 1 fragment is obvious as they are circular fragments. For ELT and TMT where the fragment are not circular but have a pie chart shape, the loss of resolution can be approximated by $\sqrt(S)$ with S the surface of each fragment. If the pupil has a surface very close to the equivalent monolithic pupil (eg if the gaps are of a negligible surface, like for the ELT), this can be related to the number of fragments as follows :

$$D_{\text{petal}} = \sqrt{(N_{\text{fragment}})} \tag{2.2}$$

With D the equivalent diameter of the telescope composed of 1 fragment.

This formula is true for the ELT and the TMT, but as the GMT doesn't cover the whole surface of the equivalent 24m telescope this formula is not relevant. For GMT as each fragment is already a circular pupil the resolution is the resolution of this circular pupil. That formula works for a long exposure with uncontrolled random petal mode. The Strehl ratio loss in a long exposure image follows the same formula $\sqrt{(N_{\text{fragment}})}$. For short exposure the SR is minimum when each lobe corresponding to each fragment is separated. The formula then becomes :

$$SR_{\text{min petal short}} = \frac{1}{(N_{\text{fragment}})} \tag{2.3}$$

With SR the Strehl Ratio limited by petalling in short exposure imaging. With uncontrolled petal mode, the ELT long exposure resolution is limited to a 15m telescope, and the GMT long exposure resolution is limited to a 8.4m telescope. This makes this mode crucial to control to allow high angular resolution applications like exoplanet imaging. We show here the ELT and GMT pupils and example of the PSF with and without petal phasing.(see Figure 2.6 and Figure 2.7). The long exposure PSF is the exact same as the average of each fragment's PSF. The PSF are shown with a Field of View (FOV) of 200 milliarcseconds @850nm to be comparable.

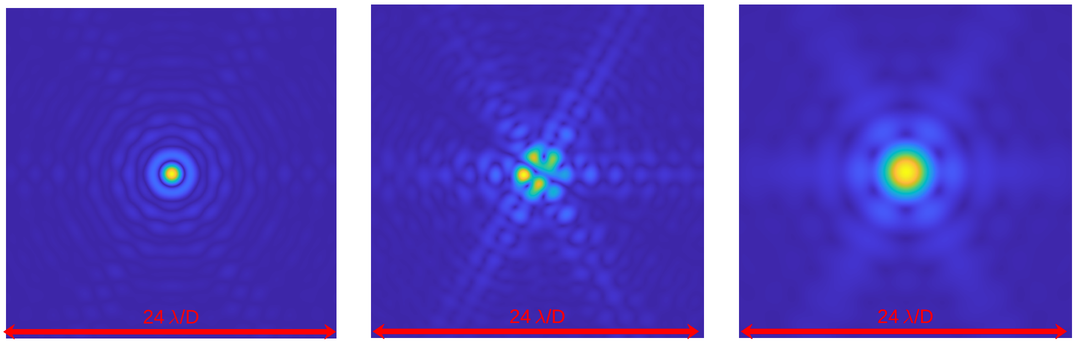

(a) ELT PSF in absence of any aberration

(b) ELT short exposure PSF for a random petal p_n = [153, 300, 526, -530, 86, 533] nm RMS on each fragment

(c) ELT long exposure PSF for a random petal p_n on each fragment

FIGURE 2.6 – ELT PSF comparison using square root scale

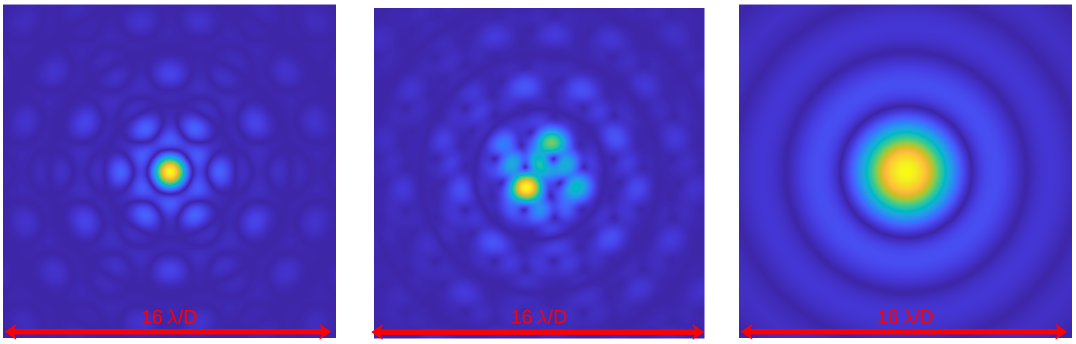

(a) GMT PSF in absence of any aberration

(b) GMT short exposure PSF for a random petal p_n = $[36, 181, -84, 209, -161, -26, -153]$ nm on each fragment

(c) GMT long exposure PSF for a random petal p_n on each fragment independant between all N exposures

FIGURE 2.7 – GMT PSF comparison using square root scale

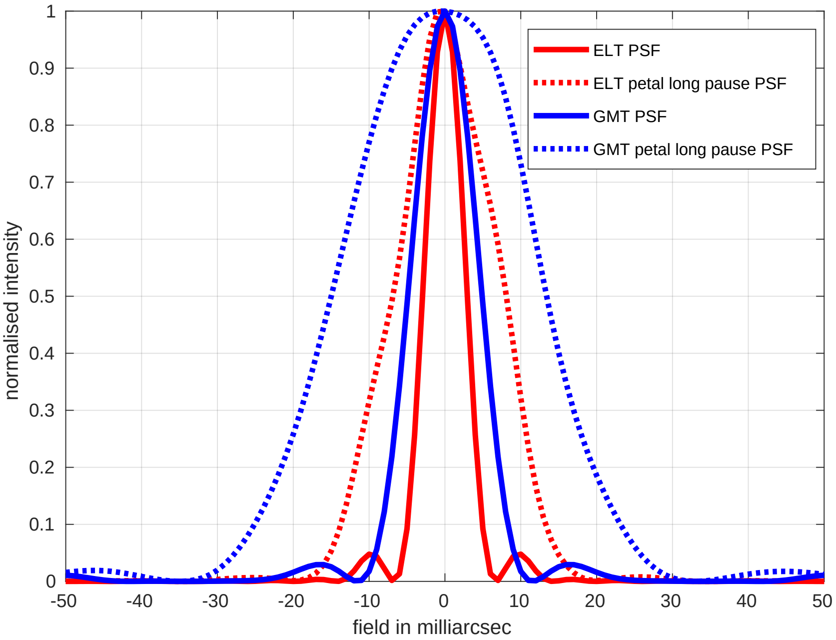

FIGURE 2.8 – Cut of ELT and GMT PSF with and without petal mode

On Figure 2.8 we measure the loss in resolution by measuring the Full Width Half Max (FWHM) for ELT and GMT, with and without petal mode. The FWHM of the ELT PSF is 7 milliarcsec @850nm. With petal mode varying between -pi rad and pi rad randomly in the phase the long exposure has a FWHM of 17 milliarcsec. For GMT FWHM is 9 milliarcsec and with the same petal mode amplitude it grows to 30 milliarcsec. We see that this follows the formula 2.2 for ELT and just the single fragment 8.4m resolution for GMT.

2.3.2 A GMT simplified case : the LBT

As was said the GMT has 7 orthonormal petal modes. In this thesis we want to simplify the problem in order to simplify the analysis and the simulation without loosing the very essence of the problematic. In addition, LBT is a world class AO assisted telescope in operation and we hope our analysis and our work will be of interest for the future SCAO system on this telescope. As such the LBT could be seen as a model for studying the petal mode with an extremely large spider. Cophasing the LBT using the AOs would show that the petal mode can be controlled with much larger spiders than on the current GSTs. It is also considered a pathfinder for the GMT AO systems and as such allows us to study a simplified GMT petal case. The LBT is comprised of two 8-meter telescope separated by a 6 meter gap. In such a configuration, it is ambiguous to define a diameter. We use D the diameter of 1 monolithic telescope and B the baseline (from the center of a telescope to the center of the next). This reduces the number of petal modes to be considered (to one instead of 7 for GMT). The gap can be considered as the 6m spider of a 22m telescopes. On Figure 2.9 we show the pupil and the corresponding perfect LBT PSF.

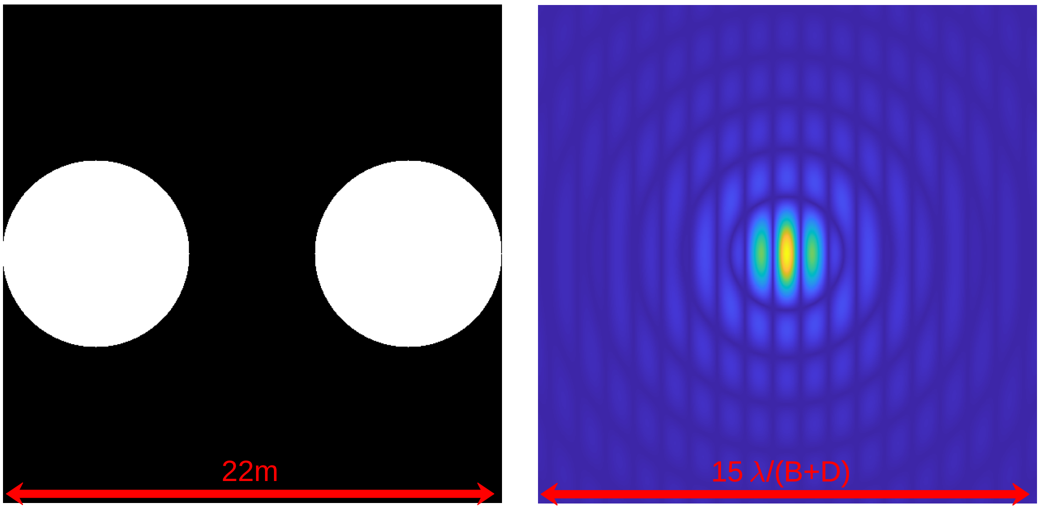

(a) ELT PSF in absence of any aberration (b) ELT short exposure PSF for a random petal p_n on each fragment

FIGURE 2.9 – LBT pupil and PSF

As it uses the same base fragment of a 8m circular telescope as the GMT, the PSF of LBT and GMT have the same long exposure PSF in the case of uncontrolled petal mode. In practice the LBT uses 2 independents AO systems (one for each mirror) and a separate fringe tracker when the light of both mirror is combined in interferometric mode to ensure the cophasing. An approach tested was to regroup the 3 functions (fringe tracker and 2 AO systems in only one AO system. This created the innovative concept of the asymetric PyWFS proposed in chapter 3.

2.3.3 A ELT simplified case : our Toymodel

Following the same scheme as GMT vs LBT our objective here was to defined a simple pupil that will allow to mimic the petal modes effects of the ELT keeping only one mode. In addition in order to speed up the simulation we have reduced the pupil diameter by a factor 4 and consider a 10m pupil for or so-called "Toymodel". For that we use a single mirror with a large vertical spider as showed in the Figure 2.10a. The corresponding petal mode is represented in Figure 2.10b. The PSF of the Toymodel with 0 phase amplitude and with a 150nm RMS petal mode amplitude are on Figure 2.11 It is to be noted that there is a factor 2 between the PTV and the RMS amplitude of the petal mode with this pupil. The Toymodel petal mode is very close to the first petal mode of the ELT showed on Figure 2.4a.

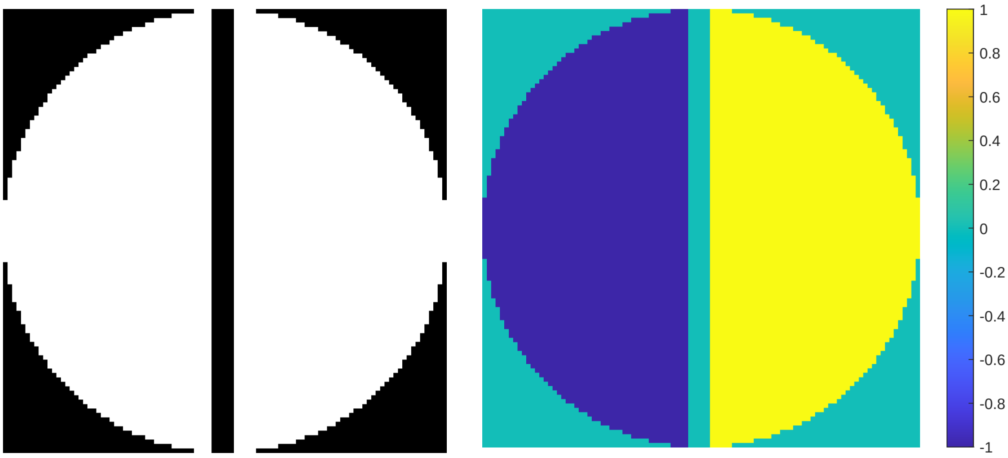

(a) Toymodel pupil

(b) Toymodel petal mode

FIGURE 2.10 – Toymodel pupil and its associated petal mode. The size of the spider is variable but the 50cm spider is the default size unless specified

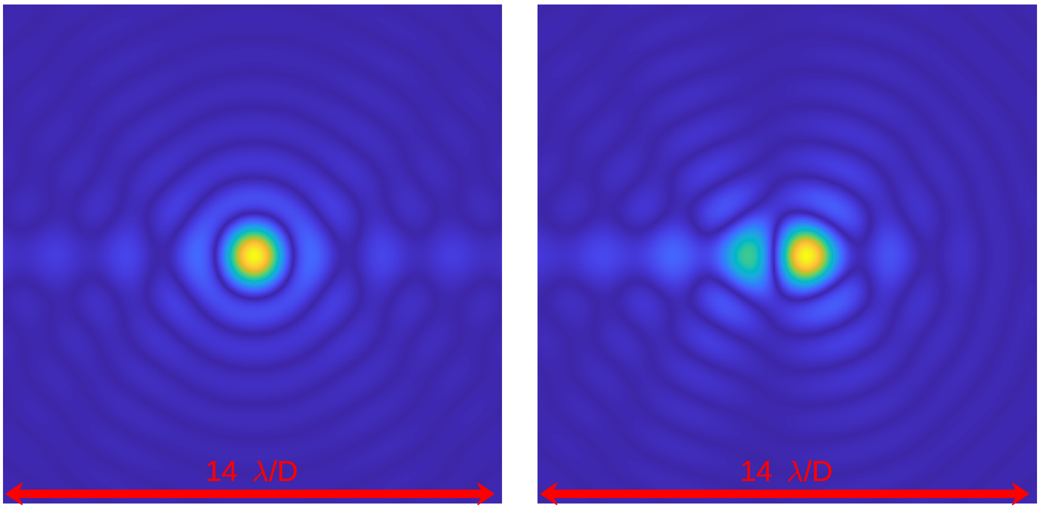

(a) Toymodel ideal PSF

(b) Toymodel short exposure PSF with 150nm of petal mode

FIGURE 2.11 – Toymodel PSF comparison

The simulations have been done using this pupil follow the parameters summed up in table 2.1 :

To confirm the interest in term of computation here are the comparison of time in OOMAO to compute the intensity pattern of a 4-sided PyWFS with a $3L/D$ modulation radius. The critical factor is the number of pixels required to accurately reproduce the pupil shadowing induced by the spider arrays size varies from more than 600 pixels for an ELT case down to 100 pixels for our Toymodel, hence a gain of 36! This gain in pixel number is roughly equivalent to the gain in simulation time as shown in Table

Pupil	Diameter = 10m Monolithic primary mirror Spiders width 50cm)
Turbulence	3 Layers r_0=15cm@550nm wind speed=5m/s Outer scale L_0=30m
DM	50cm pitch (20x20), square pattern, gaussian influence functions, 0.3coupling
PyWFS	100x100 subapertures no noise (neither photon nor readout) modulation radius = $3\lambda/D$
Target	$\lambda = 850nm$ on-axis star
Controller	Loop Rate 1000Hz 1 Frame delay (+integration) Linear matrix integrator

TABLEAU 2.1 – Toymodel simulation parameters

ELT	$N_{pixels} = 600$	computation = 5.0s
GMT	$N_{pixels} = 500$	computation = 3.4s
LBT	$N_{pixels} = 400$	computation = 2.4s
Toymodel	$N_{pixels} = 100$	computation = 0.19s

TABLEAU 2.2 – time of computation of a pyramid frame with various pupil

2.2. The main other element which changes the computational time is the modulation radius of the pyramid as a larger modulation radius means more images with various tip tilt need to be averaged. All these times of computation would get significantly longer with larger modulation radius. We stop at 100pixels for the Toymodel so that 1 pixel represents 10cm @550nm on the pupil. We define the r_0 at 550nm but our WFS makes the sensing at $850nm$. At this wavelength the r_0 is multiplied by 2.3 (see 1.15) so we have 2 pixels per r_0 at our sensing wavelength.

2.3.4 phase wrapping ambiguity and overall error

There is a modulo phase wrapping ambiguity in the petal mode. For any monochromatic system the difference between 0 and 1λ petal cannot be seen. The effect on the PSF of a 0.5λ and a 1.5λ will be the same and will be the worst PSF as the petal mode causes a periodic (sinusoidal) degradation of the PSF. This creates a problem when comparing petal residuals with other types of residuals, as while 0.5λ RMS error of astigmatism creates an large PSF, with a Strehl of 0.03, a 1.5λ petal error does not degrade as much the PSF with a Strehl of 0.50 as shown on Figure 2.12b using the

Toymodel pupil.

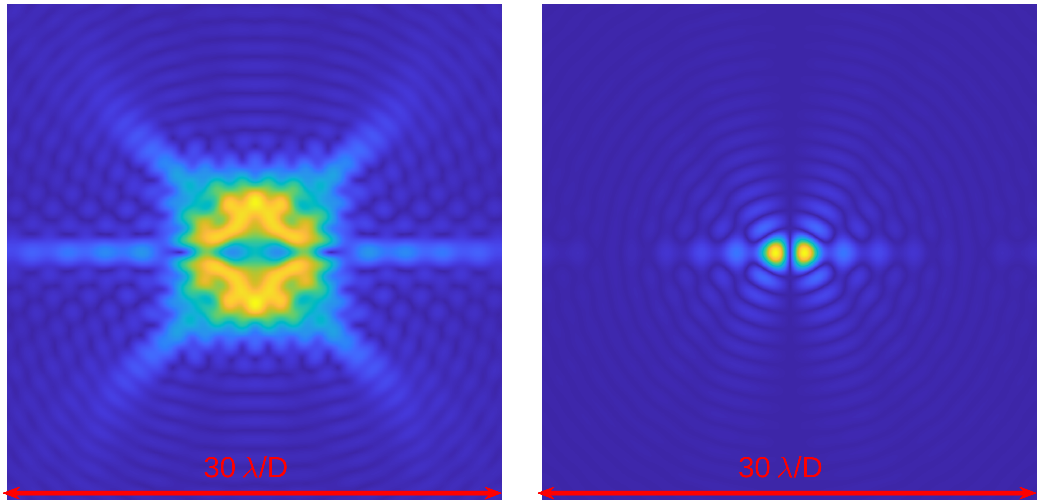

(a) PSF of 0.5λ RMS of astigmatism (square root plot), SR=0.03

(b) PSF of 1.5λ RMS of petal mode (square root plot), SR=0.5

FIGURE 2.12 – Comparison between astigmatism and petal mode effect on PSF

We see here an illustration of the short exposure degradation of the PSF quality, with the PSF separated in 2 even lobes leading to a loss of SR of $1/N_{\text{fragment}}$ so $1/2$ here. Meanwhile the Strehl ratio on the astigmatism PSF as already fallen very low (SR=0.03).

2.4 Spatial structure of petal mode

2.4.1 Orthogonalising the petal mode to Zernike phase basis

As previously said the petal mode can be projected on classical phase modes like Zernike or sinusoidal basis. Including the petal mode explicitly to one of these basis raises an orthogonality issue. The petal mode identified as the heart of our problem in AO, is not orthogonal to any of these basis. We would like to produce an orthogonal basis including the petal mode. To that end we project the petal mode to the Zernike Basis. It can be noted that other authors used the inverse approach and orthogonalise the reference basis (Karhunen–Loève basis for Engler et al. (2019)) to the petal mode. On Figure 2.13 we show the result of the projection of the Toymodel petal mode on the Zernike. The most striking feature is the tip tilt which represents 90% of the Toymodel petal mode.

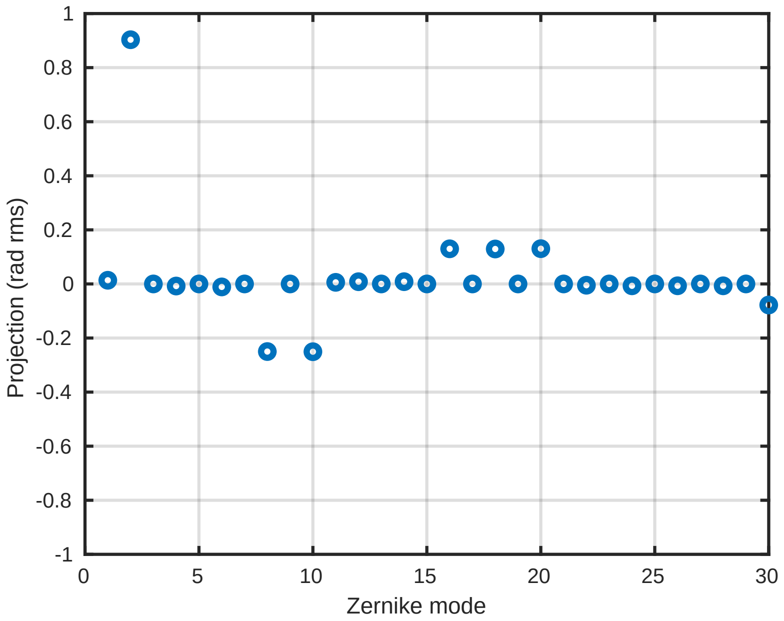

FIGURE 2.13 – Toymodel petal projected on the 30 first Zernike modes

Here we can see one of the problems to understand the petal mode. It contains a significant amount of Tip-Tilt. It can be projected on other classical AO modes. Despite these classical AO modes being easily measured and compensated by the AO system the petal mode appears in the residual.

On Figure 2.14 we show the result of the orthogonalisation of petal mode with a Zernike basis containing more and more modes following the method :

$$\perp pet_n = pet - \sum_0^n < Z_n, pet > \tag{2.4}$$

With n the last Zernike mode to which the petal is orthogonalised. It is the fitting error of the petal mode compensated by the Zernike basis. The orthogonalised petal can become quite exotic. For instance the petal mode with tip & tilt subtracted is represented in Figure 2.14a and is akin to a diffraction grating phase. The version with 30 Zernike subtracted looks like a low frequency sinusoidal and a discontinuity around the spider. As we see with the 100 Zernike orthogonalised petal, the more we push this orthogonalisation, the more this discontinuity gets exacerbated as illustrated by the case with up to 1000 Zernike mode. **The discontinuity present at the spider edge is the heart of the petal mode, it is the part of the petal mode that is orthogonal to the rest of the basis.**

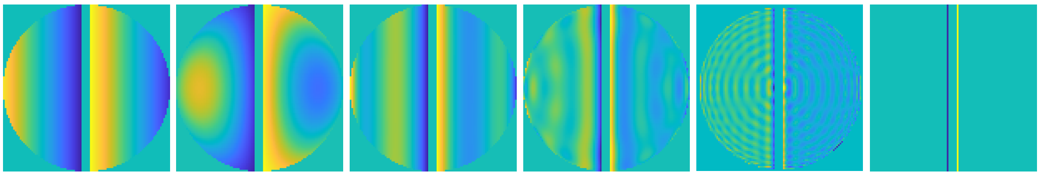

(a) Petal mode orthogonal to the first 3 Zernike modes (piston tip tilt)

(b) Petal mode orthogonal to the first 10 Zernike modes (up to trefoil)

(c) Petal mode orthogonal to the first 30 Zernike modes (up to 3rd order coma)

(d) Petal mode orthogonal to the first 100 Zernike modes

(e) Petal mode orthogonal to the first 1000 Zernike modes

(f) discontinuity mode

FIGURE 2.14 – Toymodel petal mode orhogonalised to variable number of Zernike modes. The further in term of Zernike the more it tends toward the discontinuity mode around the spider showed in the last plot

This discontinuity means that if we want to measure the petal mode while avoiding confusion with other mode of the Zernike basis, we need to measure this discontinuity mode. This discontinuity mode was tested on the toymodel which represents well the first petal mode of the ELT. An analogous mode will appear where there are differential piston jump for the other petal modes. This effect is relevant in section 2.6 and in Chapter 4.

2.4.2 Spatial PSD of petal compared to the atmospheric turbulence

The petal mode is mostly projected on the low spatial frequency modes like tip-tilt. As such we can expect that the petal mode itself is mostly a low frequency mode. On Figure 2.15a we plotted a comparison of the PSD of the petal mode, the PSD of a typical AO residual for the Toymodel and the PSD of an uncorrected atmospheric turbulence. In subfigure a), the comparison is made using a radial average of the PSD over the whole spatial frequency plane. As the petal mode is very dependant on the direction considered in the pupil, we also make a cut in the horizontal direction (where the PSD of the petal is the higher) in subfigure b) This cut of the PSD highlights in particular the high spatial frequency harmonics of the petal mode. The AO residual PSD was made using an AO following the parameters in table 2.1 but with no spider (so no petal mode in the residuals). The residual have a mean amplitude of 120nm RMS of error. The petal mode has been put to the same RMS amplitude before computing the PSD.

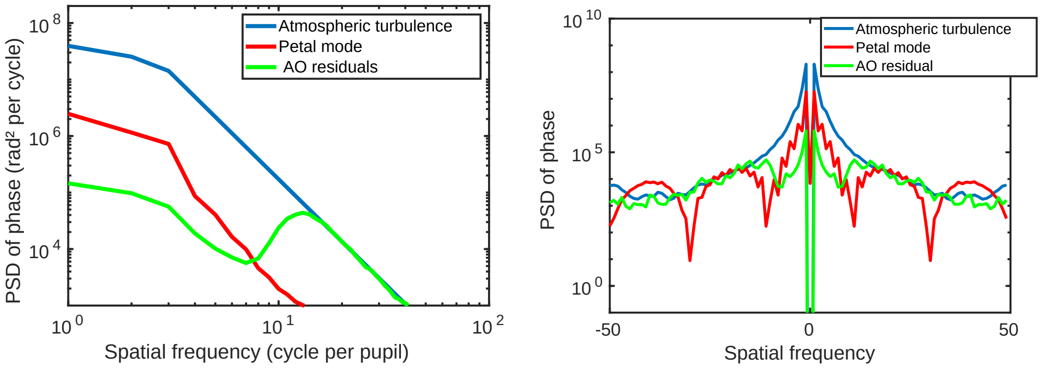

(a) PSD of petal mode, atmospheric turbulence and AO residuals

(b) horizontal cut of PSD of petal mode, atmospheric turbulence and AO residuals

FIGURE 2.15 – Comparison of PSD for petal mode, turbulence and AO residual

The petal mode has more of its energy in the low frequencies, in particular in the first 5 cycle per pupils, below the AO cutoff frequency. In comparison, the residual has more energy after the cut-off frequency of the DM as the rest is uncontrolled atmospheric phase. Due to the spider and the discontinuities around the spider, at high spatial frequency the petal has a higher energy than the atmosphere or the residual for some specific frequencies as is visible in Figure 2.15b.

This can lead us to paths to measure the petal signal in particular to separate it from the residuals. First, the signal of the petal can be searched at low order spatial frequencies where most of the energy is or look for the high frequencies where petal has more energy remaining than atmospheric phase due to the discontinuity close to the spider Filtering the low frequency would do the same as the Zernike orthogonalisation : the discontinuity would be the mode remaining after filtering the low spatial frequencies. The low frequency method seems very difficult with a full atmosphere, but would be very interesting for atmospheric residuals when keeping only phase under the cutoff frequency. This will be studied in chapter 4. Second the petal signal can be searched at the higher frequencies where it is even higher than the atmospheric residuals. The high frequency method has been studied by Usuda et al. (2014).

2.5 Treatment of petal by the AO loop

In this section we study how an AO loop behave with petal mode in absence of other residuals.

2.5.1 Petal mode in entrance phase

If there is petal mode in the entrance phase, to correct this petal mode perfectly, we need a sensor capable to measure it and a DM capable to correct it. That means a WFS able to measure the petal mode (a petallometer) and a DM capable to create a pure petal mode (a segmented DM). In the case where we use the entrance phase as the phase measured by the WFS (=we assume a perfect phase sensor), and use a segmented DM to compensate the petal mode, when we close an AO loop on a pure entrance petal mode, it is almost perfectly compensated as seen on Figure 2.17. The petal is reduced from 100nm RMS to 0.5nm RMS of petal mode in 10 iteration.

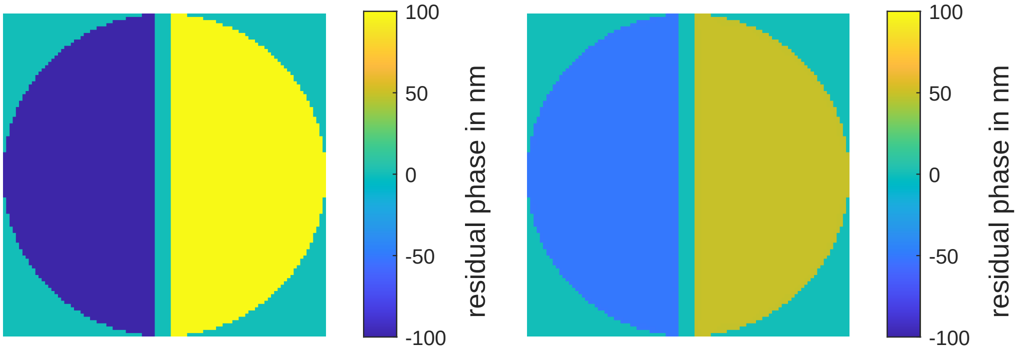

(a) Static petal phase

(b) Petal phase after first iteration of closed loop with perfect phase sensor and segmented DM

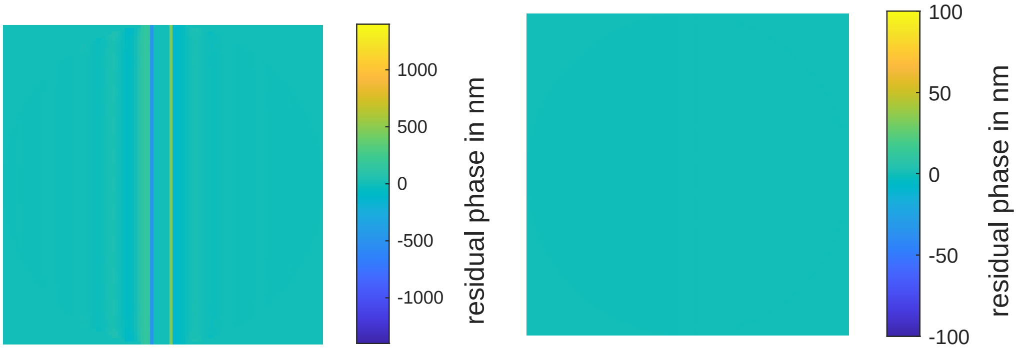

(c) Petal phase after 5 iterations of closed loop with perfect phase sensor and segmented DM

(d) Petal phase after 10 iterations of closed loop with perfect phase sensor and segmented DM

FIGURE 2.16 – closed Loop compensation of pure petal mode with a perfect phase sensor and segmented DM

If we use instead a perfect sensor but a continuous DM, we correct well the petal mode except for the discontinuity close to the spider as shown in Figure 2.17. The corrected phase will go from 100 to 9 nm RMS of petal mode. This discontinuity is the residual of the compensation of the petal mode with a continuous phase basis. As such the discontinuity effect on the PSF is essentially the effect of petal mode outside of the DM correction radius as showed on figure 2.18

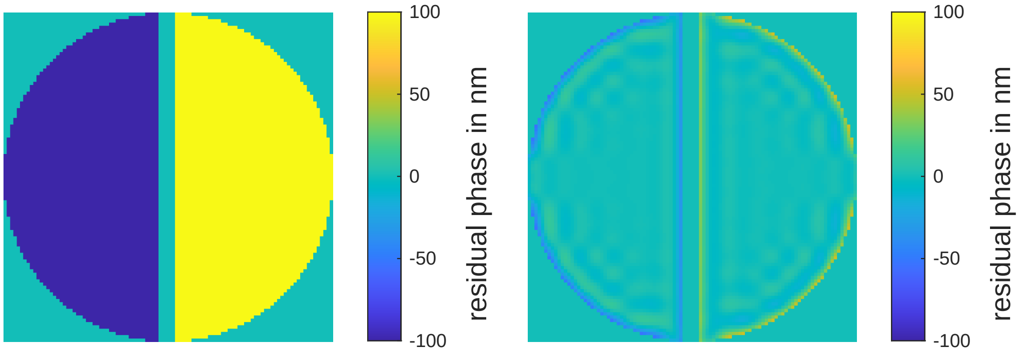

(a) Static petal phase

(b) Petal phase after first iteration of closed loop with perfect phase sensor and continuous DM

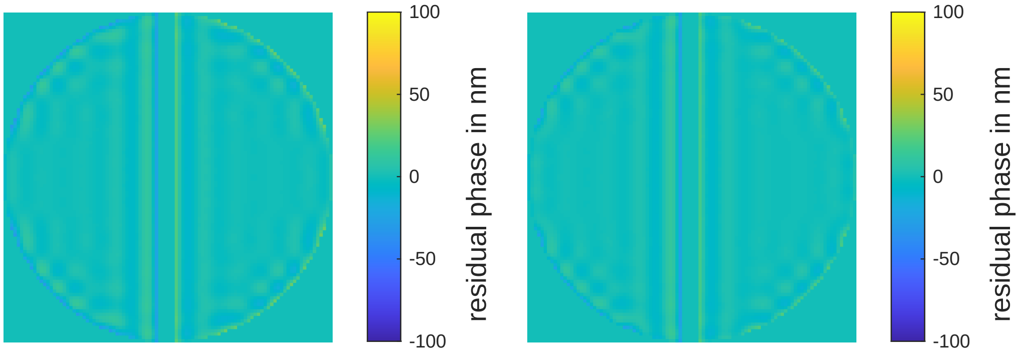

(c) Petal phase after 5 iterations of closed loop with perfect phase sensor and continuous DM

(d) Petal phase after 10 iterations of closed loop with perfect phase sensor and continuous DM

FIGURE 2.17 – closed Loop compensation of pure petal mode with a perfect phase sensor and continuous DM

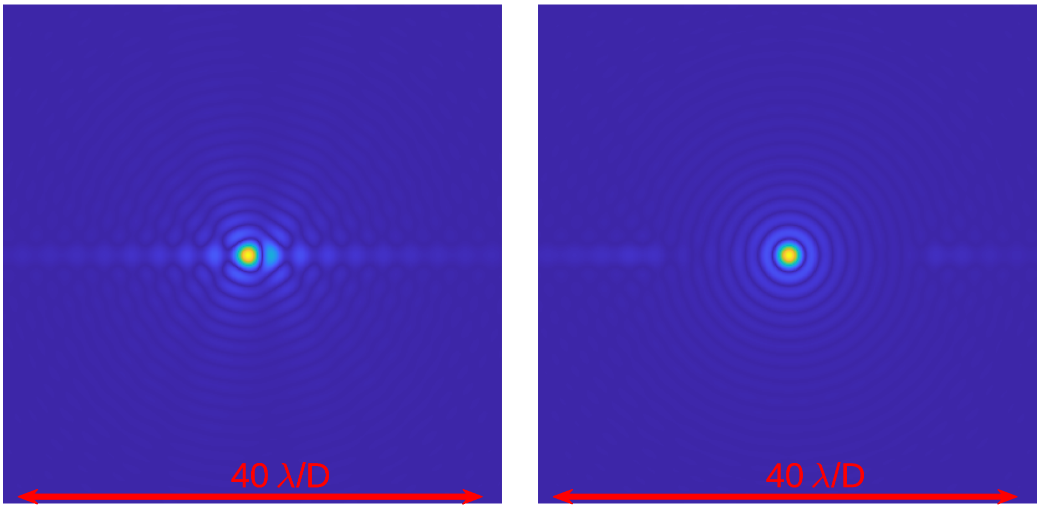

(a) PSF of petal mode (b) PSF of discontinuity mode

FIGURE 2.18 – Effect of a continuous DM on the petal mode PSF. A continuous DM will compensate the petal mode up to the discontinuity mode

But if the WFS does not measure petal mode, a pure petal mode in the phase will be untouched as shown on figure 2.19 where petal mode goes from 100 nm to ... 100nm RMS. This is true for both the segmented an continuous DM.

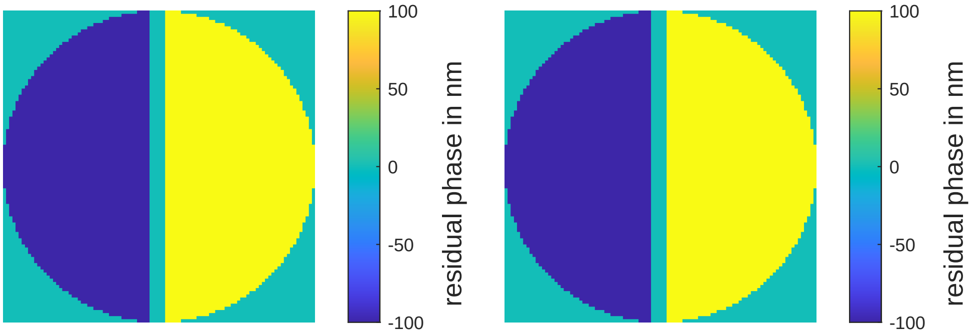

(a) Static petal phase

(b) Petal phase after first iteration of closed loop with modulated PyWFS and segmented DM

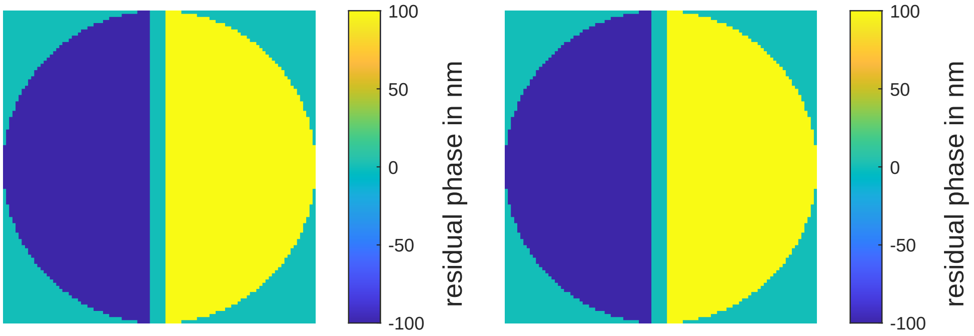

(c) Petal phase after 5 iterations of closed loop with modulated PyWFS and segmented DM

(d) Petal phase after 10 iterations of closed loop with modulated PyWFS and segmented DM

FIGURE 2.19 – closed Loop compensation of pure petal mode with a modulated PyWFS and segmented DM

In the presence of a pure petal mode, a segmented DM with perfect measurement gives the best result. A continuous DM can be used with a slight discontinuity mode appearing in the residuals. But when a slope sensor(unable to measure the petal mode) is used, the system doesn't react to the pure petal mode.

2.5.2 Discontinuous mode in entrance phase

A phase discontinuity is not naturally present in the atmospheric turbulence. But with a spider a large discontinuity appears in the turbulence. The amplitude is zero at the location of the spider, such that the phase is undefined and is not continuous anymore. And the larger the spider, the larger the discontinuity. It is essentially a result of the local tip tilt under the spider. As the discontinuity mode and petal mode are linked as shown in figure 2.14e we study the effect of this spider induced discontinuity mode on the loop.

When using a perfect sensor and a continuous DM, the discontinuity will be flattened but is part of the fitting error of the DM due to its small size in one direction as shown on Figure 2.20 We start with 100nm RMS (1200 nm PV) of discontinuity mode and the errors can only be reduced to 93nm by the DM (the result are very similar whether a segmented or continuous DM is tested).

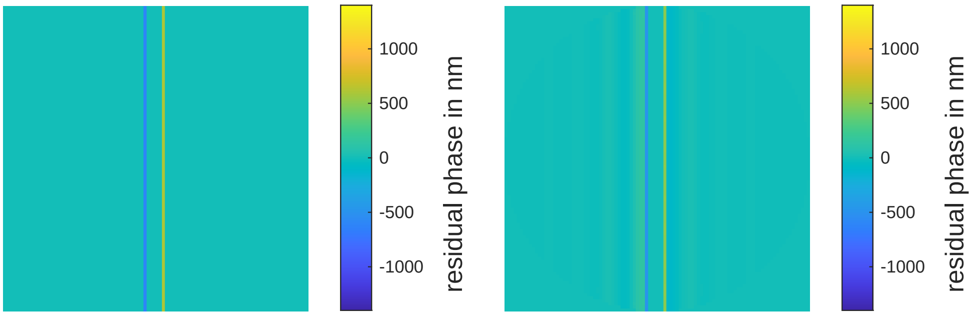

(a) Static discontinuity phase mode

(b) phase residual after 1 iteration of closed loop on discontinuity mode with perfect phase sensor

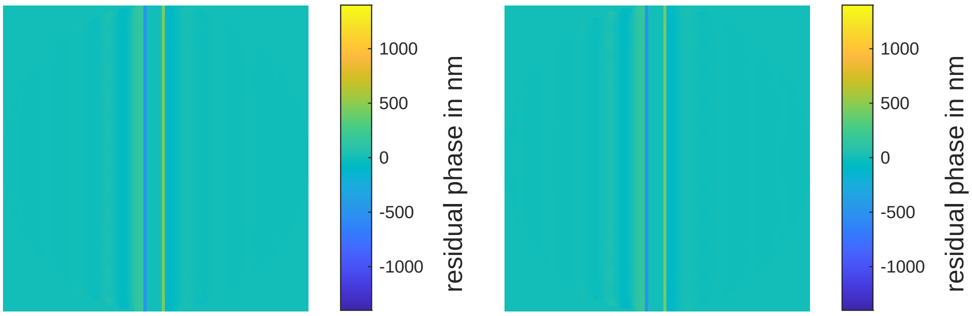

(c) phase residual after 5 iteration of closed loop on discontinuity mode with perfect phase sensor

(d) phase residual after 10 iteration of closed loop on discontinuity mode with perfect phase sensor

FIGURE 2.20 – closed Loop compensation of discontinuity mode with a perfect phase sensor

But in Figure 2.21 we show how a slope sensor measures the discontinuity mode and on Figure 2.22. the corresponding residuals. We see that the discontinuity is confused with petal mode and consequently the AO loop will add petal mode in the residual, ending at 1400nm RMS (=2800nm PV) of petal mode while it started with 100nm RMS (120nm PV) of discontinuity. This might be the source of the atmospheric petal in the case of continuous DM. Furthermore this petal mode is proportional to the entrance discontinuity mode, ie r_0 and spider size.

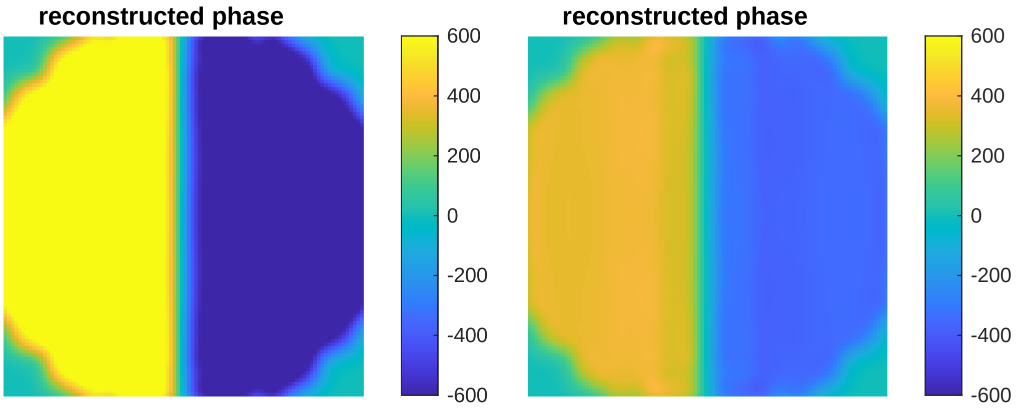

(a) Measured phase by modulated PyWFS in presence of pure discontinuity mode

(b) Measured phase by modulated PyWFS after the 1st closed loop iteration

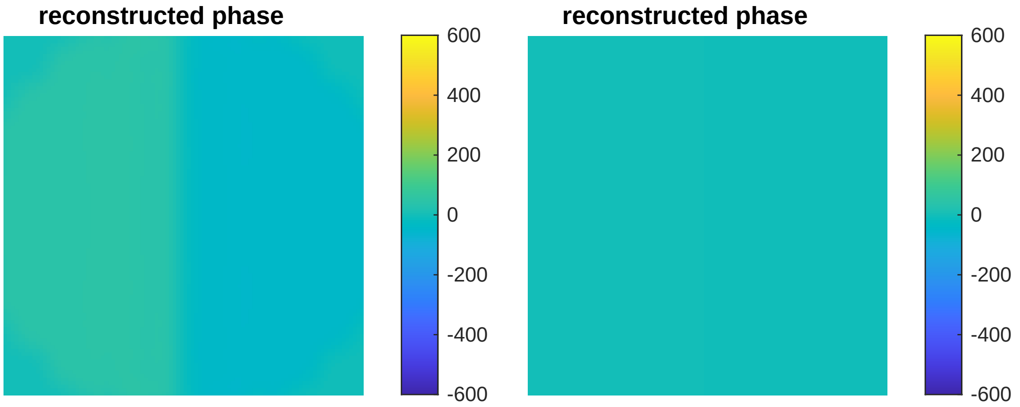

(c) Measured phase by modulated PyWFS after the 5th closed loop iteration

(d) Measured phase by modulated PyWFS after the 10th closed loop iteration

FIGURE 2.21 – Phase measured by the modulated PyWFS at each iteration of the closed loop with static discontinuity mode as entrance.

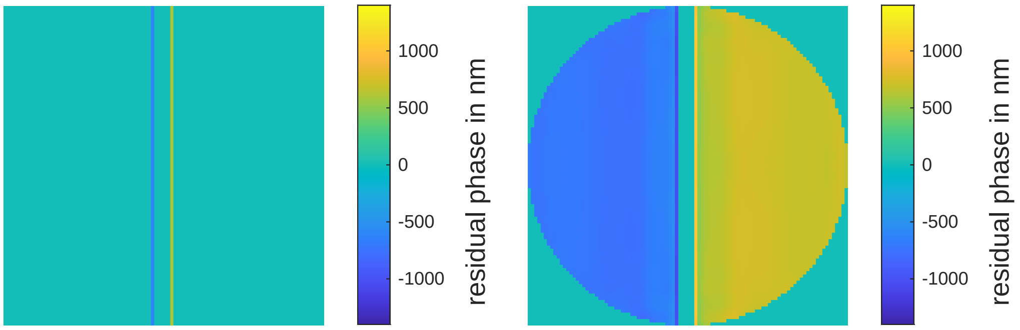

(a) Static discontinuity phase mode

(b) phase residual after 1 iteration of closed loop on discontinuity mode with modulated PyWFS

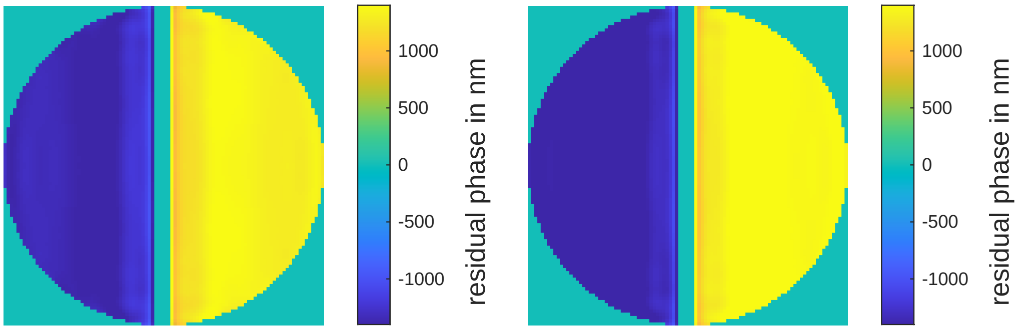

(c) phase residual after 5 iteration of closed loop on discontinuity mode with modulated PyWFS

(d) phase residual after 10 iteration of closed loop on discontinuity mode with modulated PyWFS

FIGURE 2.22 – closed Loop compensation of discontinuity mode with a modulated PyWFS

This effect comes from the confusion between petal mode and discontinuity mode, not the discontinuity mode itself. If the same mode is added in absence of spider as in Figure 2.23 the system reaches a final state very close to the perfect sensor case.

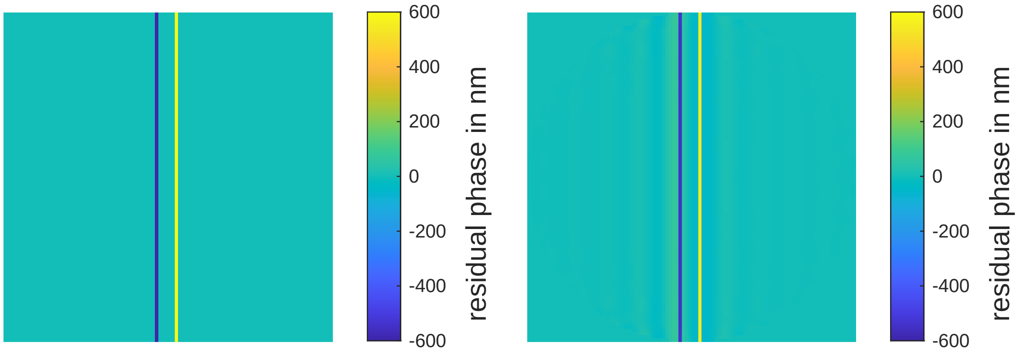

(a) Static discontinuity phase mode. this is the discontinuity around the spider tested with a pupil without spider

(b) phase residual after 1 iteration of closed loop on discontinuity mode (defined as if the 50cm spider was present) with modulated PyWFS and no spider

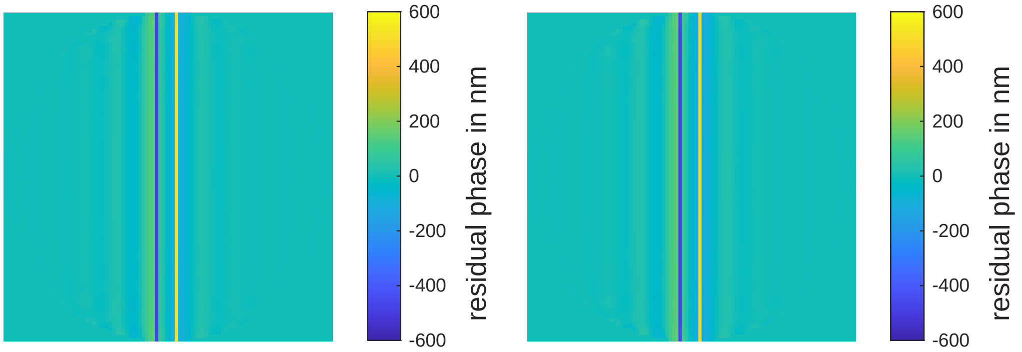

(c) phase residual after 5 iteration of closed loop on discontinuity mode (defined as if the 50cm spider was present) with modulated PyWFS and no spider

(d) phase residual after 10 iteration of closed loop on discontinuity mode (defined as if the 50cm spider was present) with modulated PyWFS and no spider

FIGURE 2.23 – closed Loop compensation of discontinuity (defined as if the 50cm spider was present) mode with a modulated PyWFS in absence of spider

On Figure 2.24 we illustrate how the presence or absence of spider will change how the discontinuity is measured. In the absence of spider, a slopes sensor measures a positive then negative derivative when passing the discontinuity 'spikes' of the discontinuity mode. When this derivative is integrated, the spikes reappears. With the spider, the negative derivative is hidden bi the spider. Only the positive derivatives appear. Integration of the signal reconstructs a Heaviside function.

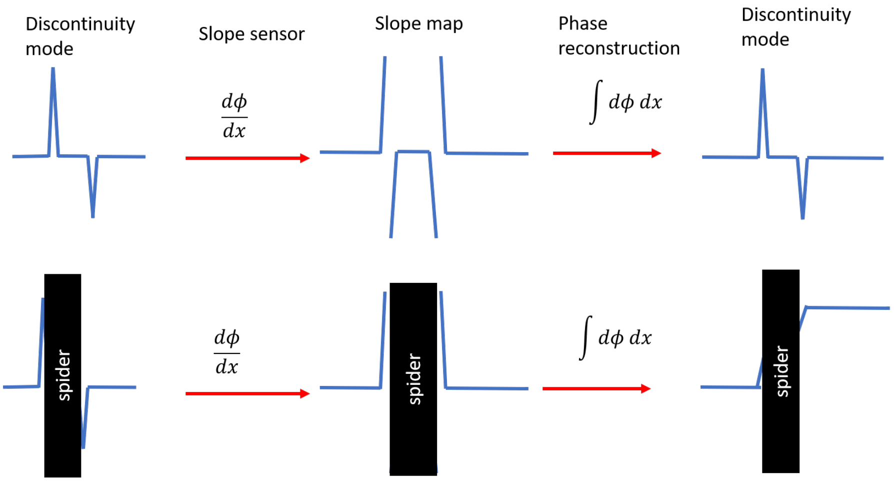

FIGURE 2.24 – Schematic of the principle behind he discontinuity mode beeing measured as petal mode with spiders only

For the discontinuity mode we see that the spider directly changes the mode reconstructed by a slope sensor. The discontinuity mode is an important issue, as it will allow an AO loop to amplify a petal mode if it appears in the phase residual around a spider unless the system is able to measure the petal mode explicitly.

2.6 Dealing with the petal mode in an AO closed loop

In the previous section we focused on the effect of pure petal mode in absence of atmosphere on the AO loop. In this section we study how the petal mode behave in a closed loop and in particular how to reduce atmospheric petal.

2.6.1 petal mode and segmented DM

The advantage of a segmented DM is that it can create a pure petal mode while a continuous DM would always be limited by the rigidity of the membrane around the discontinuity. To test the effect of a segmented DM we made a closed loop using the parameters of table 2.1 except that the DM was segmented along the spider. As seen in Figure 2.25 the AO loop measures and correct every mode except the petal mode, which stays very close to the atmospheric petal.

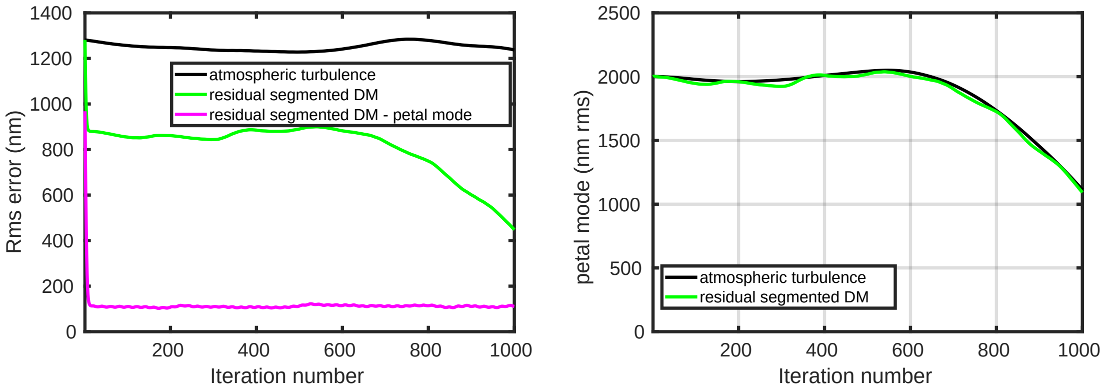

(a) RMS error of a closed loop using a segmented DM. Green curve is the RMS of the phase residual, magenta curves uses same residual with pure petal mode subtracted from the residuals

(b) Residual of a closed loop using a segmented DM projected on petal mode. The petal mode after the DM follows closely the petal in atmospheric turbulence

FIGURE 2.25 – Petal mode in a closed AO loop with segmented DM

In particular we see that with the system parameters the closed loop would be down close to the fitting error (112nm RMS) if it wasn't for the petal mode. Meanwhile the petal mode stays very close to the atmospheric petal mode. Using a segmented DM with a WFS not able to measure the petal mode let the petal mode as it appears in the atmospheric phase and gives very bad results. To reduced the petal mode we see two solutions. First reduce the discontinuity introduced by the DM which will reduce the petal mode in residuals, this method is called slaving and is studied in the following paragraph. Alternatively we can change the WFS to be able to measure the petal mode. This method will be explored in the next chapter 3 and 4.

2.6.2 Residual petal for continuous (or pseudo continuous) DM

2.6.2.1 From a segmented to a continuous DM : the minioning

The problem of correction of the petal mode with a segmented mode appear in the HARMONI simulation by Schwartz et al. (2018). To compensate for the petal mode a different kind of DM control was proposed by Schwartz et al. (2017) : the Minioning (called slaving in the original paper). It consists in a modification of the DM influence function of the actuators close to the spider to force the actuators on each side of the spider to keep the same value on each side of the spider to create a pseudo continuous DM surface. The aim of the slaved DM is to emulate the behavior of a continuous DM to petal mode presented in Figure 2.26.

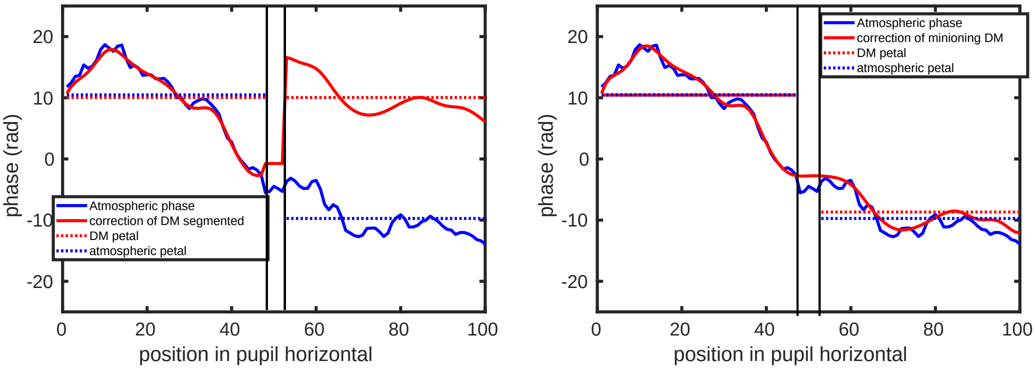

(a) Segmented DM correction and apparition of petal mode, magenta line is the atmospheric petal, green line is DM surface petal

(b) DM correction with minioning DM and reduction of petal mode, magenta line is the atmospheric petal, green line is dm surface petal

FIGURE 2.26 – Comparison of a cut phase with atmospheric phase and the DM surface used for correction a) the DM is segmented b) minioning DM.

On the segmented case on Figure 2.26b both side of the pupil (black lines) have close to the same piston so the change in piston from left to right of the atmosphere (blue line) appears in the residuals. Meanwhile we can see that with a minioning DM, the difference on the right side of the plot is due to the phase changing under the spider. This create a difference between the atmospheric phase and the DM surface which is greatly reduced compared to the segmented DM case.

The error becomes a problem of blind areas of measurement. If the changes of phase under the spiders are not measurable, the differential piston change here is not compensated. It is akin to a fitting error and the amplitude of this change is only the width of the spiders and r_0. This lowers the residual petal down to 34nm RMS of petal mode according to Schwartz et al. (2018) for the ELT case at median seeing (15cm @550nm). In practice the minioning DM solution is enough to reduce the petal to fit the design constraints of the ELT first light instruments (see Bond et al. (2022)).

But the next generation of instruments and in particular ExAO instruments require much tighter levels of petal mode residual than the one offered by the minioning DM. For instance the limit amplitude for HARMONI is 50nm RMS of petal residuals, while the coronagraphic masks proposed for 2^{nd} generation of instrument by Leboulleux et al. (2022) require a residual lower than 30nm of petal mode to avoid loss of contrasts. This constraint is relaxed by using a redundant apodised pupils but with a larger Inner Working Angle (IWA).

2.6.2.2 Residual atmospheric petalling for a continuous DM

There are different parameters which influences the appearance of the petal mode. In particular we can separate two different types of petal mode in previous litterature : the low amplitude but fast varying petal mode in the minioning DM case and the high amplitude atmospheric petal mode as shown in Schwartz et al. (2018) or Bertrou-Cantou (2021). We have tested the influence of some simulation parameters here : The size of the spider, the r_0 and the size of the actuator IF (see chapter 1 for the definition, in summary for our case, $IF_{size} = 0.75 \times pitch$),

The tests are made by closing a loop, projecting the residuals on petal mode and plotting this petal mode in the residuals as a function of the studied parameter. The closed loop uses the parameter from table 2.1 (except for the parameter beeing tested).

influence of spider size On Figure 2.27 we plot how the petal varies in the residuals (nm RMS), as a function of the spider size of the pupil using a minioning DM.For this first test we use a large r_0 of 50cm to avoid non linearity issue coming from the WFS. The spider size s varies between 10 and 150cm. It is a close loop result where the residuals are projected on the petal mode and we plot the RMS of the amplitude of the petal mode over 10s of simulation.

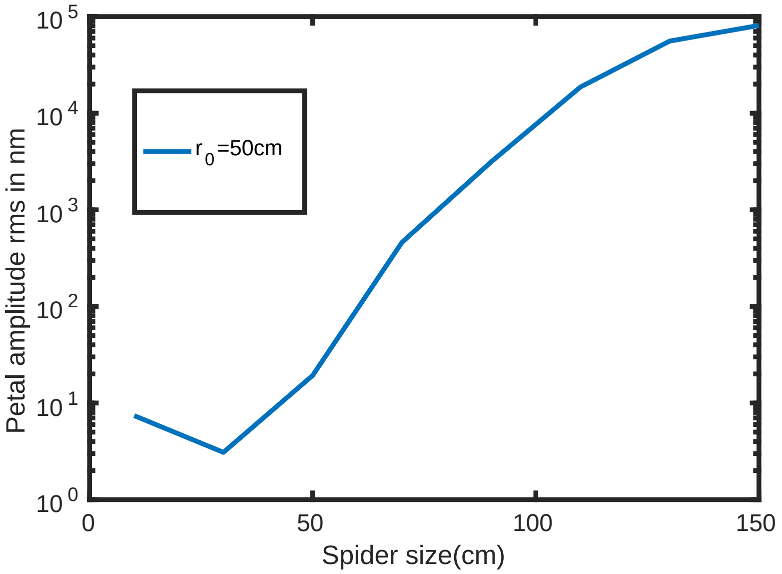

FIGURE 2.27 – Effect of spider size variation on petal mode in residuals

With the Toymodel simulation the size of the spider is a very important contributor to the amplitude of the petal mode. Once the spider gets larger than 30cm the petal mode increases with the width of the spider following $\phi_{petal} = 1/s^{5/3}$. We discuss more this limit in Chapter 3. To stay representative of the ELT case we keep the 50cm spider size.

Influence of r_0 A commonly-held belief is that the petal is only a problem for the ELT is that the spiders are larger than r_0 (see Engler et al. (2019) or Bertrou-Cantou et al. (2022). The first interpretation of this citation would be to say that with everything else beeing equal, an atmosphere with a r_0 larger than the spider would not suffer from the petal mode. On Figure 2.28a we used the previous simulation but with variable r_0 (defined @550nm, sensing at 850nm). The next plot has the same curves but multiplied by $r_0^{5/3}$ to test whether the variation between the curves comes only from the amplitude of the atmospheric turbulence.

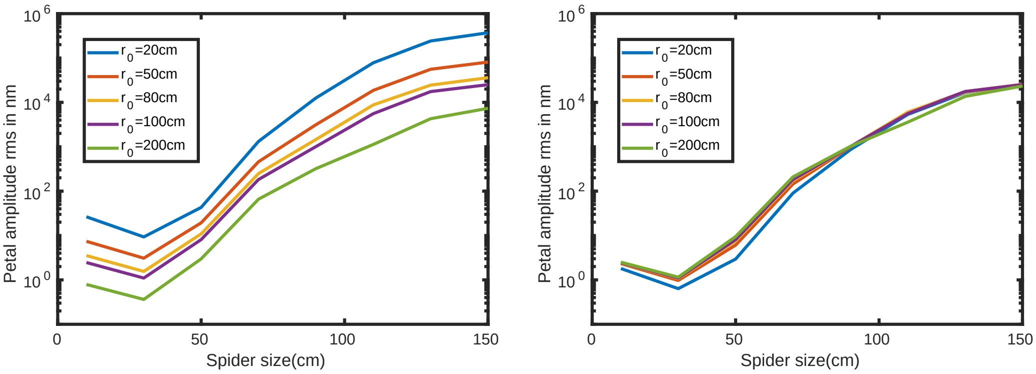

(a) Petal mode in AO residuals using different spider size and r_0 (defined for 550nm though $\lambda_{WFS} = 850nm$)

(b) Petal mode in AO residuals using different spider size and r_0 with mean amplitude of phase compensated.

FIGURE 2.28 – Test effect r_0 on petal

When compensating the overall change of phase amplitude created by the r_0 we see that the size of the spider and r_0 aren't directly linked and seem to have uncorrelated effect on the petal mode in the residuals. In particular we show that the petal mode always appear whatever the size of the r_0 even if it is magnitudes larger than the spider. But instead the petal amplitude just follows the amplitude of the phase. For a limit petal amplitude of 60nm RMS for a 50cm spider that would be achieved for a r_0 of 20cm or larger (we reach 53nm RMS at 20cm).

Influence of the DM Influence Function size The IF size of the actuators is a key parameter when dealing with petal mode. As proposed in SCAO systems for ELT, the FWHM of the actuators below the spiders are enlarged in order to cover more than the spider width. This precaution allows the DM surface to prevent discontinuities between two sides of the spiders. The difference is shown on Figure 2.29 between a segmented or a continuous DM. If the size of the Influence function is reduced (by adding more actuators in a diameter or reducing the mechanical coupling for instance), a continuous DM behaves as a segmented DM.

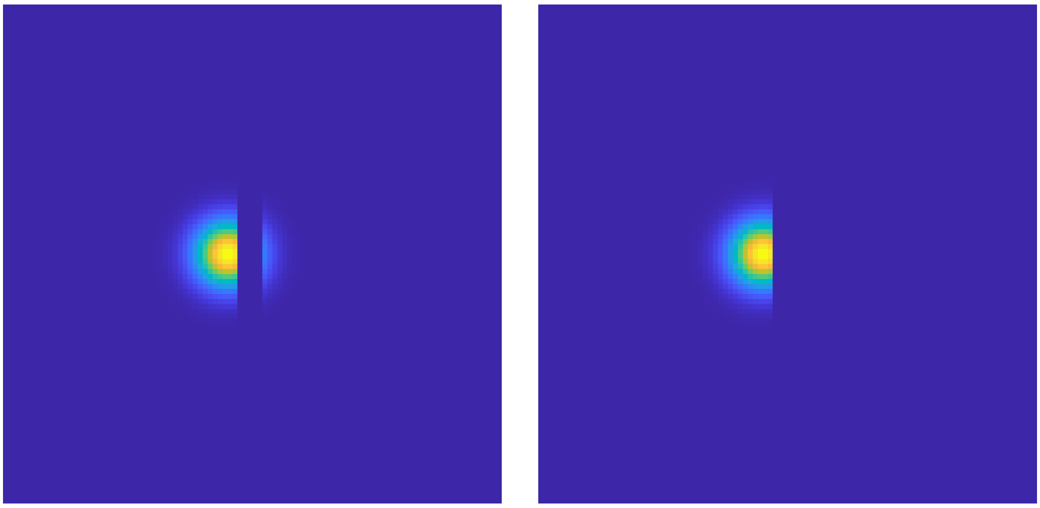

FIGURE 2.29 – DM with actuator of same size, Left is a continuous DM. Right is a segmented DM

We see this effect on Figure 2.30 where the number of actuators and consequently the size of their IF. We see the petal residual error transition from the minioning DM level to the segmented DM levels. In particular we go from a petal mode amplitude acceptable for HARMONI (40nm RMS for the 75cm actuator) to 450nm RMS with very small IF under 20cm. This simulation was made using $r_0 = 15cm$.

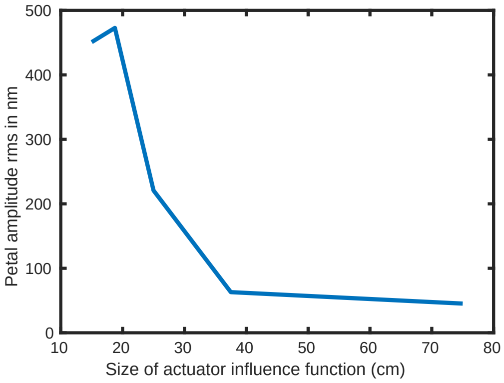

FIGURE 2.30 – evolution of residual petal error with size of the DM actuator IF of a continuous DM. Influence functions are Gaussian with a fixed coupling of 0.3

We use the FWHM as the definition of the size of the IF (see chapter 1). We see that when this size is over 35cm (pitch=50cm, the ELT $M4$ pitch), we see a petal in the residual around at 63nm RMS (which is just over the diffraction limit of $60nm$ RMS). Increasing the size of 1 actuator reduces the petal slightly to 45nm for actuators of 75cm IF width. In this simulation we have reduced the size of all actuators, but in practice it's only the size around the spider which is important for the petal mode. As was already showed by Bertrou-Cantou (2021) a larger IF around the spider improves the petal mode correction. The fitting error on the other side will increase with the size of every actuator following the law : $\sigma_{fitting} \propto (\frac{p}{r_0})^{5/3}$ with p the pitch.

2.6.2.3 Limits to minioning : Differential piston measurement

It was shown by Bonnefond et al. (2016) that even a sensor with no ability to measure the petal mode, the SH in COG measurement mode,the petal mode could be reduced if it comes from atmospheric turbulence by using an Minimum Mean-Squares Error reconstructor(see Bertrou-Cantou (2021)). The effect of the MMSE reconstructor are very close to the minioning DM as was shown by Bertrou-Cantou (2021). But this control solution only works for the atmospheric petal. Any exterior petal (like LWE) is not corrected. The result shown in the article reaches close final correction of the petal mode compared to a minioning DM such as presented by Schwartz et al. (2018).

The heart of the problem is that the WFS used for the SCAO is not able to measure the petal mode (which we abundantly study in chapter 3). The minioning DM is a control solution to a measurement issue. As such it can only control the petal mode which appears with a continuous atmospheric phase screen. But a system using minioning DM is not adapted to the correction of pre-existent or fixed differential phase steps, as those induced by LWE for instance.

The LWE contains not only petal mode and we wanted to know what the residual would be with a closed loop with a minioning DM. We used the previously shown LWE simulated shown on Figure 2.5 as a static phase screen and closed an AO loop on the static phase. To avoid running into the λ ambiguity we divide the phase screen by 4 (but the result are multiplied by 4 to show the final result). The test is made with a $3\lambda/D$ PyWFS as the WFS. The result is displayed on Figure 2.31 The residual have been projected on the petal mode presented earlier as well as the petal projection of the simulated LWE phase screen.

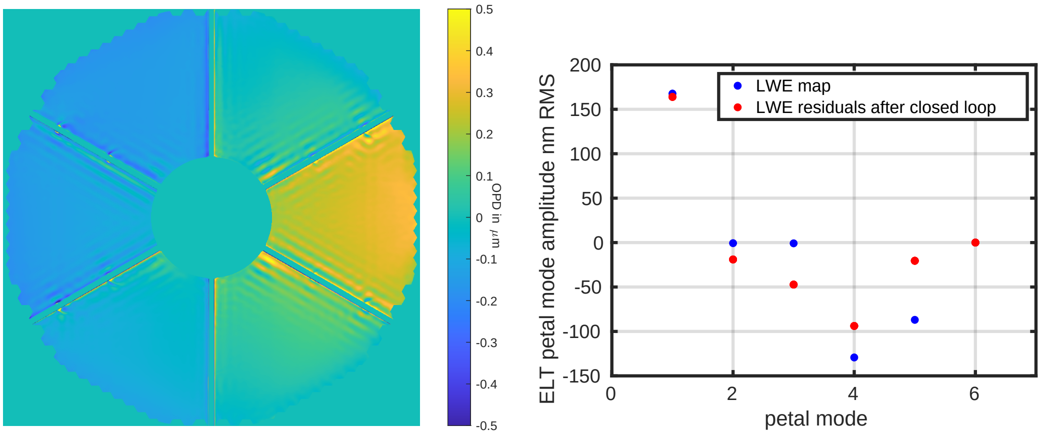

(a) LWE residual after closed loop. Petal more still present

(b) LWE phase map projected on the petal mode of the ELT. mode 6 being the global piston it stays at 0 in both case. We see that the LWE petal mode sees very little reduction after the loop.

FIGURE 2.31 – Effect of closing an AO loop on the LWE phase screen expected for the ELT using the $3\lambda/D$ PyWFS and a minioning DM.

Closing the loop has reduced the amplitude of the residuals from 328nm RMS to 170nm RMS. Most of which is the petal mode still present in the residuals after the closed loop.

On Figure 2.32 we show the residual Wavefront Error (WFE) of an AO system with a minioning DM during a closed loop. At frame 400 (time =0.4s) we have added 280nm RMS of petal mode. In the residuals we see that the petal residuals are now oscillating around the added petal mode petal instead of the 0 mean of atmospheric petal. The apparition of LWE would be much slower but the point is to show that now the petal from the minioning DM oscillates around this telescope added petal. This result shows something important about minioning DM : it doesn't change the measurement of petal, only the control of the mode.

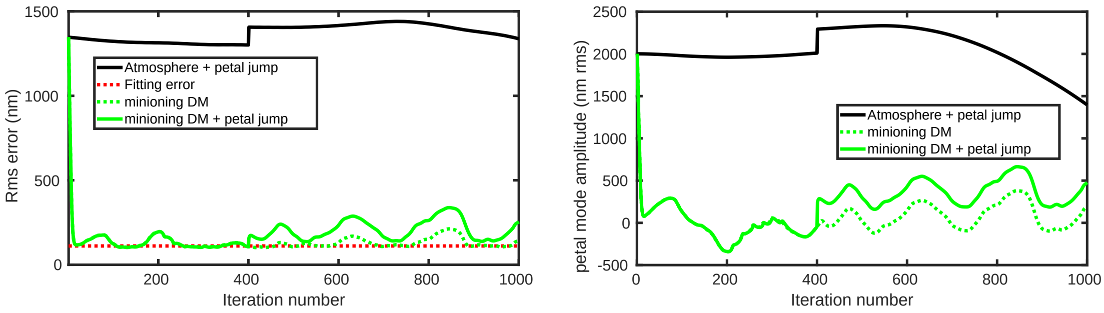

(a) RMS error of a closed loop using a minioning DM. A $\pi/3$ petal RMS is added at frame 400

(b) Residual of a closed loop using a minioning DM projected on petal mode. A $\pi/3$ petal RMS is added at frame 400

FIGURE 2.32 – Petal mode in a closed AO loop with minioning DM

If we want to reduce the petal mode in the residual under the value attained by the minioning DM (like for EXAO) or if we want to compensate other source of petal such as the LWE, we need to be able to measure the petal mode. For instance reproducing the measurement of the LWE with a WFS capable to measure the petal mode (an unmodulated PyWFS, see chapter 3) gives the residual shown on Figure 2.33.

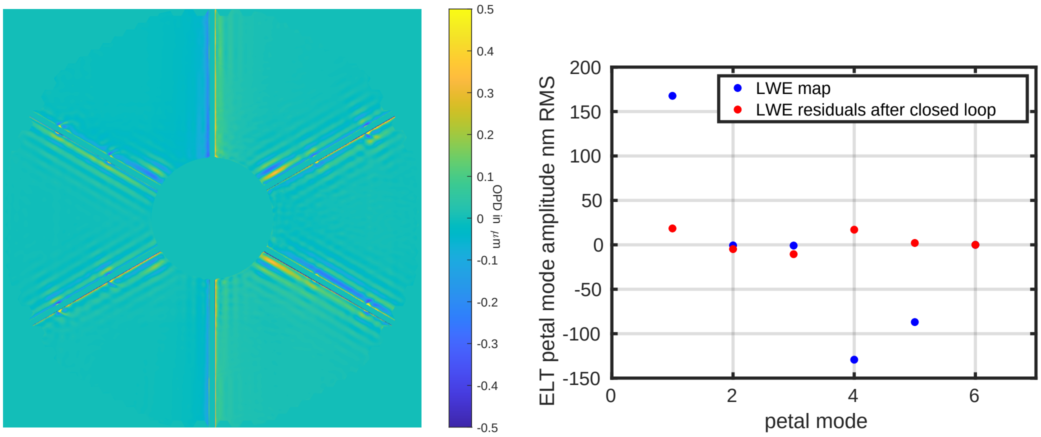

(a) LWE residual after closed loop using a WFS capable to measure the petal mode. Petal more absent but discontinuity mode remains

(b) LWE phase map projected on the petal mode of the ELT. We see that the petal mode has been greatly reduced

FIGURE 2.33 – result of closing an AO loop on the expected LWE phase screen of the ELT using a WFS capable to measure the petal mode. We see a great reduction of the petal mode but due to the minioning DM some discontinuity mode remains.

The residuals have gone from 300nm RMS with the full LWE phase screen to 75nm RMs We can see that the petal mode has almost disappeared from the residuals but some discontinuity mode remains due to the minioning DM.

We have shown that the heart of the petal problem is both the sensor and the presence of the spider. With a perfect phase sensor, or in the absence of a spider, the petal mode does not appear. Furthermore the petal mode in the residual is not a consequence of the petal mode in entrance phase only, but other modes like the discontinuity mode can provoke its apparition. In Chapter 4 we study the origin of this apparition : the petal confusion.

The objective of this chapter was to present and define the petal mode. We have defined this mode and the petal mode basis for the ELT and GMT telescope. But most importantly we have defined the simplest pupil able to create the petal mode to study it more easily in the rest of this thesis : the Toymodel pupil. The petal mode has 3 potential sources : atmospheric petal, LWE and mirror dephasing. The atmospheric petal can be greatly reduced by minioning DM. But this solution does not work for LWE petal mode and is insufficient for instrument necessitating very low phase aberrations like coronographs. The heart of the problem is that the sensors used for AO in giant telescopes cannot measure the petal mode in presence of large spiders, and can even measure other modes as petal mode, amplifying the problem. The petal mode has characteristics making this absence of measurement confusing. It is both a high and low spatial frequency modes, and it can be decomposed on classical phase aberrations which the PyWFS or SH have no trouble measuring. In the next chapter we explain this absence of measurement.

3 Analysis of the modulated pyramid sensitivity to the petal mode

In the previous chapter we described the petal mode, the main problem studied in this thesis. We established its characteristics and a simplified case name the Toymodel used to study it. As we showed in Chapter 2 the modulated PyWFS is not adapted to the measurement of the petal mode, but as the AO itself can create the petal mode, this mode needs to be measured by the AO loop to be controlled. The first part of this question illustrated in Figure 2.19 is that the modulated PyWFS doesn't measure the petal mode. But it is the sensor which will be used in the next generation of AO systems, so we want to study the origin of this lack of measurement and propose solutions in terms of sensitivity. The SH, the most common AO sensor doesn't measure this mode either, as any sensor based on measuring the local phase derivative. In particular, this chapter aims to increase the sensitivity to the petal mode and describe a first strategy to measure the petal mode.

We use the 2-norm of δI defined in chapter 1 in Eq 1.37as the measurement of how much linear signal a mode creates. It is as well the definition of the sensitivity to an uniform noise (Readout noise RON for instance) as was shown by Fauvarque (2017) and expended in Chambouleyron et al. (2022). It is noted $s(\phi_i)$.

$$s(\phi_i) = \sqrt{N_{sap}} \times \left|\left|\delta I(\phi_i)\right|\right|_2 \tag{3.1}$$

With N_{sap} the number of subaperture considered in the pupil for the WFS. For a PyWFS it is the number of detector pixels in 1 of the 4 subpupil in the detector plane. This definition of sensitivity is usable for any FFWFS. As shown by Chambouleyron et al. (2022) the sensitivity is between 0 and 2. Doubling the sensitivity means reducing by a factor of 2 the impact of noise on the reconstruction. This metric measures how much linear signals change in the detector space with a phase change. As a quadratic metric, a few points with very high values give a better sensitivity than a large area with even values. For this reason, increasing the number of faces on the PyWFS will in general decrease its sensitivity as the same signal is separated on more pixels (It's not that simple for petal mode as shown later). It doesn't say how useful this intensity is for WFS (for instance if 2 different phase screens give the same intensity pattern this would not be captured by the sensitivity criterion). It does not measure the linearity range which is another important parameter of a WFS.

3.1 Effect of modulation on petal sensing

3.1.1 Effect of modulation on $\delta I(petal)$

The modulation was originally proposed as a method to improve the dynamic range of the PyWFS. One of the effects of the PyWFS is that for modes with lower spatial frequency than the modulation radius, the signal behaves as a slope sensor. But for modes with higher frequency, it behaves as a phase sensor as shown by Vérinaud (2004). That changes where the intensity pattern appears for the same phase mode when changing the modulation radius, especially for the petal mode. For a phase sensor, the signal is distributed across the whole pupil. However, a derivative sensor only has a signal where the discontinuity of the petal mode appears. For instance in Figure 3.1 we see how the ΔI for the petal mode changes with modulation. We see in particular that for the unmodulated Pyramid Wavefront Sensor (uPyWFS) without spider (top center figure b) the intensity for petal mode is distributed in the whole pupil (at the discontinuity, but also in the rest of the pupil area) while for the modulated PyWFS (bottom center figure e) it is concentrated around the phase discontinuity position. When a spider is added, all relevant signal for petal mode is masked out when modulated. Meanwhile for the uPyWFS while some signal disappears under the spider shadow, a lot remains as was measured in Figure 3.7.

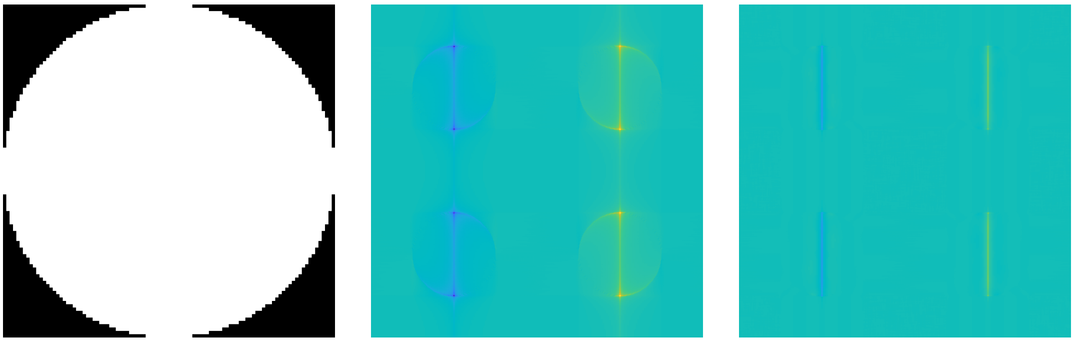

(a) Pupil without spider (D=10m) (b) uPyWFS signal without spider (c) modulated PyWFS without spider

(d) Toymodel pupil (spider = 50cm) (e) Toymodel, uPyWFS (f) Toymodel, modulated PyWFS

FIGURE 3.1 – Change of petal mode δI. All δI use the same intensity scaling

The modulation therefore brings a drop in sensitivity in general but this drop is most significant for modes with spatial frequencies lower than the modulation radius. As such the petal mode with most of its energy in the low frequencies is among the modes the most affected by modulation as shown in the Figure 3.2. In this Figure, the classical change of sensitivity with a PyWFS is represented where the sensitivity of a mode drops once the modulation radius is larger than the spatial frequency of said mode. As the petal mode is very low frequency, it drops in sensitivity for a very small modulation radius. A low frequency mode is impacted in the same way when the mode's spatial frequency becomes lower than the modulation radius. The sensitivity of each mode then tends toward the same value around 0.05. But the most striking effect is the effect of the spider. While the Fourier modes' sensitivity is not impacted by the spider, the sensitivity of petal mode both starts lower and tends to lower values than the Fourier modes. This effect seems general for any PyWFS type sensor and we have the same effect with asymmetric PyWFS. Even though the asymmetrisation allows us to adapt the sensitivity of the PyWFS for a given petal mode, the modulation reduces them too much to make the asymmetrisation worth it if we use a modulated PyWFS.

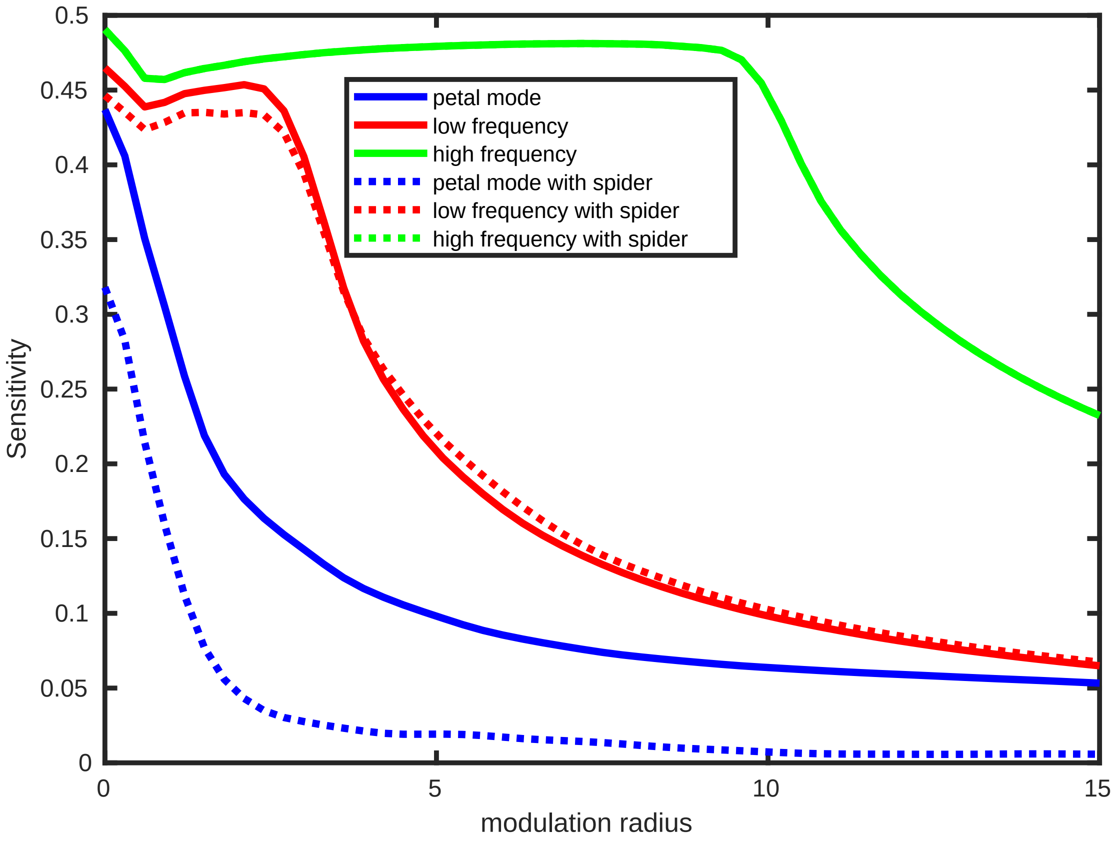

FIGURE 3.2 – Sensitivity to the petal mode with respect to the modulation radius for the petal mode and a low frequency($3\lambda/D$ sinusoidal phase mode) and a high frequency ($10\lambda/D$ sinusoidal phase mode). HARMONI uses a $3\lambda/D$ modulation radius. Dotted lines are computed with a spider in the pupil. The green dotted line and solid line are superposed

3.1.2 PyWFS sensitivity map

These two compounding effects of loss of sensitivity due to modulation and the spider presence can be plotted as a 2D map of sensitivity. For comparison, we plot the sensitivity map of the astigmatism for reference. Astigmatism being a continuous and low spatial frequency mode, is amongst the modes the most impacted by the modulation. In Figure 3.3b we see that the sensitivity to petal mode is comparable to the astigmatism sensitivity for a 20cm spider (TMT spider size) but lower by a factor 3 to 5 for 50cm spider. That might explain why the TMT reports fewer petal issues than the ELT and GMT in its SCAO simulations.

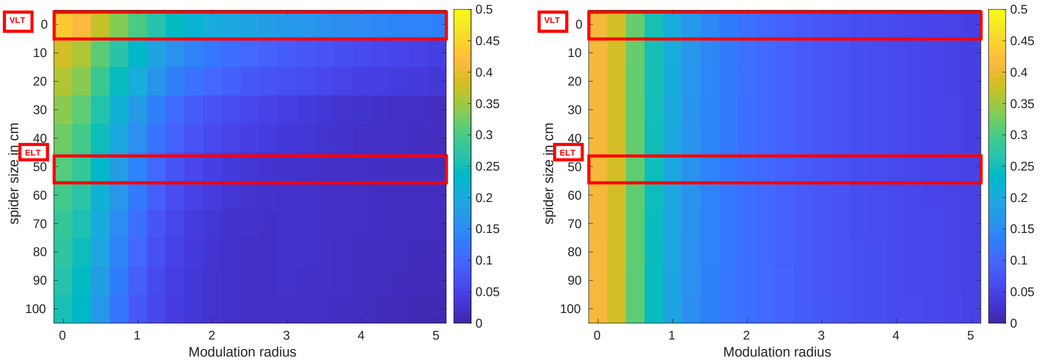

(a) Sensitivity to the petal mode (a) and astigmatism (b) as function of modulation radius and spider size. The spider size for ELT and VLT are highlighted. The sensitivity at a $3\lambda/D$ is 0.17 for the VLT but 0.020 for ELT ($3\lambda/D$ is the suggested modulation radius for HARMONI). At $5\lambda/D$, the sensitivity is 0.13 for VLT and 0.017 for ELT-type spiders.

(b) For astigmatism the size of the spider does not affect sensitivity. The Sensitivity at $3\lambda/D$ is equal to 0.08. This sensitivity is close to the sensitivity to petal mode with a 20cm spider at $3\lambda/D$ modulation

FIGURE 3.3 – Sensitivity map of petal mode and astigmatism depending on the modulation radius and spider size.

We identify two important areas in this map : without a spider, the modulation can be as high as wanted and the WFS keeps a sensitivity comparable to the sensitivity of other low spatial frequencies modes like astigmatism. When there is no modulation the spider already creates some drop of sensitivity to the petal mode contrary to other phase modes. But this drop is limited (from 0.45 to 0.3 for 1m spiders on the toymodel) compared to the drop caused by modulation and spider combined and a 0 modulation PyWFS can still be used to control the petal mode in a case where only the petal mode exists. Unfortunately, the current ELT design forces the 50cm wide spiders and it is known in the community that unmodulated PyWFS can't be used to control AO in with a full atmospheric turbulence.

3.1.3 Effect on Interaction matrix and phase measurement

As we showed the modulated PyWFS has a lower sensitivity to the petal mode than to the other phase modes. This changes the interaction matrix $Imat$ and the Command Matrix $Cmat$ which translates the PyWFS intensity into a phase measurement and DM commands (see Chapter 1). The sensitivity will influence the eigenvalue of a measured mode. The higher its sensitivity is, the higher its eigenvalue is as well. When going from the $Imat$ to the $Cmat$, a pseudo inversion is done and the modes which are represented by the lower eigenvalues are filtered to avoid reconstructing noise. We expect that with modulation the petal mode will have lower eigenvalue.

To show that effect we compute the interaction matrix, using our toymodel pupil and the associated 50cm pitch DM (20x20 for the Toymodel pupil) representative of the ELT M4 pitch. The modes calibrated during the interaction matrix acquisition are only the DM influence functions. Then a Single Value Decomposition (SVD) is performed to get the eigenmodes. To identify the indices of the petal mode, we project the eigenmodes on the petal mode. In Figure 3.4 we show this projection for different modulations values and spider size for a modulated 4-sided PyWFS. We see here how the loss of sensitivity affects the wavefront reconstruction by making the petal mode appear for lower eigenvalues. We show with the red line where the 100 conditioning (= eigenvalue of the mode after the red lines are under 1% of the maximum eigenvalue).

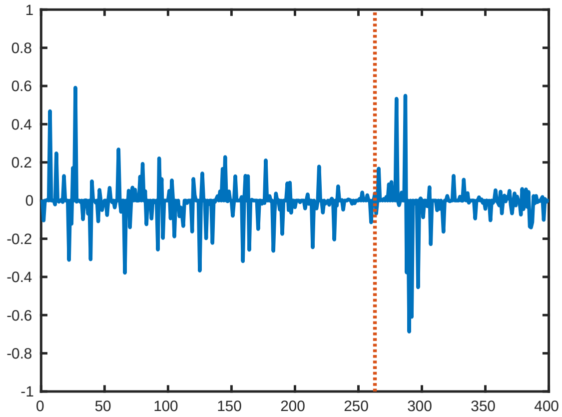

(a) Projection of the eigenmodes on the petal mode for toymodel pupil+20x20 DM and uPyWFS

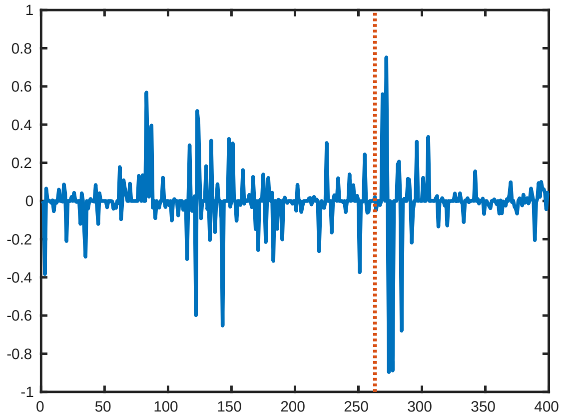

(b) Projection of the eigenmodes on the petal mode for toymodel pupil+20x20 DM and mod=1λ/D PyWFS

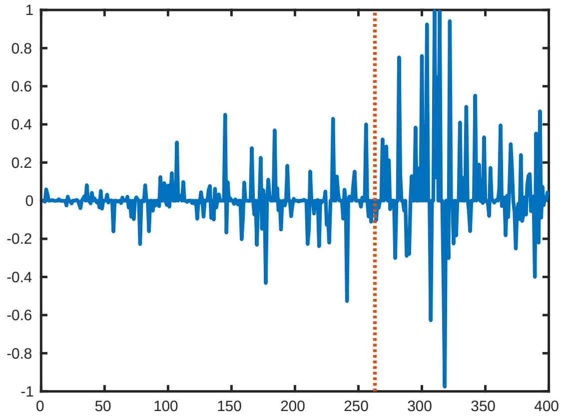

(c) Projection of the eigenmodes on the petal mode for toymodel pupil+20x20 DM and mod=3λ/D PyWFS

FIGURE 3.4 – Projection of Imat eigenmodes on the petal modes. The vertical axis represent the scalar product between the petal mode and the eigen mode. The horizontal axis represents the number of the eigenmode considered. We see that with a larger modulation radius in the presence of spiders, the petal modes are projected in the lower eigenmodes

The same mode test is performed with the ELT pupil and the minioning M4 mirror. We see on Figure 3.6 that for the ELT pupil the petal mode gets closer and closer to the tolerance limit with the modulation.

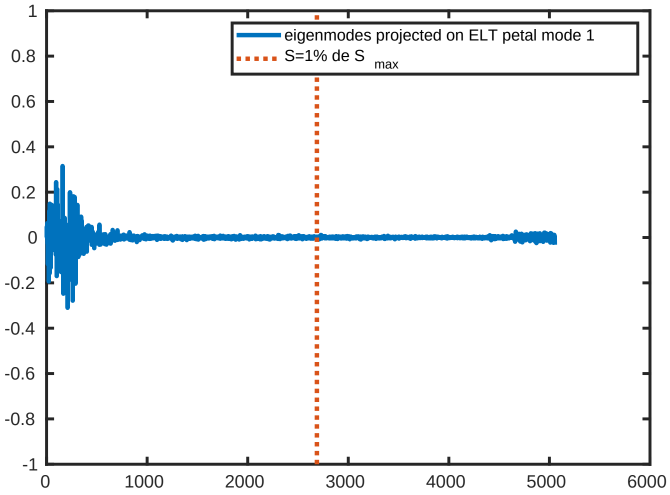

FIGURE 3.5 – eigenmodes projected on the first ELT petal mode for ELT pupil, M4 DM and mod=$0\lambda/D$ PyWFS

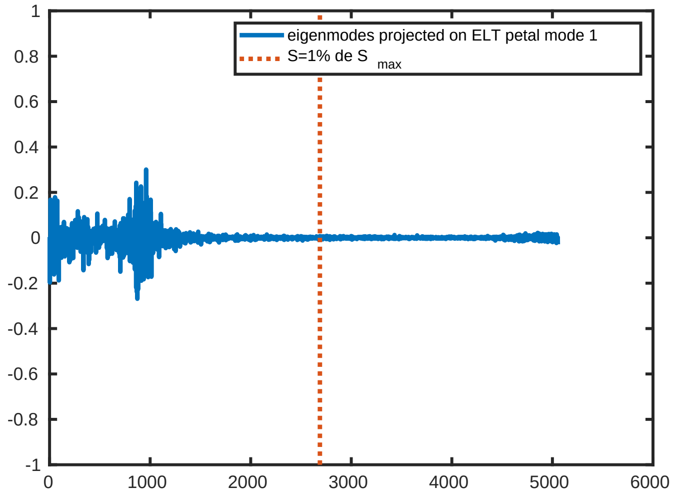

(a) eigenmodes projected on the first ELT petal mode for ELT pupil, M4 DM and mod=$1\lambda/D$ PyWFS

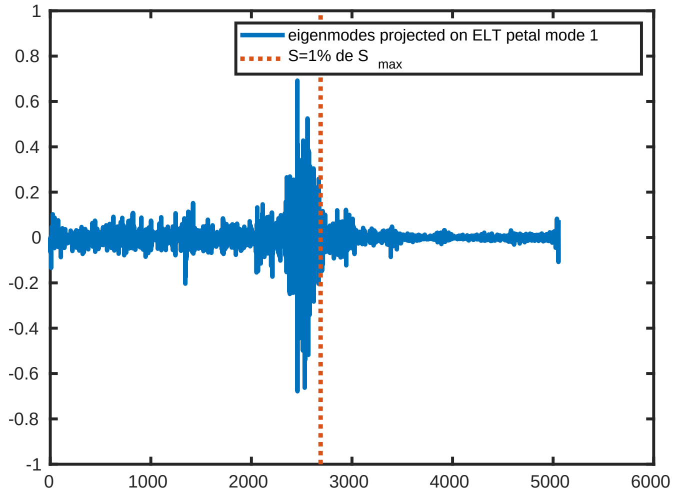

(b) eigenmodes projected on the first ELT petal mode for ELT pupil, M4 DM and mod=$3\lambda/D$ PyWFS

FIGURE 3.6 – Eigenmodes projected on petal mode for the ELT pupil, The vertical axis represent the scalar product between the petal mode 1 of the ELT and the eigen mode. The horizontal axis represents the number of the eigenmode considered.

We understand through these decompositions that the sensitivity of a PyWFS to the petal mode is not binary : seen or not seen. The Petal mode is decomposed into a large number of modes, a part of them can be seen while the other part is not. It is therefore difficult to say if a sensor is "sensitive" or "not sensitive" to the petal mode. What is certain is that the mode gets more and more difficult to measure.

3.2 Effect of spider size on Pyramid sensitivity to petal and other modes

The sensitivity can be computed on any modal basis. An important modal basis is the basis ordained by spatial frequencies. This was computed by Fauvarque (2017). This sensitivity is computed on the Fourier basis modes, but as the petal mode needs an infinity of Fourier mode to be represented due to the discontinuity, the sensitivity to petal mode is not clearly deductible from the Fourier sensitivity.

In Figure 3.7a we show the sensitivity of Fourier modes with or without a spider and for the case of an unmodulated and modulated PyWFS. The sensitivity to low order modes is decreased by the presence of a 5% spider. The loss of sensitivity is mainly visible on the low spatial frequencies. The loss for a 5% spider is at worse 0.04 of sensitivity for a non-modulated PyWFS, and 0.03 for a modulated one. A 5% spider for a 10m telescope toymodel corresponds to a 50cm wide spider, the same width as for the ELT. This represents a loss of sensitivity of less than 10% meaning the presence of a large spider increases by 10% the impact of noise on wavefront measurement for some low-order modes. This overall has a pretty limited impact compared to the effect that modulation and spider size have on the petal mode shown in Figure 3.7b. We see that with 0 modulation there is already a loss of 20% (from 0.45 to 0.35) due to the spider size from 0 to 5% spider (and even more loss for larger spider plotted). But the loss is even worse for a larger modulation. As a first step, we want to try to improve the sensitivity with no modulation to compare the highest sensitivities available for a given pupil and a PyWFS sensor.

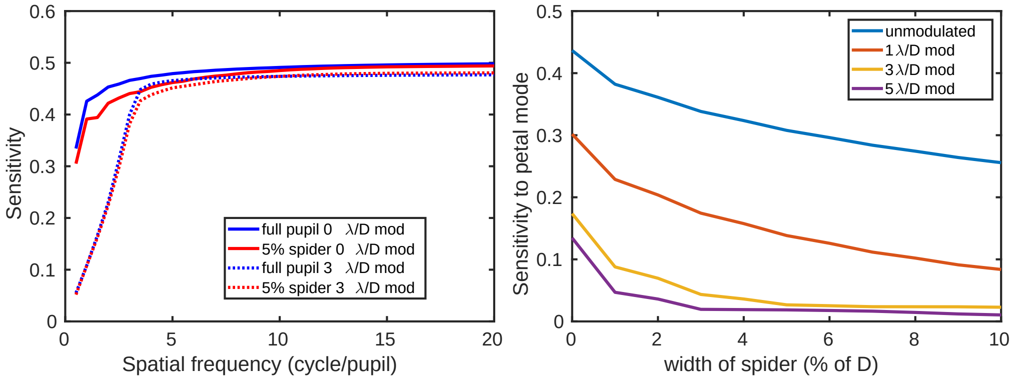

(a) Sensitivity of a PyWFS to the Fourier modes for different modulation and spider widths

(b) Sensitivity to petal mode of a PyWFS with various spider size and modulation radius

FIGURE 3.7 – Effect of the spider size and modulation on PyWFS sensitivity

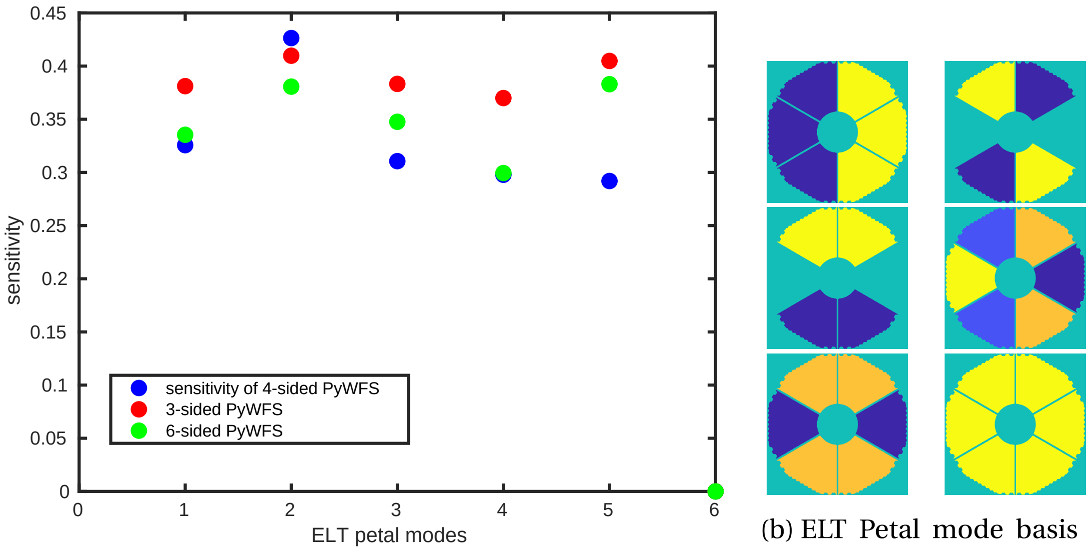

(a) sensitivity to the different petal mode presented in Figure 2.4a. Sensitivity can change greatly from one mode to another. Having the larger discontinuities, petal mode 2 has a larger sensitivity than the other.

(b) ELT Petal mode basis :
1 2
3 4
5 6

FIGURE 3.8 – sensitivity to different petal mode of different PyWFS

We measured the sensitivity of the ELT for the different petal modes for different PyWFS (by changing the number of sides on the PyWFS) in figure 3.8. We see an important effect of geometry as the sensitivity to petal mode can vary by 30% depending on the PyWFS used

3.2.1 Adapting the PyWFS to the petal mode : the asymmetric PyWFS

The geometry of the PyWFS seems to have a high effect on the measurement of the petal mode. For instance on petal mode 5 changing the PyWFS geometry can improve the sensitivity by 30%. We want to take advantage of this effect to improve the sensitivity. Another well-known effect to improve the sensitivity is flattening the PyWFS as was shown by Fauvarque et al. (2015). Following Fauvarque, we define a degree of flattening f which is defined by the degree of overlap between two subpupils when they start to overlap as shown in Figure 3.9

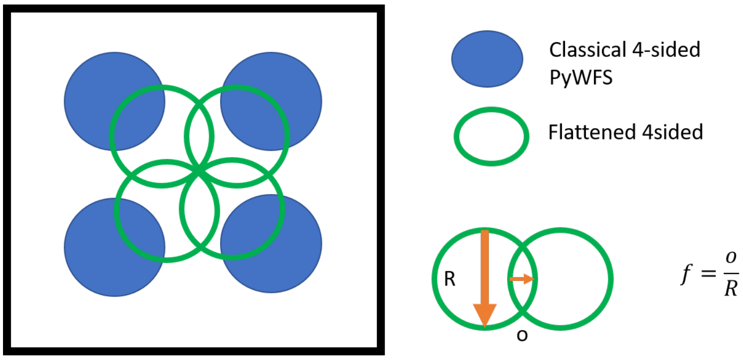

FIGURE 3.9 – Definition of the flattening parameter of a 4sided PyWFS

with R the diameter of 1 PyWFS subpupil on the detector of the PyWFS, o the width of overlap between the two subpupils.

This flattening is particularly interesting with the Large Binocular Telescope (LBT) pupil, where the gap between the two 8m mirrors can be seen as a very large spider. As an example, we can consider the LBT configuration with two separated pupil. For such a configuration, a classical 4-sided modulated pyramid has demonstrated a very low sensitivity to the differential piston between the two pupils (shown later in figure 3.16). By changing the Pyramid angle and thus making the two pupils overlap at the level of the detector (as shown in fig 3.11), we take advantage of the optical recombination between the two pupils. We see in particular an optimum of sensitivity when the overlap between the left and right mirror of LBT is at the maximum (for a flattening of 30%)

The following plots are made using an unmodulated PyWFS. All δI are plotted using the same scaling.

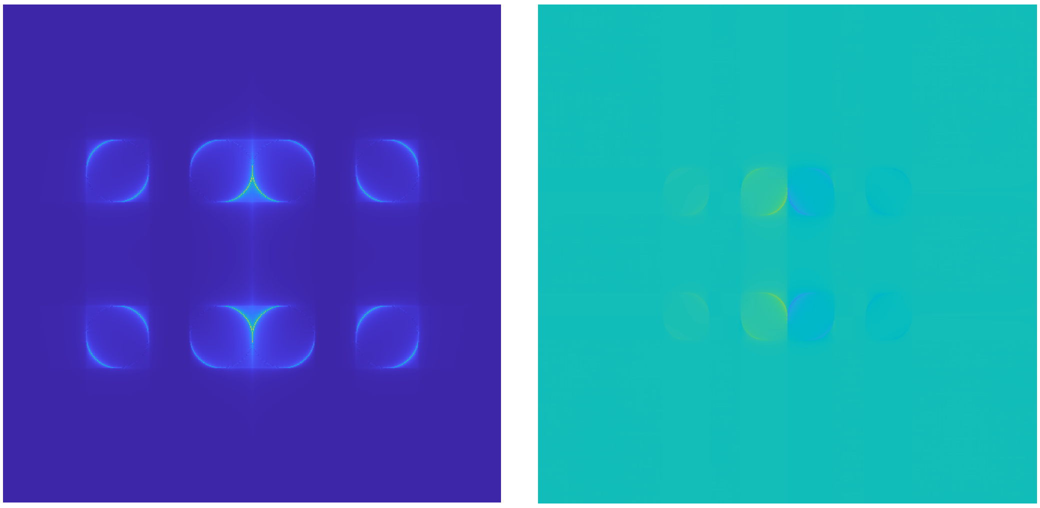

(a) Standard PyWFS reference signal for LBT

(b) Standard petal δI for LBT

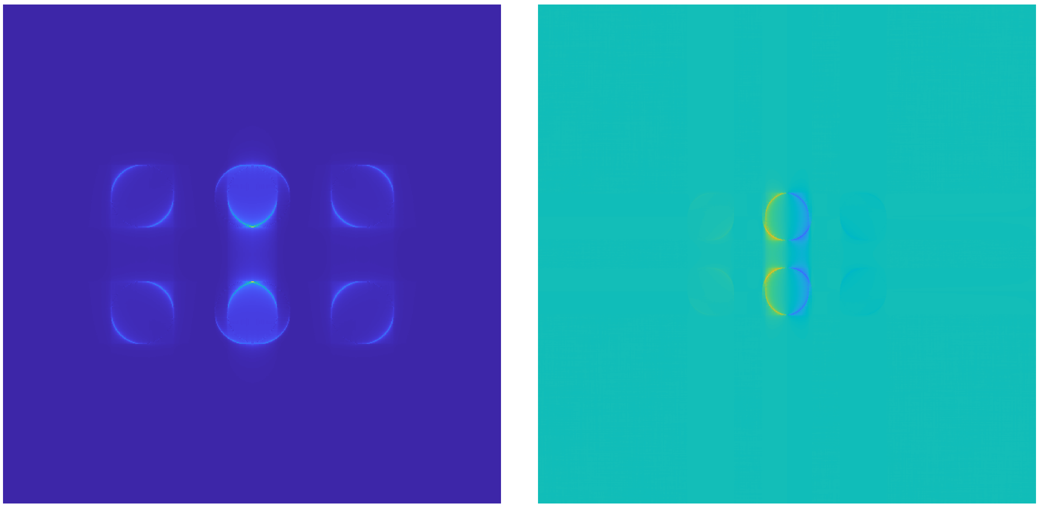

(c) 40% flattened PyWFS reference signal for LBT

(d) 40% flattened PyWFS petal δI for LBT

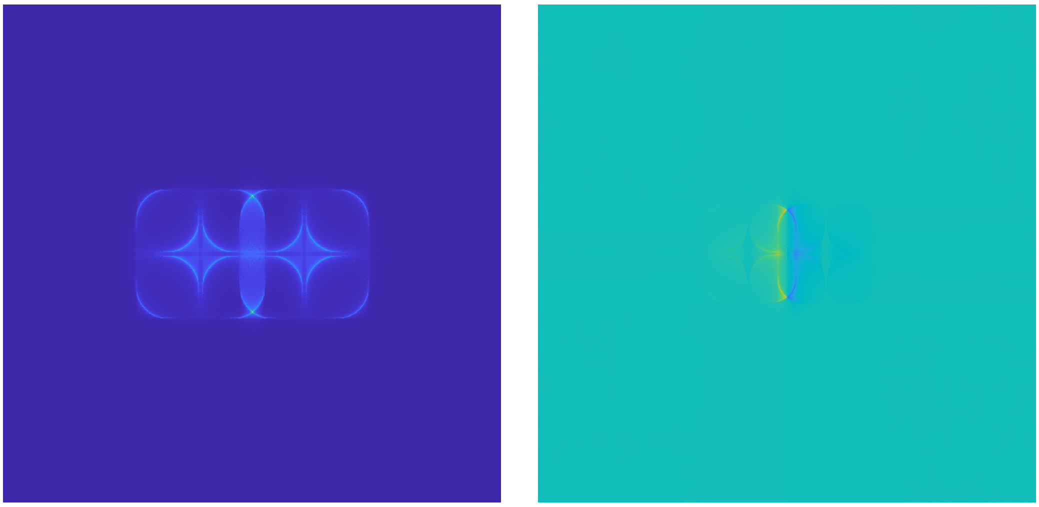

(e) 60% flattened PyWFS signal for LBT

(f) 60% flattened PyWFS δI for LBT

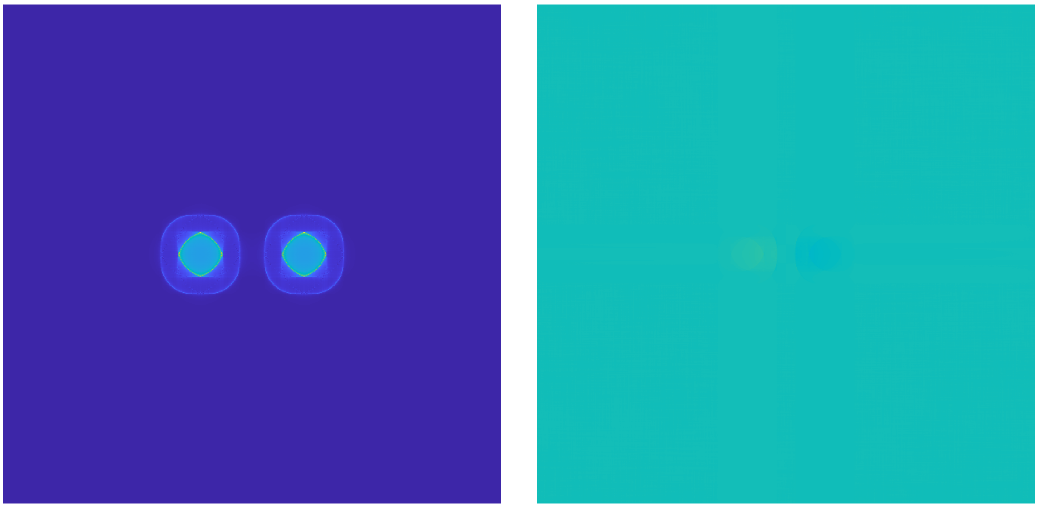

(g) Standard flattened PyWFS reference signal for LBT (90% flattened)

(h) Standard flattened PyWFS petal δI for LBT(90% flattened)

FIGURE 3.10 – Effect of flattening the PyWFS on the reference intensity I_0 and petal δI. We see that the maximum of overlap between the left and right telescope appears at 40% flattening

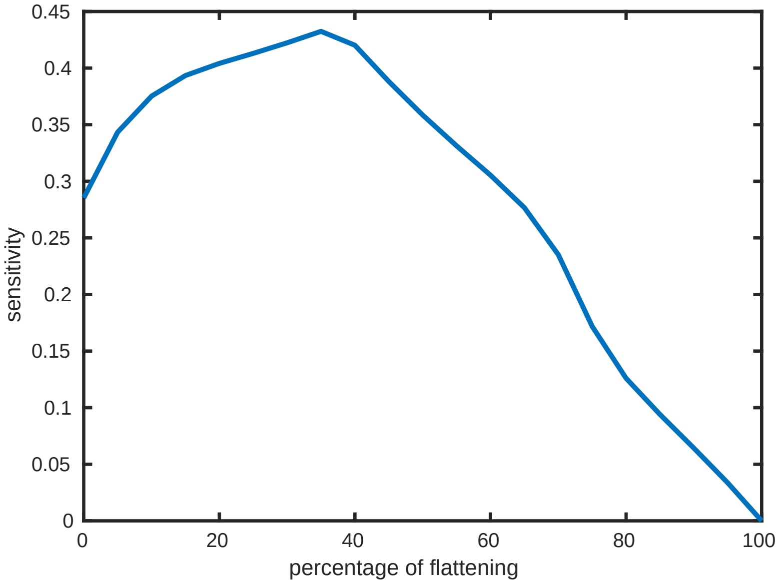

FIGURE 3.11 – Sensitivity to petal mode as function of flattening of the PyWFS.

The highest sensitivity to petal mode is obtained for 40% of flattening, which corresponds to the maximum overlap of the left and right LBT pupil as seen on 3.12d so this particular PyWFS is called the Half Flattened PyWFS (HFPyWFS). When this overlap is maximum, the sensitivity to petal mode seems maximum. It is also visible in the δI plot that the 40% is where the intensity of the petal is the most concentrated on the center subpupils and very little signal appears in the other subpupils. The half flattened pyramid has been tested on the LOOPS bench (see Janin-Potiron et al. (2019)) with the I_0 and δI shown in Figure 3.12 for the classical 4-sided and the half-flattened PyWFS on the Loops bench.

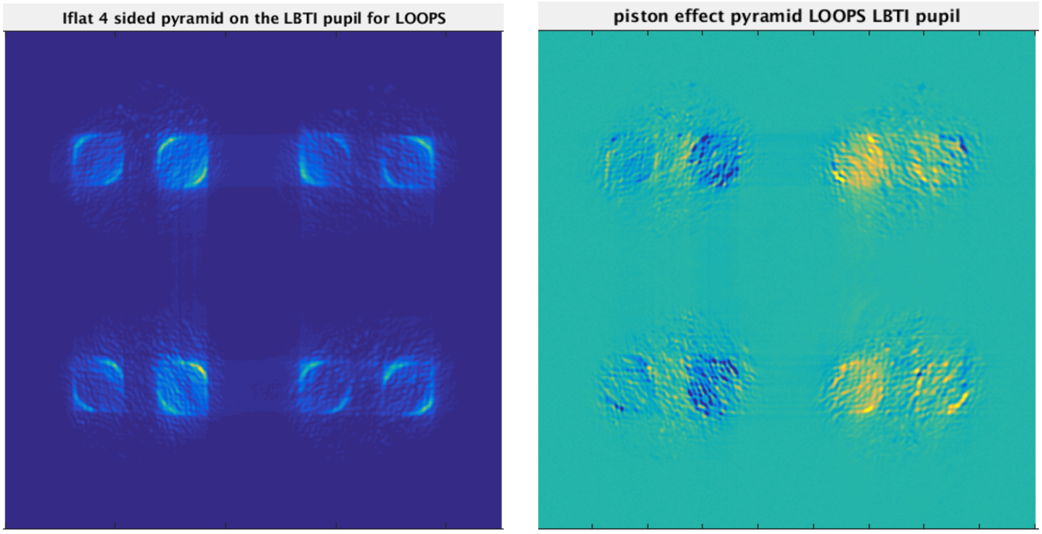

(a) Standard PyWFS reference signal for LBT on LOOPS bench

(b) Standard petal δI for LBT on LOOPS bench

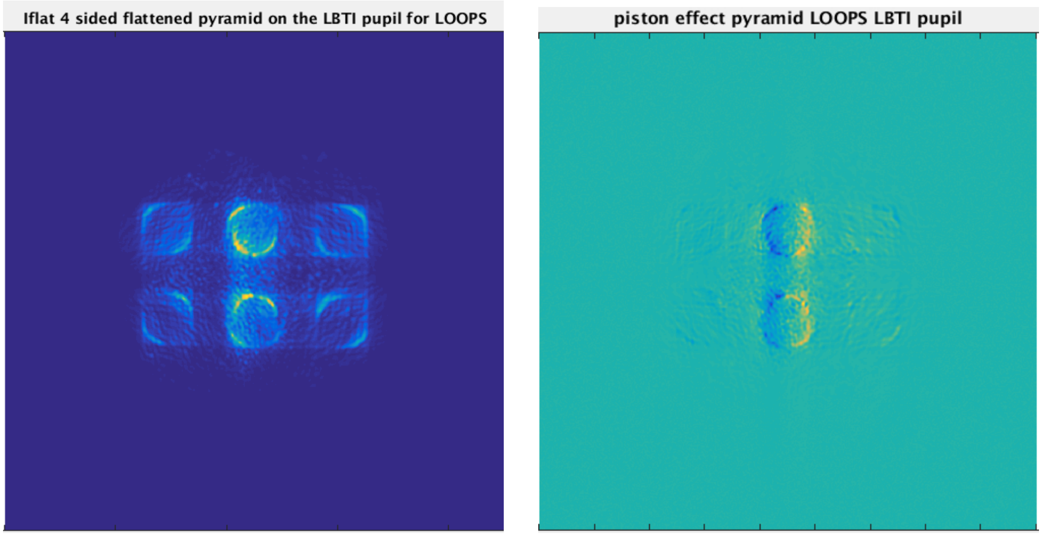

(c) 40% flattened PyWFS reference signal for LBT on LOOPS

(d) 40% flattened PyWFS petal δI for LBT

FIGURE 3.12 – Test of the half-flattened PyWFS on the LOOPS bench

For the LBT pupil, it is possible to reduce the overall angle of the PyWFS to have only the two pupil images of I_1 and I_2 overlap, but not two pupil images of I_3 and I_4 (see Chapter 1 for I_n definition). That is due to the particular shape of the LBT pupil. But if the same process is taken with a more usual circular shape like ELT or our toymodel, all I_n intensities overlap. We can produce the same overlapping without flattening the whole PyWFS but by flattening it in only the horizontal direction. This reduces the overlap with the other Intensities which are known from Fauvarque (2017) to create variable sensitivity to the Fourier modes. To that end, we create a PyWFS with different apex angles in the X and Y directions. The effect of asymmetrisation of the PyWFS angle on I_0 and δI is seen in Figure 3.14.

For the creation of this asymmetric PyWFS, we define the asymmetrisation parameter $asym$ as shown on Figure 3.13. As you can see an asymmetrisation of 100% on the 4-2 PyWFS would be equivalent to having the 90° prism. We define it that way and not by just changing the angle of the original pyramid because it's more easy to visualise for more complex asymmetrisation what is the operation ; such as when the asymmetrisation doesn't follow the same clocking angle as the original pyramid.

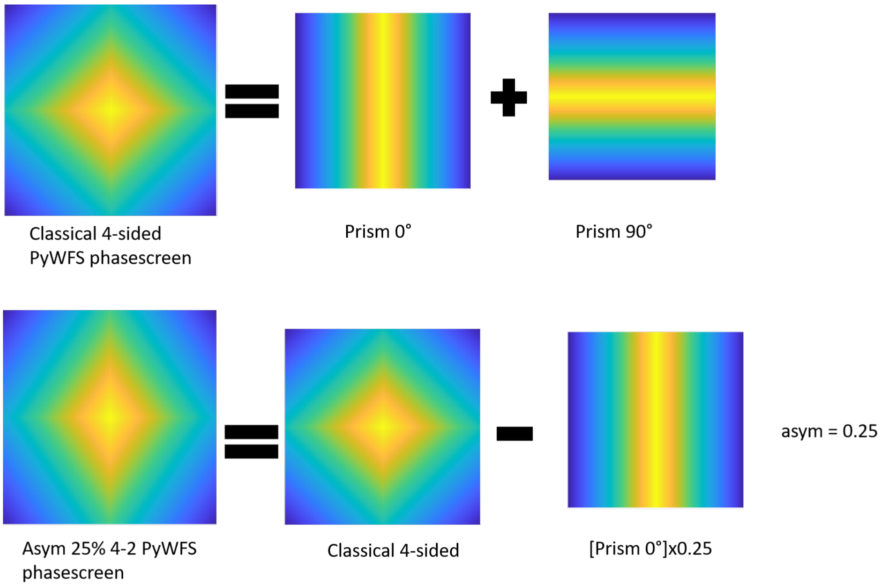

FIGURE 3.13 – Exemple of construction of an asymetric pyramid of 25% asymetrisation

The asymmetrisation can be realised in practice by adding a prism on top of the PyWFS. As in practice, the PyWFS are created not with 1 glass PyWFS but 2 (as shown in Schwartz et al. (2020)) to compensate for the chromatism of the glass, this asymmetric PyWFS could be created by using a PyWFS and a prism instead of 2 PyWFSs.

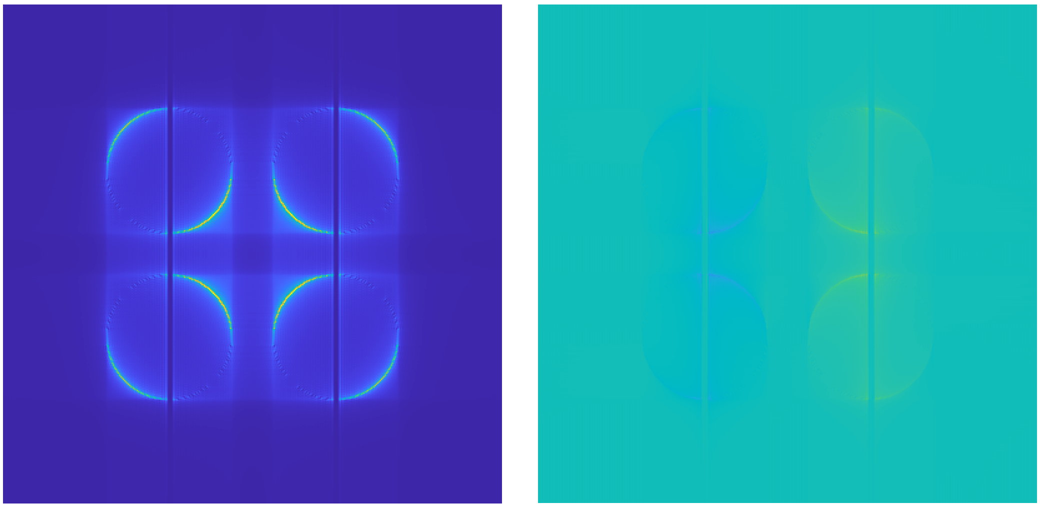

(a) Standard PyWFS reference signal for Toymodel

(b) Standard petal δI for Toymodel

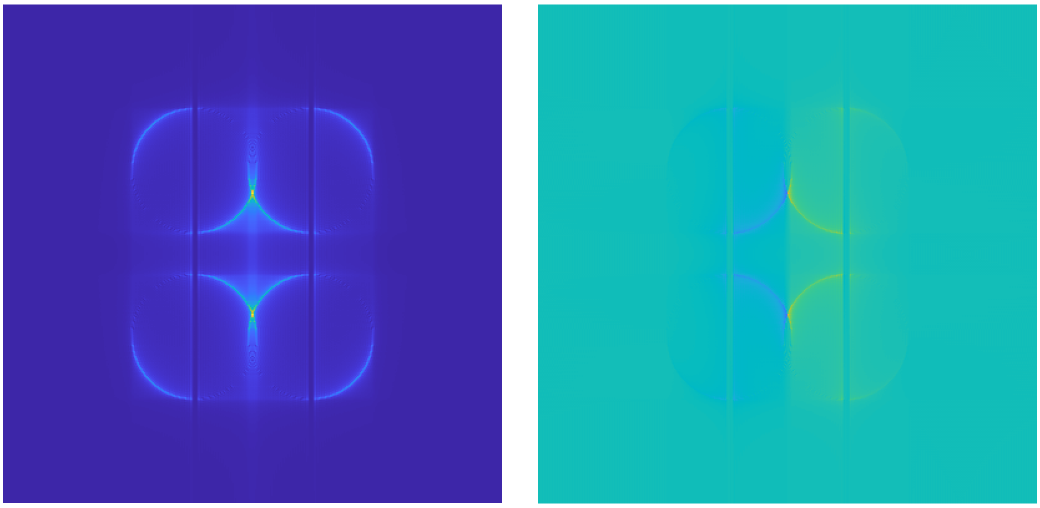

(c) 30% asymmetric PyWFS reference signal for Toymodel

(d) 30% asymmetric PyWFS petal δI for Toymodel

(e) 60% asymmetric PyWFS signal for LBT

(f) 60% asymmetric PyWFS δI for Toymodel

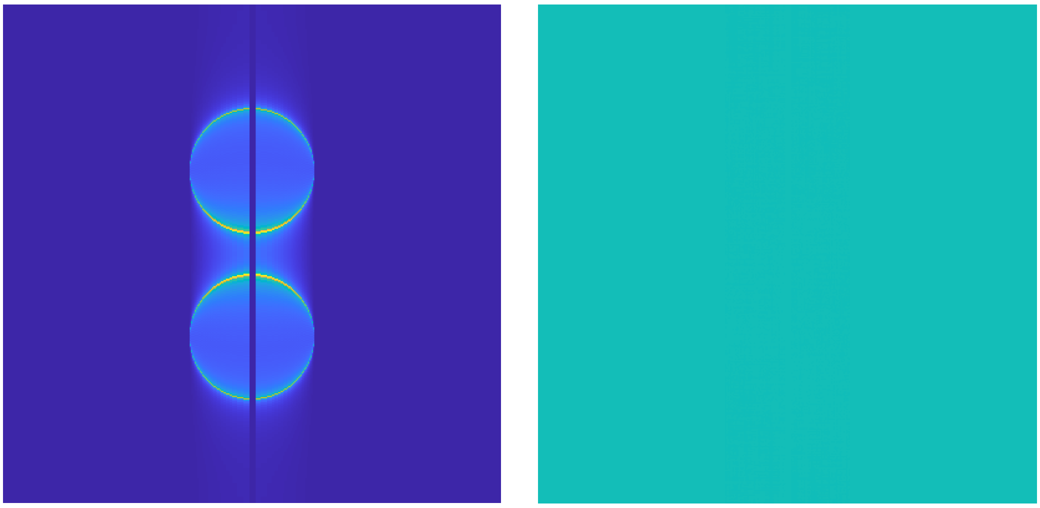

(g) Vertical prism I_0 after full asymmetrisation

(h) Vertical prism δI for toymodel (only digital noise visible)

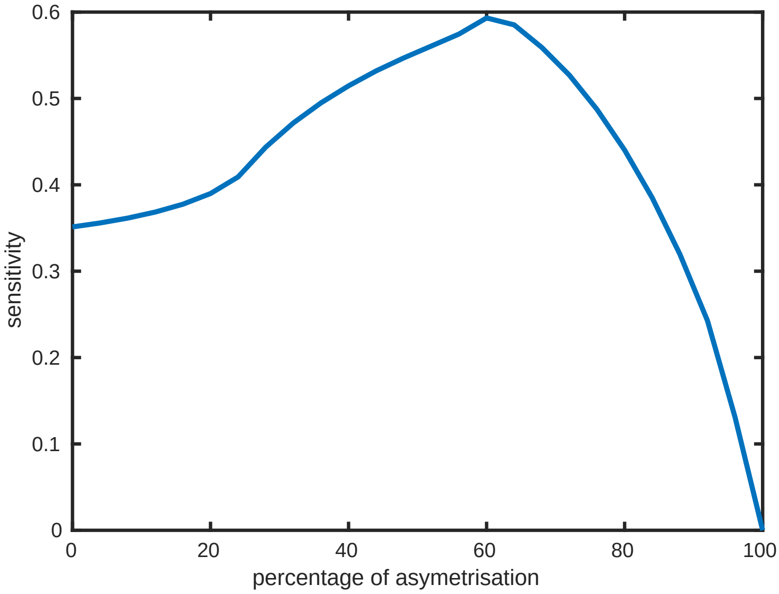

FIGURE 3.14 – Effect of flattening the PyWFS on the reference intensity I_0 and petal δI. We see on the sensitivity plot that the 60% flattened (so where the overlap of left and right pupil fragment is maximum) has the best sensitivity

In Figure 3.16 we plot the sensitivity of the different PyWFS and see that the half-flattened PyWFS and asymmetric PyWFS have much higher sensitivity than the one of the modulated PyWFS. We see again a maximum of sensitivity when the opposing pupils overlap.

3.2.2 Asymmetric Pyramid adapted to the ELT

We want to expand the principle of asymmetrisation to improve the sensitivity to petal mode on a more complex pupil than the Toymodel like the ELT with its 6 fragments. The change of the pyramid which creates a similar overlap of the fragments becomes more complex as well. As for the Toymodel, we simulate the superposition of 2 pyramids. To follow the symmetry of the pupil we consider this time a 6sided and a 3 sided pyramid for which the angle changes. In Figure 3.15 we plot on the left the resulting reference intensity (to make the pupils displacement more visible we plot here with a modulation of $1\lambda./D$) and on the right the δI for the first ELT petal mode(without modulation). The first case (a and b) is with the 6sided pyramid alone, asym=0. The second case (c and d) is when the pupils start overlapping at asym=0.4. The third case (e and f) corresponds to an overlap of 50% between the ELT subpupils with asym=0.8.

Here a clocking angle of 30° between the 6sided and 3sided pyramid has been chosen. Different of value of clocking will create different combination and enhance specific petal mode. On Figure 3.15f we see a signal appearing where the pupils overlap showing this configuration improves the signal created by the petal mode. to quantify this gain we plot the sensitivity to the ELT petal modes (reminder of the ELT petal modes on Figure 3.15j) as defined on equation 3.1 on Figure 3.15i. As for the toymodel we see a gain in sensitivity, but depending on the mode some show a maximum of sensitivity while other see a net gain with the asymmetrisationa at 1%. The position of the maximum depends on the petal mode as a given asymmetrisation will cause an overlap for a few ELT fragments and improve the signal only on a few petal modes.

This gain is important as it allows to go from 0.4 to 0.6, improving by a factor 1.5 the sensitivity to petal mode Although such a PyWFS probably has modified sensitivity to the modes of some spatial frequency as was shown for the flattened PyWFS by Fauvarque (2017). A more detailed study of this sensor as WFS should be done. Other combination such as a 12-6 PyWFS should also be studied to compare the sensitivity.

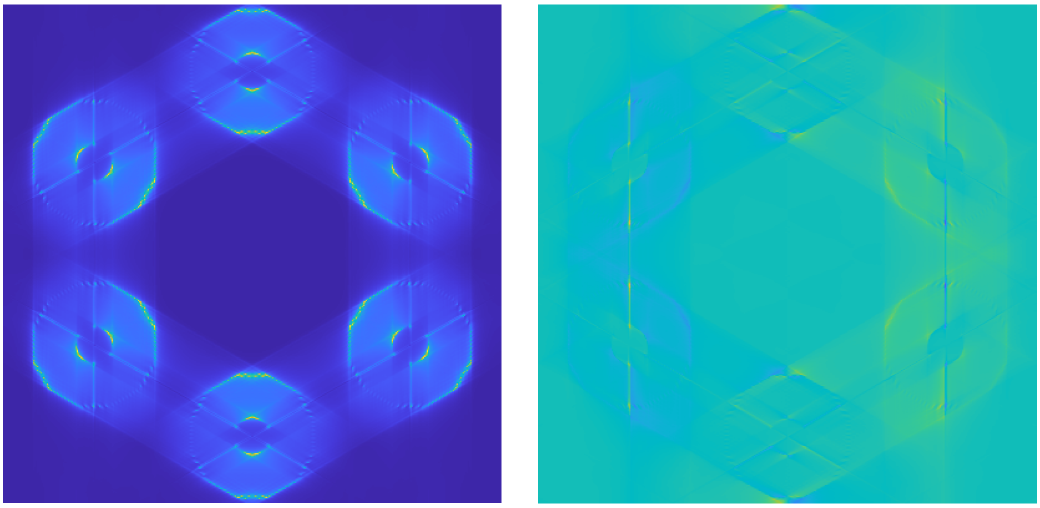

(a) Standard PyWFS reference signal for ELT with 6-sided PyWFS

(b) Standard petal 1 δI for ELT with 6-sided PyWFS

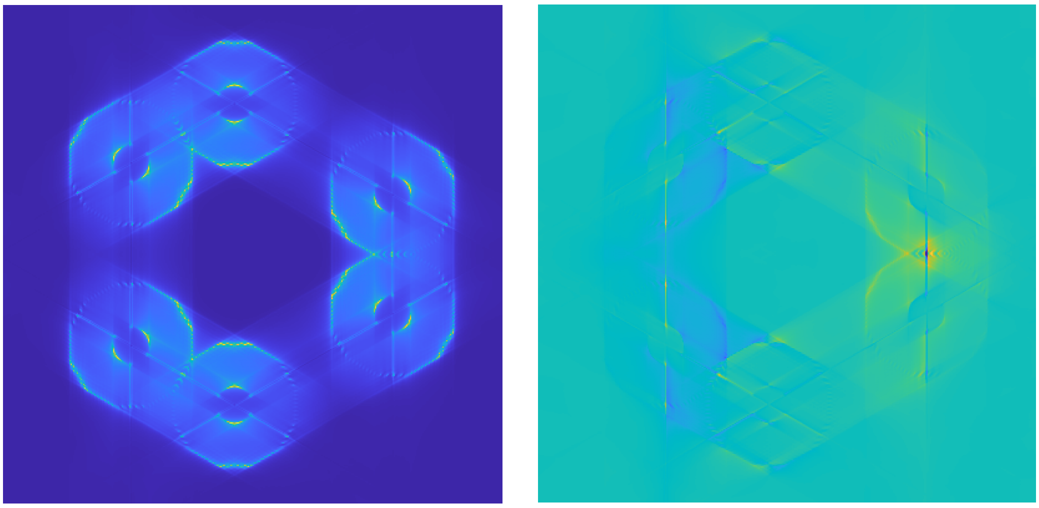

(c) 40% asymetric 6-3 PyWFS reference signal for ELT

(d) 40% asymetric 6-3 PyWFS petal δI for ELT

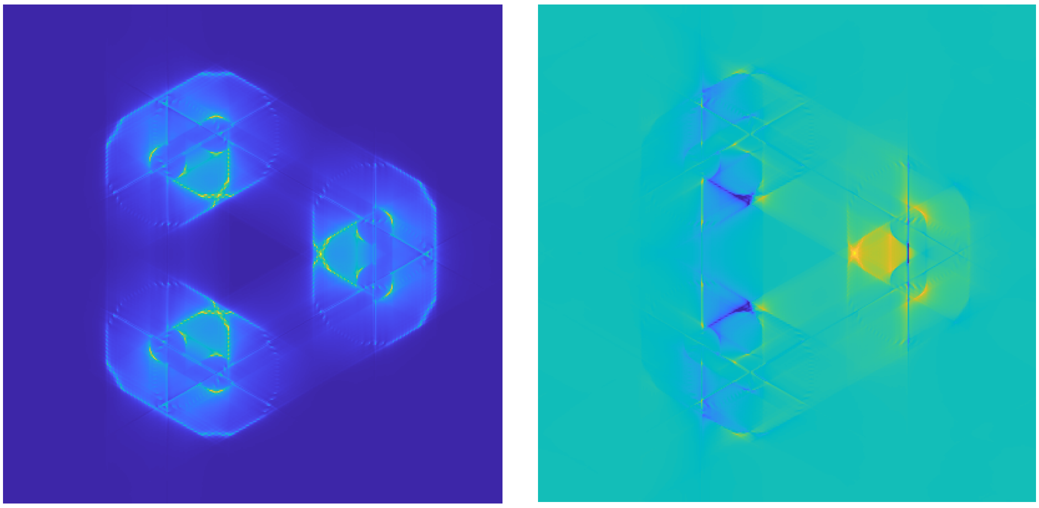

(e) 80% asymetric 6-3 PyWFS reference signal for ELT

(f) 80% asymetric 6-3 PyWFS petal δI for ELT

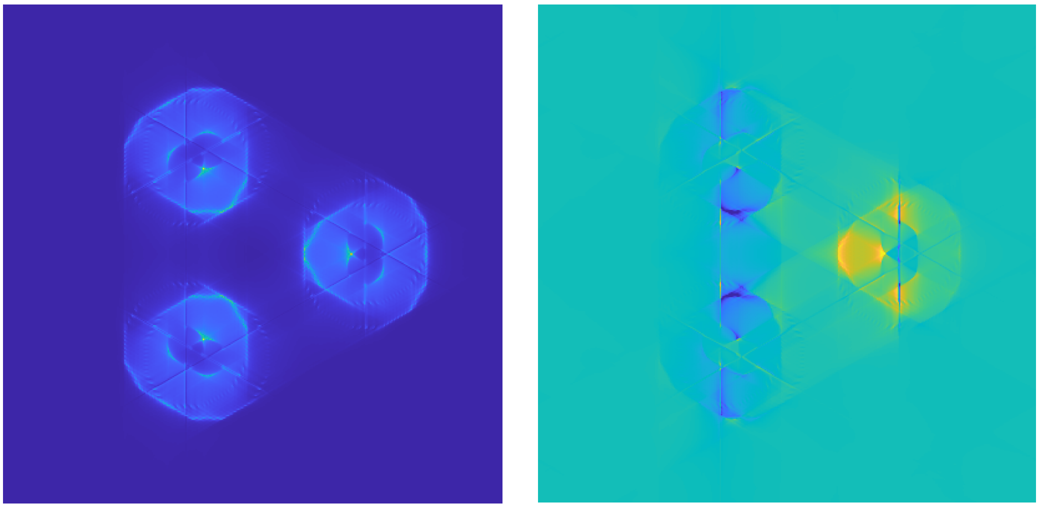

(g) 90% asymetrisation I_0 after full asymmetrisation

(h) 90% asymmetrisation δI for ELT

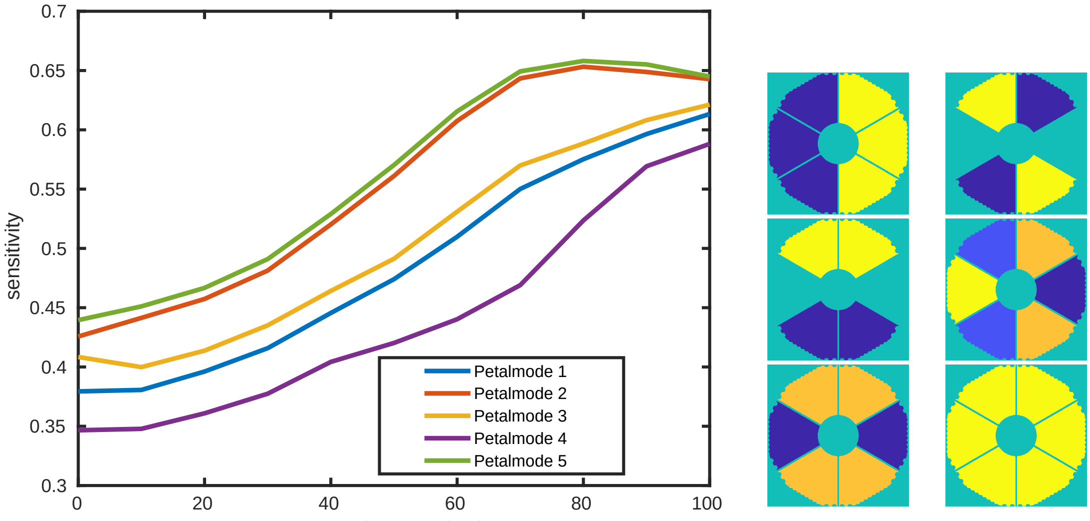

(i) sensitivity for each petal mode of the ELT depending on the asymerisation (no modulation)

(j) ELT Petal mode basis

FIGURE 3.15 – Effect of flattening the PyWFS with an ELT pupil, on the reference intensity I_0 and petal δI.

The sensitivity of the asymmetric PyWFSs adapted to each pupil for the petal mode (as it is the closest to the LBT and Toymodel petal mode, we show here the sensitivity to the petal mode 1 of the ELT) are shown on Figure 3.16 to be compared to the result of the 4sided PyWFS to the same mode. We see that although we have demonstrated a gain in sensitivity with these modified PyWFS, it disappears when we start modulating. For each pupil, the asymmetric PyWFS has the highest sensitivity. The gain in sensitivity is comparable for each pupil with roughly a doubling of the sensitivity compared to the 4−sided PyWFS. The most spectacular gain is for the LBT pupil where the large gap made the petal mode hard to measure compared to the Toymodel. But any gain in sensitivity disappears with modulation.

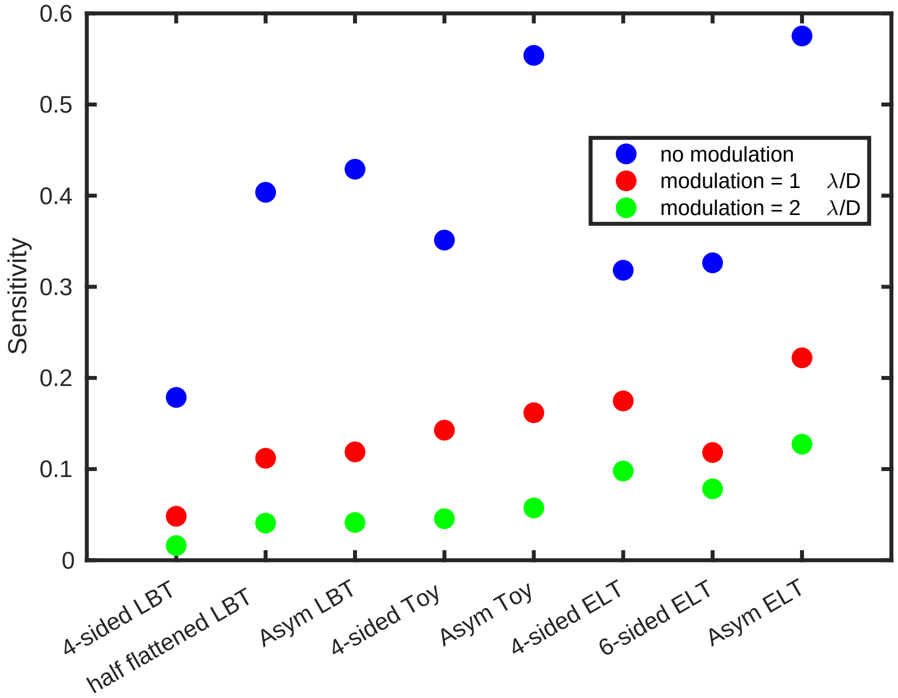

FIGURE 3.16 – Sensitivity to petal mode for ELT, LBT and toymodel pupil with various PyWFSs.

3.3 Inclusion of a petallometer to a conventional AO system

Ideally all AO designers dream about having only one sensor able to measure all perturbations : atmosphere and petal mode. However the previous work has shown that there is no obvious solution for this. As shown the modulated PyWFS has very low sensitivity to petal mode. The noise would easily be amplified. But the unmodulated PyWFS has a very small dynamic, not compatible with the typical r_0 of astronomical site. We want to show how an additional sensor dedicated to petal mode sensing, a petallometer, could be added in an AO system. We will test the unmodulated PyWFS as the first example of petallometer as it is already a well studied sensor.

To that end we start with an AO system suffering from petal mode. We use our Toymodel pupil, a modulated pyramid and have the choice between a segmented of minioning DM. Figure 3.17 shows the result of a closed loop following the conditions in Table 2.1 with either a segmented DM (green curve) or a minioning DM (red curve). While in the segmented DM case the petal mode follows closely the petal mode of the atmosphere, the minioning system has an already reduced petal mode. Of particular interest for us, the value of petal is under λ and we don't suffer the λ ambiguity with this case.

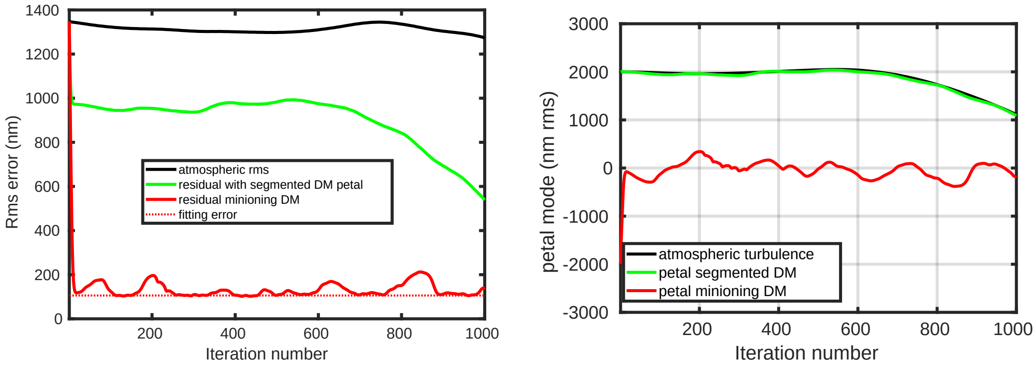

(a) Residual error of a 1st stage AO segmented DM compared to the case with a minioning DM and fitting error

(b) Residual projected on the petal mode of a 1st stage AO with segmented DM or minioning DM

FIGURE 3.17 – Comparison of an AO with DM modes orthogonal to petal compared to a classical DM

We will use this first AO loop and add a petallometer which sees the same phase. This petallometer can measure petal and other phase modes. As the AO sensor and the petallometer measure the same phase we use the term 2nd path to designate the petallometer.

The aim is first to check whether the petallometer can measure the petal mode among the residuals of the first path. In a diffraction-limited AO system (as HARMONI, MICADO), the phase residuals are reasonably small at least compared to the incoming atmospheric turbulence. Among the WFS more sensitive to petal mode, one can list the uPyWFS, the asymmetric PyWFS (see 3.16), but also the Zernike WFS (see Cisse et al. (2022)). These sensors come with a limited linear range, roughly compatible with the level of the residuals. We then can add a correction of the petal mode measured by adding offsets to the voltage of the DM. This way of correcting petal is far from ideal, as the modes controlled by the petallometer and the AO loop are not separated. But this solution seems stable since the petal mode is not seen by the AO loop (showed in chapter 2 in absence of residuals, see 2.19). the optical layout we are simulating for the 2 path system is shown in Figure 3.18.

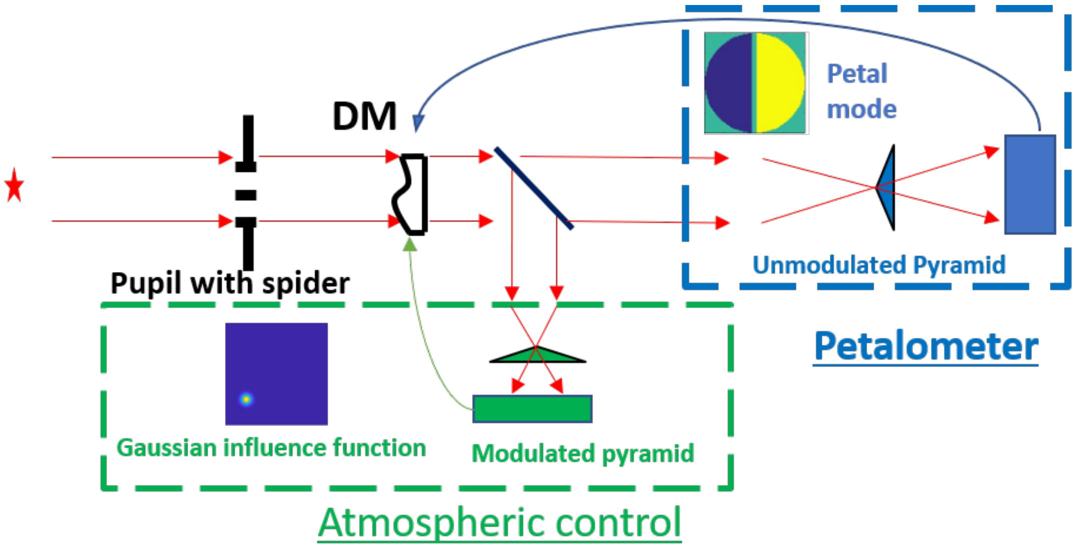

FIGURE 3.18 – 2 Path sensor scheme used for petal and atmospheric turbulence control

For the calibration of this 2 path system we have 2 sensors to calibrate. The atmospheric sensor, and the petallometer. The atmospheric sensor is calibrated classically with the continuous Gaussian DM modes as the phase modes of Imat. For the petallometer, the calibration could be simply to calibrate the petal mode alone as Imat. But in this case, the system would also measure the residual tip-tilt of the first path as a signal. To avoid that we need to calibrate more modes. As the first solution, we choose to calibrate the 30-first Zernike on top of the petal mode. But this allows us to know which mode the system should not confuse with petal mode. This is not a realistic calibration as that would mean a modal DM is present here to create these modes. Another (more realistic) option would be to calibrate the petal mode as well as the Gaussian IF controlled by the first path. On Figure 3.19 we see the result of this 2 path sensor with a very large r_0. A 140nm rms petal mode is added at iteration 400 to represent LWE. While the minioning system alone now oscillates around this static petal mode, the 2-path system goes back to 0 petal quickly.

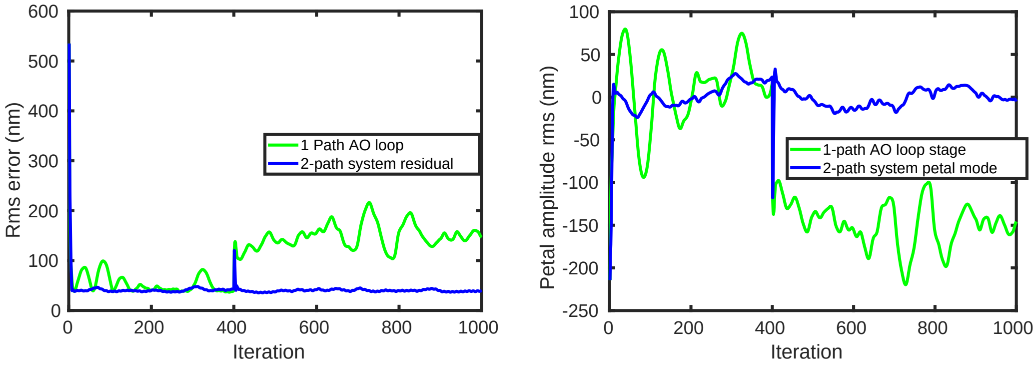

(a) Closed loop residuals at each iteration with a r_0 of 50cm

(b) amplitude of petal mode present in the residual at each iteration with a r_0 of 50cm

FIGURE 3.19 – 2-path system result with a large r_0

The same simulation done with a realistic r_0 of 15cm does not work. We see In Figure 3.20 that the 2-path system is unstable and jumps from one lambda petal to another. The aim of Chapter 4 is to find why and correct this failure.

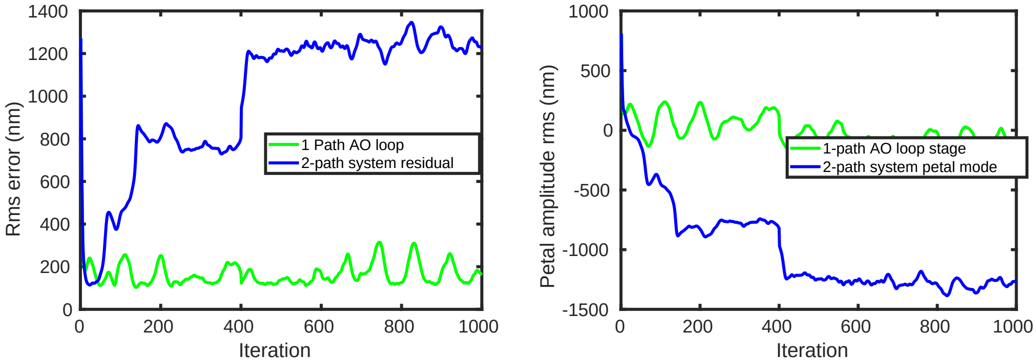

(a) Closed loop residuals at each iteration with a r_0 of 15cm

(b) amplitude of petal mode present in the residual at each iteration with a r_0 of 15cm

FIGURE 3.20 – 2-path system result with a realistic r_0

In this chapter we have shown that the size of the spiders is the origin of the drop of sensitivity for a modulated PyWFS. While the size of the spider can be mitigated by the use of asymmetric PyWFS, the modulation effect is not reduced. To avoid that we have proposed a 2path sensor with a sensor dedicated to petalometry by using an unmodulated PyWFS. The question to consider now is what kind of sensor to use in this petallometer and how to improve its measurement of petals.

4 Strategy to allow petal measurement with a pyramid

It was shown in Chapter 3 that the modulated PyWFS is not sensitive to petal mode whereas the uPyWFS is. In this chapter, we study the sensitivity but also we analyze how well the petal mode is reconstructed by the unmodulated PyWFS. In particular, the first question is whether the unmodulated PyWFS is a good petalometer and how we can improve it.

4.1 uPyWFS as 2^{nd} path petalometer

4.1.1 uPyWFS linear response to petal modes

From the sensitivity plots presented in chapter 3 3.3b, we know that the uPyWFS is sensitive to the petal mode. But sensitivity only tells us that petal mode creates linear intensities, it does not show whether this signal can be easily inverted. One way to test whether the signal is usable is to plot the linearity of the uPyWFS to petal mode to assess the dynamic of the petal mode. The difference with the linearity curve of Chapter 1 is that the linearity curve presented here is measured in the presence of an additional static phase mode ϕ_{res} in the next section. In particular, we aim to determine the relation between the petal in the entrance phase (residual of the first path in our $2-$paths system) and the measurement of petal mode. We use the linear reconstruction presented in Chapter 1.

$$\widehat{a_{pet}} = f(a_{pet}, \phi_{res}) \tag{4.1}$$

For the petal mode alone the result is known from Esposito et al. (2003) and we should have

$$\widehat{a_{pet}} = sin(a_{pet}) \tag{4.2}$$

For a_{pet} the amplitude in rad RMS. This formula also describes the phase wrapping which appears in the PSF as showed in Chapter 2.

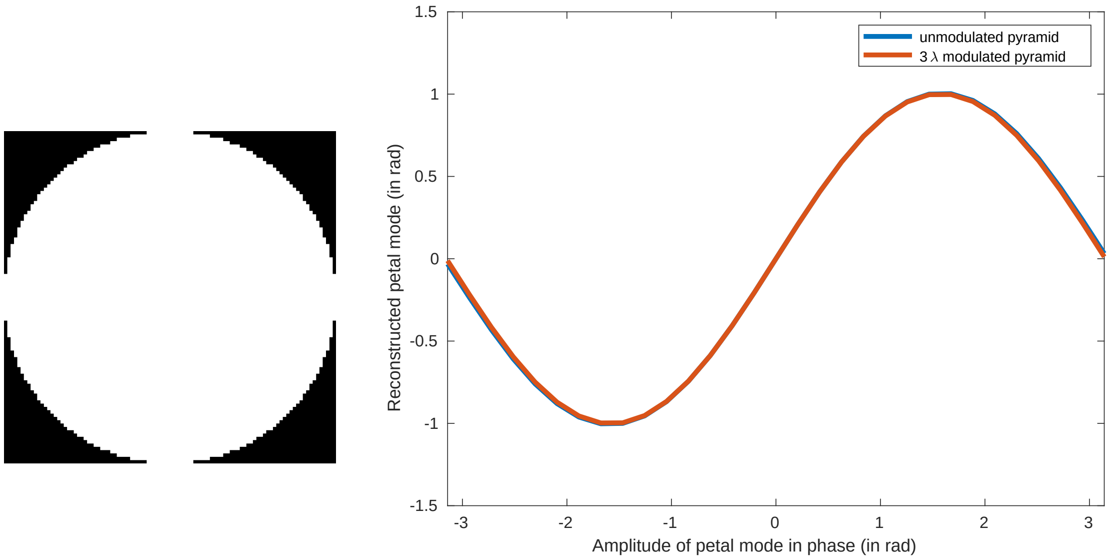

(a) Unobstructed pupil

(b) Linearity curve of petal mode alone for unobstructed pupil

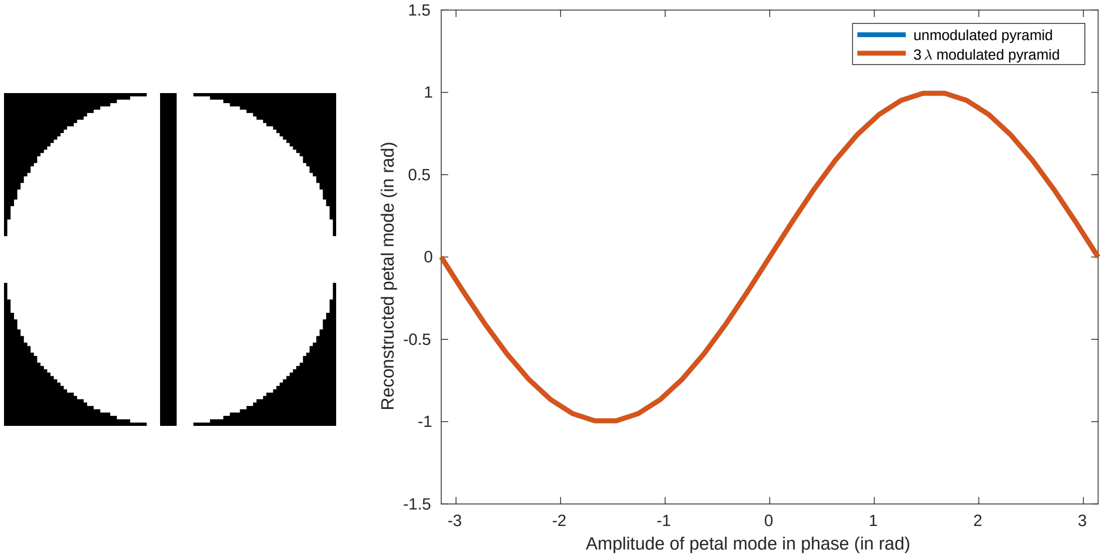

(c) Unobstructed pupil

(d) Linearity curve of petal mode alone for toymodel pupil

FIGURE 4.1 – Linearity curve for unobstructed pupil and toymodel pupil

As the modulated PyWFS is supposed to have a larger dynamic range than the uPyWFS for classical phase modes (like Fourier or Zernike) the linearity should be different (as was shown in chapter 1 on Figure1.19). However, the dynamic range for the petal mode is defined by the mode itself for a monochromatic sensor. The linearity range is the same as shown in Figure 4.1 (line for uPyWFS and PyWFS are superimposed). As shown in Chapter 3 the modulated PyWFS has a small sensitivity to petal mode and would not be a good petalometer. However, the sensitivity has no effect on linearity curves as the loss of sensitivity is compensated by the inversion of the signal. As the first question that arises when making a linearity plot is whether the result is the same with a modulated pyramid, we plot it in this case. The linearity curves presented in this chapter have been reproduced with the slopes map method (see chapter 1 1.33) for the test and have given the same results as reduced intensities. The way to process pixels (slopesmap or reduced intensities) does not have any impact on the quality of reconstruction here.

4.1.2 uPyWFS petal measurement in the presence of residuals

To push further the analysis, we test the linearity of the petal mode reconstruction in the presence of SCAO residuals. Residuals were created by simulating a closed loop using the parameters listed in table 2.1. Essentially we are testing the petalometer measurement of the system in Figure 4.2 as if we don't close the loop of the petalometer path in the 2-path system.

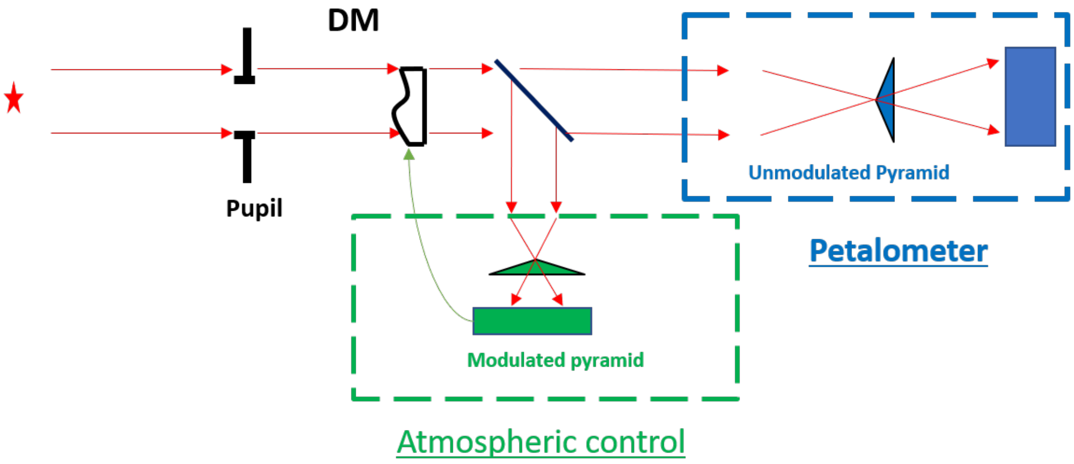

FIGURE 4.2 – Optical layout of the linearity test. We have a first AO loop of 'atmospheric control' to test whether a petalometer can measure the petal mode with 1st path residuals present

This First AO loop is a standard one as presented in Chapter 1 using a full monolithic pupil to avoid the apparition of petal mode. We want to reproduce the linearity curves as in Figure 4.1b but with a static residual phase ϕ_{res} added on top of the petal mode. To keep the linearity curve comparable, we subtract any petal mode present in ϕ_{res}. In this case we simulate the PyWFS intensity $I(a_{pet} \times \phi + \phi_{Res})$ use Cmat to estimate $\hat{a_{pet}}$ and plot $\hat{a_{pet}} = f(a_{pet})$ with a_{pet} varying between $[-\pi : \pi]$.

The resulting linearity curves are very different between the unobstructed pupil and toymodel case as seen in Figure 4.3. In the unobstructed pupil case we see mostly the OG (Figure 4.3b) g which reduce the amplitude of the reconstructed petal mode. We can make a separation here between the optical gains coming from all the other modes present in the residuals g, and the optical gain coming from the petal mode itself, the sin function (see 4.2).

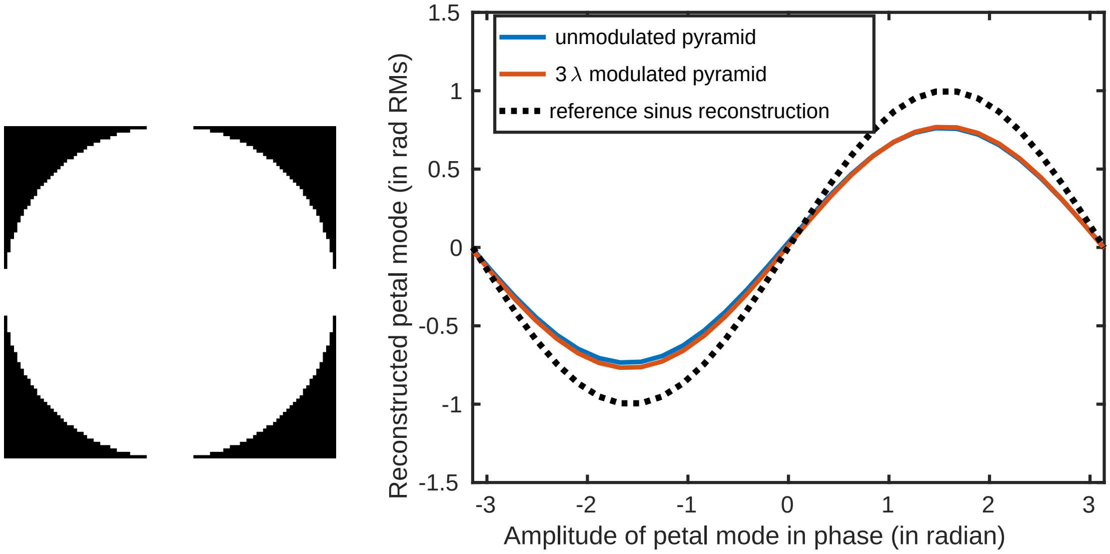

(a) Unobstructed pupil

(b) Linearity curve of petal mode in presence of AO phase residuals for unobstructed pupil

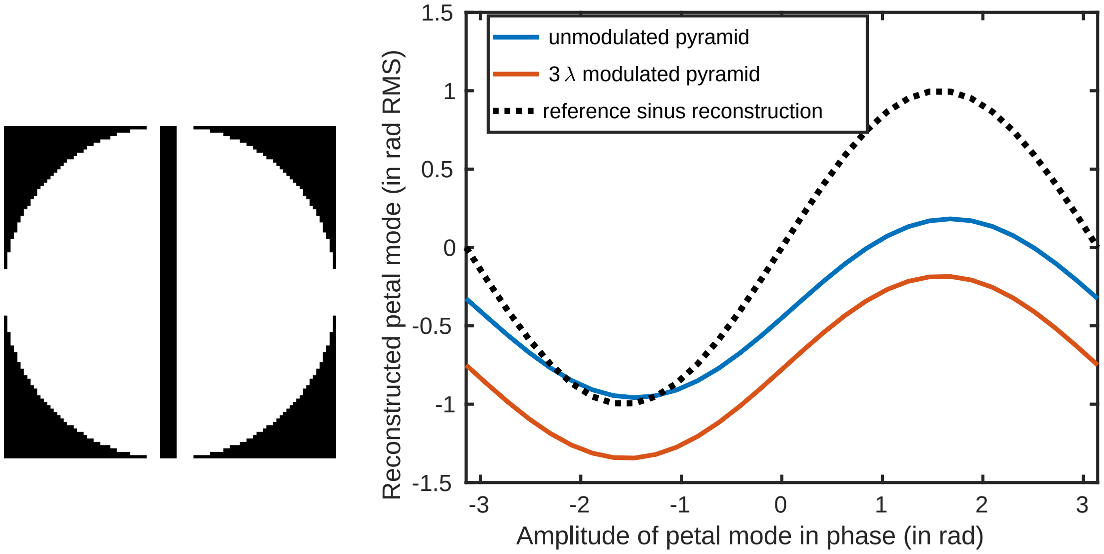

(c) Unobstructed pupil

(d) Linearity curve of petal mode in presence of AO phase residuals for toymodel pupil

FIGURE 4.3 – Linearity curve in presence of AO phase residuals for unobstructed pupil and toymodel pupil

$$\hat{a_{pet}} = g(\phi_{res}) * sin(a_{pet}). \tag{4.3}$$

In the presence of spiders, the linearity curves are displaced vertically. It means that the uPyWFS measures a petal mode amplitude when there is no petal mode in the phase, or another way to say it : it confuses another mode with petal mode. This confused mode is seen in the linearity curve as a fixed offset value added to the sinusoidal that we note c and call the "Petal Confusion". This could be a reference subtraction issue. To test that we made the linearity curve with different residuals shown in Figure4.4. The linearity curves each have a different c value, showing it depends on the atmospheric residuals.

$$\widehat{a_{pet}} = g(\phi_{res}) * sin(a_{pet}) + c(\phi_{res}). \tag{4.4}$$

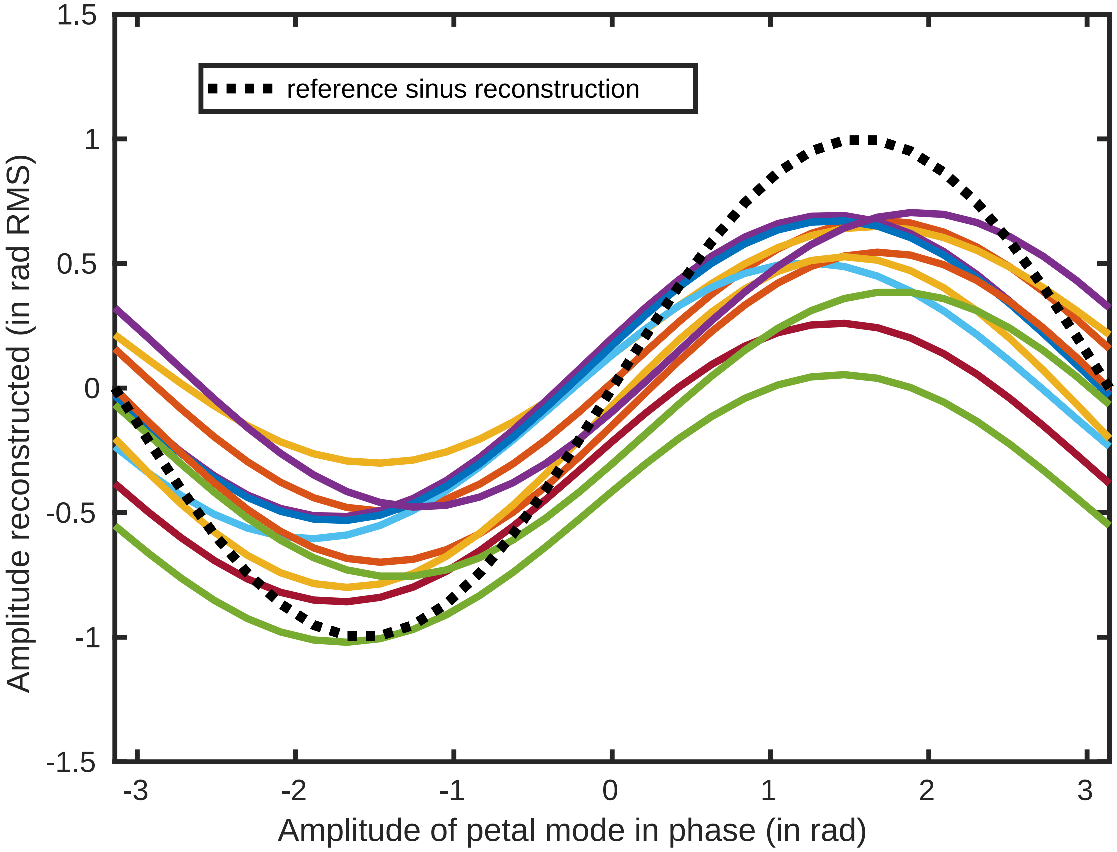

FIGURE 4.4 – Linearity curve with 10 independent residuals with uPyWFS

The typical amplitude of petal confusion c is a few tenths of rad RMS, which makes the value reconstructed by the PyWFS for a null input very far from the true value of petal (0 here). We need to understand this parameter to use the petalometer efficiently. Its existence was already reported in Bertrou-Cantou et al. (2022), in particular for the Zernike WFS. c is computed by taking the mean of the linearity curve. There is also sometimes a term of dephasing appearing, the term d in equation 4.5. The first possible origin of this dephasing would be a petal mode in the residuals, but in this simulation, we made sure to specifically subtract it. We consider it as another defect of the reconstruction. Examples can be seen with various residual on Figure 4.4.

$$\widehat{a_{pet}} = g(\phi_{res}) * sin(a_{pet} + d(\phi_r es)) + c(\phi_{res}). \tag{4.5}$$

Originally in the absence of residuals the relationship between the measured petal mode and the petal mode present in phase is only a sinusoidal. Adding a residual phase changes this relation in an expected manner by adding an optical gain (which only changes the amplitude of the sinusoidal and this effect seems independent to the presence of absence of spider). But adding the spider results in two new parameters making the measurement of the petal mode by a PyWFS less accurate : d and c, which depend on the residual phase. The following section will aim to study the parameter c in particular. We did not find an explanation for the d parameter in our studies and it is among the subjects needing further studies after this thesis.

4.2 Petal Confusion

4.2.1 Petal Confusion on petal measurement

As shown in the previous example, we identified a term that we named "Petal confusion" which acts as an offset on linearity curves. In Figure 4.4 it appears that the petal confusion value depends on the residuals. When looking at the linearity we can see some cases where the confusion c is higher than g. In that extreme case, there are no values of petal where the PyWFS measures 0 petal with a given residual phase screen. In terms of measurements, it is a very poor performance but is even worse when we consider in the closed loop aspect. A system with this no 0 phase measurement would diverge as the system would always issue commands to correct a false phase measurement. As the confusion phase seems to change quickly (each phase residual used in the plot of 4.4 is separated by 500ms) this case is probably uncommon. As for a few ms of timescale (which means a few iterations), the petal does not keep a stable value but pushes away from the 0 petal goal. With the λ ambiguity, this risks creating a jump from one value of petal to another with a $N\lambda$ difference.

4.2.2 Petal confusion identification

The goal of this section is to identify the origin of petal confusion. The first question is whether petal confusion is linear with respect to phase residuals. To test this hypothesis we plot the petal confusion 'linearity'. That is for a given residual phase screen, we compute the linearity of the PyWFS to the petal for different amplitudes of the same residual phase screen (in practice we multiply the residual by a scaling factor $s \in [-1, 1]$). From this linearity we compute the mean of the sinusoidal, this is the petal confusion value (we take the mean instead of the 0 value to avoid the impact of the dephasing). We plot $c(s \times \phi_{res})$

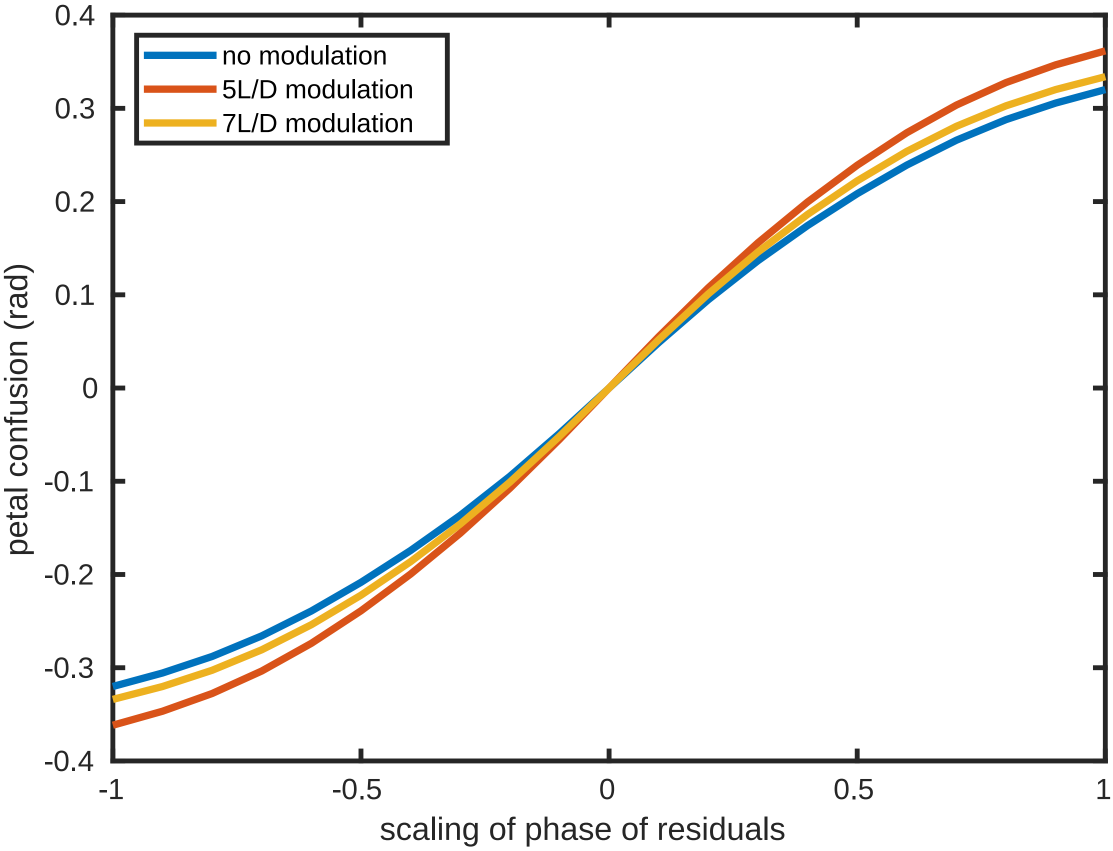

FIGURE 4.5 – Test of the linearity of petal confusion with residual phase. For the small phase, the petal confusion follows linearly the amplitude of the residual phase. Furthermore, the modulation doesn't seem to affect it, which means it's a high-frequency mode, higher than the modulation tested here.

This has been done for modulation = 0, 5 and 7 λ/D on Figure 4.5. This operation was repeated for 10 different residuals and the linearity has been averaged. We see a linearity plot very similar to a classical PyWFS linearity plot as shown in Chapter 1 (Figure 1.16). We see in particular a perfectly linear relation between the residual amplitude and the confusion for low amplitude. That implies that petal confusion comes from a given phase mode in the residuals. Furthermore, the modulation radius seems to have a low impact on the linearity plot. That would indicate that the petal confusion comes from a phase mode with high spatial frequencies and orthogonal to it in phase space (otherwise it would have been subtracted when petal was subtracted from the residuals), while it appears similar to petal mode in the PyWFS intensity space.

The next step is to try to reconstruct the shape of this petal confusion phase mode. To that end, we measure how much each pixel creates confusion. As the effect is linear, the value of confusion of each pixel can be summed to create a 'confusion map'. This phase map should be the phase mode which creates the petal confusion effect. The procedure is as follows : Create a phase screen with $\phi_{i,j} = 0$ except 1 pixel at coordinates $[x, y]$ at a very low amplitude $a_{x,y}$ (we take $a_{x,y} = 0.01$ rad for implementation). This pixel is then orthogonalised to the petal mode otherwise we would just reconstruct the petal mode. The final result is shown on figure 4.6a

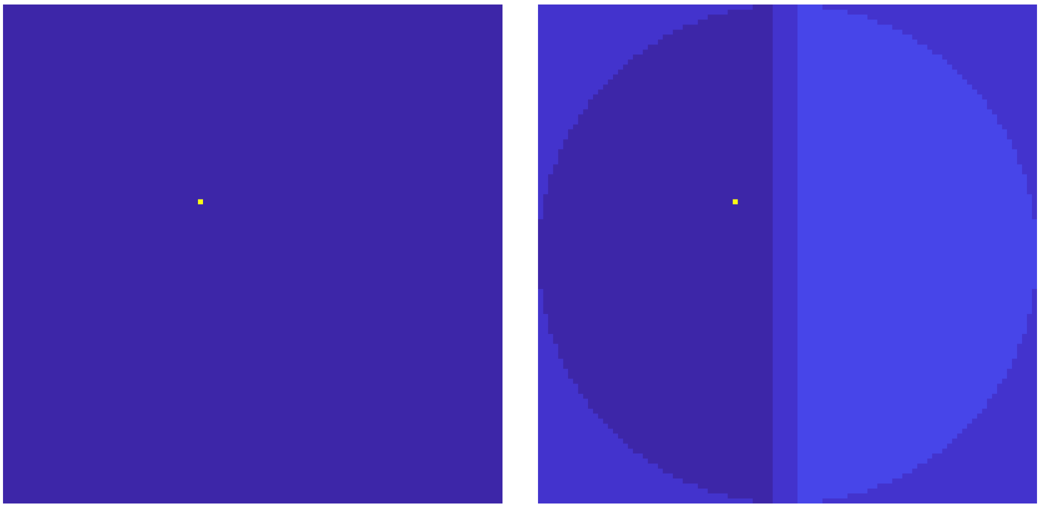

(a) Phase 'residual' for pixel [40,40]

(b) Phase of pixel [40,40] after orthogonalization to petal mode (orthogonalisation exaggerated to make the petal visible)

FIGURE 4.6 – Phase used for petal confusion map construction

We use it as a residual phase screen to compute the linearity plot and in particular the petal confusion $c_{x,y}$ associated with this pixel (as shown on Figure 4.7). As we push using only one pixel the resulting $c_{x,y}$ is very small. We compute the mean of the sinusoidal to avoid any effect of a dephasing of the sinusoidal linearity.

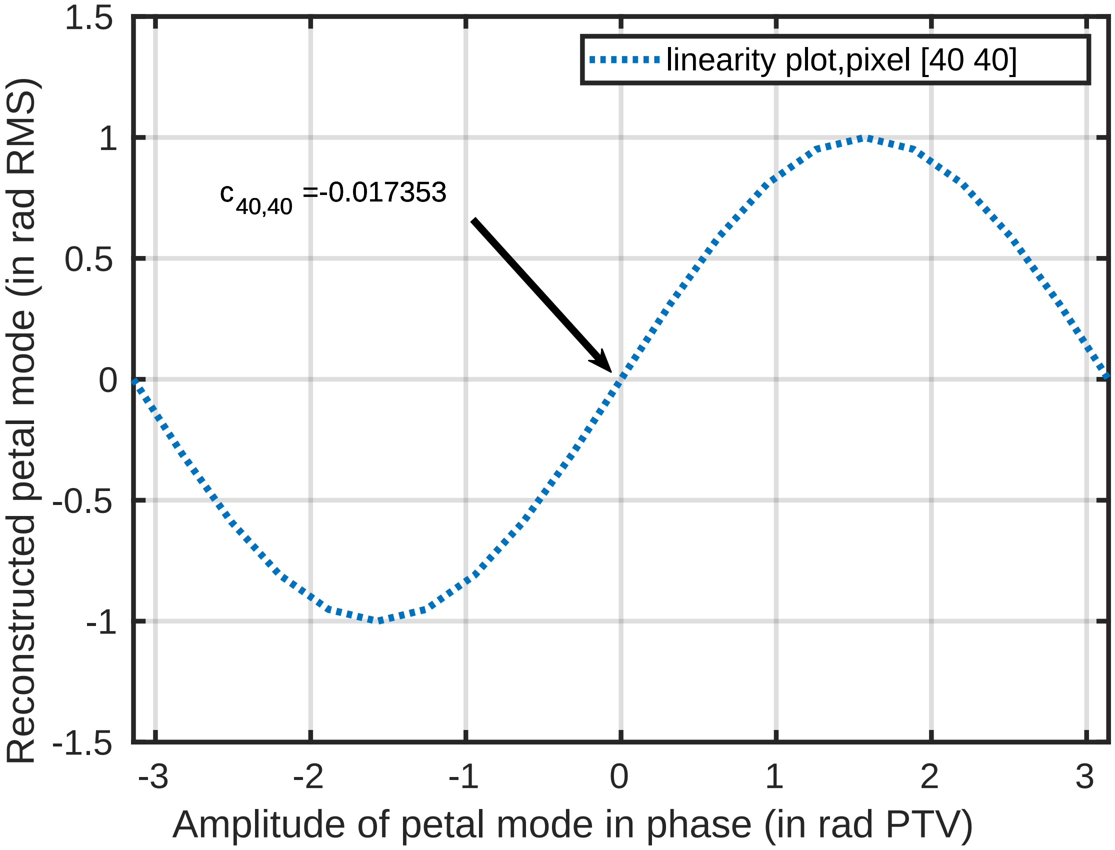

FIGURE 4.7 – Linearity plot for pixel 40,40. Petal confusion is highlighted

Once it is done for every pixel we plot the 2D map of $c_{x,y}/a_{x,y}$. The confusion map for the toymodel is plotted in Figure4.9a with a horizontal cut of the map. We see on this confusion map 2 different signals : a low frequency signal (3 λ/D quasi sinusoidal) very reminiscent of the petal orthogonalized with the 30 first Zernike modes shown in Chapter 2. And a high frequency signal concentrated on the limit of the pupil, the spider in particular.

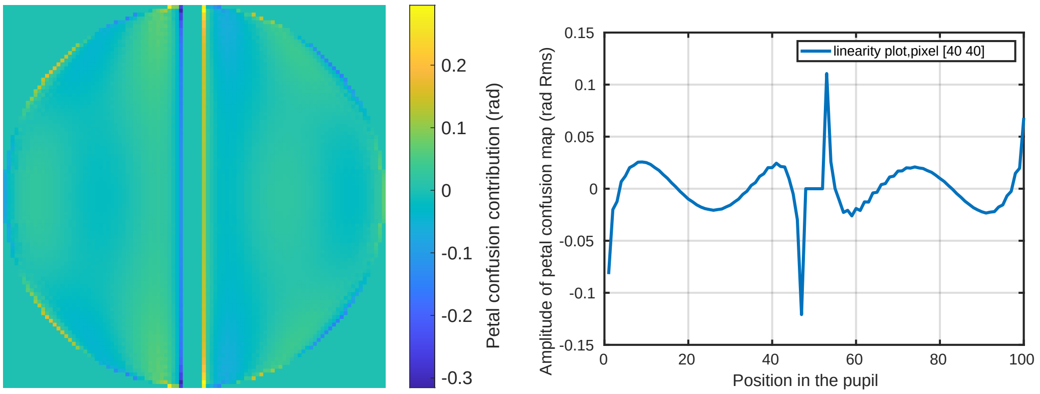

(a) Petal confusion map for toymodel pupil with petal + 30 Zernike Imat

(b) Horizontal cut of petal confusion map

FIGURE 4.8 – Petal confusion map

We see that the petal confusion reaches 0.12 rad at the border of the spider. That means that for 1 radian of phase in these pixels even with a phase orthogonal to petal mode we measure 0.12 rad of petal. It means that any discontinuity modes appearing around the spider is reconstructed as petal by the PyWFS. This confirms the problem raised in Chapter 2 for the unmodulated pyramid as well. the petal confusion mode can be seen as a generalisation of the discontinuity mode.

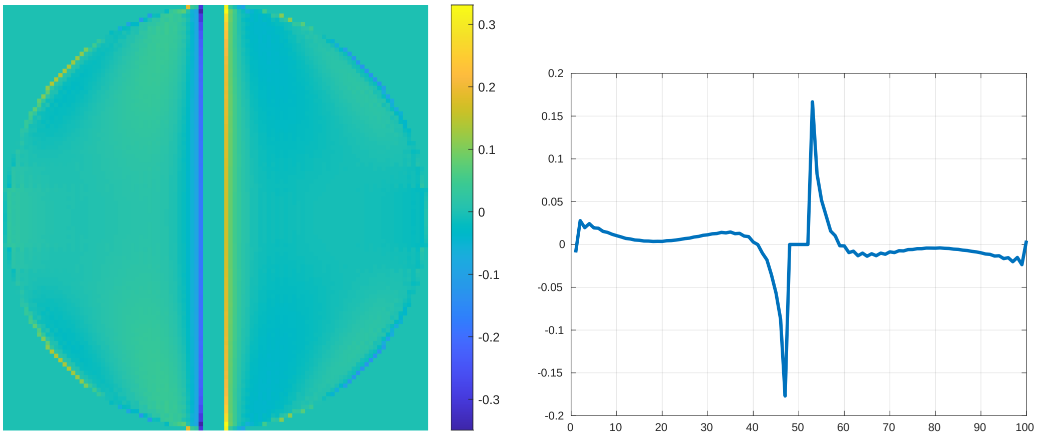

(a) Petal confusion with petal orthogonal to 30 first Zernike subtracted. The low frequency signal has been reduced while the spider signal remains

(b) Cut of Petal confusion with petal orthogonal to 30 first Zernike subtracted, the discontinuity has been increased

FIGURE 4.9 – Petal confusion with petal orthogonal to 30 first Zernike subtracted. The low frequency signal has been reduced while the spider signal remains

On Figure 4.9 we show the difference between the petal confusion and the petal orthogonalized with Zernike presented previously (Figure 2.14c) where both have been normalized to an amplitude of 1 rad RMS. The spider limit signal is amplified while the low frequency signal is reduced. While the low frequency residual is expected due to the reconstruction matrix using said 30 Zernikes, the high frequency is a surprise. Such effects were already found by Bertrou-Cantou (2021). Contrary to the petal orthogonal to the first Zernike, it is only the band of pixels around the spider that take large values and appear as the cause for petal confusion. Petal confusion is dependant on the number of modes controlled in the interaction matrix. In Figure 4.10a we show the petal confusion computed for the interaction matrix with more or less Zernike modes. On Figure 4.10c we show the petal confusion if the interaction matrix contains the DM Gaussian actuators + petal. The spider bands are always appearing though their intensity can change a lot. To satisfy the 'orthogonal to petal' condition of this mode, the spider band cannot be alone and other modes need to be present as he discontinuity around the spider alone would project on the petal mode. The 100 Zernike seems to be the best to reduce the apparition of these supplementary modes.

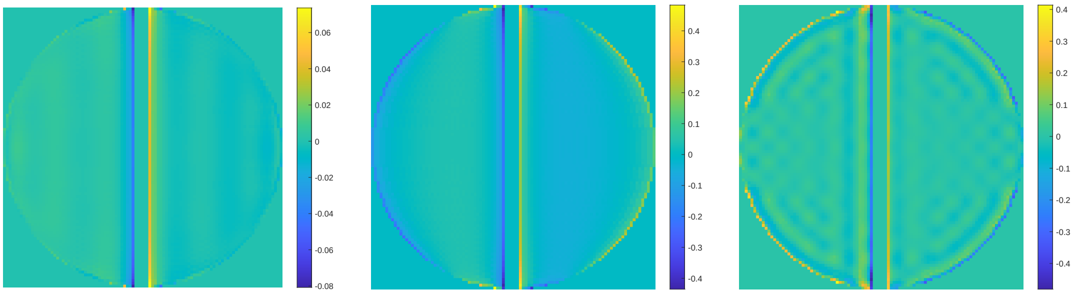

(a) confusion map made with Petal+100 Zernike in Imat

(b) confusion map made with Petal+3 Zernike in Imat

(c) confusion map made with Petal+ Gaussian DM (20x20) in Imat

FIGURE 4.10 – Change of the petal confusion map for different modes calibrated on top of the petal in the Interaction Matrix. In particular, we see that the 100 Zernike Imat has the smallest confusion.

4.2.3 Validation of petal confusion identification

To confirm that the identified mode is indeed petal confusion we made the computation of the petal confusion in Figure 4.11 with 2 methods : - in Blue, we compute the projection of the petal confusion map on in the phase residuals (same residuals as in part 4.1) for each iteration (very fast method).

- in Red, we compute petal confusion of the linearity plot associated with each frame (very slow method).

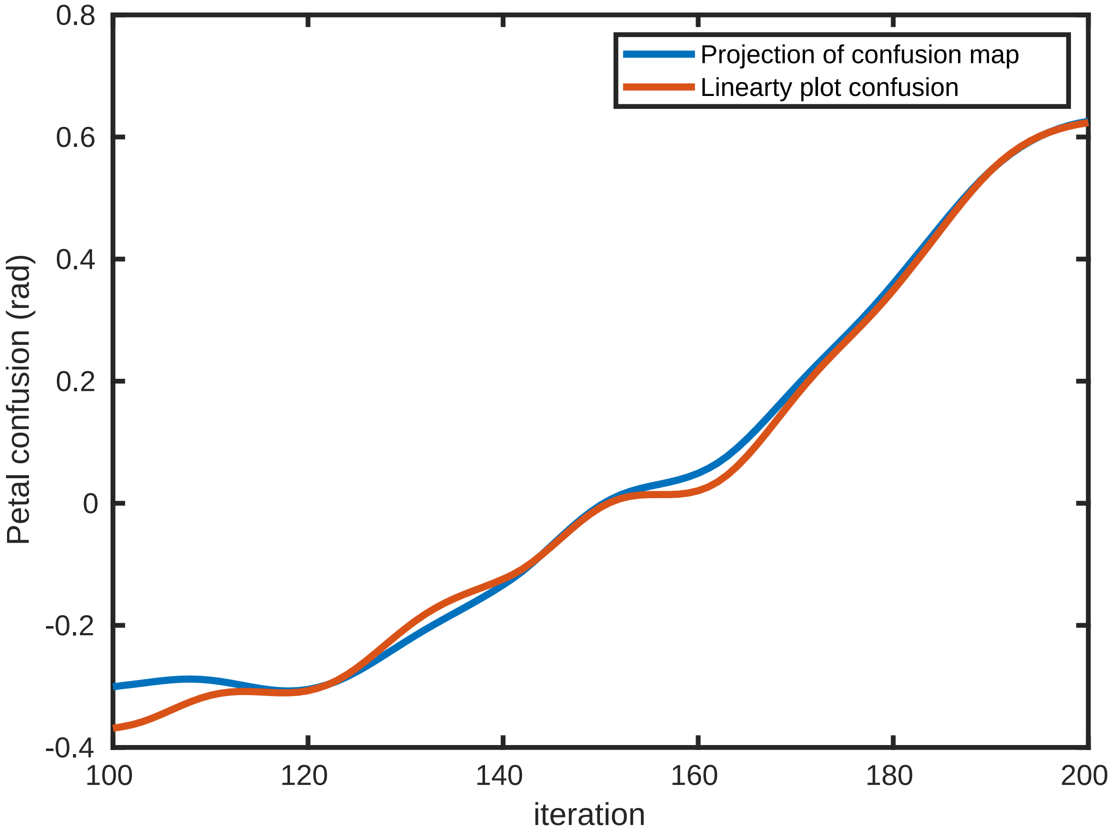

FIGURE 4.11 – Comparison of petal confusion between confusion map projection and linearity plot petal confusion. As the linearity plot petal confusion is prone to optical gains differences between the two are not unexpected

At each iteration both values are very close (the difference probably comes from the optical gains on the petal confusion mode in the linearity plot case). We can conclude that we have found the culprit of petal confusion. This mode is problematic as it is a very high frequency mode that the DM cannot completely correct.

4.2.4 Confusion and optical gains

The petal confusion mode can be present in value ranging in the tenth of rad. As we see in the linearity plot it is an effect added independently from optical gains (if anything, optical gains reduce petal confusion). Optical gain control is a common practice to improve phase reconstruction by PyWFS. If it is done it would mean using the equation :

$$a_{Rec} = \hat{a}/g_i = sin(a) + (c_i)/g_i \tag{4.6}$$

With a_{Rec} the reconstructed amplitude. The petal confusion is amplified by the optical gain compensation. It is a general problem with optical gain compensation which can decrease the accuracy of reconstruction if the non linearity appears in the signal not only as optical gain but also as modal confusion.

To allow an accurate measurement of the petal mode it seems important to reduce the effect of the residual on the petal mode measurement. There are different ways proposed for that :

- As it comes from the atmosphere, long integration averages petal confusion out
- Going to a longer wavelength reduces the phase of the atmospheric turbulence.

The longer integration solution is not compatible with the ELT case as the minioning (and possibly mirror dephasing) can vary fast and need an accurate measurement at the same rythm as the AO loop. Detectors are much more efficient in the visible than in IR in terms of noise. That makes using the longer wavelength an issue because it's noise that limits the magnitude of the star usable for SCAO. The science path is also usually more interested in IR photons.

These solutions aim to reduce the effect of phase residuals which seem to be the origin of the problem of petal mode measurement. As we saw in Figure 2.15a, most of the energy of the residuals is in the high spatial frequency. The petal confusion in particular is concentrated in the high frequency with the discontinuity mode. Meanwhile, the petal mode has most of its energy in the lower spatial frequencies. Adding a step to reduce selectively the high spatial frequency signal and keep the lower frequency should improve the petal measurement . **This leads us to add a spatial filter in a focal plane to see if that improves the measurement of the petal mode.**

4.3 Spatial filtering : effect on phase

In this section we test the effect of filtering on phase alone. The aim is to see whether it is possible to filter selectively the residual or the petal mode before adding the sensor which measures the phase. The next tests are made with the following optical 'system' (Figure 4.12). We start with the phase in the pupil plane, we focus the light in a focal plane, we add an amplitude mask, the Spatial Filter (SF), and finally, the light is propagated into another pupil plane where we study the phase (as if we had a perfect sensor in this pupil plane).

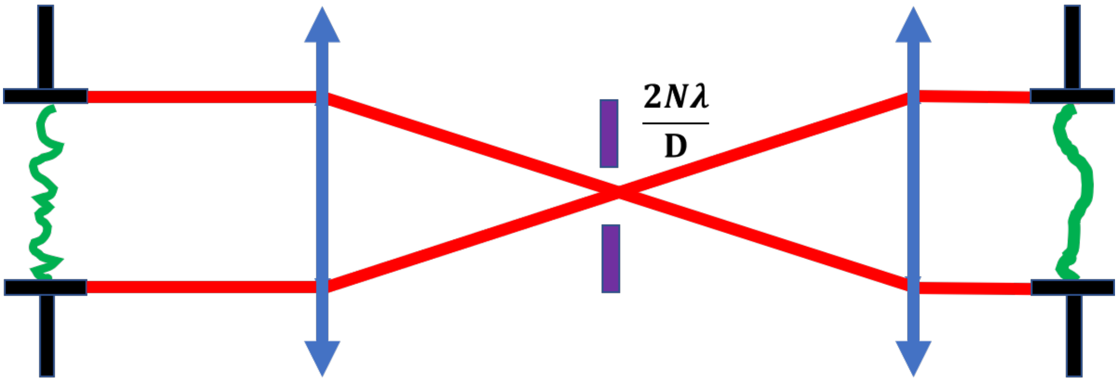

FIGURE 4.12 – Optical path used to assess the impact of a spatial filter on the phase

4.3.1 Effect on phase map

Spatial filtering allows to reduce the residual selectively when measuring petal mode among 1st-stage residuals. Due to the correction of the AO loop, most of the residuals energy is in the frequencies higher than the limit of the correction frequency of the DM. The energy remaining at lower frequency is due mostly to the other error terms (see Eq 1.30). This organization by spatial frequency is visible in the PSF as presented in Chapter 1. So by adding an amplitude filter in the focal plane, we can reduce the residual without touching the heart of the PSF (where most of the petal mode energy is as shown in Chapter 2). In Figure 4.13 we show the effect of spatial filtering in phase space after passing through the spatial filter of different size. We compare the effect between a residual phase screen (same residual as for the linearity plot earlier in this chapter), a petal mode, and the sum of them. For the sum, both have been normalised to the same RMS amplitude (120nm RMS).

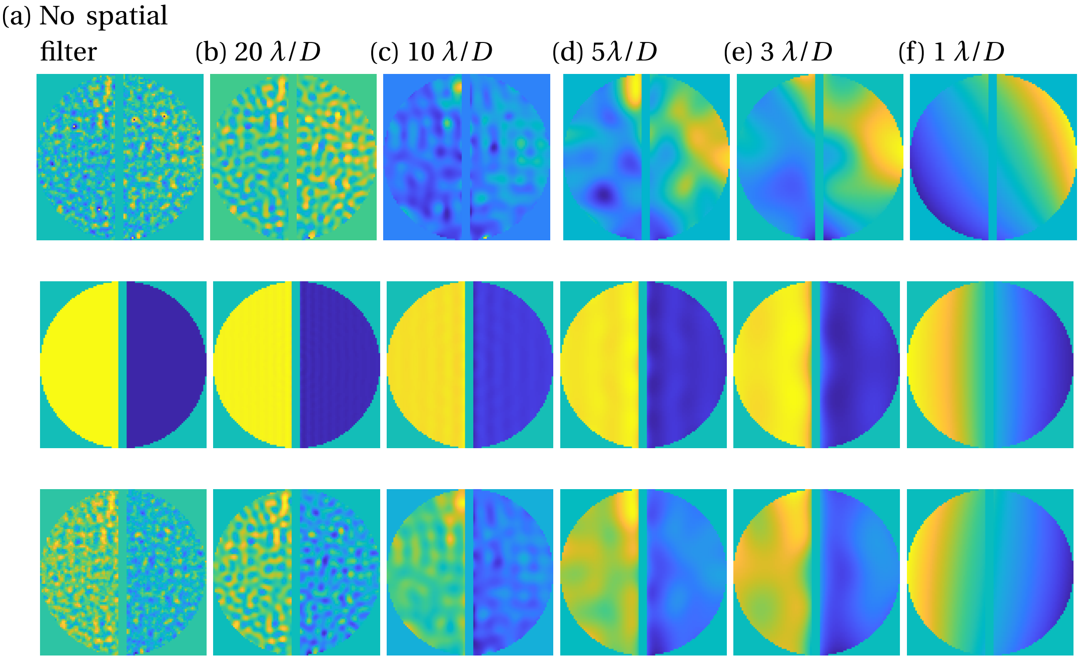
(a) No spatial filter (b) 20 λ/D (c) 10 λ/D (d) $5\lambda/D$ (e) 3 λ/D (f) 1 λ/D

FIGURE 4.13 – Effect of spatial filtering on pupil phase with 1st line : 1st path residuals, 2nd line petal mode, 3rd line sum of petal and residuals

We see that most of the energy or residuals are reduced when the SF gets smaller than the cutoff frequency of the AO loop (mostly dictated by the DM actuator number). The petal starts changing noticeably when the filter gets as small as $1\lambda/D$.

4.3.2 Effect on phase Power Spectral Density

Meanwhile the Petal has most of its energy in the lower spatial frequencies. As shown in figure 4.14 when comparing the PSD of petal and residual we see that at lower spatial frequencies, the petal mode actually dominates over the phase residuals. This PSD has been computed by averaging 100 residual phase screens and a petal mode of the same RMS amplitude.

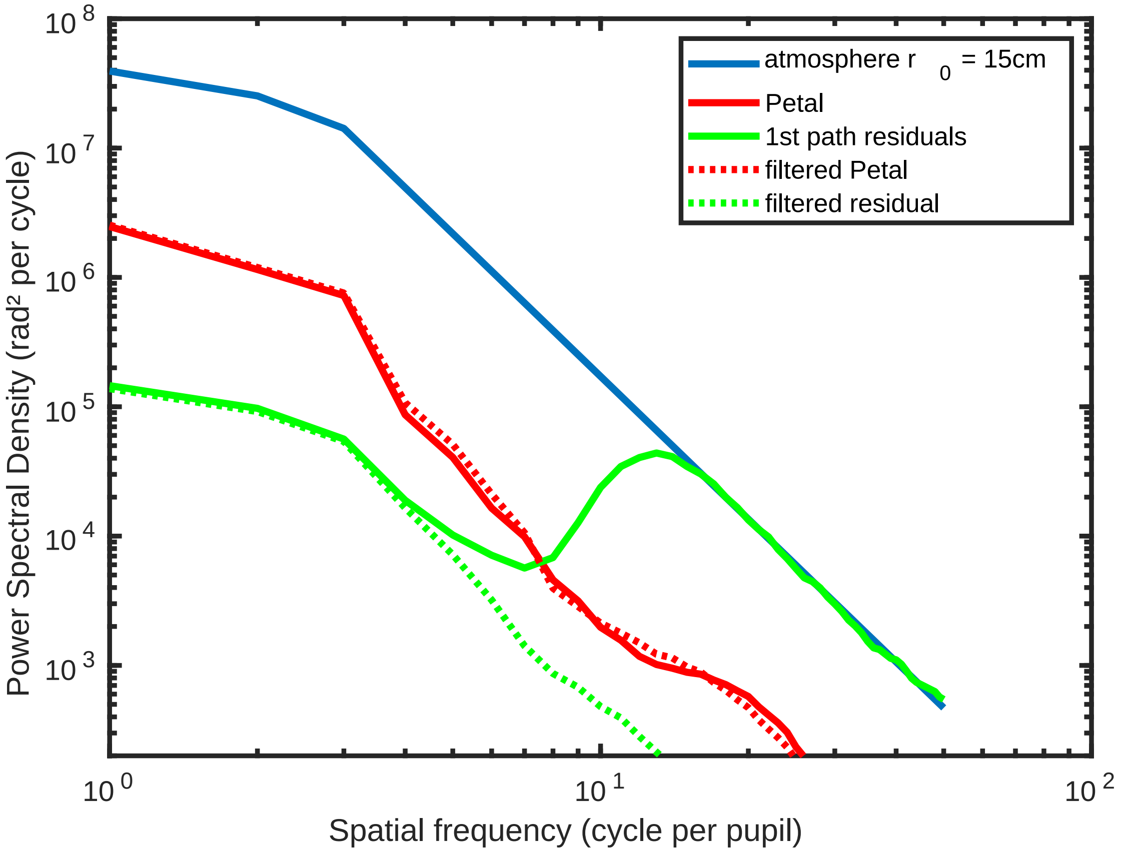

FIGURE 4.14 – PSD of atmospheric turbulence, 1s path residuals and petal modes. The dotted lines are for PSD after spatial filtering by a $5\lambda/D$ SF

When looking at the phase after filtering if the SF is small enough to cut the residual, the only mode that goes through is the petal mode. It is possible to cut the petal mode as well if one uses a very small pinhole but it happens for SF under the λ/D range where petal mode gets turned into its tip-tilt component.

4.3.3 Optimal filter size

We can consider the residual as a 'noise' for the measurement of petal mode and the petal as the signal we want to measure. We can define a Signal to Noise Ratio (SNR) between the petal mode and the residuals that go through. To compute this SNR, we compute the variance of 1st stage phase residuals after passing through the SF and the variance of petal mode with different SF sizes. It allows us to evaluate which SF size would be the most efficient for the measurement of petal mode.

$$SNR(SFsize) = \frac{\sigma^2_{petal}}{\sigma^2_{residual}} \tag{4.7}$$

To decide what is the optimal size of the SF, this SNR is the first parameter to consider, the other is the light lost to the filter. As the spatial filter pinhole gets smaller more light is lost, making a smaller pinhole less efficient for an AO system using limited light. In Figure 4.15 we show the two antagonist effects. There are 3 interesting values : for $1\lambda/D$, for $3\lambda/D$ and for $10\lambda/D$.With the spatial filter a $1\lambda/D$, we are at the maximum of SNR, but at the minimum of intensity which goes through the SF. With the Spatial filter over $3\lambda/D$, most of the PSF restored by the AO goes through, so there is less light to integrate by having a larger SF. Once we go over the $10\lambda/D$, the untouched atmospheric turbulence PSF starts coupling in. But at this same frequency, the SNR starts dropping fast. In practice, the $5\lambda/D$ value seems to be a good compromise.

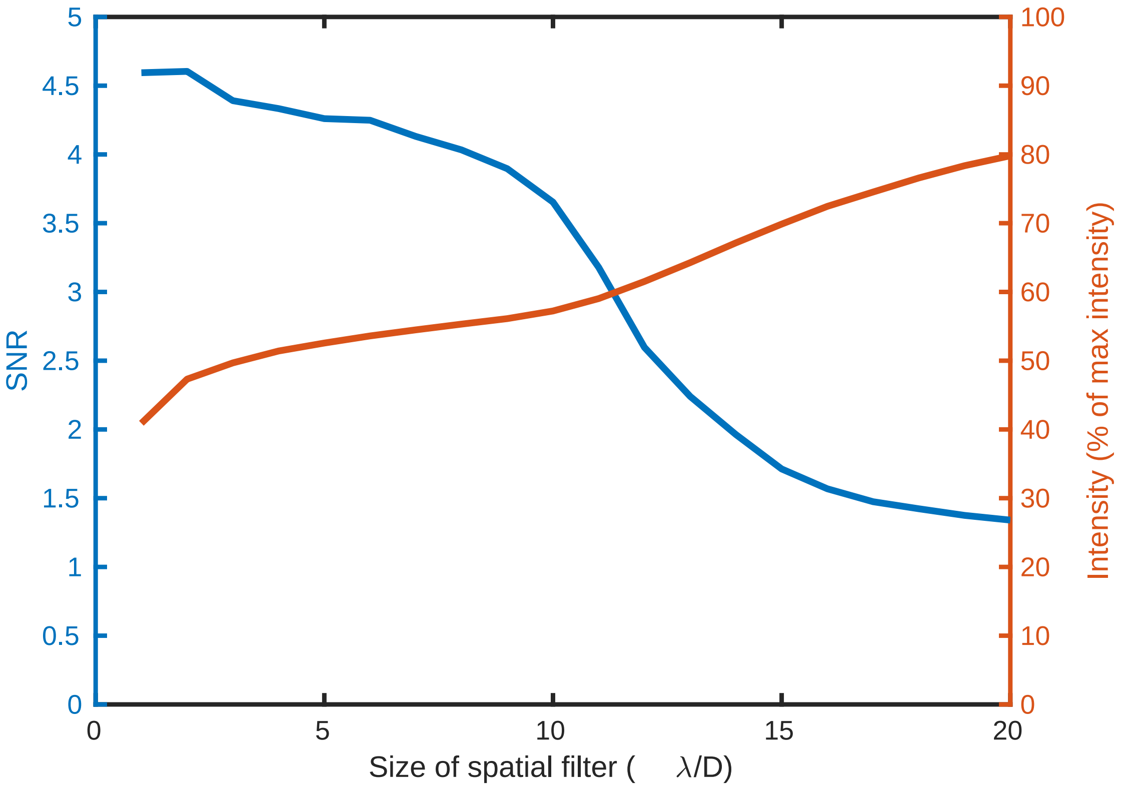

FIGURE 4.15 – Effect of spatial filtering on phase and intensity of light going through the spatial filter. With the size of spatial filter considered ($5\lambda/D$), the spatial filter causes a loss of half of light

As both the $\sigma^2_{residual}$ and the light concentrated at the center of the PSF depend on the correction level, the Figure 4.15 depends on the system and the atmospheric conditions. In particular, the cutoff spatial frequency of the DM used for atmospheric control will decide where the SNR drops to tend to 1, here with a 20x20DM, it's at $10\lambda/D$).

4.4 Spatial filtering : effect on the pyramid Interaction Matrix

4.4.1 Change of unmodulated pyramid signal

With a PyWFS there is already a guaranteed focal plane where we can place the pinhole to create the SF (in practice a field stop) : the tip of the pyramid. From a simulation standpoint, it just corresponds to adding an amplitude component to the phase mask of the PyWFS. This creates a new kind of sensor : Spatially filtered Pyramid Wavefront sensor (SF+uPyWFS) ; This sensor has very similar properties to the pyramid as the conditions exposed in Chapter 1 to have a linear wavefront sensor are still verified. But its behavior changes in particular in terms of spatial frequency sensitivity. It has an inverse behavior compared to modulation. While modulation impacts low frequency modes by reducing their sensitivity, spatial filtering impacts high frequency modes in the same way (although the reduction is much stronger). It works as a low pass filter for spatial frequencies essentially. This can be seen directly in Figure 4.16 where we plot the sensitivity of SF+PyWFS of different sizes (without modulation) for Fourier mode of different Spatial frequencies. As the filter gets larger the sensitivity tends toward the classical uPyWFS sensitivity.

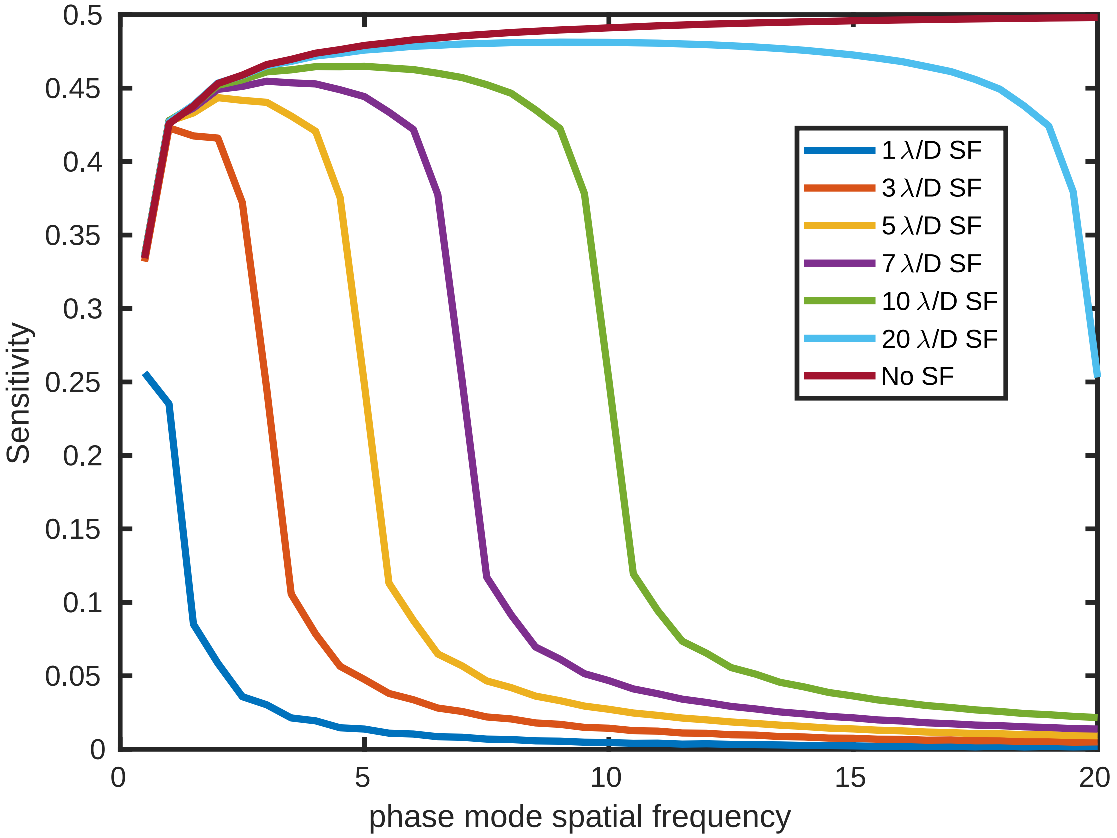

FIGURE 4.16 – Sensitivity of SF+uPyWFS to pure spatial frequency phase mode. The only effect of spatial filtering appears for spatial frequencies higher than the SF size where the sensitivity collapses

In Figure 4.17 we see the comparison between the sensitivity for the SF+PyWFS for the petal mode, a low frequency (3 cycles in the pupil) sinusoidal mode, and a high frequency (10 cycles in the pupil) sinusoidal mode (This Figure is to be compared to Figure 3.2 in chapter 3 which shows the effect of modulation on sensitivity).

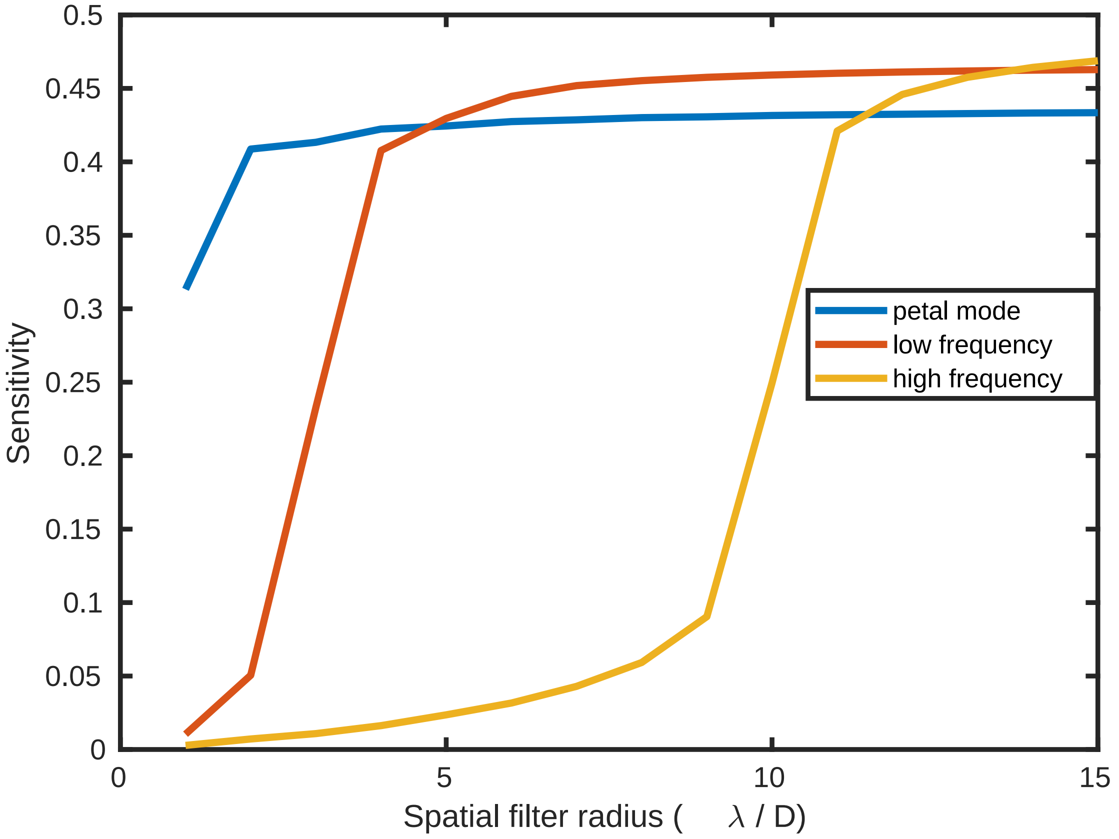

FIGURE 4.17 – Effect of spatial filtering on sensitivity of the SF+uPyWFS to a petal mode, a low (3 cycle/pupil) frequency Fourier mode, and a high (10 cycles/pupil) Fourier mode.

In Figure 4.19 we plot the reference intensity I_0 and $deltaI$ of petal mode for various spatial filter sizes. There is an interesting phenomenon happening in the reference intensity but even more in the δI of the petal mode. The spider can be considered as an amplitude signal with most of its energy over 20 cycles per pupil. So it is among the modes filtered. In the δI, we see that there is now a linear signal appearing in the spider area of the pupil, in particular, for the 1 and 3 λ/D

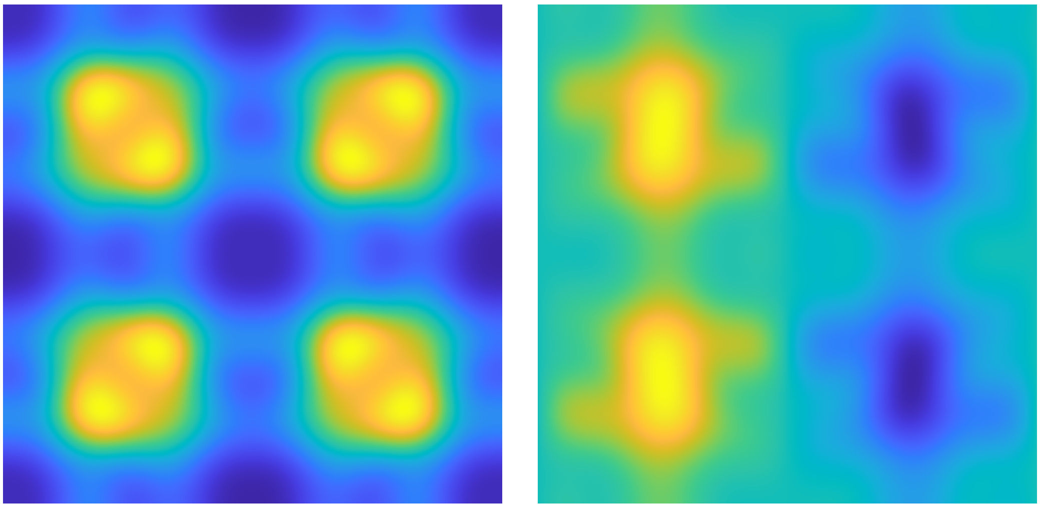

(a) I_0 and δI of petal mode for an SF+uPyWFS with a SF of $1\lambda/\mathrm{D}$

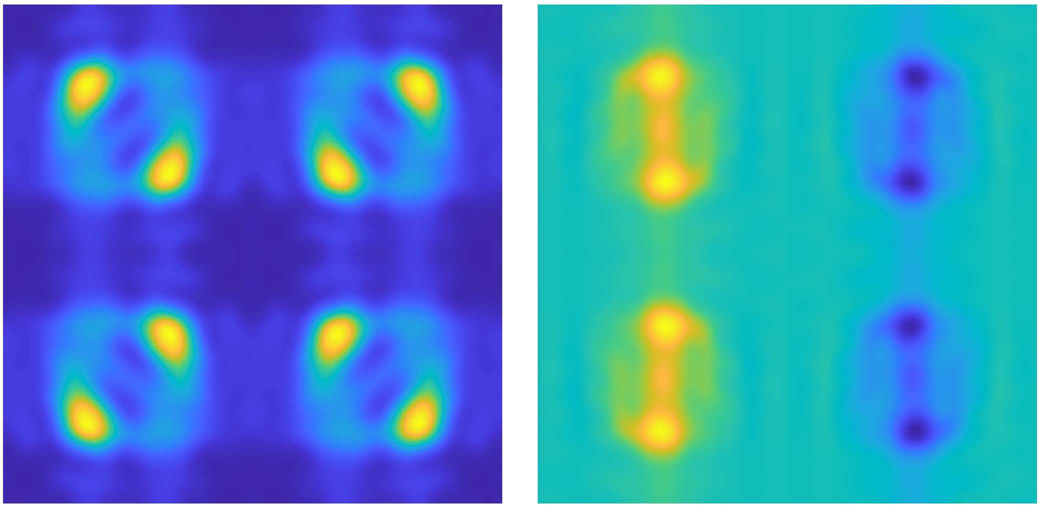

(b) I_0 and δI of petal mode for an SF+uPyWFS with a SF of $3\lambda/\mathrm{D}$

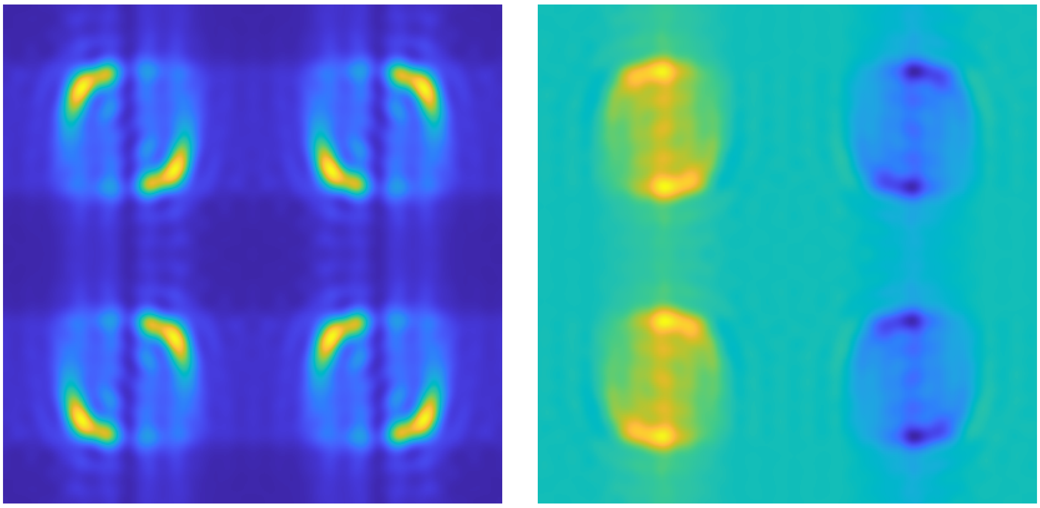

(c) I_0 and δI of petal mode for an SF+uPyWFS with a SF of $5\lambda/\mathrm{D}$

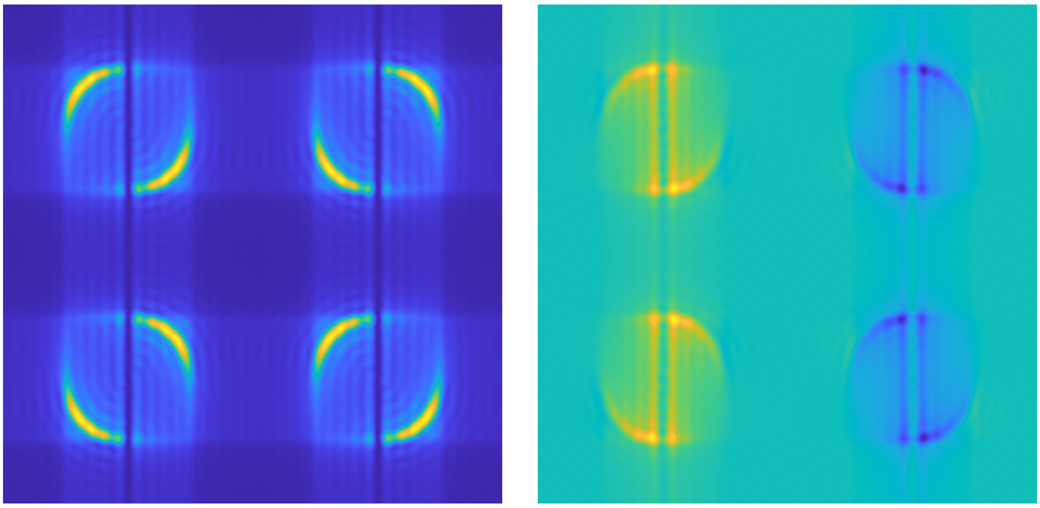

(a) I_0 and δI of petal mode for an SF+uPyWFS with a SF of $10\lambda/D$

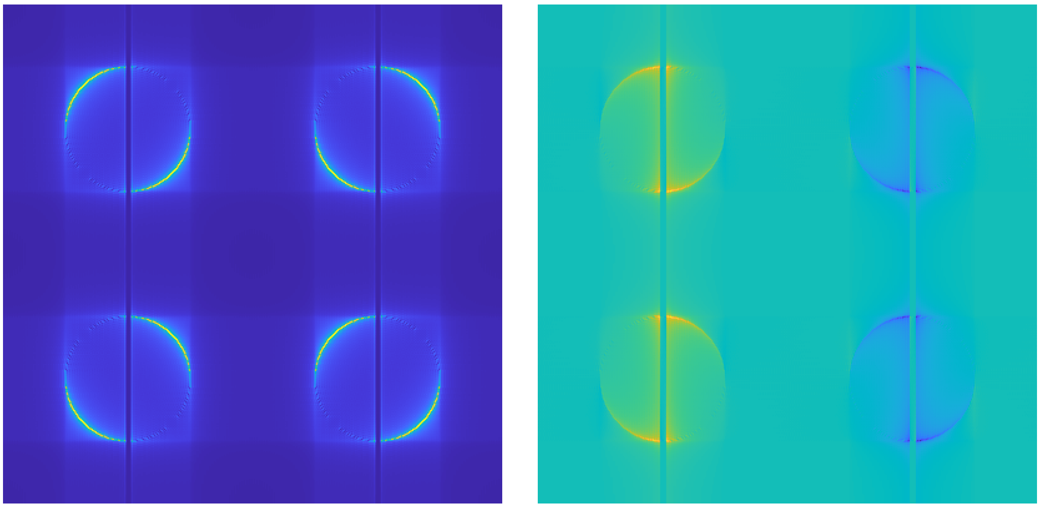

(b) I_0 and δI of petal mode for an uPyWFS with no SF

FIGURE 4.19 – Effect of SF on reference intensity I_0 and δI of petal mode for uPyWFS

As one of the effects of the SF is to reduce high frequency modes, the petal confusion map is greatly reduced with the SF+uPyWFS compared to the uPyWFS. In Figure 4.20 we show the petal confusion map for the SF+uPyWFS (with the previous confusion map of Figure 4.9a for comparison). As expected the high frequency signal has disappeared and the overall amplitude of the petal confusion map has been reduced.

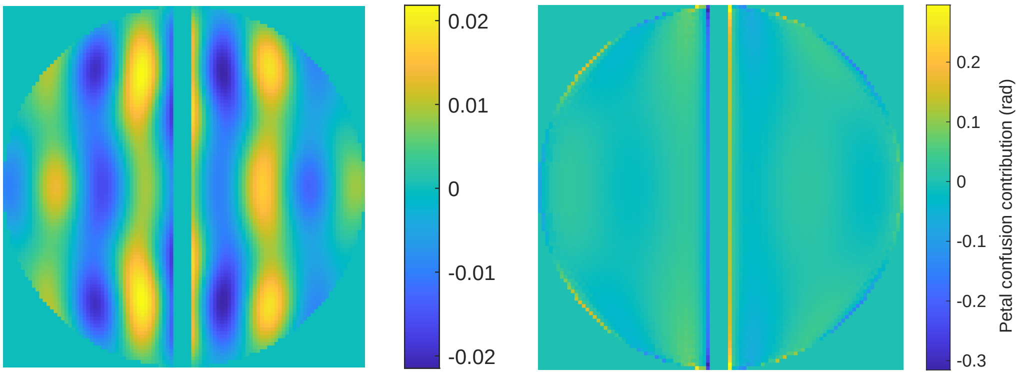

FIGURE 4.20 – Confusion map of SF+uPyWFS for a spatial filter radius of $5\lambda/D$ and confusion map without the SF reproduced for comparison

We see that the petal confusion has been greatly reduced, by a factor of 10 roughly, and what remains is mostly the low-order signal.

4.4.2 Change of modulated pyramid signal

Due to the small size of the spider compared to the telescope, its effect appears mostly in the high spatial frequencies as well. As such the spider could be filtered by the spatial filter as well, thus reducing its effect on the measure of the petal mode, which would be the most beneficial in the case of a modulated PyWFS. We made the same computation as in Chapter 3 Figure 3.1 with a modulated spatially filtered pyramid. It's more complicated to implement both in simulation and in practice as the SF must be in a focal plane before the modulation mirror in the optical layout. Spatial filtering in a focal point where the PSF is modulated risks cutting the modulation. We see in Figure 4.21f That there is indeed the same reappearance of intensity under the spider.

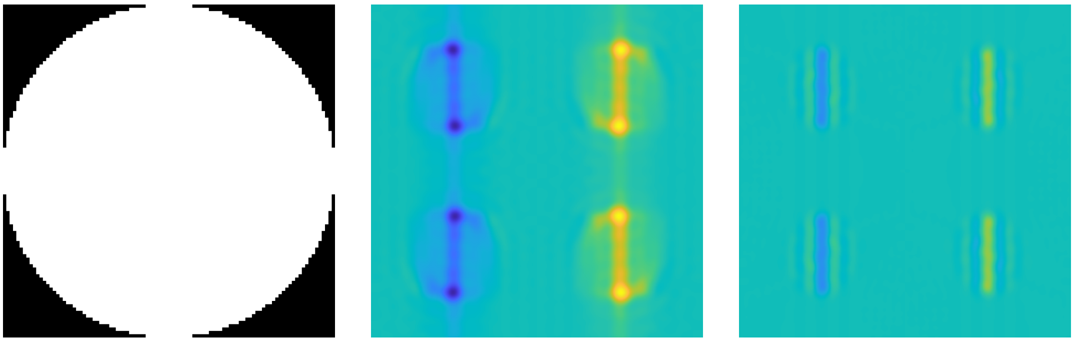

(a) Full monolithic pupil (D=10m)

(b) Fullpupil, SF ($5\lambda/D$) +uPyWFS

(c) Fullpupil, SF ($5\lambda/D$)+ $3\lambda/D$ mod PyWFS

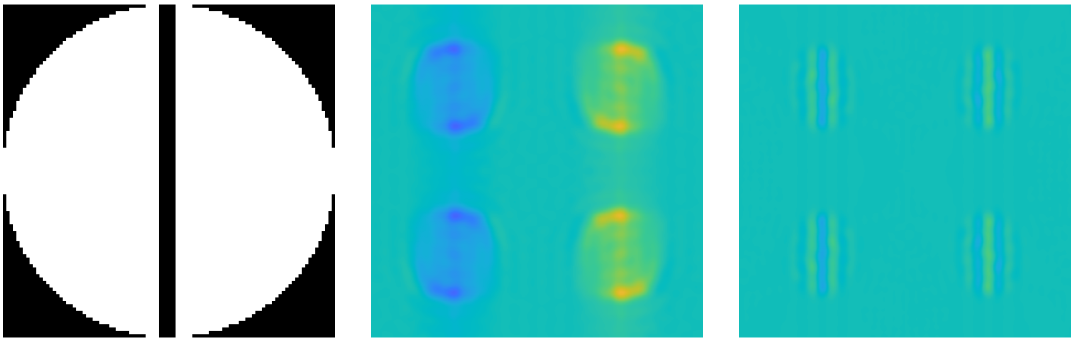

(d) Toymodel pupil (spider = 50cm)

(e) Toymodel,SF ($5\lambda/D$) +uPyWFS

(f) Toymodel, SF($5\lambda/D$) + 3λ/D mod PyWFS

FIGURE 4.21 – Change of petal mode δI with SF 5λ/D. All δI use the same intensity scaling. As the sharp edges of the spider represent high spatial frequencies in the pupil plane, the intensity gap is reduced in these reference intensities compared to the classical PyWFS reference intensity, allowing the δI to show signal under the spider

When looking at the sensitivity of the petal mode in particular we see that the previous phenomenon of loss of sensitivity with modulation radius is compensated by the Spatial filter filtering out the spider. this is particularly visible in Figure 4.22 where we redo the plot of sensitivity map as a function of the spider size and modulation radius as in chapter 3 (Figure 3.3a showing the petal mode with no spider is reproduced here for easy comparison). We see that the sensitivity to petal mode though it starts at a comparable value in the no modulation and no spider case (0.42 for the no spatial filter case, 0.40 with the spatial filter), drops significantly less with the Spatial filter than without. This spatially filtered modulated PyWFS could be used as an atmospheric and petal mode sensor.

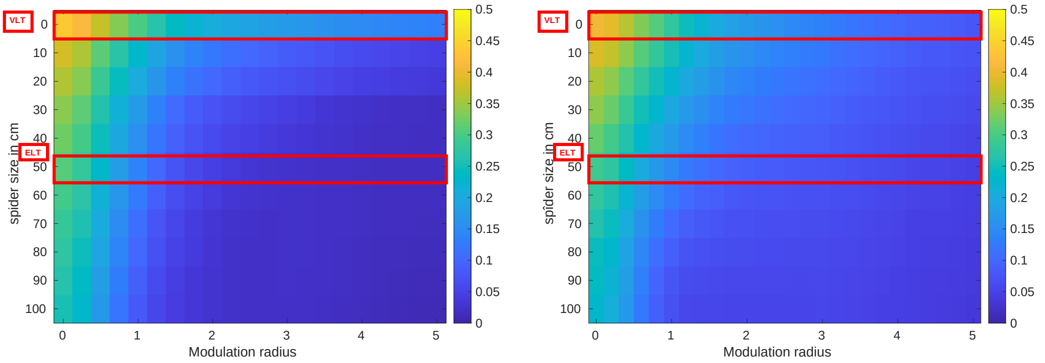

(a) Sensitivity to the petal mode as function of modulation radius and spider size without a Spatial Filter. The spider sizes for ELT and VLT are highlighted. The sensitivity at a $3\lambda/D$ is 0.17 for the VLT but 0.020 for ELT ($3\lambda/D$ is the suggested modulation radius for HARMONI). At $5\lambda/D$, the sensitivity is 0.13 for VLT and 0.017 for ELT-type spiders.

(b) Sensitivity With Spatial Filter (5λ/D radius). The Sensitivity at $3\lambda/D$ of modulation for the ELT spider is equal to 0.08, 4 times superior to the PyWFS without a spatial filter . At $5\lambda/D$, the sensitivity is 0.05 for ELT-type spiders, 2.5 times higher than without the spatial filter

FIGURE 4.22 – Sensitivity map of petal mode for a pyramid With and without Spatial Filter (5λ/D depending on the modulation radius and spider size.

What would be the interest of using a modulated pyramid in that case ? The only obvious advantage is a more linear behavior when residuals are added. When looking at the linearity plot the optical gains coming from residuals are smaller than with the SF+uPyWFS.

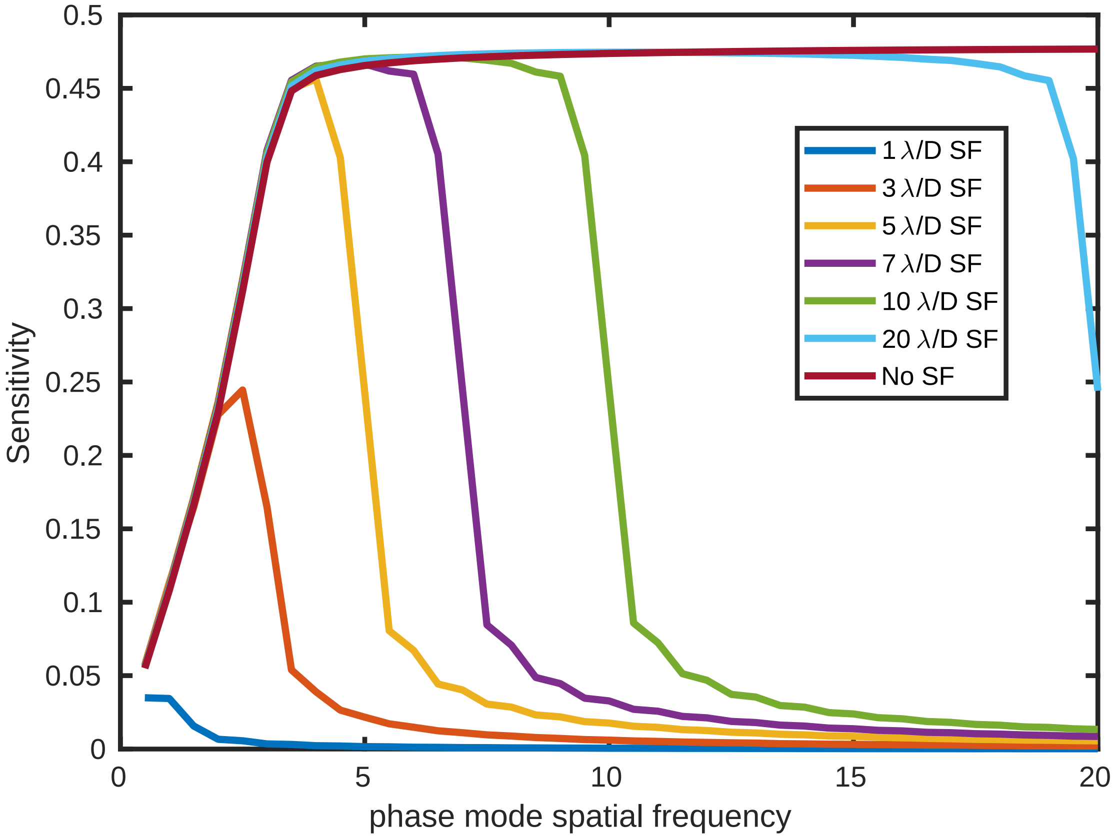

FIGURE 4.23 – Sensitivity of SF+3λ/DPyWFS to pure spatial frequency phase mode. The effect of the spatial filter and modulation seem decoralated as the sensitivity seems a product of the sensitivity of unmodulated with various sizes of the spatial filter and the 3λ/DPyWFS

The sensitivity of these Spatially filtered pyramids (Figure 4.23) shows that they are usable for any mode with spatial frequencies under the radius of the spatial filter. Tip tilt needs to be controlled though, as the intensity going through the spatial filter could fall sharply if the COG of the PSF is out of the pinhole. One could imagine having a first stage loop with tip tilt controlled before and a spatial filter radius corresponding to the cutoff frequency of the DM, allowing a good control of the PSF inside the radius and being less impacted by the residuals than a classical Pyramid.

4.5 SF+uPyWFS linear response to petal mode

We recomputed the linearity plot using a SF+uPyWFS shown in Figure 4.24 We see that the effects coming from the residuals, namely the optical gains and the petal confusion are greatly reduced.

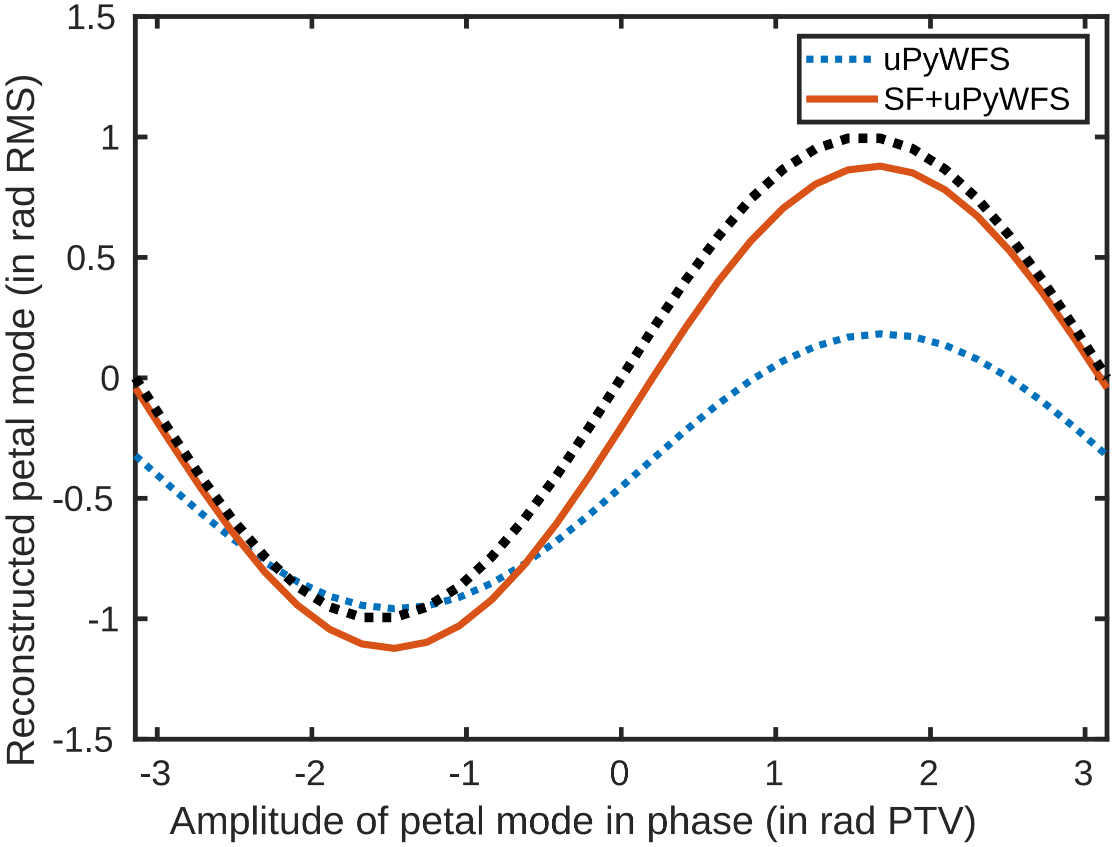

FIGURE 4.24 – linearity plot for a SF+uPyWFS. We see that the optical gain and petal confusion have been greatly reduced

In practice when averaging the change in petal confusion over 100 independent residuals, the petal confusion is reduced by a factor 6. It is to be noted that for the optical gains to reduce, the normalization must be done with the current intensity map, not the reference intensity. As the reference intensity has a perfect phase in simulation, all the light filtered by the SF as part of the residual is counted as optical gains. This step needs attention because a large instantaneous residual tip-tilt could filter out a significant part of the PSF and a division by 0 could occur in the ΔI computation, making the wavefront reconstruction overestimate the wavefront. It can already happen with the current setup as is attested by Figure 4.25 where we follow the optical gain present on the petal mode for various phase residuals by monitoring the amplitude of the linearity plot sinusoidal. You can see that the OG sometimes gets over 1. This test was made with the same residuals as the linearity test in Figure 4.4 but for each iteration of the loop.

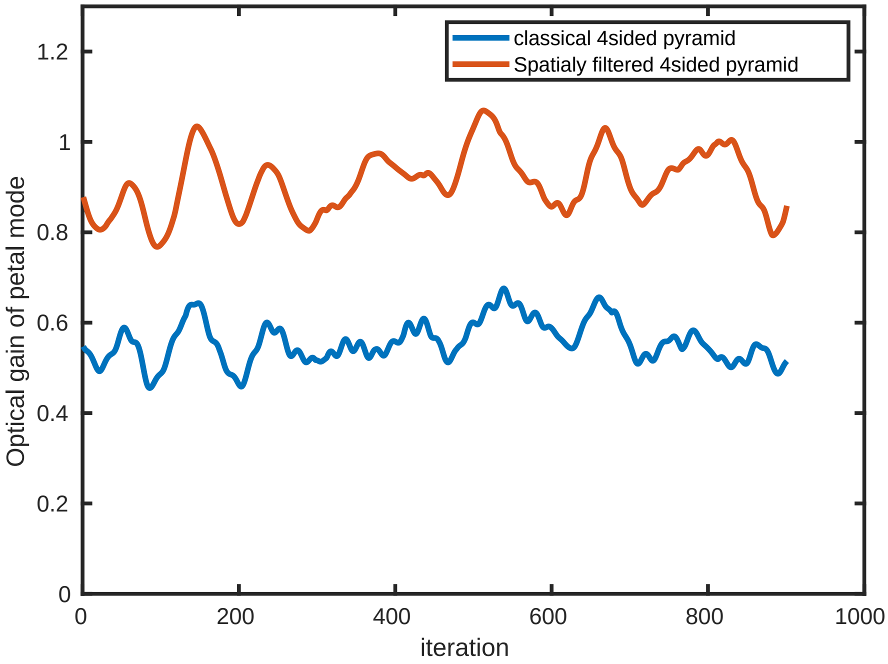

FIGURE 4.25 – Comparison of the OG on the petal mode with a classical 4sided pyramid and a spatially filtered pyramid. We see that the OG are much higher on the SF pyramid but also sometimes go over 1.

On Figure 4.26. We show the change in the linearity curve with independent phase residuals

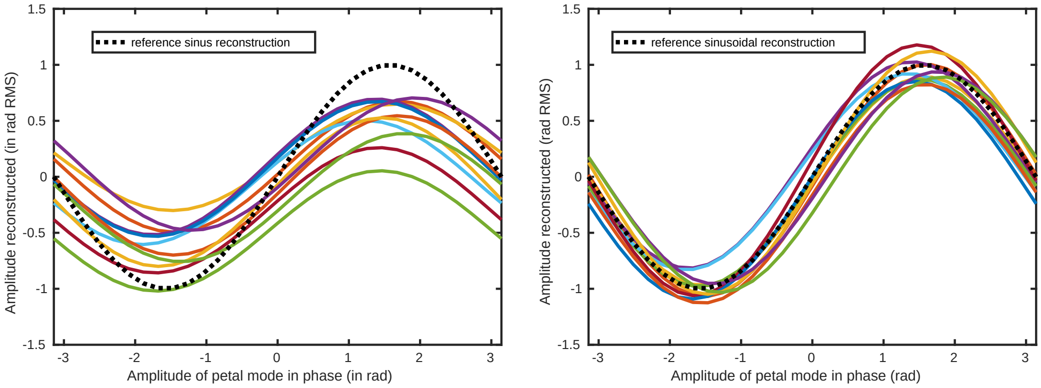

(a) Petal mode reconstruction with 10 independent residuals with uPyWFS presented earlier (Figure 4.4

(b) Petal mode reconstruction with 10 independent residuals with SF+uPyWFS

FIGURE 4.26 – Petal mode reconstruction with 10 independent 1st path residuals. Comparison between uPyWFS and SF+uPyWFS behavior. The optical gain are greatly reduced as well as the petal confusion (reduced by a factor of 6 in average)

We see that the petal measurement seems greatly improved, in particular the effect of $g(\phi_{res})$ and $c(\phi_{res})$ has been reduced making the inversion of petal mode more precise. Now that we have a good petalometer thanks to Spatial filtering, it is time to see if we can close a loop with realistic atmospheric conditions.

4.6 SFuPyWFS as petalometer

4.6.1 Complete 2-path system closed loop test

we simulate the full system of the 2-path sensor to test the proposed concept of petalometer as presented in Figure3.18. We compare an uPyWFS and a SF+uPyWFS. The full system is described previously in Chapter 3. The AO first path sensor (a modulated PyWFS) controls the DM (with simple gaussian continuous influence functions, 20x20 actuators), so it creates minioning type petal residuals. The petalometer commands a hypothetical DM with a pure petal mode as an influence function. We subtract the atmospheric petal mode at frame 0 from the atmospheric phase screen during the whole loop to start from a 0 petal. Since we are using monochromatic PyWFS the best possible result is to have petal mode locked at its initial value (zero) during the whole simulation. A bad petalometer would not be able to lock the petal mode at a stable value. Furthermore, we add (starting at frame 400 = 0.4ms of simulation a 300nm RMS static petal mode in the atmospheric phase. The aim is to test if our proposed strategy is able to measure and compensate for petal mode from other sources than the atmosphere. The parameters are the same as in Table 2.1 and cover a $1s$ simulation. the results in RMS error and projected on petal mode are shown in Figure 4.27 and 4.28 respectively

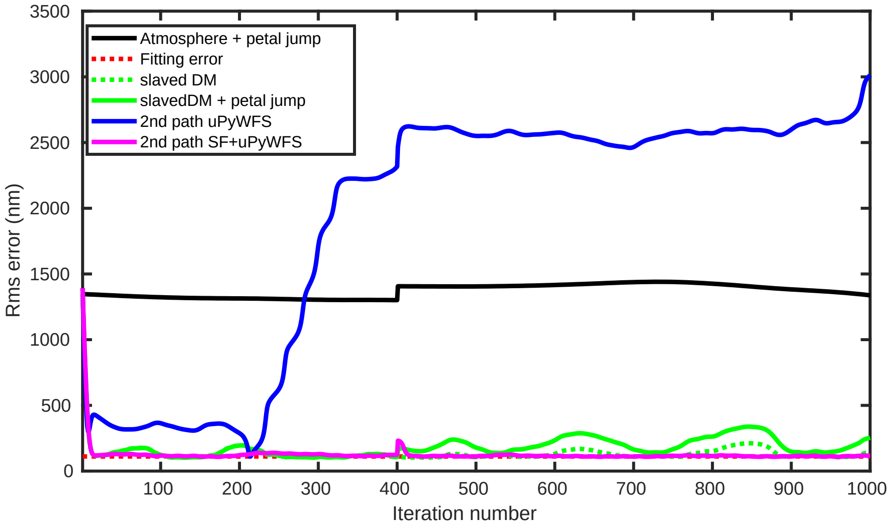

FIGURE 4.27 – RMS error from atmosphere in black, first path AO residuals in green, first path assisted by uPyWFS-petalometer in blue and first path assisted by SF+uPyWFS-petalometer in magenta. A pure petal mode is added at frame 400 of 300nm PTV to simulate a petal mode exterior to the atmosphere. We see regular flares of the first path PyWFS while the SF+uPyWFS helps to keep the residual stable around zero petal during the whole sequence fitting error is mostly hidden by the SF+uPyWFS residuals as we reach the fitting error with this method.

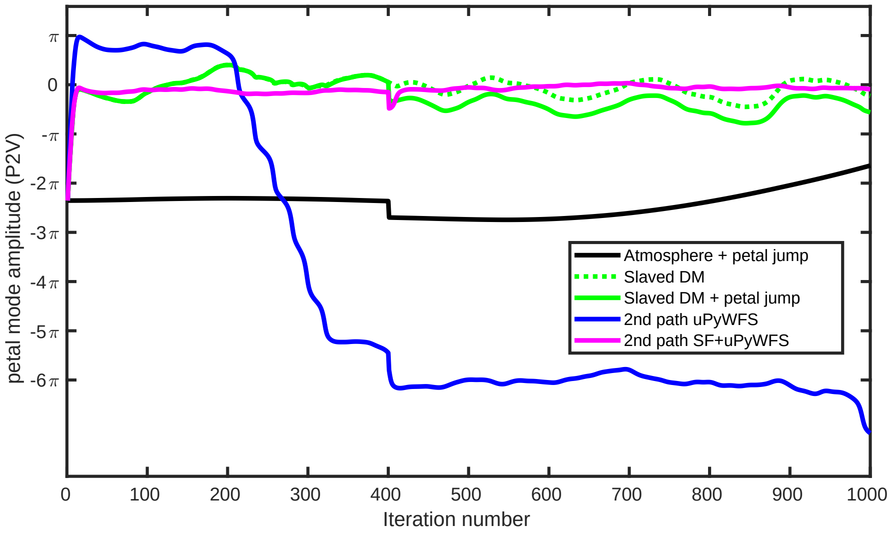

FIGURE 4.28 – Residual phase of Figure 4.27 projected on petal mode. The first path creates petal mode residuals visible as oscillations between $-\pi$ and $+\pi$. uPyWFS keeps the residual petal closer to 0 petal, but with a jump of -6pi (around iteration 250) where it loses it locking of petal, while SF+uPyWFS stays locked around zero petal

The result shows that our continuous influence functions allows the petal mode to stay around zero with the petal flares. The residuals are mostly dominated by fitting error (dotted red line) + petal mode. But if an exterior petal mode is added during the simulation it is not measured and remains uncorrected as shown by the difference between the green and dotted green line (respectively with and without the 300nm petal mode jump). The uPyWFS is not a good petalometer : due to the first path residuals it does not measure correctly the petal mode and jumps randomly of 2π petal mode value. On the contrary, the SF+uPyWFS is able to measure correctly the petal mode surrounded by AO residuals and to use this measurement in a correction loop. Moreover, it is able to measure a sudden petal mode jump during the whole simulation. This 2-path system allows the AO to stay as close to its theoretical limit.

4.6.2 Limit of 2-path AO system : effect of SF size

We have shown that with a r_0 of 15cm, on our 10m Toymodel, we are capable of measuring and correcting the petal mode thanks to the SF+uPyWFS. This has been shown with a $5\lambda/\mathrm{D}$ SF but other sizes are available and the question of the minimum r_0 for the 2-path system to operate. To that end, we simulated the closed loop with different parameters. The first test we show here is with a variable SF size. We plot only the residuals without filter, with a uPyWFS **without filter**, and a uPyWFS **with filter**

The first case tested is with a larger SF. At $10\lambda/\mathrm{D}$, the SF will let a lot of residuals through, and indeed we see in Figure 4.29 that the residuals are very close between the large spatial filter, and the absence of spatial filter.

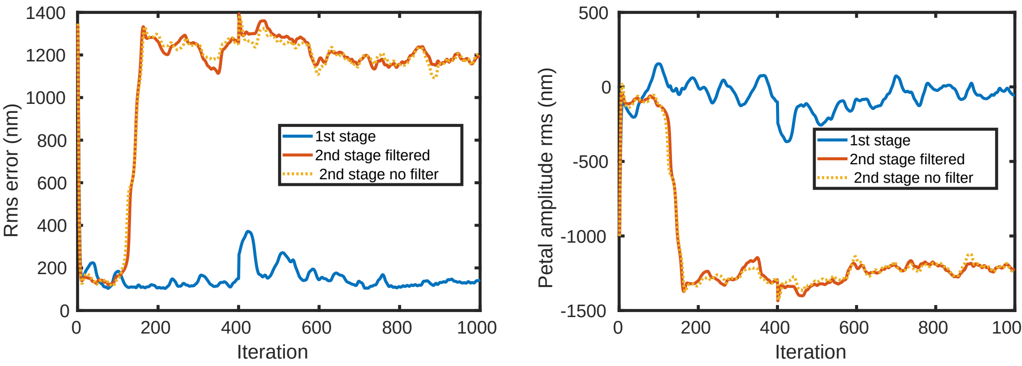

(a) phase residuals (nm rm),$\sigma_{\phi \text{1st path}} = 151nm$,$\sigma_{\phi \text{2nd path}} = 1134nm$,$\sigma_{\phi \text{1st path+SF}} = 1137nm$

(b) petalmode present in the residuals,$\sigma_{\text{petal 1st path}} = 115nm$,$\sigma_{\text{petal 2nd path}} = 1116nm$,$\sigma_{\text{petal 1st path+SF}} = 115nm$

FIGURE 4.29 – Result of 2 path system closed loop for r_0=15cm, SF= $10\lambda/D$

As the linearity plot has shown this SF+uPyWFS sensor is much more accurate when estimating the petal mode amplitude in presence of residuals. We see with a closed loop in Figure 4.30 that this petalometer is able to keep the petal at a stable value during the closed loop. We have reduced the residual by a factor of 2 between the petal flares and the SF+uPyWFS. Closing the SF seems to improve even more the measurement as shown in Figure 4.31 with a final petal residual going under 30nm RMS.

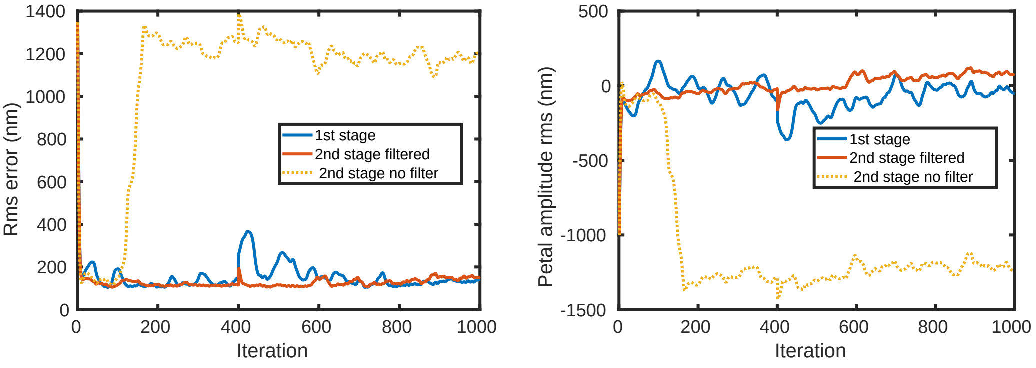

(a) phase residuals (nm rm),$\sigma_{\phi \text{1st path}} = 151nm$,$\sigma_{\phi \text{2nd path}} = 1134nm$,$\sigma_{\phi \text{1st path+SF}} = 1137nm$

(b) petal mode present in phase residuals,$\sigma_{\text{petal 1st path}} = 115nm$,$\sigma_{\text{petal 2nd path}} = 1116nm$,$\sigma_{\text{petal 1st path+SF}} = 58nm$

FIGURE 4.30 – Result of 2 path system closed loop for r_0=15cm, SF= $5\lambda/D$

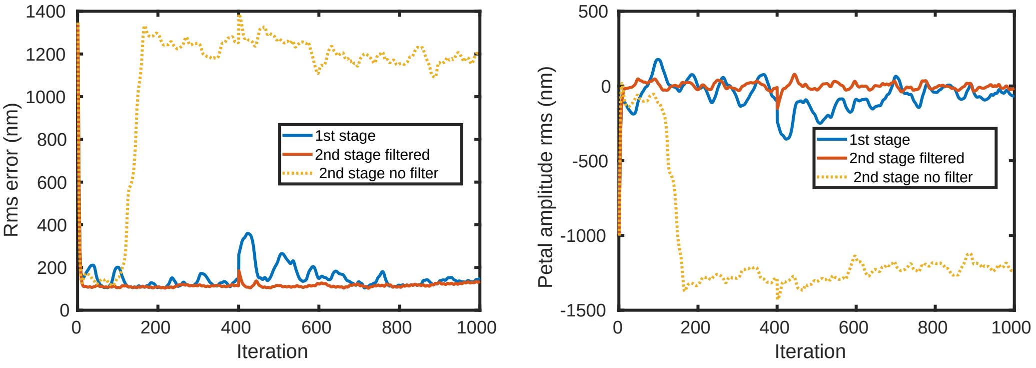

(a) phase residuals (nm rm),$\sigma_{\phi \text{1st path}} = 151nm$,$\sigma_{\phi \text{2nd path}} = 1134nm$,$\sigma_{\phi \text{1st path+SF}} = 1137nm$

(b) petalmode present in the residuals,$\sigma_{\text{petal 1st path}} = 115nm$,$\sigma_{\text{petal 2nd path}} = 1116nm$,$\sigma_{\text{petal 1st path+SF}} = 23nm$

FIGURE 4.31 – Result of 2 path system closed loop for r_0=15cm, SF= $1\lambda/D$

A smaller spatial filter seem to improve the phase measurement and in turn reduces the petal mode in the residuals of the 2-path system.

In this chapter we showed that the uPyWFS is not a good petalometer in particular due to petal confusion. This petal confusion makes the petalometer path unstable and prone to jump from one λ to another. We improved its capacity by adding the SF step and showed its interest even for other WFS. In particular the addition of the SF makes the petalometer path stable with an r_0 of 15cm

Conclusion

We have been working on adaptive Optics (AO) for 30 years and the 10m telescope delivered the result promised by AO : direct imaging of exoplanets. The 30m telescope originally seemed like a rescaling of the same problem in terms of AO and most efforts were in developing the Pyramid Wavefront Sensor (PyWFS) as an alternative to the Shack-Hartmann (SH). But the unprecedented scale of these telescopes creates a new issue that forces us to rethink AO : the petal mode.

This petal mode comes from the large spiders necessary in the 30m Telescopes. The first origin is the gap in the wavefront measurement caused by the spiders. As the wavefront sensors (WFS) used for the AO measure the phase on each fragment separated by spiders, their mean moves independently creating a pattern akin to Young interference's. This pattern reduces the resolution of the 39m ELT to the resolution of a 17m telescope. This effect can be reduced greatly by adding continuity constraints on the deformable mirror. Minioning the DM is a way to implement this continuity but this continuity will prevent the system from creating a pure petal mode if it appears in the phase. Unfortunately, we know of another petal mode origin : the LWE. This effect comes also from the size of the spider and is not solved by minioning. To solve the petal mode, it seems necessary to find a way to measure the Petal mode in the AO system.

We showed that the lack of sensitivity comes from the modulation, a necessary step to make the PyWFS accurate for the measurement of atmospheric turbulence. Without the modulation, the atmospheric turbulence creates wavefront variations larger than the dynamic range of the PyWFS. We studied a possible modification of the PyWFS which improves its measurement of the petal mode specifically. The result is the asymmetrisation of the PyWFS : by forcing the interaction between the fragments of the pupil, we increase the signal created by the petal mode. This asymmetrisation can be adapted depending on the petal mode that we want to measure and the pupil. Although the gains in signal created are important (>50% on our metric, the sensitivity of the sensor to this mode), it is not enough to compensate for the loss of signal due to modulation for the petal mode. To be able to measure the petal mode, we must use an unmodulated PyWFS, which means it can't measure the full atmospheric turbulence.

We explore this possibility by adding the sensor as a second WFS sensor on an existing AO loop. This second sensor is dedicated to the measure of the petal mode : a petalometer. To test this system we first study whether the petalometer can measure petal mode among the residuals of a first AO loop. As the petal is measured among AO residuals the low spatial frequencies are lower but the high frequencies are still present. These high frequencies alone degrade the measurement as the high-frequency mode we call petal confusion is confused with the petal mode and degrades its measurement. This effect appears only in the presence of spiders. To reduce this effect we need to reduce the 1st stage residuals seen by the PyWFS and not the petal mode. This is accomplished by adding a spatial filter, in practice a pinhole on top of the PyWFS, creating the Spatially Filtered PyWFS (SF+PyWFS). This SF+PyWFS used as a petallometer can measure accurately the petal mode and allows the 2-sensor AO system proposed to control this mode as well as the rest of the turbulence with realistic atmospheric turbulence.

Overall this thesis aimed at tackling the petal problem of the ELT. We have studied deeply the origin of the petal mode and pointed out its origin and main parameter in the AO loop. We have proposed 2 improvements possible to the current AO to solve the problem : the petalometer with Spatial filter, and the Asymmetric PyWFS to improve the sensitivity specifically to this mode. These two improvements are compatible and can be combined in the future to measure the petal mode as accurately as possible. Hopefully, after more extensive testing this thesis's solution to petal mode can be integrated into the AO of of the 30-m telescopes.

Perspectives

This thesis has been tasked with solving the petal mode, a problem the AO community has been struggling with for the last ten years. We have proposed some new analysis, and proposed simulation-based solutions and a new understanding of the origin of the petalling. But some results call for further investigations that are listed below.

As we showed the discontinuity mode can be measured as petal mode by a slope sensor. The discontinuity present in the atmosphere (or its more complex version, the petal confusion mode) could be the origin of the petal mode present in the AO residuals in the minioning DM case. If the origin of these flares can be identified as the discontinuity mode, it means that this very specific mode has to be analysed in the atmosphere instead of the petal mode. A specific sensor dedicated to its measurement can be set up.

We need a larger study of the properties of the asymetric pyramid, in particular its behaviour to other modes and the measurement of petal in presence of residuals. Combining the pyramids dedicated to petal mode measurement with the spatial filter would also be of great interest. Finally, the Zernike WFS can also benefit from spatial filtering. Such a study would allow us to find an optimal petalometer among the Fourier Filtering WFS (FFWFS).

Finally, the simulations presented in this thesis are in a noiseless environment. Proposing the addition of a second WFS means a loss of light and a study of the effect of noise on the petal mode measurement with the second path needs also to be performed. There is a tradeoff to establish between the SR that control of the petal mode gives and the SR coming from the noise effect with a dim source. Another point to study is the wavelength to be used for petal mode measurement. To overcome the lambda ambiguity a possibility is to make measurements at two different wavelengths and combine their measurement. Another question is whether the most efficient is to use longer wavelengths where there is a better AO correction, or whether we should use the same wavelength as the AO WFS.

On a median timescale, the result of this thesis needs to be confirmed on optical bench and sky. The LOOPS bench at LAM could be used to simulate the petalometer and study the impact of noise in particular. The instrument PAPYRUS could be used to confirm that the apparition of the petal mode is linked directly to the size of the spiders by increasing artificially the size of one of its spiders, and also confirm the behavior of continuous/minioning DM toward the petal mode.

Implementation of a Spatially filtered PyWFS and the asymmetric PyWFS would be easy on LOOPS as it can be created by a device called a Spatial Light Modulator (SLM), which can create any phasescreen in focal plane on LOOPS, including any FFWFS. But their implementation on sky will need a change of the current design of the WFS path of PAPYRUS to accommodate the spatial filter or the double-sided PyWFS.

A very important shortcut has been taken during this PhD for the petalometer. We have used a pyramid WFS for the petalometer (unmodulated, spatially filtered). This choice is a shortcut that should be thoroughly revisited. We have defined "a" possible petalometer, but not "the ideal" petalometer. Of course this is due to lack of time, but this choice is an open question for the next work to be done. What is the best observable, the best optical signal, that holds the signature of the petal, and would allow its measurement ? Is it a focal or pupil plane observable ? Mono or poly chromatic ? Full pupil or part of the pupil ? All these questions have to be raised again, using the light of this PhD (discontinuity mode, spatial filtering, asymetric pyramid).

But the study of the effect of the spatial filter is still relevant as it follows arguments before introducing the pyramid to it. Spatial filters already exist on most instruments with the goal to cut parasite light or reflections of the bench, as well as selecting an object on sky. They are comparatively much larger than the spatial filter tested in this thesis. We have shown that by allowing the selection of a few mode of interests, focal plane filtering can be of interest for AO. More importantly, at least for the SF+uPyWFS, the loss of light inherent to a focal plane impacts only the mode outside of the focal plane, the modes with spatial frequency small enough to go through the focal plane do so without any loss to their sensitivity. This creates problem in term of design to guaranty that the center of the PSF will reach the center of the spatial filter. But for 2nd stage AO where the tip-tilt is already controlled, and where there are generally less mode controled on the 2nd stage than the first, using a spatially filtered PyWFS seems like a pure improvment.

The final perspective of this thesis would be to have its proposed sensor integrated into the future 30-m telescope AO. In particular, it appears necessary to add a sensor dedicated to the petal mode as even though minioning reduces the atmospheric petal to acceptable levels, the LWE expected will greatly degrade the PSF. More largely we showed that it is possible to create a sensor dedicated to a given mode or problem in the AO. The next generations of telescopes might push AO even further in this path with sensors dedicated to each problem raised by wavefront measurement.

Bibliography

Babcock, H. W. 1953, Publications of the Astronomical Society of the Pacific, 65, 229

Bertrou-Cantou, A. 2021, Thése défendue, Université de Paris (2019-....)

Bertrou-Cantou, A., Gendron, E., Rousset, G., et al. 2022, Astronomy & Astrophysics, 658, A49

Bond, C., Sauvage, JF., Schwartz, N., et al. 2022, in SPIE Astronomical Telescopes + Instrumentation (SPIE)

Bonnefond, S., Tallon, M., Le Louarn, M., & Madec, PY. 2016, in SPIE Astronomical Telescopes + Instrumentation, ed. E. Marchetti, L. Close, & JP. Véran, Edinburgh, United Kingdom, 990972

Born, M. & Wolf, E. 2013, Principles of Optics : Electromagnetic Theory of Propagation, Interference and Diffraction of Light (Elsevier)

Brown, R. A. 2015, The Astrophysical Journal, 805, 188

Cayrel, M. 2012, in SPIE Astronomical Telescopes + Instrumentation, ed. L. Stepp, R. Gilmozzi, & H. Hall, Amsterdam, Netherlands, 84441X

Chambouleyron, V., Fauvarque, O., Plantet, C., et al. 2022, in Adaptive Optics Systems VIII, 100

Chauvin, G., Lagrange, A.-M., Dumas, C., et al. 2004, Astronomy & Astrophysics, 425, L29

Cisse, M., Chambouleyron, V., Fauvarque, O., et al. 2022, in SPIE Astronomical Telescopes + Instrumentation 2022 (Montréal, Canada : SPIE), 121850X

Conan, J.-M. 1994, These de doctorat, Paris 11

Conan, R. & Correia, C. 2014, in Astronomical Telescopes and Instrumentation

Conan, R., Ziad, A., Borgnino, J., Martin, F., & Tokovinin, A. 2000, in Interferometry in Optical Astronomy, Vol. 4006 (SPIE), 963–973

Crépy, B., Chaillot, S., Conan, J., et al. 2010, in 1st AO4ELT Conference - Adaptive Optics for Extremely Large Telescopes (Paris, France : EDP Sciences), 06001

Deo, V., Gendron, É., Rousset, G., et al. 2018, Astronomy & Astrophysics, 619, A56

Engler, B., Wedell, S., Miska, LL., Vérinaud, C., & R, C. 2019

Esposito, S., Pinna, E., Tozzi, A., Stefanini, P., & Devaney, N. 2003, in Astronomical Adaptive Optics Systems and Applications, Vol. 5169 (SPIE), 72–78

Fauvarque, O. 2017, These de doctorat, Aix-Marseille

Fauvarque, O., Janin-Potiron, P., Correia, C., et al. 2019, Journal of the Optical Society of America A, 36, 1241

Fauvarque, O., Neichel, B., Fusco, T., & Sauvage, J. F. 2015, Optics Letters, 40, 3528

Fauvarque, O., Neichel, B., Fusco, T., Sauvage, JF., & Girault, O. 2016, Optica, 3, 1440

Fried, D. L. 1965, JOSA, 55, 1427

Gillessen, S., Genzel, R., Fritz, T. K., et al. 2013, The Astrophysical Journal, 774, 44

Hudgin, R. 1977, JOSA, 67, 393

Janin-Potiron, P., Chambouleyron, V., Schatz, L., et al. 2019, Journal of Astronomical Telescopes Instruments and Systems, 5, 1

Kolmogorov, A. 1941, Akademiia Nauk SSSR Doklady, 30, 301

Kulcsár, C., Raynaud, H.-F., Petit, C., Conan, J.-M., & de Lesegno, P. V. 2006, Optics Express, 14, 7464

Leboulleux, L., Carlotti, A., N'Diaye, M., et al. 2022, in Advances in Optical and Mechanical Technologies for Telescopes and Instrumentation V, 63

Mahajan, V. N. 1982, Journal of the Optical Society of America, 72, 1258

Marois, C., Macintosh, B., Barman, T., et al. 2008, Science, 322, 1348

Martins, D., Holzlöhner, R., Vérinaud, C., & Kleinclaus, C. 2022, in Modeling, Systems Engineering, and Project Management for Astronomy X, ed. G. Angeli & P. Dierickx (Montréal, Canada : SPIE), 70

Mayor, M. & Queloz, D. 1995, Nature, 378, 355

Miles, B. E., Biller, B. A., Patapis, P., et al. 2023, The JWST Early Release Science Program for Direct Observations of Exoplanetary Systems II : A 1 to 20 Micron Spectrum of the Planetary-Mass Companion VHS 1256-1257 b

N'Diaye, M., Vigan, A., Dohlen, K., et al. 2016, in Adaptive Optics Systems V, Vol. 9909 (SPIE), 1993–2006

Noll, R. J. 1976, JOSA, 66, 207

Oboukhov, A. M. 1962, Journal of Fluid Mechanics, 13, 77

Petit, C., Quiros-Pacheco, F., Conan, J.-M., et al. 2004, in Advancements in Adaptive Optics, Vol. 5490 (SPIE), 1414–1425

Plantet, C., Meimon, S., Conan, J.-M., & Fusco, T. 2015, Optics Express, 23, 28619

Pourré, N., Le Bouquin, J.-B., Milli, J., et al. 2022, in Adaptive Optics Systems VIII, ed. D. Schmidt, L. Schreiber, & E. Vernet (Montréal, Canada : SPIE), 201

Quirós-Pacheco, F., Dam, M., Bouchez, A., et al. 2022, in Adaptive Optics Systems VIII, Vol. 12185 (SPIE), 348–360

Ragazzoni, R. 1996, Journal of Modern Optics, 43, 289

Roddier, F. 1981, Progess in Optics, 19, 281

Sauvage, JF. 2019, ESO_internal_document, 112

Sauvage, JF., Fusco, T., Guesalaga, A., et al. 2015

Schwartz, N., Sauvage, J.-F., Renault, E., et al. 2020, Design of the HARMONI Pyramid WFS Module

Schwartz, N., Sauvage, JF., Correia, C., et al. 2018, in Adaptive Optics Systems VI, ed. D. Schmidt, L. Schreiber, & L. Close (Austin, United States : SPIE), 75

Schwartz, N., Sauvage, JF., Correia, C., et al. 2017, in Proceedings of the Adaptive Optics for Extremely Large Telescopes 5 (Instituto de Astrofísica de Canarias (IAC))

Smith, B. A. & Terrile, R. J. 1984, Science, 226, 1421

Tamai, R. & Spyromilio, J. 2014, in SPIE Astronomical Telescopes + Instrumentation, ed. L. M. Stepp, R. Gilmozzi, & H. J. Hall, Montréal, Quebec, Canada, 91451E

Tatarski, V. I., Silverman, R. A., & Chako, N. 1961, Physics Today, 14, 46

Tokovinin, A. 2002, Publications of the Astronomical Society of the Pacific, 114, 1156

Usuda, T., Ezaki, Y., Kawaguchi, N., et al. 2014, in SPIE Astronomical Telescopes + Instrumentation, ed. L. Stepp, R. Gilmozzi, & H. Hall, Montréal, Quebec, Canada, 91452F

Véran, J.-P., Rigaut, F., Maître, H., & Rouan, D. 1997, Journal of the Optical Society of America. A, Optics and image science, 14, 3057

Vérinaud, C. 2004, Optics Communications, 233, 27

Vernin, J., Munoz-Tunon, C., & Sarazin, M. 2008, Proceedings of SPIE - The International Society for Optical Engineering, 7012

Wolszczan, A. & Frail, D. A. 1992, Nature, 355, 145

Zernike, v. F. 1934, Physica, 1, 689

ANNEXES

Astronomy & Astrophysics manuscript no. output
September 29, 2023

Strategy for sensing petal mode in presence of AO residual turbulence with pyramid wavefront sensor

Nicolas Levraud[1, 2, 3], Vincent Chambouleyron[4], Jean François Sauvage[1, 3], Benoit Neichel[3], Mahawa Cisse[1, 3], Olivier Fauvarque[5], Guido Agapito[2], Cédric Plantet[2], Anne Laure Cheffot[2], Enrico Pinna[2], Simone Esposito[2], and Thierry Fusco[1, 3]

[1] DOTA, ONERA, Université Paris Saclay, F-91123 Palaiseau, France e-mail: `nicolas.levraud@onera.fr`
[2] INAF - Osservatorio Astronomico di Arcetri, 50125 Firenze FI, Italie
[3] Aix Marseille Univ, CNRS, CNES, LAM, 13013 Marseille, France
[4] University of California Santa Cruz, 1156 High St, Santa Cruz, USA
[5] IFREMER, Laboratoire Detection, Capteurs et Mesures (LDCM), Centre Bretagne, ZI de la Pointe du Diable, CS 10070, 29280, Plouzane, France

September 29, 2023

ABSTRACT

Context. With the Extremely Large Telescope-generation telescopes come new challenges. The complexity of these telescopes' pupil creates new problems for Adaptive Optics, which prevent reaching the theoretical resolution that their size shall allow. In particular, the large spiders necessary to hold the massive optics of these telescopes create discontinuities in the wavefront measurement. These discontinuities appear as a new phase error dubbed petal mode. This error is described as a differential piston between the fragment of the pupil separated by the spiders and is responsible for a strong degradation of the imaging quality and reduces European ELT's (ELT) resolution to the one of a 15m telescope.

Aims. The aim of this paper is to study the measurement of the petal mode by adaptive optics sensors and in particular we want to understand why the Pyramid Wavefront Sensor (PyWFS), the first light wavefront sensor of all ELT-generation telescopes, cannot measure this petal mode in normal condition and how to allow this measurement by modifying the Adaptive optics control scheme and the PyWFS.

Methods. To facilitate our study we consider a simplified version of the petal mode, with a simpler pupil than the ELT. This allows us to quickly simulate the properties of the petal mode and its measurement by the PyWFS. In particular, we show that a pyramid cannot measure petal mode and the full atmospheric turbulence at the same time with visible light. We studied how a system that separates the atmospheric turbulence and the petal measurement would behave. Studying the petal mode's power spectral density, we propose to use a spatial filter to reduce the contribution of AO residuals to the benefit of petal mode contribution, eventually helping its measurement. Finally, we demonstrate our proposed system with end-to-end simulations.

Results. We show that the sensitivity of the PyWFS to the petal mode is dramatically decreased by the spider size and by the modulation step of the pyramid. This means this mode is filtered out when computing the control matrix or is vulnerable to noise if its reconstruction is forced. A solution is to use an unmodulated PyWFS (uPyWFS) but the uPyWFS does not make accurate measurements in the presence of atmospheric residuals. A spatial filtering step consisting of a pinhole around the pyramid tip reduces the first path residuals seen by the uPyWFS and restores its accuracy. This system was able to measure and control petal mode during the end-to-end simulation.

Conclusions. To address the petal problem, a 2-path adaptive optics with a sensor dedicated to the measurement of the petal mode seems necessary. The question remains as to what could be used as the second path petalometer. With this paper, we show that an uPyWFS can confuse the petal mode with the residuals from the first path, but adding a spatial filter on top of said uPyWFS makes it a good petalometer candidate. This spatial filtering step makes the PyWFS less sensitive to the first path residuals while retaining its ability to measure the petal mode.

Key words. Adaptive optics – Pyramid Wavefront Sensor – Petalling

1. Introduction

Due to the atmospheric turbulence, building a telescope bigger than 15 centimeters in visible light lies only in its capacity to collect more light and not in the improvement of the angular resolution. The telescopes bigger than this threshold have to use Adaptive Optics (AO) to compensate for the effect of the atmosphere before the light reaches the science instruments. This AO compensation step allows one to restore the diffraction limit and the gain in resolution promised by a larger primary pupil. The next generation of 30m-class telescopes is under construction and will have AO capability on first light. In particular, in this paper, we focus on the Extremely Large Telescope (ELT) (Cayrel (2012)).

To meet the challenge of the size of these new telescopes, the classical AO wavefront sensor, the Shack-Hartmann (SH), is less adapted. Its separation of the pupil in multiple subpupils makes it less sensitive for each subpupils as was shown by Vérinaud (2004).

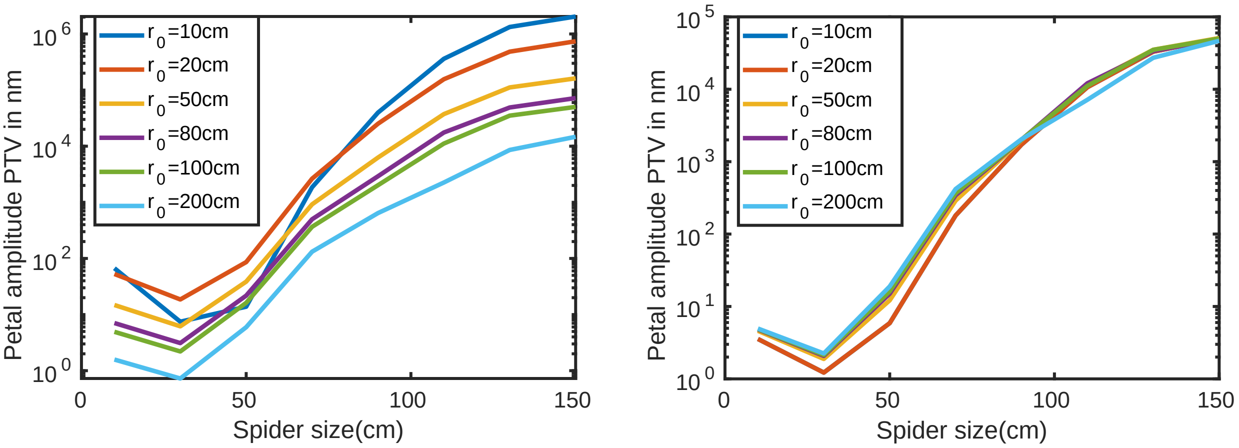

(a) Petal variation for large spiders and variable r0 in first stage residuals. For spider larger than the pitch of the ELT DM, the petal mode increases quickly

(b) Petal variation for large spiders and variable r0 in first stage residuals corrected of atmospheric turbulence amplitude.

Fig. 1: Petal mode with variable r_0 and spider size

To produce a diffraction-limited Point Spread function (PSF) on a larger telescope, the number of actuators needed and consequently the number of subpupils required for the measurement increases. The SH becomes more vulnerable to noise and is then not adapted to low flux regimes. Furthermore, the SH needs more pixels than the pyramid to the point where it is not compatible with current AO cameras. The SH is therefore being replaced by a new kind of WaveFront Sensor (WFS) for Single Conjugated Adaptive Optics (SCAO) where our only source of light is a Natural Guide Star (NGS). This kind of WFS is called the Pyramid Wavefront Sensor (PyWFS) proposed by Ragazzoni (1996) and is used in the SCAO mode of each 30m-class telescope.

The utility of SCAO is to provide high-quality wavefront correction near a bright natural guide star. In particular, the most demanding science case for such a system is the search for exoplanets, which requires high AO performance to detect faint objects close to their stars. The PyWFS allows the ELT-class telescopes to reach their diffraction limit and angular resolution with fainter targets than a SH.

Simulations of the HARMONI SCAO module taking the ELT pupil and the segmented M4 (Schwartz et al. (2017)) showed a new limit to the SCAO performances with differential piston appearing between the pupil fragment separated by the large spiders of the ELT. This is due to the inability of the SCAO system to measure this differential piston (which we will study more in part 4) and the absence of constraints on this differential piston with a segmented DM. Due to the appearance of this differential piston in multiple systems, it has received the specific denomination of the petal mode basis (linear combination of the differential pistons between the pupil fragments). This effect can be greatly reduced by adding constraints on the ELT deformable mirror with techniques such as minioning (originally called slaving) or a continual DM basis Bertrou-Cantou et al. (2020). This reduces the differential piston to an atmospheric turbulence contribution under the spider rather than in the whole pupil. In this configuration, the turbulence mostly depends on the size of the spider, and the r_0. In Figure 1a we simulate how the Petal residuals of an OA loop using a modulated pyramid are impacted by the petal mode with minioning of the DM actuators (done in the simulation by using a continuous DM). In particular for the ELT-size spider at 50cm, with 15cm r0 (not plotted) we measure a mean petal residuals of 80nm Peak-To-Valley (PTV) in residual phases (= 40nm rms). In particular corrected by the amplitude change caused by $\phi(r_0) \propto \frac{1}{(r_0)^{5/3}}$ on Figure 1b we see that the amplitude of petal is directly proportional to the one of the phase amplitude of the atmosphere. For the current SCAO instruments, this level of petal residuals is within error budgets.

There are multiple questions about the origin of the petal mode and ways to mitigate it. In particular, one possibility is to study the efficiency of different reconstructors. As this paper is tackling the petal problem by improving the sensor's measurement of petal mode, we used the simplest wavefront reconstruction available for our sensor: a matrix linear reconstruction using full frame intensities as presented in Fauvarque et al. (2016). It has been shown by Bertrou-Cantou (2021) that an MMSE reconstructor has similar performances to a minioned DM basis with a linear reconstructor as in Schwartz et al. (2018). In particular, an interesting fact is that using a sensor that is not sensitive to the petal mode, the Shack Hartmann **in a center of gravity measurement mode or if the subapertures are smaller than the spider**, can still reduce greatly the petal mode but the petal will reach error comparable to the remaining petal flares in minioned system as seen in Bonnefond et al. (2016).

We detail in part 2.2 the different petal sources and why this approach is not adapted to all of them. Suffice to say that while this approach is adapted for 1st light instrument where the residual petal after slaving is within the error budget it will not be adapted to all petal mode sources. It will also not be within the error budget for the $2_{n}d$ generation instruments and their Extreme Adaptive Optics (EXAO).

The aim of this paper will be to understand why the pyramid wavefront sensor cannot measure the petal mode and use this knowledge to propose a second path to the AO system dedicated to the sensing of petal mode. We separate here the problem of the ELT phasing of the segments of the ELT (the 798 x 1.45m hexagonal mirrors which we don't consider) and the phasing of the fragments of the pupil (the 6 areas separated by the spiders). This would allow the measurement of residual petal mode after minioning and the measurement of exterior petal mode like Low Wind Effect (LWE) (explained in section 2.2), allowing EXAO instruments on the ELT. For the system to be quickly adaptable to an ELT instrument we will use the same constraint in terms of wavelength as the HARMONI instrument with a sensing wavelength $850nm$. As it must measure the fast evolving atmospheric turbulence petal, it needs to be an AO-type sensor with a high sensitivity and linear reconstruction, so we will start with the already used AO sensor as the baseline for this paper.

2. State of the problem: the petal mode

2.1. Petal Properties

To reach the diffraction limit the petal mode would need to be lower than a few tens of nanometers in the residuals.

Uncorrected petal mode creates light residuals in the PSF comparable to slit interference patterns. The resolution on long exposure (with completely uncorrected petal mode) is then limited not by the size of the pupil of the telescope, but by the size of one fragment (≈15m). This means petal mode can be responsible for a loss of resolution up to $\sqrt{N_{fragment}}$. With the atmospheric petal only the loss of resolution is not of this order as the mode doesn't reach high values. But LWE petal is expected to reach values over λ. From the differential piston between each fragment we can define a petal mode basis constituted of 5 orthogonal petal modes for the ELT (as appears in Bertrou-Cantou et al. (2022)). One of the particularities of the petal mode is that although it appears in the residual after an AO stage, it can be projected on modes that are measured and compensated by the AO stage. The most obvious is Tip-Tilt on which most of the first petal mode (or the one from our simplified pupil seen on Figure 2. One could be tempted to orthogonalize this petal mode with the other mode of the basis. As the petal mode can be described in phase space as a Heaviside function, this can be done with an infinity of modes. The resulting petal orthogonalised to a Zernike mode basis will tend to a discontinuity phase mode around the spider. **The orthogonalized petal mode resulting in this operation becomes very different from the mode appearing in AO residuals such as Schwartz et al. (2018). To keep the same mode as our studied mode,** we choose to keep the original differential piston petal mode definition, but to avoid confusing it with other mode when doing phase reconstruction we also calibrate the basic Zernike modes (like tip-tilt, see section 4.2 for more details). To simplify the problem we will consider a pupil with only 1 spider and consequently only 1 petal mode.

2.2. Toymodel

For a simplification of the problem, we will study a simplified pupil with a single spider and only 2 fragments and therefore only have 1 petal mode. This simple case scaled to a 10m diameter telescope can be simulated with a coarser sampling and considerably reduces our computational time. To keep the representativity of the ELT case it uses the following parameters: Spider size = 50cm. 20x20 DM (same pitch of a DM actuator = 50cm as the ELT M4).

The petal mode is shown in Figure2. Note that this petal is defined with an RMS amplitude of 1 radian and thus has a PTV of 2 radians between the left and right fragment. To stay consistent throughout this article, we will use an RMS unit for petal mode. With this normalization, an amplitude of π radians RMS means a PTV of 2π radians, hence a λ OPD wrap.

2.3. Sources of petal mode

As was shown by Bertrou-Cantou (2021), the petal mode is badly sensed by the modulated PyWFS. This means an effect akin to the waffle mode can appear where the mode is amplified by the reconstruction of the AO. Furthermore, if the DM is able to create this mode, it will create loop instabilities. As the petal mode in this case comes from the AO loop and in particular its control, it evolves as fast as the AO correction. It is currently solved by a technique called minioning (Bond et al. (2022)). This technique acts on the control part of the AO loop by forbidding the creation of any differential piston by the DM. The remaining error is the atmospheric petal which exists under the spider. This residual atmospheric petal's amplitude depends on the size of the spider and the r_0 as was shown in the introduction in Figure 1a. There are 2 problems with this approach. First, this approach only works for atmospheric turbulence petalling. As the petal is not measured if it comes from other sources than atmospheric turbulence it will not fall within the acceptable first light instruments constraints. Then for the Extreme Adaptive Optic (EXAO) system, this is not an acceptable level of residual wavefront error. For a coronographic system for instance, while it is possible to design coronographs less impacted by this type of wavefront error(Leboulleux et al. (2022)), it is at the cost of angular resolution.

Another source of petal mode in the phase is the LWE. It is a phenomenon that was discovered on the VLT during the first light of the SPHERE instrument described in Sauvage et al. (2015)). This effect was mitigated on the VLT by improving the emissivity of the spider (i.e. the temperature of the spider is close to the temperature of the environment), but with the larger spiders of the ELT-class telescopes, LWE is expected to be stronger. A simulation of the airflow around the spiders has recently shown a 1μm OPD around the spiders according toMartins et al. (2022), much larger than the petal residual after minioning. As the LWE is poorly understood we will consider it in this paper only as an uncontrolled source of petal mode. It will appear in the end to end simulation as a brutal petal mode appearing in the phase. It is to be separated from the atmospheric petal as it is a perturbation created by the telescope and not by the atmosphere though the final phase mode is equivalent.

2.4. Wavefront sensing measurement problem

The petal mode being a differential piston, means that in monochromatic light the whole phase screen wraps every λ. This makes a petal larger than λ impossible to detect correctly with a monochromatic sensor and thus the petal mode has a 'built-in' limited range of measurements. This comes back to a phase-unwrapping problem, that we leave aside for the study presented here. In this paper, we only consider monochromatic light and test whether a measurement can be done accurately in ELT conditions.

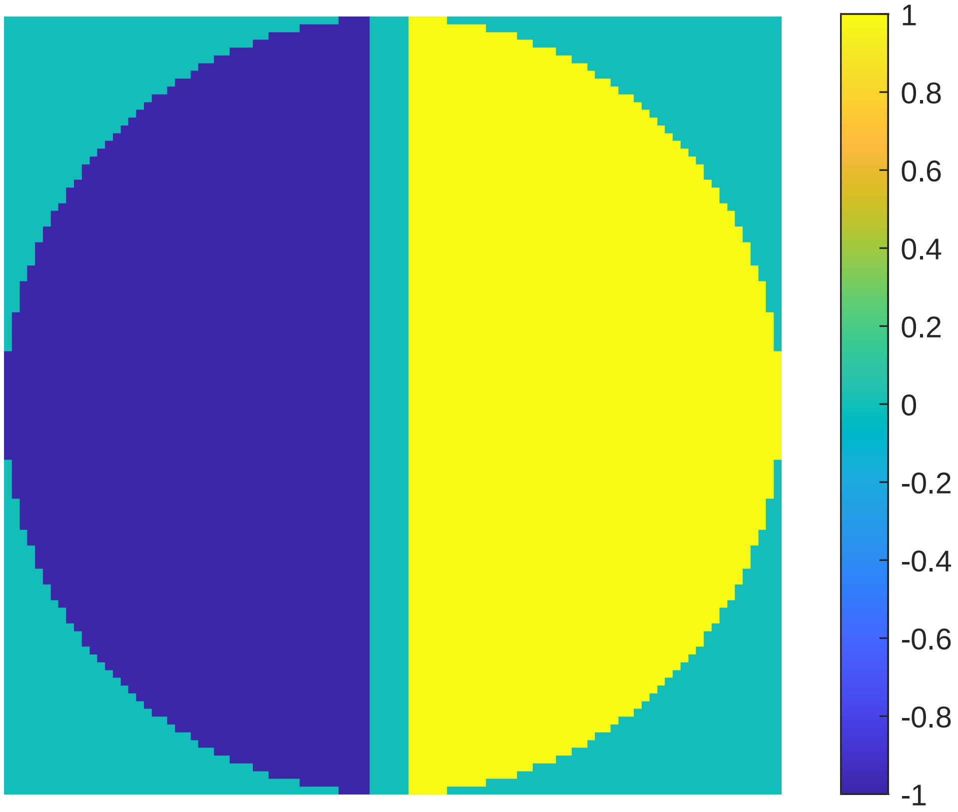

Fig. 2: Toymodel petal mode

2.5. Solutions proposed to the petal problem in the literature

Any slope sensor will not be able to measure the petal mode in a subpupil. It is not a problem when the spiders are small like on the VLT where the petal created by the spiders is negligible. But with 50cm spiders, it becomes a mode large enough to decrease EXAO performances. Phase sensors like the Zernike Wavefront Sensor (ZWFS) or the unmodulated PyWFS (uPyWFS) have been proposed as their intrinsic response is more sensitive to phase discontinuities. However, their dynamic is not large enough to measure the atmosphere at the same time.

There are two ways to solve the petal problem proposed in the literature: modify the AO wavefront sensor, and add an additional sensor dedicated to measuring the petal mode, a petalometer. The first solution appears when studying the METIS instrument. This instrument senses the Wavefront at a longer wavelength. Thanks to a lower turbulence phase and more linear sensor, it doesn't show any petal mode in its residuals (see Hippler et al. (2019) and Carlomagno et al. (2020)). Another solution is the flip-flop method proposed by Engler et al. (2022) where the modulation of the PyWFS is cut to use a temporary uPyWFS and measure the petal mode in the residual. The GMT has opted for the second solution with the development of the the Holographic Dispersed Fringe Sensor (HDFS, see Haffert et al. (2022)), a sensor dedicated ot the phasing of the GMT mirrors.

Moving all AO systems to IR looks like a simple solution but there are a lot of advantages to keeping the sensing in the visible light. IR detectors are slower and noisier than their visible counterparts, meaning fainter stars can be used as NGS by visible systems. Astronomical observations are mainly using IR for most of first-light instruments. We make our simulation with the wavelength used in the HARMONI instrument: 850nm. We instead study the petalometer approach in the rest of this paper.

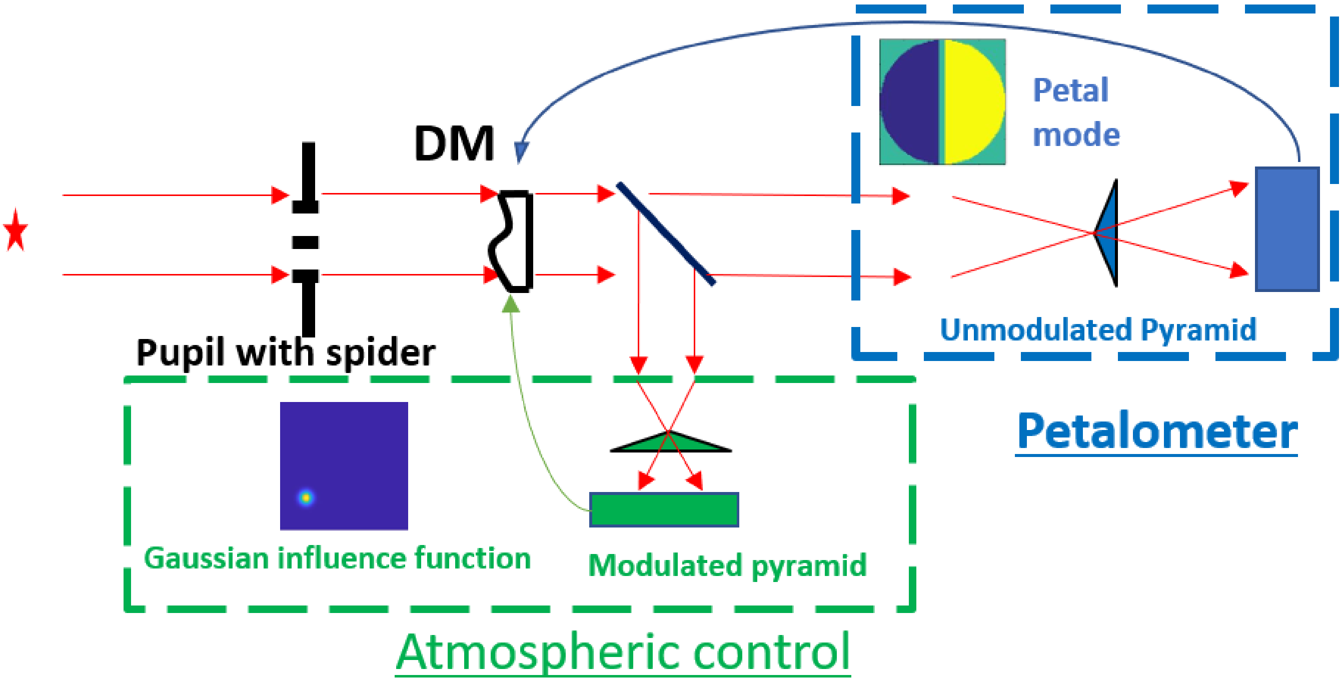

Fig. 3: 2 Path sensor scheme considered. The green path is dedicated to atmosphere wavefront sensing and features a modulated PyWFS and a classical 20x20 actuator DM. The blue path is dedicated to the sensing of petal mode and features an uPyWFS and controls only the petal mode of the DM

3. Measurement of petal mode in AO residuals

3.1. 2-Path AO system

As was shown by Bertrou-Cantou (2021) the uPyWFS produces a strong signal for the petal mode even in the presence of spider compared to the modulated PyWFS. **But it is not able to measure the petal mode accurately among the whole atmospheric turbulence for a realistic r_0. It is proposed instead to use the uPyWFS to measure the petal mode among the residuals of an AO loop, as a petalometer.** The question in this part is whether the uPyWFS can reconstruct accurately the petal mode among AO residuals. To test this capability we analyze the petal mode reconstructed by the PyWFS used as a petallometer with the 2path system shown in Figure 3.

There is a single Deformable Mirror (DM) correcting the aberrations in the AO loop. This mirror is described by a modal basis including a pure petal mode of our toymodel pupil, as well as Gaussian influence functions of a 20x20 regular actuator grid. The Gaussian influence functions are controlled by the modulated PyWFS and are dedicated to the atmospheric turbulence compensation. The second path includes a petalometer which controls the pure petal mode of the DM. Diverse sensors could be proposed as petalometers for the second path. As we showed that the uPyWFS is a possible alternative in terms of sensing, we use it in this first test. The uPyWFS only controls the petal mode though it can measure other modes.

The first source of petal mode is atmospheric turbulence. We use this configuration to take advantage of the reduced atmospheric petal mode in the residuals after a first stage using a minioning DM. The aim of the petalometer is to measure and allow the control of both atmospheric petals and LWE. We also add a fixed petal after some iterations to simulate LWE.

3.2. uPyWFS petal mode reconstruction

We use the Intensity Map method described in Fauvarque (2017) so using all the pixels. The linearity curves presented later have been reproduced with the slopes map method and have given the same results. There does not seem to be a preferred method for measuring petal mode. The first step is to calibrate the interaction matrix of our system. We create this interaction matrix by simulating the reduced intensity (see Equation **??**) for a variety of modes. For the atmospheric control, the calibrated phase modes will be the zonal base of the 400 actuators. For the petal mode interaction matrix, we need not only to measure the petal mode but also other Zernike modes in particular tip and tilt to avoid confusion between these low-order modes and the petal modes. In practice, we calibrate a modal basis containing the Petal mode + 30 Zernikes phase modes.

$$\mathcal{D} = (\delta I(\phi_1), ..., \delta I(\phi_i), ..., \delta I(\phi_N)) \tag{1}$$

See equation **??** for the computation of $\delta I(\phi_1)$ Then the interaction matrix is inverted using a Moore–Penrose pseudo inverse to get the control matrix $D^{\dagger}$. We use a conditioning number of 100. Assuming small phase we should have the relationship :

$$\hat{\phi} = \mathcal{D}^{\dagger} \Delta I(\phi) \tag{2}$$

We express any phase as its decomposition on the modal basis used

$$\hat{\phi} = \sum_{i=1}^{N} a_i \phi_i \tag{3}$$

with a_i the amplitude of the mode ϕ_i

$$\begin{pmatrix} \hat{a_1} \\ \hat{a_2} \\ ... \\ \hat{a_N} \end{pmatrix} = \mathcal{D}^{\dagger} \Delta I(\phi) \tag{4}$$

with $\hat{a_i}$ the estimated amplitude of the mode ϕ_i.

3.3. Linearity curve of petal mode reconstruction

We want to test the measurement of petal mode with a PyWFS used as a petalometer. To that end, we compute the linearity curve to a petal mode first without AO residuals to set the ideal case, and then with typical AO residuals. To plot this linearity curve we take a given phase screen and add a given petal mode amplitude, varying between $[-\pi : \pi]$. As we are using monochromatic light the signal is wrapped outside of these boundaries and computing the linearity curve for higher amplitude is of no use.

In the absence of residuals we see the expected result previously shown by Esposito et al. (2003):

$$\hat{a_1} = sin(a_1) \tag{5}$$

with $\hat{a_1}$ the estimated petal mode amplitude for an input of a_1 expressed in rms value. This expression emphasizes the wrapping of the petal mode estimation with monochromatic light. In the absence of residuals, there is no difference in whether there is a spider or modulation as these are noiseless tests. We see here the intrinsic non-linearity of the PyWFS and specifically the non-linearity of the petal mode itself. The linearity of both modulated and uPyWFS is tested here because the first question that arises with any feature is whether the feature would remain with a modulated pyramid. However, it is inefficient for a real system to try to reconstruct petal mode with a modulated PyWFS and we only keep this curve to demonstrate that the problem remains.

3.4. linearity curve in presence of residuals

Pupil	**Diameter = 10m** **Monolithic primary mirror** **Variable spiders (reference case at 50cm)**
Turbulence	**3 Layer r_0=15cm@550nm** **wind speed=5m/s** **Outer scale L_0=30m**
Dm	**50cm pitch (20x20), square pattern, gaussian influence functions, 0.3coupling**
PyWFS	**100x100 subapertures** **no noise (photon or readout)** **Atmospheric control modulation = $3\lambda/D$**
Target	$\lambda = 850nm$ **on axis star**
Controller	**Loop Rate 1000Hz** **1 Frame delay (+integration)** **Matrix-Vector-Multiplication + Integrator**

Table 1: Toymodel simulation parameter

We simulate the AO residuals with an AO loop using the parameters summed up in table 1. As the petal mode has very high frequency parts aliasing could be the source of a lot of issues. To reduce that problem we will be using a large oversampling here with 100x100 subapertures. All the further results have been confirmed with a 20x20 subapertures case. The resulting residuals have an amplitude of 120nm RMS and give a 55% SR at the top of the pyramid. The residuals are simulated without a spider and filtered from petal mode to make sure that the further injected petal will be the only petal mode present in the phase. The tip-tilt which could be changed by the petal mode filtering has a negligible amplitude as it is already phase residuals and has an RMS amplitude of 14nm.

The linearity curves are now plotted with the same procedure as before (Figure **??**) but in presence of AO residuals.

The resulting linearity curves are very different between the unobstructed pupil and toymodel case as seen in Figure 4. In the unobstructed pupil case we see mostly the Optical Gains (OG) (Figure 4b) g which reduce the amplitude of the reconstructed petal

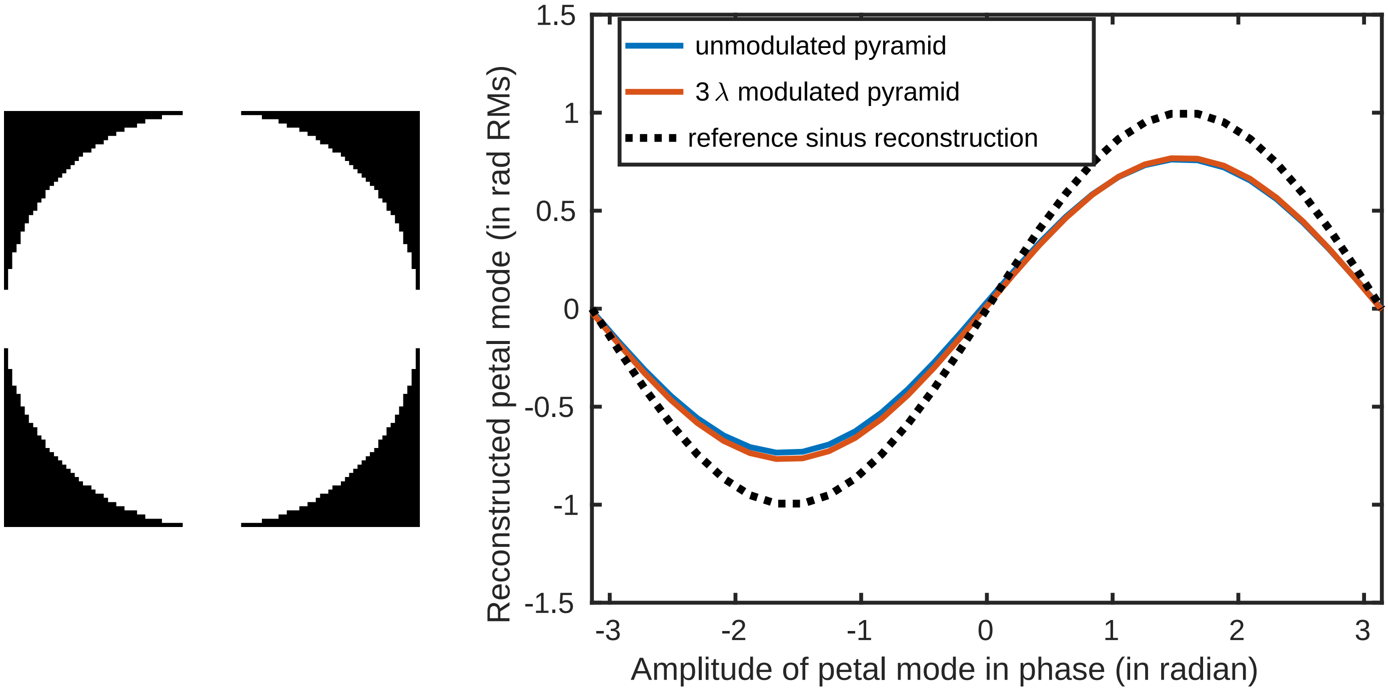

(a) Unobstructed pupil

(b) Linearity curve of petal mode around residual phase screen for unobstructed pupil

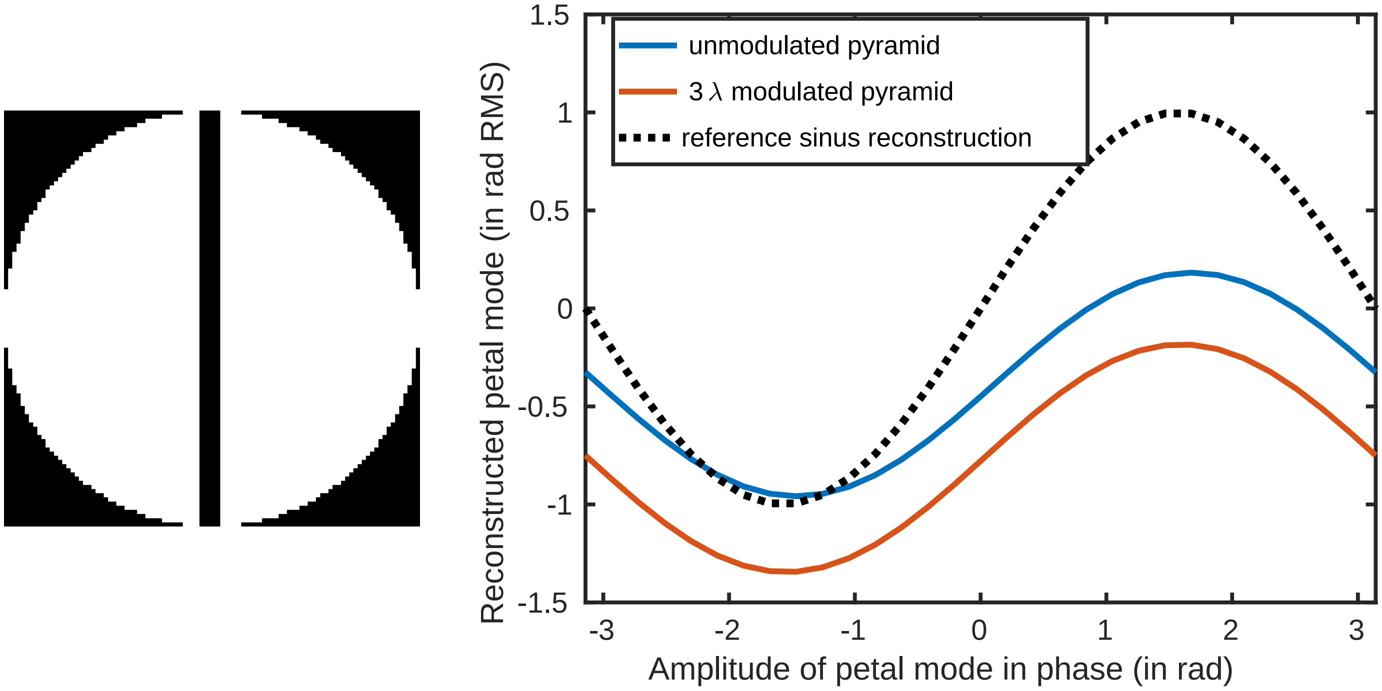

(c) Unobstructed pupil

(d) Linearity curve of petal mode around residual phase screen for toymodel pupil

Fig. 4: Linearity curve in presence of residuals for unobstructed pupil and toymodel pupil

mode. We can make a separation here between the optical gains coming from all the other modes present in the residuals g, and the optical gain coming from the petal mode itself, the sin function.

$$\hat{a}_1 = g * sin(a_1). \tag{6}$$

With the spider present, the linearity curves are offset. It means that the uPyWFS measures a petal mode amplitude when there is no petal mode in the phase, it confuses another mode with petal mode. This confused mode is seen in the linearity curve as a fixed offset value added to the sinusoidal that we note c and call the "Petal Confusion". Furthermore, as is shown in Figure 5, c depends on the AO residual.

$$\hat{a}_1 = g * sin(a_1) + c. \tag{7}$$

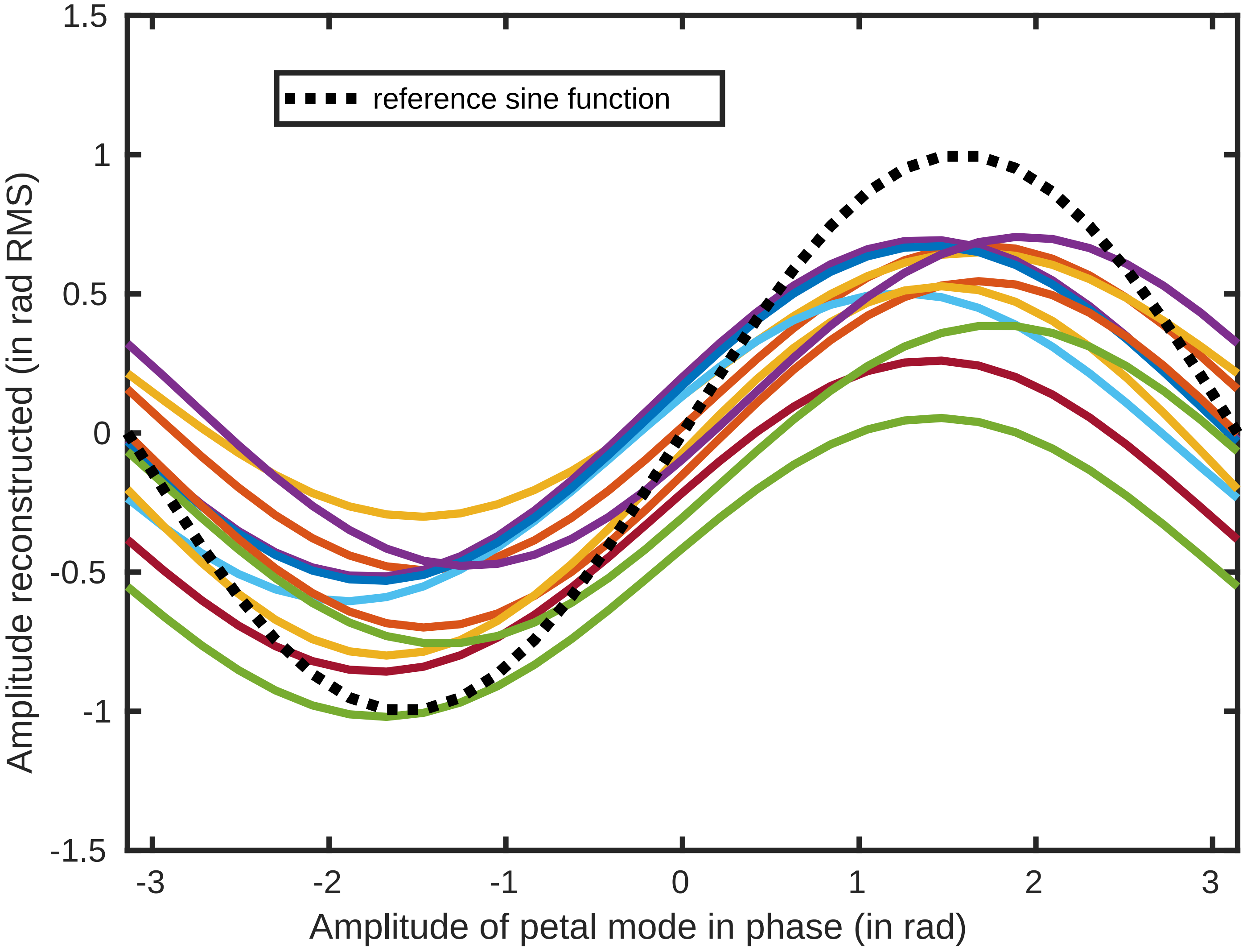

Fig. 5: Linearity curve with 10 independent residuals with uPyWFS

The typical amplitude of petal confusion c is a few tenths of a radian, which makes the value reconstructed by the PyWFS for a null input very far from the true value of petal (0 here). We need to understand this parameter in order to use the petalometer efficiently. c is computed by taking the mean of the linearity curve. There is also sometimes a term of dephasing appearing. The first possible origin of this dephasing would be a petal mode in the residuals, but in this simulation, we made sure to specifically filter it. We consider it as another defect of the reconstruction. Examples can be seen with various residual on Figure 5

$$\hat{a_1} = g * sin(a_1 + d) + c. \tag{8}$$

We also note that for some extreme cases the petal confusion is so large that the linearity curves only estimates non zero values of petal mode. Its phase reconstruction doesn't cross the 0 petal mode measured line. Another important parameter is its speed. each curve plotted in Figure 5 is separated by $500ms$. The petal confusion changes fast with each phase screen.

3.5. Dependence of petal confusion to AO residuals

The first possible origin of this petal confusion comes from the non-linearity of the uPyWFS. We test the dependence of the petal confusion on the amplitude of AO residuals. To do so, we plot the petal confusion (as the average value of the linearity curve) with respect to the amplitude of AO residuals. The scaling parameter is a multiplier on the original AO phase residuals. To this end, we use the same residual phase screen as before and scale them by a multiplicative factor $s \in [-1, 1]$. The dependence curve of c with respect to AO residuals is plotted in Figure 6 as a function of this scalar. 10 uncorrelated residual realisations were averaged. When s is close to 0 we can write : $c(s * \phi) = s \times c(\phi)$. The petal confusion is very much a linear effect.

3.6. Origin of the petal confusion

The origin of the petal confusion seems nonetheless to be in the phase residuals. We have found a specific shape it takes for the PyWFS, but its effects were already reported for the PyWFS and Zernike wavefront sensor by Bertrou-Cantou et al. (2022). Furthermore, it

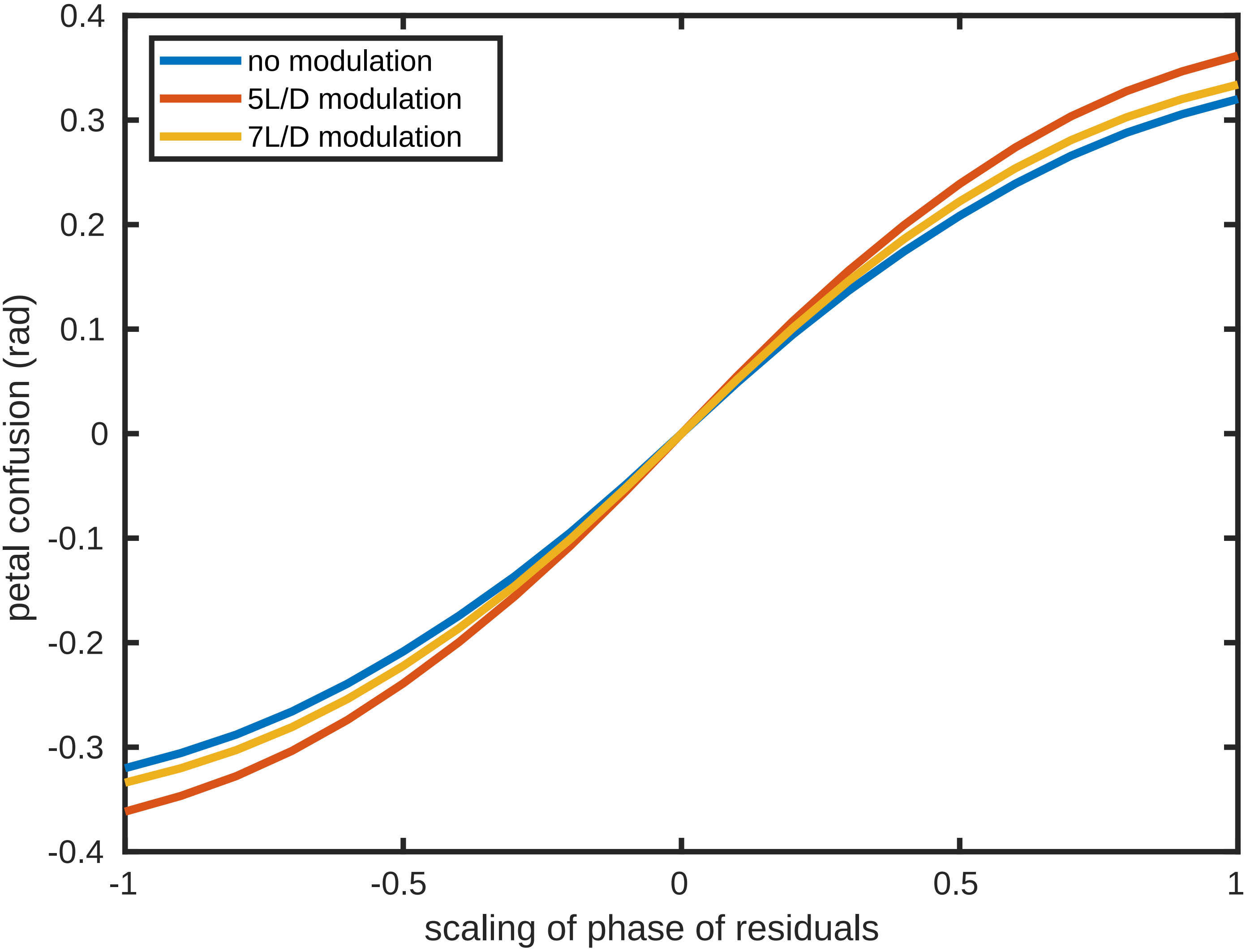

Fig. 6: Petal confusion variation with change of phase residual amplitude

seems to be a linear effect as was shown by the scalar test. The linearity of the confusion effect means we can construct the phase mode associated with it.

To that end, we compute a map of the confusion, e.g. how much each phase pixel creates petal confusion separately. As it is a linear effect we can then sum the petal confusion contribution of each pixel into a phase map. For this construction, we put all phase pixels at 0 except one which is at 1 rad. We orthogonalize this phase pixel to the petal mode to avoid our reconstruction creating petal mode. We use this phase as the residual and test the linearity of the petal mode with this residual. Then we compute the petal confusion caused by this pixel $c_{x,y}$. We then plot the full map of confusion shown in Figure 7.

This map, which we refer to as "confusion map", is expressed in phase space and can be interpreted as the phase mode responsible for the petal confusion. The mode creating petal confusion seems to have two distinct parts: a high-frequency line on each side of the spider (or discontinuity mode), and a low spatial frequency sinusoidal phase. This low-order mode comes from the number of modes calibrated in the interaction matrix for the reconstruction of the petal mode. This stems from the petal mode which can be projected on an infinity of spatial frequencies. The high-frequency signal always appears even with very high-frequency Zernike integrated in the petalometer interaction matrix. This mode is too high frequency to be controlled by our DM and cannot be separated from the rest of the typical AO residuals. As petal mode contains high frequency due to its discontinuity talking about a high frequency being reconstructed as a lower frequency is tricky but petal confusion (in particular the spider discontinuity component) can be seen as a form of aliasing. It is not a classical aliasing as oversampling the phase measurement was tested and doesn't solve the problem.

The conclusion of the analysis on petal confusion identification is there will always be some petal confusion that cannot be separated from residuals. Therefore to measure petal mode efficiently we need to reduce the effect of AO residuals in order to naturally increase the sensitivity to the petal mode.

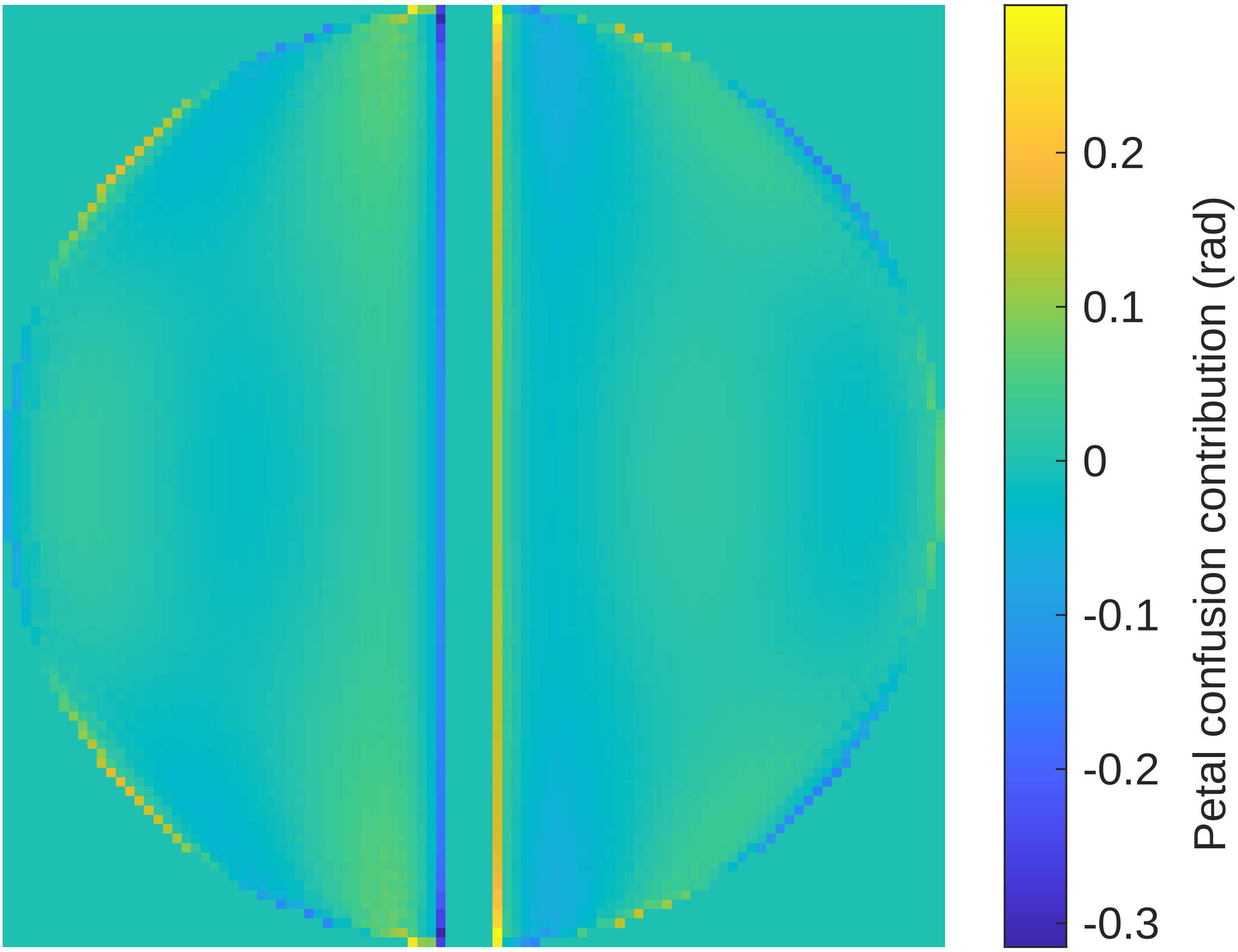

Fig. 7: Petal confusion map

4. Reduce the impact of residuals on petal mode measurement

To reduce the impact of the residuals on the signal, a solution would be a longer integration time, or moving to longer wavelength for sensing. This is not compatible with our original aim that was a fast measurement in the visible, so we need a new strategy to reduce the impact of residuals on the measurement.

4.1. Reduce the effect of residuals in phase space

We now compute the PSD of atmosphere contribution and the PSD of the petal mode. The residuals PSD is computed using the same first stage system as in part 4 and then their PSF are averaged over 1000 independent residual phase screens. We can see on Figure8 (solid lines) that they have a different distribution in the spatial frequency domain. The PSD of petal mode is plotted for a the same RMS amplitude of petal mode as the RMS amplitude of residuals.Residuals have lower PSD values than petal mode in the low spatial frequencies but dominate in the high spatial frequencies. So if one can filter selectively to keep only the low spatial frequencies, it makes the separation between the petal mode and residuals easier. One can consider the residual as a form of noise on our petal mode measurement, then we want to improve the SNR by filtering selectively the residuals. In the focal plane there is already this organisation by frequency and there is a focal plane already accessible when using a PyWFS : the tip of the PyWFS. We have a new kind of sensor adapted to be a petalometer : a spatially filtered uPyWFS (SF+uPyWFS).

It is to be noted that Usuda et al. (2014) already proposed such a PyWFS for their second WFS channel with the purpose of lifting the λ uncertainty but with a reverse filtering. It was proposed for GMT to filter the low order frequencies with a chip hiding the heart of the PSF. When looking at the PSD, the petal mode does indeed evolve differently at higher frequencies than the atmosphere or residuals. Due to the discontinuity in the phase, at high spatial frequencies, the petal mode PSD is over the atmospheric PSD for a comparable amplitude. In term of petal confusion that would mean reduction of the low order part of the petal confusion so it would be interesting to test in a further paper.

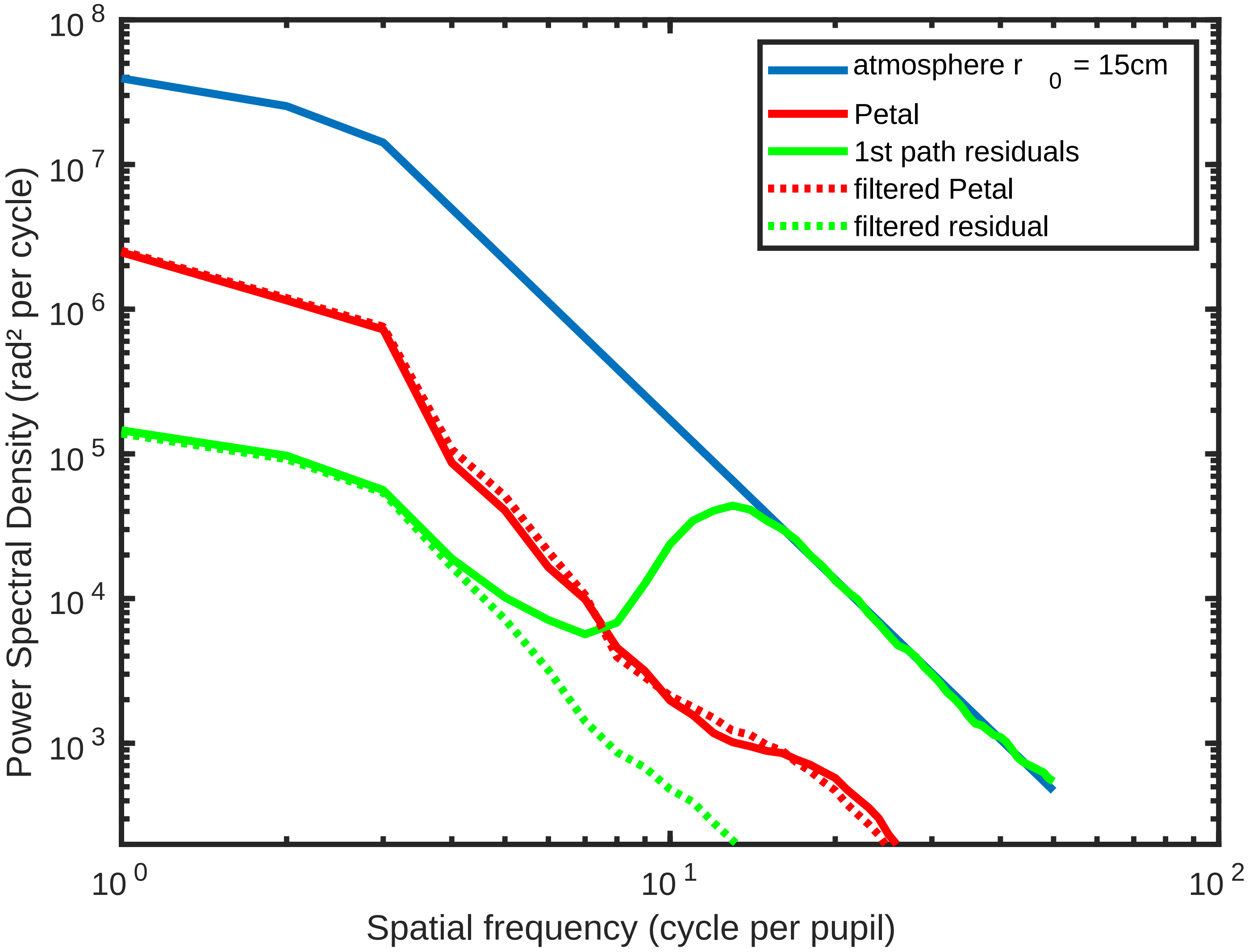

Fig. 8: PSD comparison Atmosphere and first path Residual and petal mode without (plain line) and with 5λ/D filter (dotted line)

We simulate the effect of a spatial filter at the tip of the pyramid, as observed from the pupil phase. In this example we start with the electric field in the entrance pupil plane, propagate it to a focal plane, use a focal plane filter (a circular pinhole) and propagate to a pupil plane following Figure 9a.

We then computed the PSD of residuals and petal mode after focal plane filtering (Figure 8). The pinhole size used for this computation is $5\lambda/D$ of radius.

We see that the first path residuals are suppressed before the petal mode by this focal plane filter. The balance has to be found between reducing the first stage residual and keeping the spatial filter opened to let as much light as possible still. To decide what would be the best size of filter we can think in term of Signal to noise Ratio. The Signal we are interested in is the petal mode. The 'noisy signal' are the residuals. We compute the variance of residuals and variance of petal mode with different Spatial Filter size (SF size).

$$SNR(SFsize) = \frac{\sigma^2_{petal|filtered}}{\sigma^2_{residual|filtered}} \tag{9}$$

With our simulation parameter, the $2\lambda/D$ spatial filter has the best phase SNR (see Figure 9). But having a small SF means limiting the intensity entering the WFS. There is a compromise to find here between SNR and loss of intensity. We make the following simulation with a $5\lambda/D$ spatial filter. With this spatial filter we have a SNR of 4 and loose 50% of the intensity. On the 9) curve we see a drop of SNR starting at $10\lambda/D$. this is due to the residual of the AO (in particular the fitting error) which appear as intensity at spatial frequency higher than $10\lambda/D$. In practice the spatial filter doesn't filter the AO residuals anymore if it is larger than this radius.

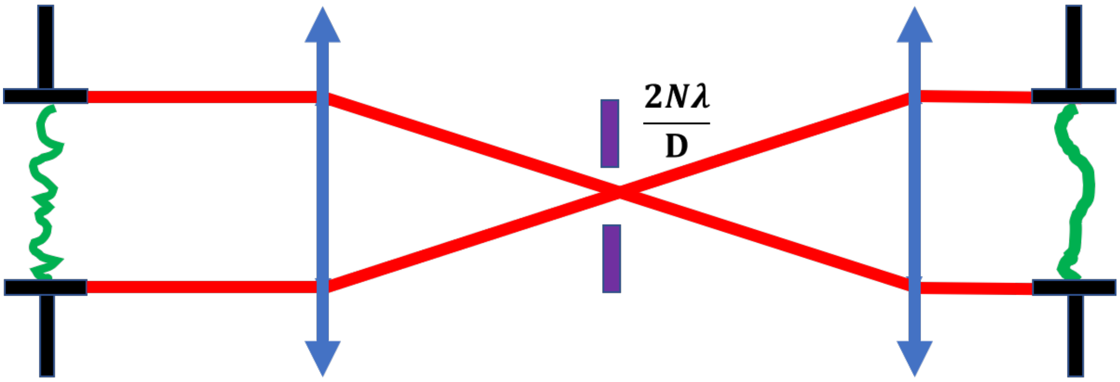

(a) Optical path considered for the spatial filtering tests

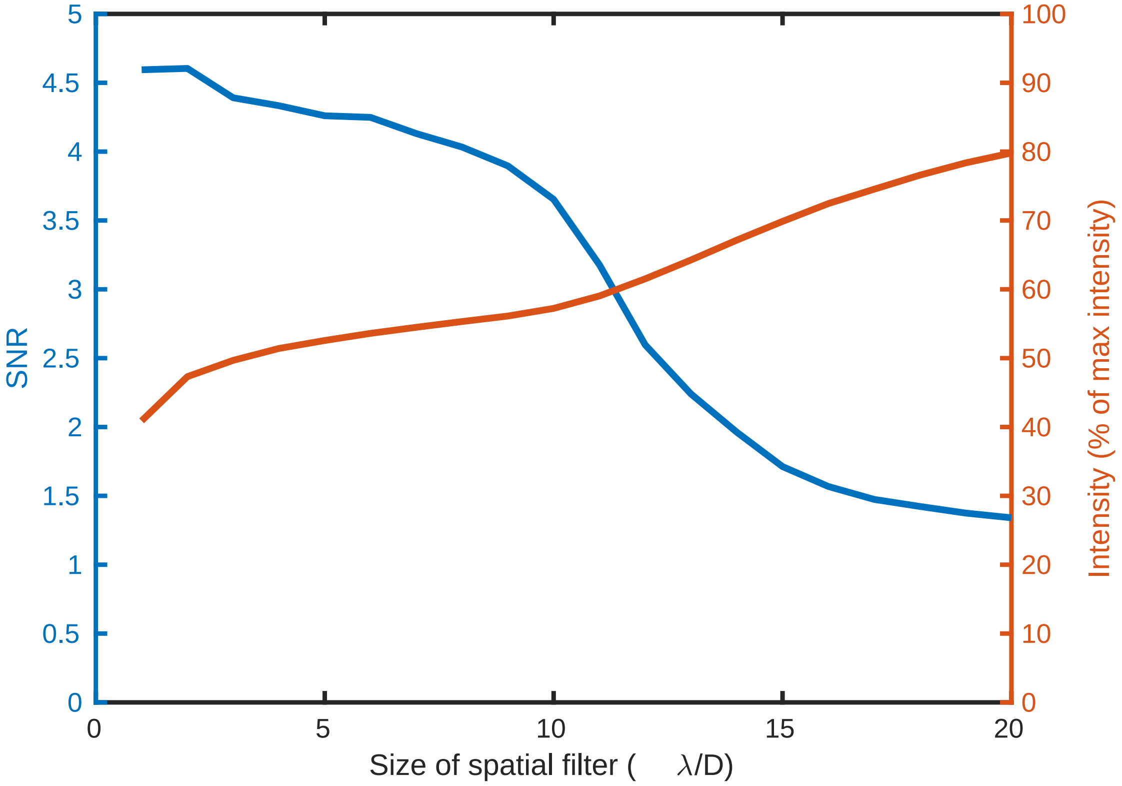

(b) Signal to noise ratio for petal mode and first path residuals **compared to the intensity going through the spatial filter**

Fig. 9: Petal mode to Residual ratio for variable spatial filter size.

4.2. effect of spatial filter on PyWFS signal

A spatially filtered PyWFS (SF+PyWFS) is implemented in simulation. From a mathematical point of view, a SF+uPyWFS has a phase (PyWFS) and amplitude mask (SF) in the focal plane. A modulated PyWFS needs the spatial filtering step before the modulation step and is not simply a change of the focal plane mask.

4.3. Effect of spatial filter on linearity curve of PyWFS

The previous linearity test was done using the SF+uPyWFS as the second path petalometer (Figure 10)

There are two remarkable effects of spatial filtering. The first is less impact on the optical gains. As the spatial filter reduces the residuals drastically, the PyWFS is used in a regime closer to the low aberration approximation. Hence the linearity of the signal improves visible here as OG closer to 1. Another effect is in the modes impacted by the spatial filter. The sensitivity to modes now drops when the spatial filter radius is under the spatial frequency of the mode. In Figure11a we compare the sensitivity of petal mode, a $3\lambda/D$ and $10\lambda/D$ sinusoïdal mode with respect to spatial filter size. The sensitivity drops fast once modulation radius is

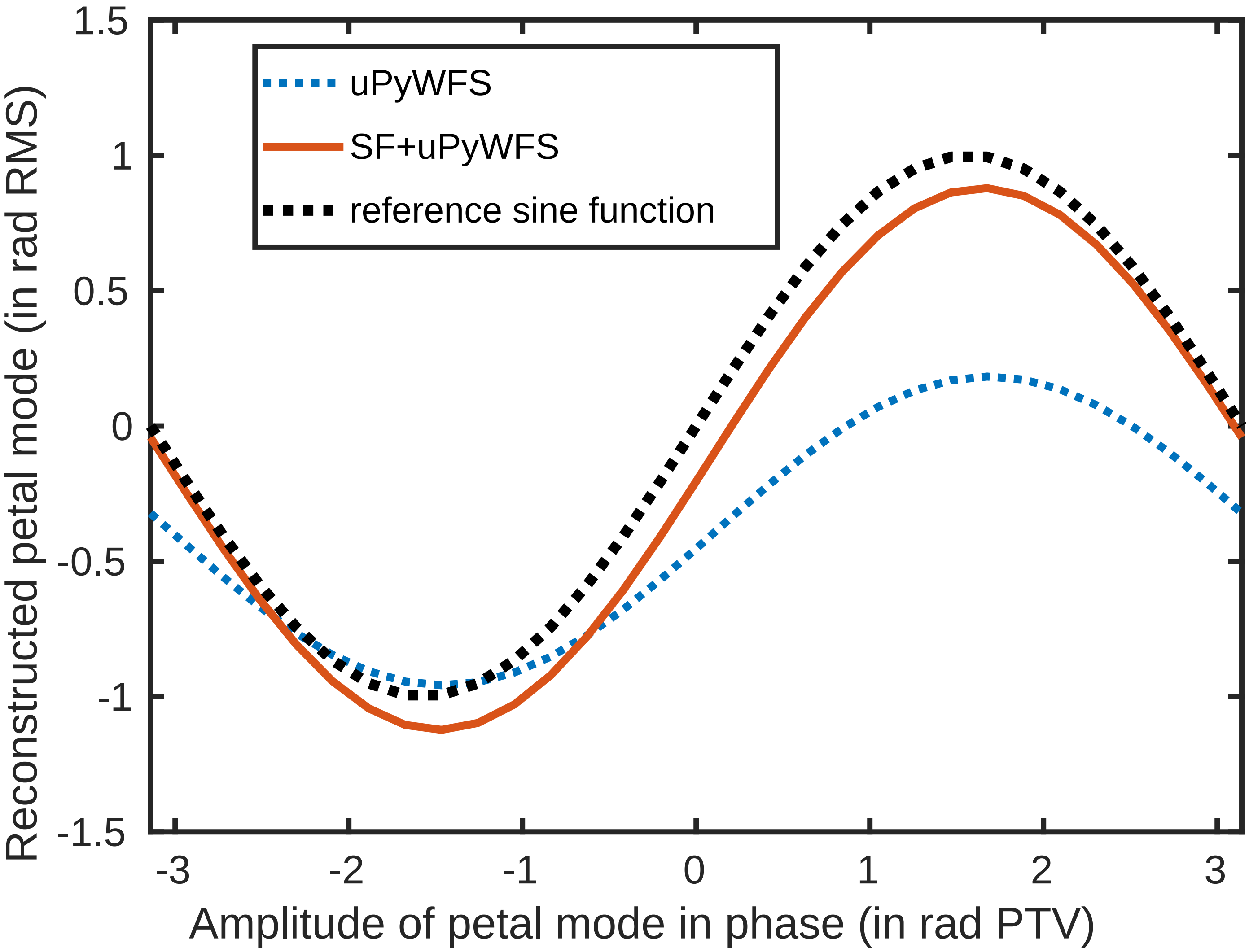

Fig. 10: Comparison of the petal mode reconstruction between a uPyWFS and SF+uPyWFS

under the spatial frequency of the phase mode. **In Figure 11b we computed the sensitivity of different SF+uPyWFS compated to uPyWFS (dark red curve).** These two effects make the measurement of petal mode with a SF+uPyWFS more accurate, as is visible with multiple different residuals in Figure 12. Compared to Figure 5, the petal mode reconstruction is closer to the expected sinus reconstruction when using a SF+uPyWFS.

5. Performance on an AO system assisted by a petallometer

Finally we simulate the full system of the 2-path sensor to test the proposed concept of petalometer as presented in Figure3. We compare an uPyWFS and a SF+uPyWFS. The full system is described previously in Part 3. The AO first path sensor (a modulated PyWFS) controls the DM (with simple gaussian continuous influence functions, 20x20 actuators), so it creates minioning type petal residuals. The petalometer commands an hypothetical DM with a pure petal mode as influence function. We subtract the atmospheric petal mode at frame 0 from the atmospheric phase screen during the whole loop to start from a 0 petal. Measuring the petal with a SF+uPyWFS is equivalent to using the pyramid in a full aperture gain mode. With an optimized sensor, we can at least expect a flux distribution between AO-WFS and petal-WFS of 4000 / 6: number of modes used for AO, and number of petal modes. This would turn into a very small reduction (1/1000th in flux) in term of system limit magnitude. On top of this, the characteristic times might be different between petal mode and atmosphere mode, depending on their origin. If the petal mode is slow enough (like LWE for instance), its measurement can be averaged with time on a few frames of AO loop, allowing to reduce furthermore the flux taken for the petalometer path. Since we are using monochromatic PyWFS the best possible result is to have petal mode locked at its initial value (zero) during the whole simulation. A bad petalometer would not be able to lock the petal mode at a stable value. Furthermore, we add (starting at frame 400 = 0.4ms of simulation a 300nm RMS static petal mode in the atmospheric phase. The aim is to test if our proposed strategy can measure and compensate for petal mode from other sources than the atmosphere. The parameters are the same as in Table 1 and cover a $1s$ simulation. the results in RMS error and projected on petal mode are shown in Figure 13 and 14 respectively

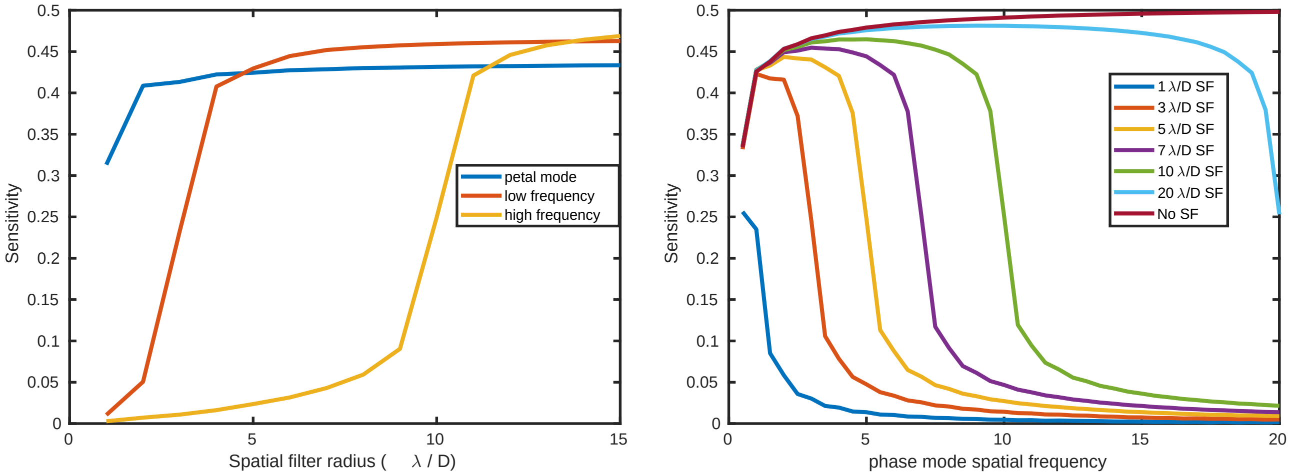

(a) Comparison of sensitivity of 3 modes for various spatial filter radius. Low spatial frequency is a $3\lambda/D$ sinus and high spatial frequency is $10\lambda/D$ sinus

(b) **Comparison of sensitivity to pure spatial frequency modes. We see that the SF+uPyWFS has the same sensitivity as the uPyWFS until the spatial frequency are close to the SF radius.**

Fig. 11: **Effect of spatial filter on sensitivity. a) For a given mode how the size of spatial filter affects its sensitivity b) How much sensitivity a given spatial filter size for different spatial frequency of phase mode**

The result shows that our continuous influence functions allows the petal mode to stay around zero with the petal flares. The residuals are mostly dominated by fitting error (dotted red line) + petal mode. But if an exterior petal mode is added during the simulation it is not measured and remains uncorrected as shown by the difference between the green and dotted green line (respectively with and without the 300nm petal mode jump). The uPyWFS is not a good petalometer: due to the first path residuals it does not measure correctly the petal mode and jumps randomly of 2π petal mode value. We have shown that the SF+uPyWFS is able to measure correctly the petal mode surrounded by AO residuals, and to use this measurement in a correction loop. Moreover it is able to measure a sudden petal mode jump during the whole simulation. This 2-path system allows the AO to stay as close from its theoretical limit.

6. Conclusion

When the 30m-Class telescopes sill be completed and take their first scientific images, the petal mode will most certainly be an issue. Either for first light instrument where LWE is not controled or for 2nd generation instrument and in particular ExAO where the current petal is unacceptable. The aim of this article is to propose a way to measure and control the petal mode in the loop using visible light. For this aim **we study** a 2-path system with one sensor dedicated to atmospheric turbulence measurement and a second one dedicated to the measurement of the petal mode. As a first proposed implementation we simulate a 2 path system using a modulated PyWFS for the atmospheric control and an uPyWFS as the petalometer. We show that the residuals of the first path still prevent the accurate reconstruction of the petal mode even by an uPyWFS. Another step is needed to reconstruct accurately the petal mode. By analysing the spatial structure of the residuals and the petal mode we show that a focal plane spatial filter can improve significantly the petal mode reconstruction. After simulation and optimization of the spatial filter size the spatial filter seems to greatly improve our reconstruction. With end-to-end simulation we confirm its interest as a petalometer, precise enough to lock petal mode during the AO loop and capable of measuring unexpected petal flares. The next steps are three fold. First the spatial filtering assisted reconstruction of petal mode should be tested on bench then on-sky using respectively the LOOPS bench at Laboratoire d'Astrophysique de Marseille and the PAPYRUS instrument at Observatoire de Haute Provence. Other potential petalometer solutions can be proposed and would surely benefit from the spatial filtering step as well (interferometric measurement with a adapted number of observables). Finally the solution must also be optimized to real system: ELT and GMT proposed SCAO systems to prepare for the second generation of instruments.

Acknowledgements. This work benefited from the support of the the French National Research Agency (ANR) with WOLF (ANR- 18-CE31-0018), APPLY (ANR-19-CE31-0011) and LabEx FOCUS (ANR-11-LABX-0013) the Programme Investissement Avenir F-CELT (ANR-21-ESRE-0008), the Action Spécifique Haute Résolution Angulaire (ASHRA) of CNRS/INSU co-funded by CNES, the ECOS-CONYCIT France-Chile cooperation (C20E02), the ORP H2020 Framework Programme of the European Commission's (Grant number 101004719) and STIC AmSud (21-STIC-09)

References

A. Bertrou-Cantou. *Validation Des Composants Clefs de l'optique Adaptative de Première Lumière de l'instrument MICADO Pour l'ELT.* These en préparation, Université de Paris (2019-....), 2021.

A. Bertrou-Cantou, E. Gendron, G. Rousset, F. Ferreira, A. Sevin, F. Vidal, Y. Clénet, T. Buey, and S. Karkar. Petalometry for the ELT: Dealing with the wavefront discontinuities induced by the telescope spider. In *Adaptive Optics Systems VII*, volume 11448, pages 213–224. SPIE, December 2020. .

A. Bertrou-Cantou, E. Gendron, G. Rousset, V. Deo, F. Ferreira, A. Sevin, and F. Vidal. Confusion in differential piston measurement with the pyramid wavefront sensor. *Astronomy & Astrophysics*, 658:A49, February 2022. ISSN 0004-6361, 1432-0746. .

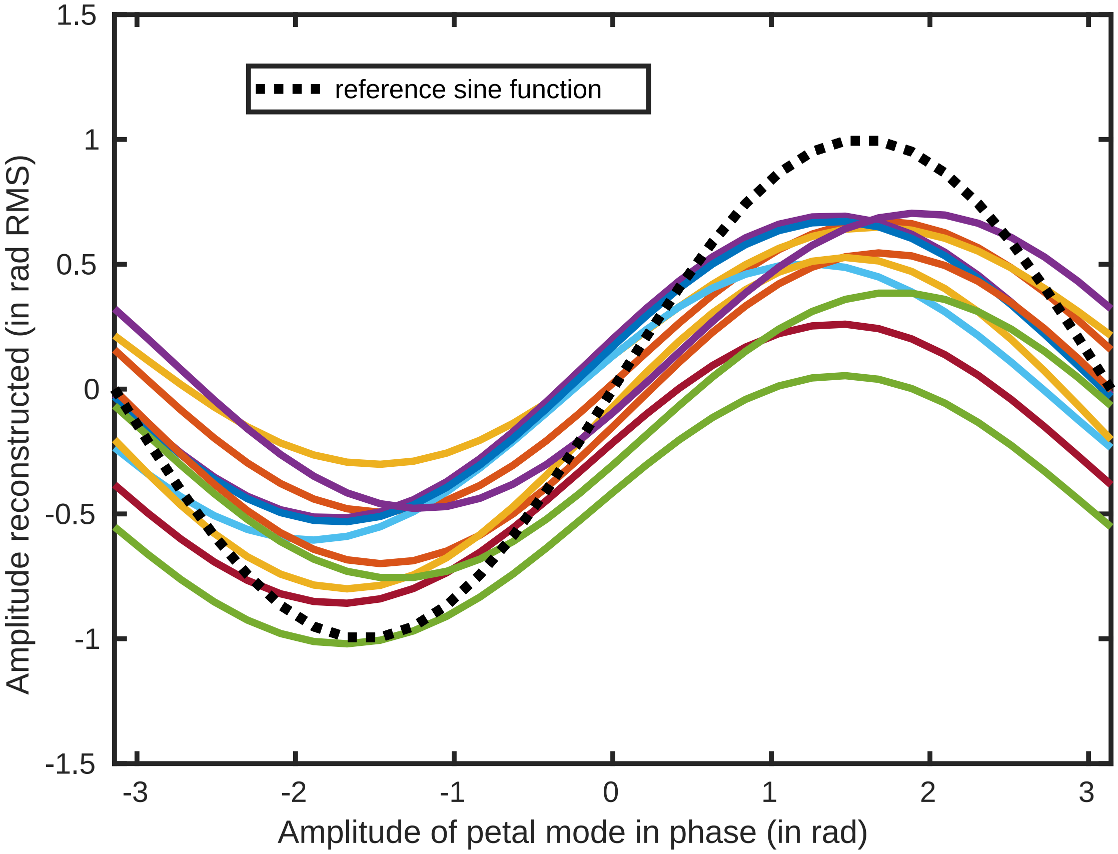

(a) Petal mode reconstruction with 10 independent residuals with uPyWFS presented earlier (Figure 5

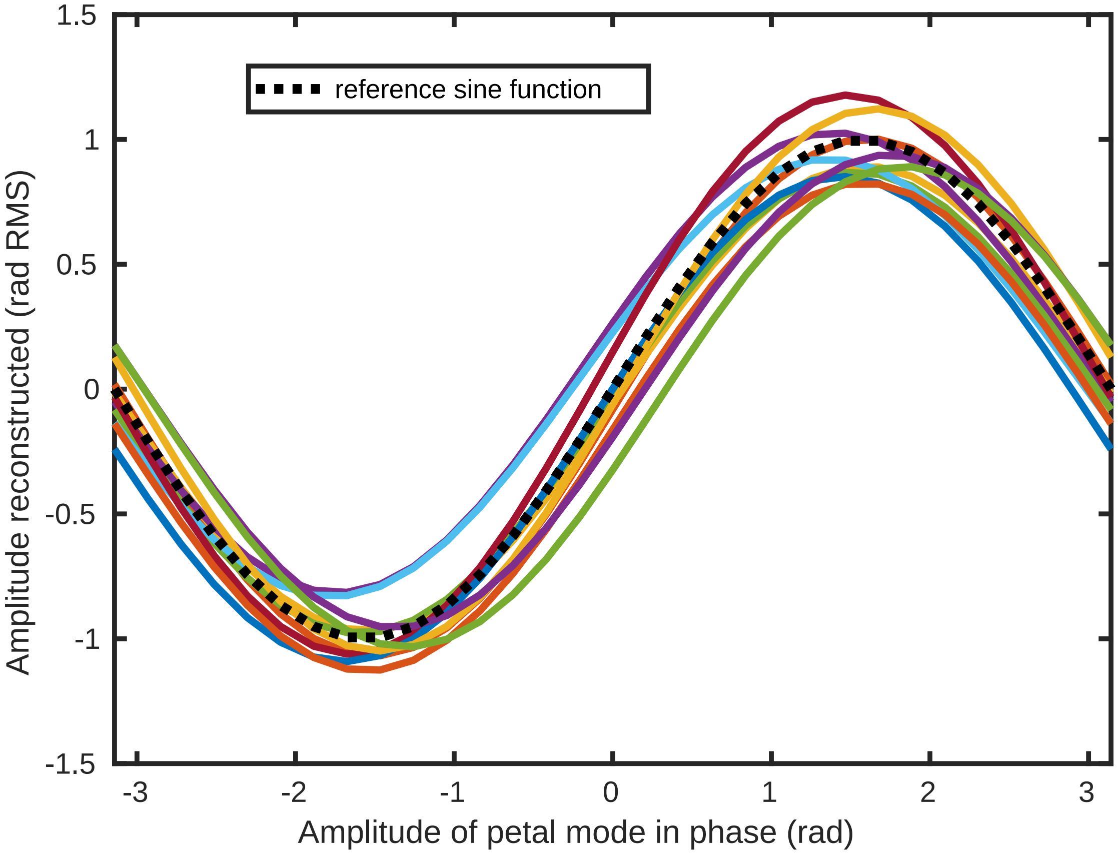

(b) Petal mode reconstruction with 10 independent residuals with SF+uPyWFS

Fig. 12: Petal mode reconstruction with 10 independent 1st path residuals. Comparison between uPyWFS and SF+uPyWFS behaviour. The optical gain are greatly reduced as well as the petal confusion (reduced by a mean of a factor 6

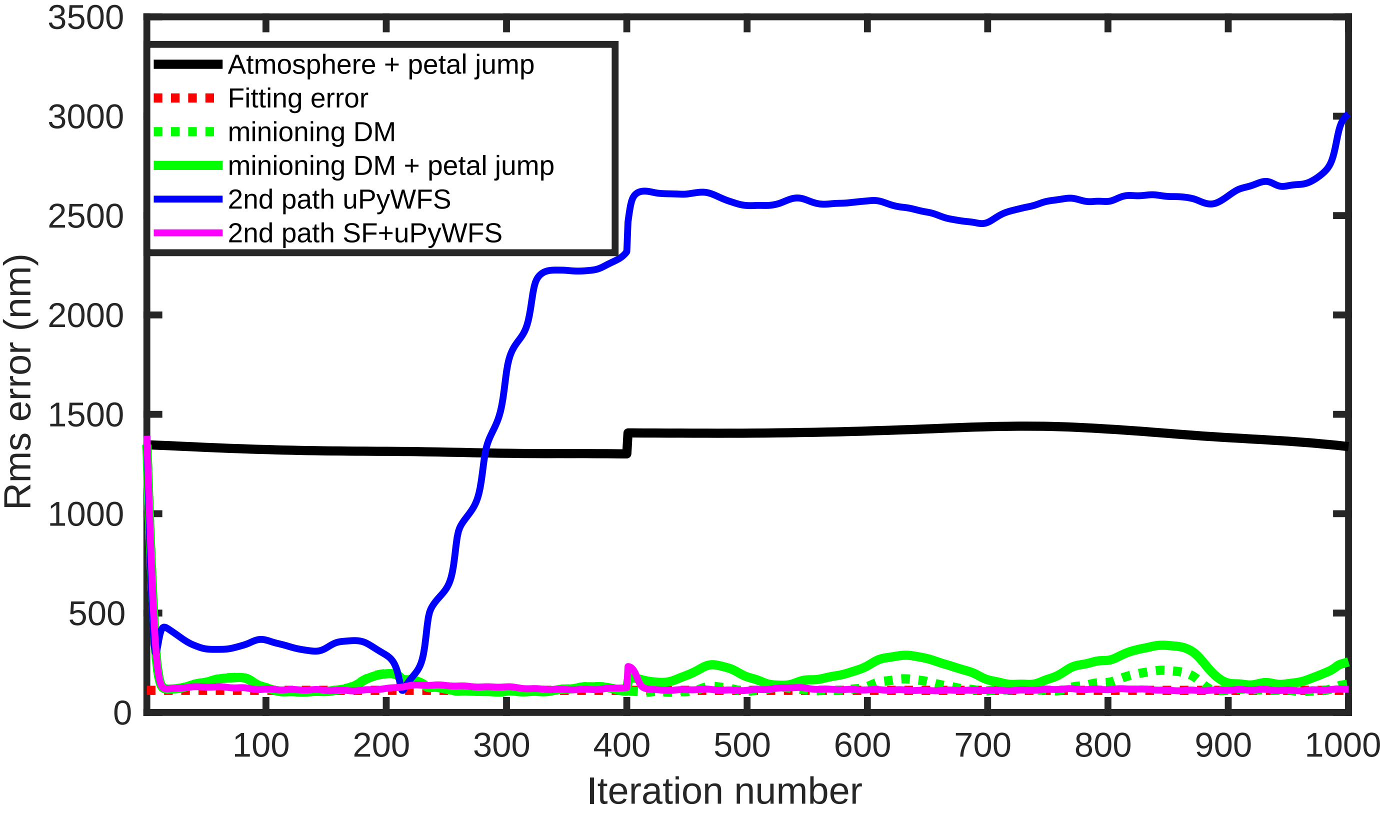

Fig. 13: RMS error from atmosphere in black, first path AO residuals in green, first path assisted by uPyWFS-petalometer in blue and first path assisted by SF+uPyWFS-petalometer in magenta. A pure petal mode is added at frame 400 of 300nm PTV to simulate a petal mode exterior to the atmosphere. We see regular flares of the first path PyWFS while the SH+uPyWFS helps to keep the residual stable around zero petal during the whole sequence

C. Bond, JF. Sauvage, N. Schwartz, N. Levraud, V. Chambouleyron, C. Correia, T. Fusco, and B. Neichel. HARMONI at ELT: Wavefront control in SCAO mode. In *SPIE Astronomical Telescopes + Instrumentation*. SPIE, July 2022. .

S. Bonnefond, M. Tallon, M. Le Louarn, and PY. Madec. Wavefront reconstruction with pupil fragmentation: Study of a simple case. In E. Marchetti, L. Close, and JP. Véran, editors, *SPIE Astronomical Telescopes + Instrumentation*, page 990972, Edinburgh, United Kingdom, July 2016. .

B. Carlomagno, C. Delacroix, O. Absil, F. Cantalloube, GO. Xivry, P. Pathak, T. Agocs, T. Bertram, B. Brandl, L Burtscher, D. Doelman, M. Feldt, A. Glauser, S. Hippler, M. Kenworthy, Emiel H. Por, F. Snik, R. Stuik, and R. Boekel. METIS high-contrast imaging: Design and expected performance. *Journal of Astronomical Telescopes, Instruments, and Systems*, 6(3):035005, September 2020. ISSN 2329-4124, 2329-4221. .

M. Cayrel. E-ELT optomechanics: Overview. In L. Stepp, R. Gilmozzi, and H. Hall, editors, *SPIE Astronomical Telescopes + Instrumentation*, page 84441X, Amsterdam, Netherlands, September 2012. .

B. Engler, M. Louarn, C. Vérinaud, S. Weddell, and R. Clare. Flip-flop modulation method used with a pyramid wavefront sensor to correct piston segmentation on ELTs. *Journal of Astronomical Telescopes, Instruments, and Systems*, 8(2):021502, March 2022. ISSN 2329-4124, 2329-4221. .

S. Esposito, E. Pinna, A. Tozzi, P. Stefanini, and N. Devaney. Cophasing of segmented mirrors using the pyramid sensor. In *Astronomical Adaptive Optics Systems and Applications*, volume 5169, pages 72–78. SPIE, December 2003. .

O. Fauvarque. *Optimisation Des Analyseurs de Front d'onde à Filtrage Optique de Fourier*. These de doctorat, Aix-Marseille, September 2017.

O. Fauvarque, B. Neichel, T. Fusco, JF. Sauvage, and O Girault. General formalism for Fourier-based wave front sensing. *Optica*, 3(12):1440–1452, December 2016. ISSN 2334-2536. .

S. Haffert, L. Close, A. Hedglen, J. Males, M. Kautz, A. Bouchez, R. Demers, F. Quiros-Pacheco, B. Sitarski, K. Van Gorkom, J. Long, O. Guyon, L. Schatz, K. Miller, J. Lumbres, A. Rodack, and J. Knight. The Holographic Dispersed Fringe Sensors (HDFS): Phasing the Giant Magellan Telescope, June 2022.

S. Hippler, M. Feldt, T. Bertram, W. Brandner, F. Cantalloube, B. Carlomagno, O. Absil, A. Obereder, J. Shatokhina, and R. Stuik. Single conjugate adaptive optics for the ELT instrument METIS. *Experimental Astronomy*, April 2019. .

L Leboulleux, A. Carlotti, M. N'Diaye, F. Cantalloube, J. Milli, A. Bertrou-Cantou, D. Mouillet, N. Pourré, and C. Vérinaud. Redundant Apodized Pupils (RAP) for high-contrast imagers robust to segmentation-due aberrations and island effects. In *Advances in Optical and Mechanical Technologies for Telescopes and Instrumentation V*, page 63, August 2022. .

D. Martins, R. Holzlöhner, C. Vérinaud, and C. Kleinclaus. Transient wavefront error from cooled air downwind of telescope spiders. In G. Angeli and P. Dierickx, editors, *Modeling, Systems Engineering, and Project Management for Astronomy X*, page 70, Montréal, Canada, August 2022. SPIE. ISBN 978-1-5106-5355-9 978-1-5106-5356-6. .

R. Ragazzoni. Pupil plane wavefront sensing with an oscillating prism. *Journal of Modern Optics*, 43(2):289–293, February 1996. ISSN 0950-0340. .

JF. Sauvage, T. Fusco, A. Guesalaga, P. Wizinowitch, J. O'Neal, M. N'Diaye, A. Vigan, J. Grard, G. Lesur, D. Mouillet, JL. Beuzit, M. Kasper, M. Le Louarn, J. Milli, K. Dohlen, B. Neichel, P. Bourget, P. Heigenauer, and D. Mawet. Low Wind Effect, the main limitation of the SPHERE instrument. 2015. .

N. Schwartz, JF. Sauvage, C. Correia, C. Petit, F. Quiros-Pacheco, T. Fusco, K. Dohlen, K. El Hadi, N. Thatte, F. Clarke, J. Paufique, and J. Vernet. Sensing and control of segmented mirrors with a pyramid wavefront sensor in the presence of spiders. In *Proceedings of the Adaptive Optics for Extremely Large Telescopes 5*. Instituto de Astrofísica de Canarias (IAC), 2017. .

N. Schwartz, JF. Sauvage, C. Correia, B. Neichel, T. Fusco, F. Quiros-Pacheco, K. Dohlen, K. El Hadi, G. Agapito, N. Thatte, and F. Clarke. Analysis and mitigation of pupil discontinuities on adaptive optics performance. In D. Schmidt, L. Schreiber, and L. Close, editors, *Adaptive Optics Systems VI*, page 75, Austin, United States, July 2018. SPIE. ISBN 978-1-5106-1959-3 978-1-5106-1960-9. .

T. Usuda, Y. Ezaki, N. Kawaguchi, K. Nagae, A. Kato, J. Takaki, M. Hirano, T. Hattori, M. Tabata, Y. Horiuchi, Y. Saruta, S. Sofuku, N. Itoh, T. Oshima, T. Takanezawa, M. Endo, J. Inatani, M. Iye, A. Sadjadpour, M. Sirota, S. Roberts, and L. Stepp. Preliminary design study of the TMT Telescope structure system: Overview. In L. Stepp, R. Gilmozzi, and H. Hall, editors, *SPIE Astronomical Telescopes + Instrumentation*, page 91452F, Montréal, Quebec, Canada, July 2014. .

C. Vérinaud. On the nature of the measurements provided by a pyramid wave-front sensor. *Optics Communications*, 233(1):27–38, March 2004. ISSN 0030-4018. .

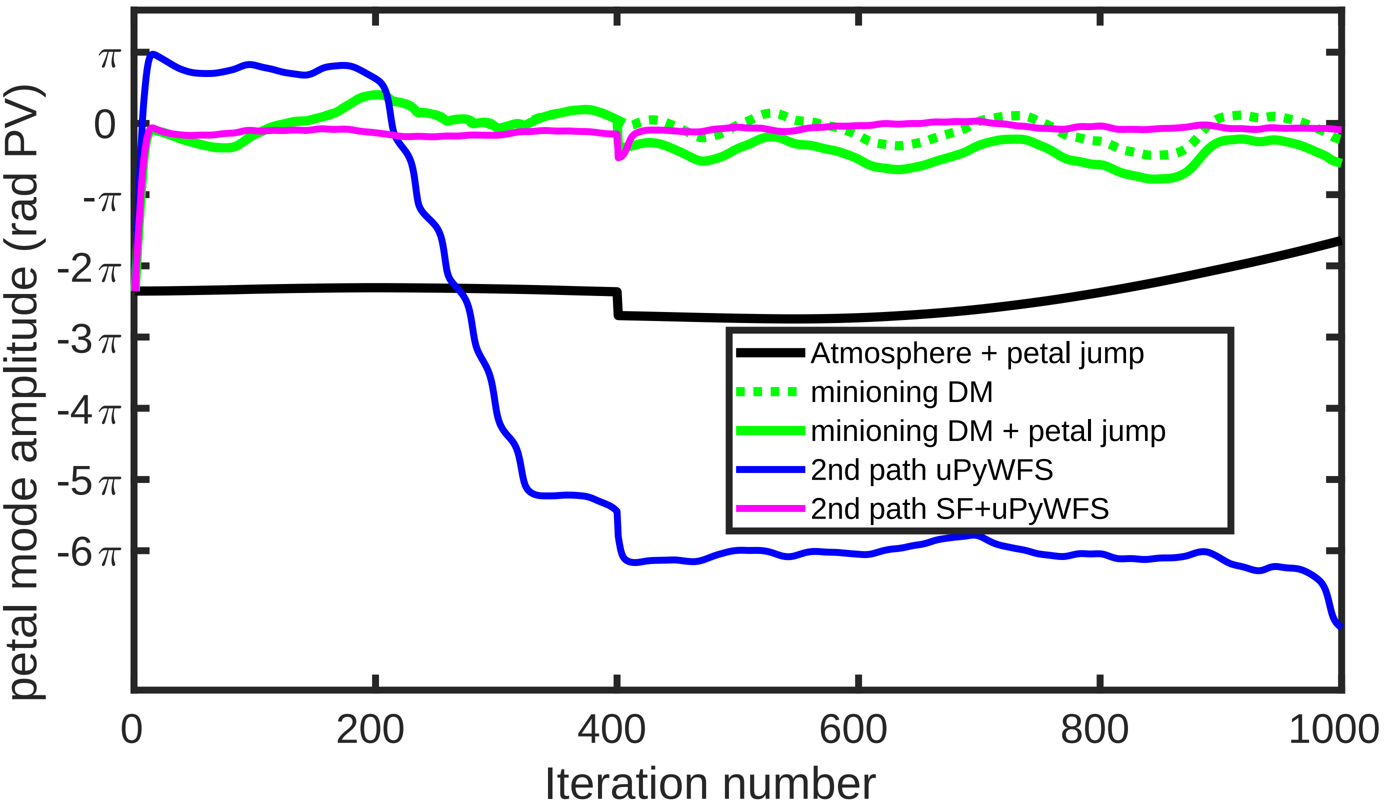

Fig. 14: Residual phase of Figure 13 projected on petal mode. The first path creates petal mode residuals visible as oscillations between $-\pi$ and $+\pi$. uPyWFS keeps the residual petal closer to 0 petal, but with a jump of -6pi (around iteration 250) where it looses it locking of petal, while SF+uPyWFS stays locked around zero petal